TUM

TUM School of Engineering and Design

Energy dissipation by acoustic radiation
A multiphysics approach for damping quantification

Suhaib Koji Baydoun-Hidding

Kurzfassung

Diese Dissertation leistet einen Forschungsbeitrag zur Energiedissipation durch Schallabstrahlung dynamisch belasteter Strukturen. Das Phänomen wird oftmals als *Dämpfung durch Schallabstrahlung* bezeichnet und hat bisher nur wenig wissenschaftliche Beachtung erhalten, obwohl es vor allem bei Leichtbaustrukturen einen beträchtlichen Beitrag zur Gesamtdämpfung leistet. In dieser Arbeit werden neuartige Ansätze zur Bestimmung der Dämpfung durch Schallabstrahlung erarbeitet, welche tiefgreifende Einblicke in dieses Phänomen ermöglichen.

Die Schallabstrahlung ins Fernfeld wird mittels der akustischen Randelementemethode (BEM) modelliert, wodurch lediglich die Oberfläche der Struktur diskretisiert werden muss. Verglichen mit experimentellen Verfahren zur Bestimmung der abgestrahlten Schallleistung, welche eine spezielle Infrastruktur mit begrenztem Anwendungsbereich erfordern, kann BEM in breiteren Frequenzbereichen und für komplexe Geometrien verwendet werden. Die Kombination der BEM mit einem Finite Elemente Modell der Struktur bildet die methodische Grundlage für eine rein numerische Quantifizierung der Dämpfung durch Schallabstrahlung. Zusätzlich wird ein hybrides, auf Simulationen und Experimenten beruhendes Verfahren entwickelt, in welchem die Struktur durch gemessene Übertragungsfunktionen charakterisiert wird. Beide Ansätze - sowohl der rein numerische als auch der hybride - ermöglichen die Berechnung von frequenz- und anregungsabhängigen Verlustfaktoren. Außerdem werden numerische Modalanalysen durchgeführt, um sturktur-akustische Moden und die dazugehörigen modalen Verlustfaktoren zu bestimmen. Diese modalen Verlustfaktoren bieten eine alternative Weise, das Ausmaß der Dämpfung zu quantifizieren, und sind unabhängig von der Frequenz und der Art der Anregung.

Während BEM einerseits eine vielseitig einsetzbare Methode zur Simulation von Schallabstrahlung ist, so birgt sie andererseits den entscheidenden Nachteil frequenzabhängiger Koeffizientenmatrizen, was besondere Herausforderungen bei Modal- und Frequenzgangsanalysen impliziert. Die vorliegende Arbeit widmet sich auch dieser Problematik. So wird ein auf dem Greedy-Algorithmus basierendes Reduktionsverfahren entwickelt, um Frequenzgangsanalysen zu beschleunigen. Die Besonderheit dieses Greedy-Verfahrens liegt in der Auswahl von Frequenzabtastpunkten, welche auf Grundlage eines Optimalitätskriteriums getroffen wird. Des Weiteren wird ein neuartiger Löser für nichtlineare struktur-akustische Eigenwertprobleme entwickelt. Dieser Eigenwertlöser ermöglicht selbst bei schwach ausgeprägter Struktur-Akustik-Interaktion eine akkurate Berechnung modaler Verlustfaktoren und somit eine genaue Quantifizierung der Dämpfung durch Schallabstrahlung.

Abstract

This thesis contributes to the research on the energy dissipation by sound radiation - a phenomenon commonly denoted as *acoustic radiation damping*. Although radiation damping accounts for a significant share in the overall damping of lightweight structures, it has yet received only little attention. Novel methods are developed in this work for quantifying the extent of radiation damping and provide deep insights into this phenomenon.

The far field sound radiation is evaluated using the acoustic boundary element method (BEM), which results in a discretization that is restricted to the submerged surface of the vibrating structure. Compared to an experimental assessment of sound radiation, which requires special facilities with limited scope of application, BEM allows to cover a large frequency intervals and geometrical configurations. The combination of acoustic BEM with the structural finite element model is the methodological basis in this work for a numerical assessment of radiation damping. In addition, a hybrid numerical-experimental method is developed by combining acoustic BEM with structural mobility measurements. Both frameworks - the numerical and the numerical-experimental one - are derived in a unified manner and facilitate computation of frequency and excitation dependent radiation loss factors. Moreover, numerical modal analysis is applied to compute loss factors associated with acoustically loaded structural modes. These modal loss factors are an alternative measure for radiation damping and independent of frequency and excitation.

While BEM is a versatile method for evaluating sound radiation, its advantages come at the cost of frequency dependent coefficient matrices, which impose a significant computational burden when conducting modal analyses or harmonic response analyses. This issue is addressed in this thesis as well. In particular, a novel greedy reduced basis method is developed for accelerating frequency sweeps. Its main feature is the optimal choice of frequency samples so that a small number of snapshots is sufficient to calculate vibroacoustic responses in large frequency ranges. Moreover, a novel strategy for solving nonlinear vibroacoustic eigenvalue problems involving BEM is developed in this thesis. It facilitates accurate computation of modal radiation loss factors even in the case of weak structural acoustic interaction.

Danksagung

Ein großes Dankeschön an alle, die mich auf dem Weg begleitet und unterstützt haben.

Allen voran an meinen Doktorvater Steffen Marburg, dessen riesiges Vertrauen ich während der gesamten Zeit genießen durfte. Gleichzeitig erhielt ich immer den kleinen Anstoß oder Hinweis, der den Stein wieder zum Rollen brachte.

An alle Mitarbeitende am Lehrstuhl, die für den guten Zusammenhalt sorgten und damit eine furchtbare Arbeitsumgebung schufen. Was das Fachliche betrifft, geht mein Dank an Marcus Mäder, der mich in die experimentelle Vibroakustik heranführte und vor allem an Christopher Jelich, der auf der gegenüberliegenden Seite meines Bildschirms sitzend immer ein offenes Ohr für meine Anliegen hatte. Ohne Christopher wäre ich vermutlich noch immer dabei, meinen Code zu debuggen.

An alle (ehemals) Studierende, die meine Forschung durch Ihren Einsatz in Bachelor-, Semester- und Masterarbeiten bereicherten. Allen voran Benedikt Goderbauer, Mateusz Hoffert und Hannes Panzer.

To Valeria Antonelli, with whom I had the pleasure to work together in my first academic job during undergraduate studies. She made me believe in my scientific abilities and certainly played a major role in my decision to apply for a position as a PhD student.

An Matthias Voigt, der mit seinem mathematischen Wissen immer wieder für sehr fruchtbaren Input sorgte. Unser erster gemeinsamer Zeitschriftenartikel hatte seinen Ursprung in ein paar Zeilen Pseudocode, die Matthias auf einem losem Stück Papier notierte. Ein eindrucksvoller Beweis dafür, wie sehr die Ingenieurswissenschaften und die Mathematik voneinander profitieren können.

To Bert Roozen, who has supervised the experimental part of my PhD project and helped me to overcome my hesitation to do measurements. In the end, doing measurements was even enjoyable.

An meine Eltern, die auch zu Schulzeiten immer an meine akademische Befähigung glaubten, und auf deren bedingungslose Unterstützung ich mich immer verlassen konnte.

An Florian Albrecht. Unsere Mechanikdiskussionen auf den langen Autofahrten in südliche Klettergebiete werden unvergessen bleiben. Am Ende waren wir nicht nur (Studien-)Freunde und Kletterpartner, sondern auch Koautoren.

An alle weiteren Familienmitglieder, Freunde und Kletterpartner, die in den Jahren für einen gesunden Ausgleich zu meiner Arbeit sorgten.

Und an Aaltje, der ich in den letzten sechs Jahren so viel zu verdanken habe, dass jeder Versuch, es hier zusammenzufassen, dem nicht gerecht werden würde. Ich freue mich auf unsere Zukunft mit Aliya und allem, was noch auf uns zukommen wird.

Contents

x

1 Introduction

During the last decades, the use of lightweight materials and structures has constantly increased in many technical applications. Pioneered by the aerospace industry, lightweight design has soon become an essential concept in automotive, naval and civil engineering with the view to reduce environmental impact and operational costs. While these structures demand for high stiffness and strength relative to their mass in order to retain functionality, exactly these properties make them prone to unwanted vibrations. In this regard, engineers exploit various energy dissipating mechanisms in order to mitigate unwanted vibrations and associated implications. The different approaches range from the application of materials with high inherent damping [1] to the use of special devices such as particle dampers [2] and electrorheological valves [3].

This thesis focuses on another, often overlooked damping phenomenon, commonly referred to as *acoustic radiation damping*. That is the dissipation of vibrational energy by far field sound radiation, which often accounts for a significant share in the overall damping of lightweight structures. While radiation damping in most cases is rather understood as a side effect than a deliberately introduced damping mechanism, it nevertheless requires accurate quantification. In fact, attempts to deliberately mitigate vibrations by means of damping devices are only effective, if the extent of added damping is at least within the same order of magnitude as radiation damping [4]. Considering the effect of radiation damping is crucial in order to accurately reflect the vibroacoustic behavior in simulations.

Early theoretical methods for assessing radiation damping of rectangular plates date back to the 1960s [5, 6]. These methods either apply to certain resonant modes of the plate [5, 7], or they determine frequency-averaged damping values based on principles of power flow [6, 8], assuming a sufficiently high modal density of the plate. A couple of decades later, those theoretical expressions have been extended to plates with arbitrary boundary conditions [9], and to configurations in which air flow occurs between the two sides of the plate [10]. Analytical expressions for modal radiation damping of cylindrical shells have been derived as well [11]. Although many structures can be treated as plates or cylinders as first approximation, the increasing complexity of lightweight design also demands more versatile approaches for assessing radiation damping. This is particularly important in the low frequency range, where frequency-averaged, energy-based expressions

[8, 12] fail due to well-separated modes, where idealized assumptions such as *baffled* or *unbaffled* are insufficient, and where sound radiation is strongly dependent on the actual mounting condition of the structure at hand. The applicability of the above-mentioned theoretical expressions to more complicated geometries and to inhomogeneous materials is also difficult to judge.

Besides, a few experimental approaches for assessing radiation damping have been reported in the last decades. The earliest and perhaps most intuitive experimental method is based on reference measurements inside a vacuum chamber [13, 14]. Clarkson and Brown obtained damping values of a satellite structure by relating the input power of a shaker to the spatially averaged velocity [13]. By performing the same measurements at ambient pressure and in-vacuo, they were able to differentiate between acoustic radiation damping and other sources of dissipation.

Zhou and Crocker followed a different experimental approach and determined radiation damping of sandwich panels based on the principles of power flow [15]. Their analysis covered panels that were mounted in a window between two reverberation chambers as well as freely hanging panels. The radiation loss factors were obtained by measuring both the surface velocity and the sound pressure in the receiving room.

Compared to theoretical expressions for radiation damping, both of these experimental methods allow to consider geometries that are more complex and also to accurately reflect elastic properties. If the measurements are conducted in the actual mounting condition, even the effect of the boundary conditions is realistically included. However, in many cases the experimental set-up represents a vast approximation of the practical application. For example, the fitting of a specimen into the window cut-out of a sound transmission facility hardly resembles the actual mounting condition [16]. Moreover, both a vacuum chamber and a window test rig restrict the size and dimension of the specimen. Even if a vacuum chamber can accommodate the specimen, it might be cumbersome to capture the motion of all surfaces by scanning laser Doppler vibrometry (LDV). Another major limitation of experimental assessment of radiation damping concerns excitation by diffuse incident acoustic fields: Vacuum chamber measurements naturally prohibit acoustic excitation and even in reverberation rooms, the diffuseness of a sound field is impaired by modal behavior in the low frequency range [17, 18].

The main purpose of this thesis is to extend the currently available techniques for assessment of radiation damping. To this end, existent and newly developed numerical methods are introduced to accompany the above-mentioned experimental methods as well as to replace experiments altogether. Most of the theoretical content of this thesis revolves around the acoustic boundary element method (BEM) - a powerful tool for analyzing sound radiation [19]. Combining BEM with a structural simulation model [20] or with an experimental characterization of structural mobility [21, 22] sheds a new light on the phenomenon of acoustic radiation damping.

The use of BEM in the context of this thesis offers some advantages compared to other approaches for evaluating sound radiation. Where domain-based numerical methods such as the finite element method (FEM) [23] necessitate special treatments for truncating the far field sound radiation [24, 25], BEM results in a discretization that is restricted to the submerged surface of the structure. Moreover, compared to experimental approaches, which require special facilities with limited scope of application, application of BEM allows to cover a large range of frequencies and geometrical configurations. However, those advantages come at the cost of frequency dependent coefficient matrices, which impose a significant computational burden when conducting modal analyses or harmonic response analyses [26].

Modal analyses are widely used for acquiring the dynamical behavior of structures as they provide structure-inherent properties such as vibration modes and eigenfrequencies [27]. When considering the structure as vibrating in-vacuo, modal analysis only requires solving a linear eigenvalue problem (EVP). However, the study of acoustic radiation damping requires including the effect of acoustic loading in the modal analysis of the structure. In this way, modal damping values associated with the radiation damping of each vibration mode can be obtained [20]. Moreover, the resulting (wet) eigenfrequencies can be significantly shifted compared to the in-vacuo eigenfrequencies. The downside of modal analyses including acoustic loading is that they require solution of the underlying nonlinear EVP, since the boundary element matrices implicitly depend on the eigenfrequency parameter.

Besides the aforementioned modal values for radiation damping, harmonic radiation loss factors represent an alternative measure for radiation damping and are obtained by frequency-wise response analyses [20]. The frequency-wise evaluation of loss factors is particularly important for structures that exhibit significant radiation damping in the low frequency range, where the modes are well separated. In those cases, the extent of radiation damping is strongly dependent on the given excitation, which may stem from structural forces or incident acoustic fields. Harmonic response analyses in vibroacoustic simulations are associated with a significant computational burden, since they require a solution of a linear system at each frequency point of interest.

Although acoustic radiation damping can significantly influence structural vibrations, it is presently not taken into account in vibroacoustic simulations by most engineers. Furthermore, even when there is awareness of the phenomenon of radiation damping, it is still either neglected altogether or addressed by general damping models without physical basis. This hesitation may be attributed to the above-mentioned computational challenges that go along with modal analyses and harmonic response analyses. In this thesis, latest developments in the field of numerical linear algebra are employed to mitigate these issues and thereby pave the way to a computationally efficient assessment of radiation damping. In particular, this thesis contributes to the research on radiation

damping in the following aspects:

- First, a numerical framework based on FEM and BEM is applied for the quantification of radiation damping by means of harmonic response analyses as well as modal analyses [20].

- Second, a hybrid numerical-experimental framework is developed for an in-situ assessment of radiation damping. It is based on mobility measurements and acoustic BEM [22].

- Third, frequency sweeps in vibroacoustic simulations are accelerated by a greedy reduced basis scheme [28].

- Last, a subspace iteration method based on rational Cauchy approximation is developed for an efficient numerical modal analysis of vibroacoustic systems. The method facilitates an accurate computation of modal radiation loss factors [29].

2 Assessment of acoustic radiation damping in free and forced vibrations

2.1 Numerical formulation of structural acoustic interaction

This section describes a fully coupled numerical formulation for modeling the vibrations of solid structures interacting with the surrounding acoustic field. It represents the methodological basis for three of the main achievements accumulating to this thesis - namely the numerical investigation of radiation damping (Sec. 3.1), the greedy algorithm (Sec. 3.2) and the vibroacoustic eigensolver (Sec. 3.3). The mesh coupling procedure presented below is also part of the newly developed numerical-experimental framework (Sec. 3.4).

In the upcoming derivations, a harmonic time dependency of $e^{-\mathrm{i}\omega t}$ is assumed, where $\mathrm{i} = \sqrt{-1}$, the angular frequency is $\omega = 2\pi f$ and t denotes the time. The vibrations of solid structures are described by the equations of linear elasticity. After discretization by FEM, the resulting system of equations reads [30]

$$\left(\mathbf{K} - \mathrm{i}\omega\mathbf{D} - \omega^2\mathbf{M}\right)\mathbf{u} = \mathbf{f}_\mathrm{s} + \mathbf{f}_\mathrm{f}, \tag{2.1}$$

in which the unknown vector $\mathbf{u}$ contains the displacement degrees of freedom (DOF) at the nodes. The stiffness, damping and mass matrices are denoted by $\mathbf{K}$, $\mathbf{D}$ and $\mathbf{M}$, respectively. Structural damping can be included by a hysteretic damping model with [27, 31]

$$\mathbf{D} = \frac{\eta_\mathrm{s}}{\omega}\mathbf{K}, \tag{2.2}$$

which would result in a frequency independent damping force. The hysteretic loss factor is denoted by η_s. Note that other damping models such as viscous damping [31] could be used as well. The structure is excited by a combination of structural forces $\mathbf{f}_\mathrm{s}$ and fluid forces $\mathbf{f}_\mathrm{f}$. The latter act by virtue of the sound pressure field, which is characterized by the inhomogeneous Helmholtz equation [32]

$$\Delta p(\mathbf{x}) + \frac{\omega^2}{c^2}p(\mathbf{x}) = -q, \tag{2.3}$$

5

in which q is the source and c refers to the speed of sound. The (complete) sound pressure solution is the sum of the scattered solution p^s and the incident solution p^i. The same applies to the fluid particle velocity v_f, i.e.

$$p(\mathbf{x}) = p^s(\mathbf{x}) + p^i(\mathbf{x}) \tag{2.4}$$

$$v_f(\mathbf{x}) = v_f^s(\mathbf{x}) + v_f^i(\mathbf{x}). \tag{2.5}$$

Reformulation of Eq. (2.3) by the Kirchoff integral theorem and collocation discretization using boundary elements yields the linear system of equations [32]

$$\mathbf{H}(\omega)\mathbf{p} = \mathbf{G}(\omega)\left(\mathbf{v}_f - \mathbf{v}_f^i\right) + \mathbf{H}(\omega)\mathbf{p}^i \tag{2.6}$$

for the description of the acoustic field. Therein, $\mathbf{p}$ is the unknown vector containing the complete sound pressure solution at the nodes. The frequency dependent coefficient matrices $\mathbf{H}(\omega)$ and $\mathbf{G}(\omega)$ relate the fluid particle velocity $\mathbf{v}_f$ to the sound pressure. Acoustically rigid baffles can be taken into account by evaluating $\mathbf{H}(\omega)$ and $\mathbf{G}(\omega)$ using a half-space formulation with a modified Green's function [33]. The incident sound pressure field is denoted by $\mathbf{p}^i$ and the corresponding incident particle velocity is $\mathbf{v}_f^i$.

Equation (2.6) is the most general formulation for considering acoustic sources when using BEM. Besides, an alternative formulation can be derived for full-space problems based on consideration of the integral equation in the complementary (interior) acoustic domain yielding [32]

$$\mathbf{H}(\omega)\mathbf{p} = \mathbf{G}(\omega)\mathbf{v}_f + \mathbf{p}^i. \tag{2.7}$$

This thesis particularly focuses on problems that involve a strong mutual interaction between the vibrating structure and the surrounding acoustic field. In such cases, it is insufficient to compute the in-vacuo response of the structure by solving Eq. (2.1) and to subsequently determine the sound pressure field via Eq. (2.6) (Eq. (2.7) respectively). Instead, normal tractions due to the acoustic sound pressure need to be considered as well besides the continuity condition. The two coupling conditions on the sound radiating surface are expressed as

$$\mathbf{f}_f = \mathbf{C}_{sf}\mathbf{p}, \quad \text{and} \quad \mathbf{v}_f = -\mathrm{i}\omega\mathbf{C}_{fs}\mathbf{u}, \tag{2.8}$$

in which the matrices $\mathbf{C}_{sf}$ and $\mathbf{C}_{fs}$ establish the coupling between the structural and the acoustic

subdomains. They are obtained by a Galerkin projection and defined as [34]

$$\mathbf{C}_{\mathrm{sf}} = \int_{\Gamma} \mathbf{N}_{\mathrm{s}}^{\mathrm{T}} \mathbf{n}_{\Gamma} \mathbf{N}_{\mathrm{f}} \mathrm{d}\Gamma, \tag{2.9}$$

$$\mathbf{C}_{\mathrm{fs}} = \mathbf{\Theta}^{-1} \mathbf{C}_{\mathrm{sf}}^{\mathrm{T}}. \tag{2.10}$$

The interpolation functions $\mathbf{N}_{\mathrm{f}}$ and $\mathbf{N}_{\mathrm{s}}$ are defined for boundary element (BE) and finite element (FE) nodes and approximate the sound pressure and displacement on the coupling interface Γ. Nodal normal vectors $\mathbf{n}_{\Gamma}$ are defined for each BE node and point inside the structural subdomain. Moreover, $\mathbf{\Theta}$ is the boundary mass matrix of the acoustic subdomain and given by

$$\mathbf{\Theta} = \int_{\Gamma} \mathbf{N}_{\mathrm{f}}^{\mathrm{T}} \mathbf{N}_{\mathrm{f}} \mathrm{d}\Gamma. \tag{2.11}$$

Discontinuous boundary elements are employed, and hence, the acoustic and the structural nodes do not coincide. Moreover, for the sake of computational efficiency, different mesh sizes may be used for each of the subdomains. In the latter case, it is not possible to evaluate the integral in Eq. (2.9) element-wise, since the interpolation functions $\mathbf{N}_{\mathrm{f}}$ are not continuously defined across the structural finite elements. The same holds for $\mathbf{N}_{\mathrm{s}}$ and the acoustic boundary elements. To overcome this issue, a Mortar coupling for non-conforming meshes is applied [34, 35], in which the structural elements are defined as the slave elements, and the boundary elements are defined as the master elements. A search algorithm based on the advancing front method [36] identifies pairs of overlapping elements. The master element is then projected onto an auxiliary plane that is defined based on the slave element. The resulting intersection polygon is found by a simplex search method and then subdivided into triangular elements, over which integration in Eq. (2.9) can be performed. The coupling procedure is illustrated in Fig. 1.

Structural acoustic interaction is a particularly relevant aspect in thin-walled structures, which are usually discretized by shell finite elements. Some applications, such as sandwich structures with a thick core, however require discretization by solid finite elements in order to capture thickness deformations. Since a direct BE formulation is used in this thesis, the acoustic mesh has to cover a closed surface, regardless of whether shell or solid finite elements are employed.

The above-described coupling procedure is derived with the purpose of coupling an FE to a BE model. But actually, its applicability is more versatile and it can also be used to exchange experimentally obtained quantities with a numerical model. In the hybrid numerical-experimental framework described in Sec. 3.4, coupling matrices similar to the ones in Eqs. (2.9) and (2.10) are set up in order to couple an experimentally obtained structural transfer matrix to an acoustic BE model [22].
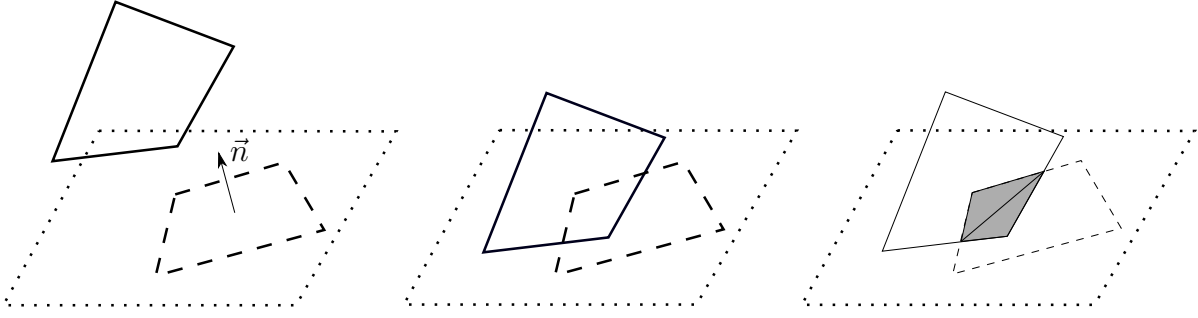
Figure 1: Schematic of the mortar projection of a master fluid element (solid) onto the auxiliary plane (dotted) defined by an overlapping slave structural element (dashed) and subsequent definition of triangular integration cells (filled in grey). This figure is adopted from [22].

Combining Eqs. (2.1), (2.7) and (2.8) yields the fully coupled linear system

$$
\begin{bmatrix}
\mathbf{K} - \mathrm{i}\omega\mathbf{D} - \omega^2\mathbf{M} & -\mathbf{C}_{\mathrm{sf}} \\[2ex]
\mathrm{i}\omega\mathbf{G}(\omega)\mathbf{C}_{\mathrm{fs}} & \mathbf{H}(\omega)
\end{bmatrix}
\begin{bmatrix}
\mathbf{u} \\[2ex]
\mathbf{p}
\end{bmatrix}
=
\begin{bmatrix}
\mathbf{f}_{\mathrm{s}} \\[2ex]
\mathbf{p}^{\mathrm{i}}
\end{bmatrix}. \tag{2.12}
$$

Note that a similar system of equations can be derived using the alternative formulation of acoustic sources given by Eq. (2.6). When the structure interacts with two independent acoustic fields separated by an acoustically rigid baffle, the coupled linear system reads

$$
\begin{bmatrix}
\mathbf{K} - \mathrm{i}\omega\mathbf{D} - \omega^2\mathbf{M} & -\mathbf{C}_{\mathrm{sf}}^{(\mathrm{I})} & -\mathbf{C}_{\mathrm{sf}}^{(\mathrm{II})} \\[2ex]
\mathrm{i}\omega\mathbf{G}^{(\mathrm{I})}\mathbf{C}_{\mathrm{fs}}^{(\mathrm{I})} & \mathbf{H}^{(\mathrm{I})} & \mathbf{0} \\[2ex]
\mathrm{i}\omega\mathbf{G}^{(\mathrm{II})}\mathbf{C}_{\mathrm{fs}}^{(\mathrm{II})} & \mathbf{0} & \mathbf{H}^{(\mathrm{II})}
\end{bmatrix}
\begin{bmatrix}
\mathbf{u} \\[2ex]
\mathbf{p}^{(\mathrm{I})} \\[2ex]
\mathbf{p}^{(\mathrm{II})}
\end{bmatrix}
=
\begin{bmatrix}
\mathbf{f}_{\mathrm{s}} \\[2ex]
\mathbf{p}^{\mathrm{i}} \\[2ex]
\mathbf{0}
\end{bmatrix}, \tag{2.13}
$$

where $(\cdot)^{(\mathrm{I})}$ and $(\cdot)^{(\mathrm{II})}$ denote the respective sides of the baffle. Equation (2.13) only considers an incident sound field on one side of the structure, which actually resembles the situation in many practical applications, in which the second side is considered as the receiving side. If the geometry of the structure is symmetric about the plane of the baffle, the BE matrices are identical, i.e. $\mathbf{H}^{(\mathrm{I})} = \mathbf{H}^{(\mathrm{II})}$ and $\mathbf{G}^{(\mathrm{I})} = \mathbf{G}^{(\mathrm{II})}$ hold.

Forming the Schur complement of $\mathbf{H}(\omega)$ and thereby eliminating the pressure DOFs from Eq. (2.12)

yields [37]

$$\left[\mathbf{K} - \mathrm{i}\omega\mathbf{D} - \omega^2\mathbf{M} + \mathrm{i}\omega\mathbf{C}_{\mathrm{sf}}\mathbf{H}^{-1}(\omega)\mathbf{G}(\omega)\mathbf{C}_{\mathrm{fs}}\right]\mathbf{u} = \underbrace{\mathbf{f}_{\mathrm{s}} + \mathbf{C}_{\mathrm{sf}}\mathbf{H}^{-1}(\omega)\mathbf{p}^{\mathrm{i}}}_{\mathbf{f}_{\mathrm{t}}}, \qquad (2.14)$$

which can be interpreted as a structural equation with an additional term corresponding to the mass and damping contributions of the fluid. The total force vector $\mathbf{f}_{\mathrm{t}}$ in Eq. (2.14) comprises both, structural loading $\mathbf{f}_{\mathrm{s}}$ and acoustic loading due to the incident pressure field $\mathbf{p}^{\mathrm{i}}$. Note that $\mathbf{f}_{\mathrm{t}}$ is of slightly different form when using the alternative formulation of acoustic sources given by Eq. (2.6). A similar structural equation can be derived from the 3×3 block linear system in Eq. (2.13) by eliminating both $\mathbf{p}^{(\mathrm{I})}$ and $\mathbf{p}^{(\mathrm{II})}$.

As an alternative to Eq. (2.14), the displacement DOFs can be eliminated from the block linear system in Eq. (2.12) by forming the Schur complement of $\mathbf{K} - \mathrm{i}\omega\mathbf{D} - \omega^2\mathbf{M}$, which yields

$$\begin{aligned}\left[\mathrm{i}\omega\mathbf{G}(\omega)\mathbf{C}_{\mathrm{fs}}\left(\mathbf{K} - \mathrm{i}\omega\mathbf{D} - \omega^2\mathbf{M}\right)^{-1}\mathbf{C}_{\mathrm{sf}} + \mathbf{H}(\omega)\right]\mathbf{p} = \\ -\mathrm{i}\omega\mathbf{G}(\omega)\mathbf{C}_{\mathrm{fs}}\left(\mathbf{K} - \mathrm{i}\omega\mathbf{D} - \omega^2\mathbf{M}\right)^{-1}\mathbf{f}_{\mathrm{s}} + \mathbf{p}^{\mathrm{i}}.\end{aligned} \qquad (2.15)$$

Equation (2.15) can be interpreted as an acoustic equation including the dynamic behavior of the structure as admittance boundary condition [38, 39]. The proper choice between those two structural acoustic formulations depends on the specific problem at hand and has not yet been discussed comprehensively in the literature. In the case of heavy fluid loading as occurring in underwater applications, many researchers use the acoustic Eq. (2.15) [39–41]. On the other hand, in the context of acoustic radiation damping, it is more intuitive to use the structural Eq. (2.14) and handle the acoustic field as additional mass and damping contributions [20, 37]. Efficient solution strategies for both types of structural acoustic equations are reviewed in Sec. 2.3.2.

2.2 Evaluation of harmonic and modal radiation loss factors

This section reproduces the equations for quantifying acoustic radiation damping, which accounts for one of the main contributions of this thesis. The numerical investigation of radiation damping (Sec. 3.1) as well as the hybrid numerical-experimental framework (Sec. 3.4) are largely based on what follows.

As already anticipated by the title of this section, radiation damping can be quantified by either harmonic or by modal radiation loss factors. The former one is obtained by relating the time-averaged radiated sound power P to the time-averaged total energy E_{tot} of the vibration. The

resulting harmonic loss factor is defined as [42]

$$\eta_{\rm r} = \frac{P}{|\omega E_{\rm tot}|}. \tag{2.16}$$

For harmonic problems, the time-averaged radiated sound power in the continuous setting is defined as

$$P = \frac{1}{2}{\rm Re}\left(\int_\Gamma p v_{\rm f}^* \, {\rm d}\Gamma\right), \tag{2.17}$$

where $(\cdot)^*$ denotes the conjugate complex. Note that only the real part ${\rm Re}\,(\cdot)$ of the complex sound power is associated with radiation damping. The imaginary part of the sound power corresponds to near field sound radiation, which has a mass-like effect on the structure and hence, does not dissipate energy. When the acoustic field is discretized by BEM, the radiated sound power can be obtained from

$$P = \frac{1}{2}{\rm Re}\left(\mathbf{p}^{\rm T}\boldsymbol{\Theta}\mathbf{v}_{\rm f}^*\right). \tag{2.18}$$

The particle velocity $\mathbf{v}_{\rm f}$ can be derived from the structural displacement via the coupling condition (2.8) in a post-processing step. In harmonic problems, the time-averaged total vibrational energy in Eq. (2.16) can be substituted by twice the time-averaged potential energy, which gives [30]

$$E_{\rm tot} = \frac{1}{2}\mathbf{u}^{\rm T}\mathbf{K}\mathbf{u}^* - \frac{1}{2}\mathbf{f}_{\rm t}^{\rm H}\mathbf{u}. \tag{2.19}$$

The first term in Eq. (2.19) is the potential energy due to the elastic deformation. The second term corresponds to the work done by external forces and implicitly includes the dissipated energy. Alternatively, the time-averaged total vibrational energy can be expressed as twice the sum of time-averaged kinetic and dissipated energies of the structural acoustic system, i.e.

$$E_{\rm tot} = \frac{1}{2}\mathbf{u}^{\rm T}\left(\omega^2\mathbf{M} + {\rm i}\omega\mathbf{D} - {\rm i}\omega\mathbf{C}_{\rm sf}\mathbf{H}^{-1}(\omega)\mathbf{G}(\omega)\mathbf{C}_{\rm fs}\right)\mathbf{u}^*. \tag{2.20}$$

Besides the inertial and damping terms corresponding to the structural matrices $\mathbf{M}$ and $\mathbf{D}$, Eq. (2.20) also includes energy contributions of the acoustic field. The imaginary part of $\mathbf{H}^{-1}(\omega)\mathbf{G}(\omega)$ is associated with the additional mass effect of the fluid, and its real part corresponds to energy dissipation by sound radiation.

The energy expressions in Eqs. (2.19) and (2.20) are fully equivalent to each other, which becomes obvious in view of the balance of forces in Eq. (2.14). Hence, in the context of a coupled FEM-BEM analysis, the harmonic radiation loss factor in Eq. (2.16) can be evaluated using either of the two expressions. In practice, the potential energy approach given by Eq. (2.19) is slightly more favorable since it does not involve fully populated BE matrices. However, the situation is different

when characterizing the structural behavior experimentally as is done in the hybrid framework developed in the context of this thesis [22]. In that case, neither the (static) stiffness matrix $\mathbf{K}$ nor the damping matrix $\mathbf{D}$ are available, while the mass matrix $\mathbf{M}$ can be estimated with reasonable accuracy. Assuming that the damping contributions are negligible compared to the inertial terms and radiation damping, the total energy can be computed via Eq. (2.20) in the case that the structural behavior is governed experimentally rather then by FEM [22].

The harmonic loss factor given by Eq. (2.16) is a result of a frequency-wise response analysis and depends on the type of the excitation. Alternatively, excitation independent modal loss factors can be derived for each acoustically loaded structural mode. Given a complex eigenfrequency $\tilde{\omega}_j$, the modal loss factor corresponding to the j-th mode is defined as [4, 43]

$$\eta_j = -2 \frac{\mathrm{Im}\,(\tilde{\omega}_j)}{\mathrm{Re}\,(\tilde{\omega}_j)}, \tag{2.21}$$

in which $\mathrm{Im}\,(\tilde{\omega}_j)$ is negative since the harmonic time dependency is defined as $e^{-\mathrm{i}\omega t}$. Details on structural acoustic modal analyses and solution techniques for the underlying nonlinear EVP are described in Sec. 2.4.

When structural damping is omitted, i.e. $\mathbf{D} = \mathbf{0}$ holds, then the energy loss due to sound radiation accounts for the only damping contribution. In that case, the modal loss factor in Eq. (2.21) quantifies the extent of radiation damping for the corresponding acoustically loaded structural mode. Furthermore, one can expect that the modal loss factor in Eq. (2.21) equals the harmonic loss factor given by Eq. (2.16) at the respective eigenfrequency $f_j = \mathrm{Re}\,(\tilde{\omega}_j)\,/2\pi$, of course assuming that the respective mode is actually excited in the harmonic response analysis. Otherwise, when that particular mode is not excited, the harmonic loss factor will deviate from the modal loss factor. This is illustrated in Fig. 2, which compares harmonic and modal loss factors of a honeycomb sandwich panel. The harmonic loss factors of the panel are shown for two load cases, i.e. point excitation and excitation by a diffuse acoustic field. As expected, the respective loss factors differ significantly apart from the resonances, while at the actual resonance frequencies, they consistently agree with the modal loss factors. However, there is also an apparent exception at the eigenfrequency $f_{11} = 389\,\mathrm{Hz}$. The corresponding in-plane mode is not excited by point excitation, and hence, the harmonic loss factor deviates significantly from the modal loss factor. In contrast, the diffuse acoustic field indeed excites the in-plane mode, which thus determines the extent of sound radiation at the respective excitation frequency (note that the side edges of the panel are coupled with the fluid domain as well). The resulting harmonic loss factor conforms with the modal loss factor. Details on the properties of the sandwich panel and the numerical model can be found in [20].

Recently, the occurrence of spurious numerical damping in BEM has received scientific attention
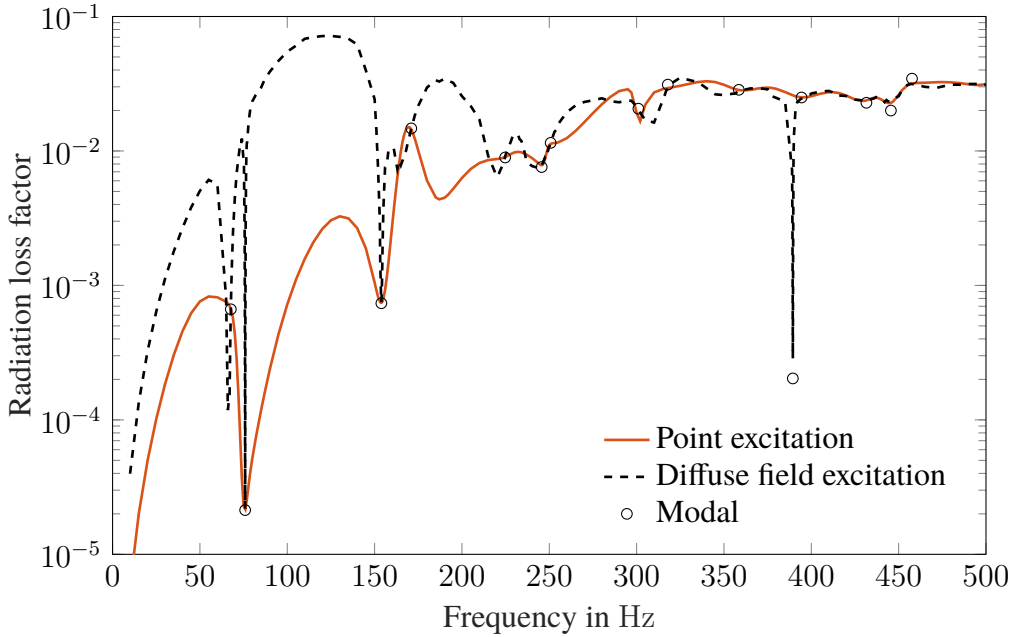
Figure 2: Harmonic radiation loss factors of a honeycomb sandwich panel subject to point and diffuse field excitations. In addition, modal loss factors are potted at their respective eigenfrequencies. This figure is adopted from [20].

[44–46], but this it does not seem to affect the results in exterior acoustics.

2.3 Review of methods for accelerating harmonic response analyses

Harmonic response analyses in vibroacoustic simulations are associated with a significant computational effort, which is mainly attributed to the assembly of the BE matrices $\mathbf{H}(\omega)$ and $\mathbf{G}(\omega)$ at each frequency point of interest as well as the solution of the resulting sequence of linear systems of equations. This section reviews the main efforts reported in the literature to accelerate such frequency sweeps - however without claiming that the list is exhaustive. It is the aim of this section to provide a context for the development of the greedy algorithm (Sec. 3.2) - one of the main achievements of this thesis. Some of the concepts described below are also essential parts of the newly developed vibroacoustic eigensolver (Sec. 3.3).

2.3.1 Remedies for frequency dependent boundary element matrices

Early approaches for accelerating harmonic response analyses with BEM are based on entry-wise frequency interpolations of BE matrices [47, 48]. Kirkup and Henwood [48] proposed a truncated
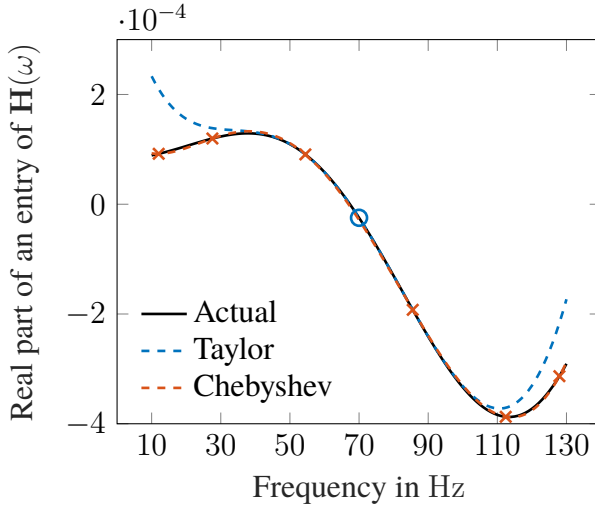
Figure 3: Real part of an exemplary entry of $\mathbf{H}(\omega)$ for a sphere. Additionally, Taylor and Chebyshev approximations with $N = 6$ terms each are plotted.
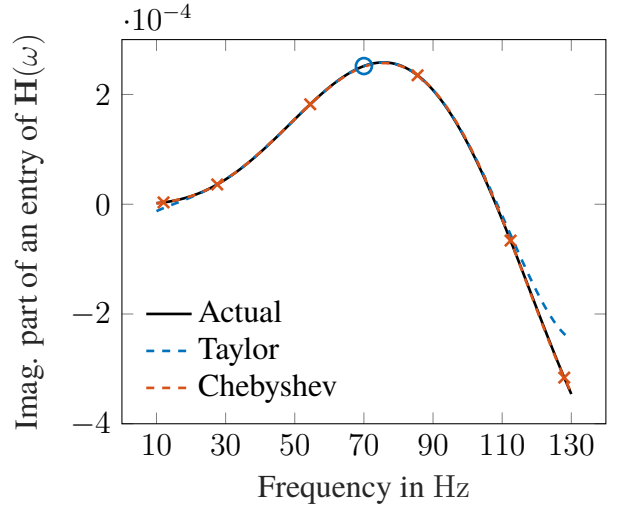
Figure 4: Imaginary part of an exemplary entry of $\mathbf{H}(\omega)$ for a sphere. Additionally, Taylor and Chebyshev approximations with $N = 6$ terms each are plotted.

Taylor expansion of the BE matrices. The resulting polynomial approximations of degree $N - 1$ read

$$\mathbf{H}(\omega) \approx \sum_{j=0}^{N-1} \frac{\mathbf{H}^{(j)}(\omega_0)}{j!} (\omega - \omega_0)^j \quad \text{and} \quad \mathbf{G}(\omega) \approx \sum_{j=0}^{N-1} \frac{\mathbf{G}^{(j)}(\omega_0)}{j!} (\omega - \omega_0)^j, \qquad (2.22)$$

in which ω_0 is the expansion frequency and $(\cdot)^{(j)}$ denotes the j-th derivative with respect to ω. Those matrix derivatives are either obtained numerically (e.g. by finite difference approximation) or by analytical differentiation of the kernel functions. A Taylor expansion results in an exponentially convergent approximation around the expansion frequency, but it requires subdividing the frequency interval and computing a Taylor approximation in each sub-frequency interval in order to mitigate large deviations at the edges of the frequency interval - an issue that is also known as Runge's phenomenon [49].

Runge's phenomenon can also be overcome by using a Chebyshev interpolation [50, 51], i.e. a polynomial approximation that satisfies interpolation conditions at Chebyshev nodes. The resulting polynomials of degree $N - 1$ read

$$\mathbf{H}(\omega) \approx \sum_{j=0}^{N-1} \omega^j \mathbf{H}_j \quad \text{and} \quad \mathbf{G}(\omega) \approx \sum_{j=0}^{N-1} \omega^j \mathbf{G}_j. \qquad (2.23)$$

In order to compute the frequency independent coefficient matrices $\mathbf{H}_j$ and $\mathbf{G}_j$, the original ma-
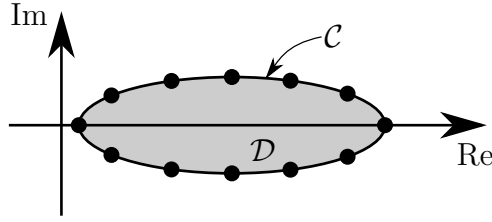
Figure 5: Elliptic contour $\mathcal{C}$ enclosing a complex domain $\mathcal{D}$, in which the BE matrices are approximated. The contour is discretized using a few nodes. This figure is adopted from [29].

trices $\mathbf{H}(z_j)$ and $\mathbf{G}(z_j)$ are first assembled at N Chebyshev nodes of the first kind. Considering a frequency interval $[f_{\min},\ f_{\max}]$, those Chebyshev nodes are given as

$$z_j = \gamma + \delta \cos\left(\frac{2j-1}{2N}\pi\right), \quad j = 1, ..., N, \tag{2.24}$$

where $\gamma = (f_{\max} + f_{\min})/2$ and $\delta = (f_{\max} - f_{\min})/2$. With the BE matrices $\mathbf{H}(z_j)$ and $\mathbf{G}(z_j)$ at hand, the unknown coefficient matrices $\mathbf{H}_j$ and $\mathbf{G}_j$ are determined by solving a sequence of linear systems of dimension N. A Chebyshev interpolation guarantees exponential decay of the interpolation error with increasing polynomial degree. Compared to the Taylor approximation, it also results in a more uniformly distributed error over the considered frequency interval. This is illustrated in Figs. 3 and 4, in which an exemplary entry of $\mathbf{H}(\omega)$ for a sphere ($r = 5$m) is plotted in the frequency interval from $10\,$Hz to $130\,$Hz. Additionally, Taylor and Chebyshev approximations of $\mathbf{H}(\omega)$ with $N = 6$ terms each are plotted. The Taylor approximation is computed at an expansion frequency of $f_0 = 70\,$Hz considering derivatives up to 5-th order. The Chebyshev approximation is computed using $N = 6$ samples frequencies as given in Eq. (2.24). As expected, the Taylor approximation results in large deviations at the edges of the frequency interval, while the Chebyshev approximation yields a uniformly distributed error over the whole frequency interval. Details on the considered reference problem can be found in e.g. [28, 51].

As an alternative to the above-described polynomial approximations, Cauchy integral representations of BE matrices were recently proposed [52]. Compared to a Chebyshev approximation, which is based on real-valued frequency samples, this method uses complex-valued frequency nodes that are located on an elliptic contour $\mathcal{C}$. The resulting rational approximation is exponentially convergent within the domain $\mathcal{D}$ that is enclosed by $\mathcal{C}$ [53]. Figure 5 schematically depicts an elliptic contour for a Cauchy integral representation and associated nodes for an N-point trapezoidal rule discretization. The resulting approximate BE matrices read

$$\mathbf{H}(\omega) \approx \sum_{j=1}^{N} \mathbf{H}(z_j) v_j(\omega) \quad \text{and} \quad \mathbf{G}(\omega) \approx \sum_{j=1}^{N} \mathbf{G}(z_j) v_j(\omega), \tag{2.25}$$

where the scalar-valued rational functions v_j are given by

$$v_j(\omega) = \frac{w_j}{z_j - \omega} \left(\sum_{k=1}^{N} \frac{w_k}{z_k - \omega} \right)^{-1}. \tag{2.26}$$

While in the context of Chebyshev approximations, z_j was used to denote real-valued frequency samples, here, z_j denotes the complex frequency nodes. They can be chosen as e.g.

$$z_j = \gamma + \delta \left(\cos \left(2\pi j/N \right) + \mathrm{i} \zeta \sin \left(2\pi j/N \right) \right), \quad j = 1, ..., N, \tag{2.27}$$

where ζ defines the aspect ratio of the ellipse. The associated weights w_j are given by

$$w_j = \frac{\delta}{N} \left(\zeta \cos \left(2\pi j/N \right) + \mathrm{i} \sin \left(2\pi j/N \right) \right), \quad j = 1, ..., N. \tag{2.28}$$

As will be explained in Sec. 3.3, rational approximations of the form Eqs. (2.25) to (2.28) are a key ingredient of the vibroacoustic eigensolver [29] developed in the framework of this thesis. A more general overview of approximations inside complex regions can be found in [54].

The relative error in the BE matrix $\mathbf{H}(\omega)$ that is introduced by the Chebyshev interpolation in Eq. (2.23) can by assessed by

$$\varepsilon_{\mathrm{p}} = \frac{\|\mathbf{H}(\omega) - \sum_{j=0}^{N-1} \omega^j \mathbf{H}_j\|_{\mathrm{F}}}{\|\mathbf{H}(\omega)\|_{\mathrm{F}}}, \tag{2.29}$$

where $\|\cdot\|_{\mathrm{F}}$ denotes the Frobenius norm. Similarly, the error introduced by the rational approximation in Eq. (2.25) is defined as

$$\varepsilon_{\mathrm{r}} = \frac{\|\mathbf{H}(\omega) - \sum_{j=1}^{N} \mathbf{H}(z_j) v_j(\omega)\|_{\mathrm{F}}}{\|\mathbf{H}(\omega)\|_{\mathrm{F}}}. \tag{2.30}$$

Figures 6 and 7 display ε_{p} and ε_{r} when using $N = 12$ frequency nodes respectively for the above-mentioned sphere problem. The plots are generated by 1779 uniformly distributed points in the complex plane and linear interpolation in-between them. Both approximations methods achieve errors of order $\mathcal{O}(10^{-10})$ in the considered complex frequency region. The common concern that Chebyshev approximations inside a real frequency interval quickly deteriorate apart from the real axis does not seem to be an issue here. The relevance of complex frequency approximations will become clear in Sec. 2.4, which deals with nonlinearly frequency dependent EVPs.

While accelerating the matrix set-up at a reasonable accuracy, all of the above-discussed frequency approximation techniques require storage of multiple (N) fully populated coefficient ma-
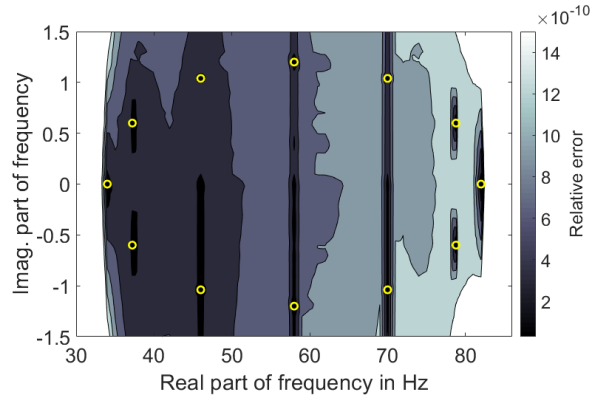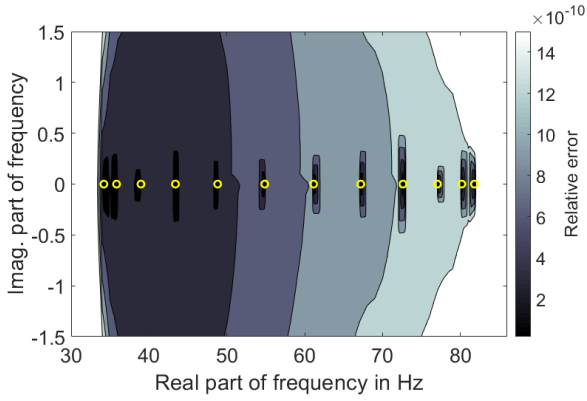
Figure 6: Relative error ε_p of the polynomial Chebyshev approximation given by Eq. (2.29) when using $N = 12$.

Figure 7: Relative error ε_r of the rational Cauchy approximation given by Eq. (2.30) when using $N = 12$.

trices. The associated memory requirements can be prohibitive for large-scale vibroacoustic problems. The memory issue of single frequency BEM has been addressed by several data sparse formats such as hierarchical matrices [55, 56]. Recently, Dierckx et al. [57] combined an adaptive cross approximation with a rational frequency approximation resulting in a data sparse representation of BE matrices in a frequency range.

Besides frequency approximations, several other strategies are available to deal with frequency dependent BE matrices. Wu et al. [58] proposed a spatial interpolation of the Green's function, which allows to eliminate the frequency dependent term from the integrands. Similar methods that confine the numerical integration to a frequency independent kernel were developed thereafter [59, 60]. Approximating the acoustic response itself can be more efficient when only a small part of the solution is of interest. This may include the sound pressure at a small number of field points or the evaluation of integrated quantities such as radiated sound power. A Padé technique allows to construct an approximation in a frequency interval by using the derivatives of a response at a single expansion frequency [61, 62]. The coefficients of a Padé approximation can be computed by e.g. the Lanczos algorithm, which has been applied to multi-frequency calculations of radiated sound power [63, 64].

2.3.2 Solution strategies for coupled linear system of equations

With increasing number of DOFs, the solution of the sequence of linear systems of equations

$$\mathbf{T}(\omega_j)\mathbf{x}_j = \mathbf{b}_j, \quad j = 1, ..., m \tag{2.31}$$

becomes the computationally most expensive part of a harmonic response analysis. Depending on whether the structural Eq. (2.14) or the acoustic Eq. (2.15) is employed, the system matrix $\mathbf{T}(\omega)$ reads

$$\mathbf{T}(\omega) = \mathbf{K} - \mathrm{i}\omega\mathbf{D} - \omega^2\mathbf{M} + \mathrm{i}\omega\mathbf{C}_{\mathrm{sf}}\mathbf{H}^{-1}(\omega)\mathbf{G}(\omega)\mathbf{C}_{\mathrm{fs}} \quad \text{or} \tag{2.32}$$

$$\mathbf{T}(\omega) = \mathrm{i}\omega\mathbf{G}(\omega)\mathbf{C}_{\mathrm{fs}}\left(\mathbf{K} - \mathrm{i}\omega\mathbf{D} - \omega^2\mathbf{M}\right)^{-1}\mathbf{C}_{\mathrm{sf}} + \mathbf{H}(\omega). \tag{2.33}$$

The solution of both types of linear systems by iterative schemes as well as model order reduction (MOR) is discussed in what follows.

Iterative solvers

Large-scale linear systems of equations are usually addressed by iterative solution schemes [65, 66], which are based on successive matrix vector multiplications. For example, application of an iterative scheme to a (single) linear system in Eq. (2.31) requires multiplication of the matrix with an intermediate solution vector $\mathbf{x}^{(k)}$ in each iteration k. When rearranging the coupled system into the form given by Eq. (2.33), this would necessitate solving an inner linear system in each iteration in order to evaluate the term $\left(\mathbf{K} - \mathrm{i}\omega\mathbf{D} - \omega^2\mathbf{M}\right)^{-1}\mathbf{C}_{\mathrm{sf}}\mathbf{x}^{(k)}$. Such nested iterations can be avoided by computing a factorization of the sparse and symmetric FE matrix $\mathbf{K} - \mathrm{i}\omega\mathbf{D} - \omega^2\mathbf{M}$, which then facilitate efficient application of iterative solvers to the system in Eq. (2.33). In the case of frequency sweep analyses, the successive solution of linear systems by an iterative scheme can be further accelerated by subspace recycling [67, 68]. More recently, low-rank approximations have been exploited to achieve an efficient frequency range solution of BE equations within a single iteration scheme [51].

Close examination of Eq. (2.32) reveals that an application of an iterative solver to this system would either require a factorization of the dense matrix $\mathbf{H}(\omega)$ or two nested iterations. Both of these approaches are rather inefficient so that structural acoustic systems of the form in Eq. (2.32) are better addressed by MOR and subsequent direct solution of the reduced linear system.

Model order reduction

In the context of structural acoustic systems, MOR provides a powerful tool to reduce the dimension of the linear system and is particularly appealing when one is interested in the responses at many frequency points [69] or responses for different excitations [70]. The application of MOR to the

sequence of linear systems in Eq. (2.31) yields

$$\mathbf{V}^{\mathrm{T}}\mathbf{T}(\omega_j)\mathbf{V}\mathbf{x}_{\mathrm{r},j} = \mathbf{V}^{\mathrm{T}}\mathbf{b}_j, \quad j = 1, ..., m, \tag{2.34}$$

in which $\mathbf{V}$ is the reduction basis and should be chosen such that the approximation error is small in the whole frequency range of interest. The actual solution of the reduced system is of negligible computational effort when $\mathbf{V}$ possesses only a few columns. The original solution vector is recovered from $\mathbf{x}_j = \mathbf{V}\mathbf{x}_{\mathrm{r},j}$.

Essentially, all multi-frequency MOR techniques, including the greedy algorithm [28] developed in this thesis (Sec. 3.2), exploit the fact that solutions at different frequency points are usually contained in a small subspace. In other words, the spatial pattern of vibroacoustic responses usually exhibit a certain degree of correlation among different frequency points. In the simplest case, the basis vectors spanning $\mathbf{V}$ are solutions $\mathbf{x}_j$ at some (less then m) suitably chosen frequency samples ω_j. The newly developed greedy algorithm [28, 71] provides an optimal frequency sampling strategy for this approach.

Alternative constructions of $\mathbf{V}$ are also possible, such as modal bases or Krylov subspaces. The application of Krylov subspaces to coupled FEM-BEM systems was pioneered by the work of Puri et al. [72] and is highly efficient in the case of light fluid loading (e.g. for assessing radiation damping of lightweight structures in air). The authors of [72] propose a unilateral MOR for the system in Eq. (2.32), in which the Krylov subspace is solely based on the structural subsystem $\mathbf{K} - \mathrm{i}\omega\mathbf{D} - \omega^2\mathbf{M}$. After MOR, Eq. (2.14) becomes [72, 73]

$$\mathbf{V}^{\mathrm{T}}\left[\mathbf{K} - \mathrm{i}\omega\mathbf{D} - \omega^2\mathbf{M} + \mathrm{i}\omega\mathbf{C}_{\mathrm{sf}}\mathbf{H}^{-1}(\omega)\mathbf{G}(\omega)\mathbf{C}_{\mathrm{fs}}\right]\mathbf{V}\mathbf{u}_{\mathrm{r}} = \mathbf{V}^{\mathrm{T}}\left[\mathbf{f}_{\mathrm{s}} + \mathbf{C}_{\mathrm{sf}}\mathbf{H}^{-1}(\omega)\mathbf{p}^{\mathrm{i}}\right]. \tag{2.35}$$

Once $\mathbf{V}$ is computed, the reduced system matrix is explicitly formed by evaluating the term $\mathbf{H}^{-1}(\omega)$ $\mathbf{G}(\omega)\mathbf{C}_{\mathrm{fs}}\mathbf{V}$. The latter requires solving a linear system with multiple right-hand sides for which many efficient strategies are available [74, 75]. A unilateral MOR as described in [72] is applicable as long as the coupled structural acoustic system admits accurate MOR solely based on the structural subsystem, which is generally the case for applications with light fluid loading. However, when addressing heavy fluid loading by the acoustic Eq. (2.15), the application of MOR is much more intricate. Modal reduction requires solving a nonlinear EVP in the first place (see Sec. 2.4), which can outweigh the actual benefit of the subsequent dimension reduction. And while a small number of Krylov basis vectors is sufficient to match the first moments of FE matrices with quadratic frequency dependence, implicitly frequency dependent BE matrices require a subdivision of the frequency range. The most recent efforts in this field [76, 77] are based on frequency approxi-

mation of the BE kernel function by truncated Taylor expansion (c.f. Sec. 2.3.1) and subsequent reduction of the frequency independent coefficient matrices by Krylov subspaces. Although these papers [76, 77] are limited to acoustic BEM, one can expect that the techniques therein will be extended to coupled FEM-BEM systems such as the one in Eqs. (2.15) and (2.33) in the future.

2.4 Review of nonlinear eigensolvers for structural acoustic modal analyses

Besides the harmonic response analyses discussed in the previous section, modal analyses account for another fundamental tool for acquiring the dynamic properties of structural acoustic systems. In this thesis in particular, they facilitate quantification of acoustic radiation damping by modal loss factors. The purpose of this section is to briefly review the current research on structural acoustic modal analysis with FEM and BEM. The contour integral method described below is the algorithmic basis of the work on modal radiation damping in this thesis (Sec. 3.1). It is also the aim of this section to provide a context for the development of a vibroacoustic eigensolver based on subspace iteration (Sec. 3.3) - an accomplishment of this thesis that allows accurate and efficient computation of modal radiation loss factors.

Modal analyses of interior acoustic problems such as closed cavities are well established. They are best addressed by FEM [78] or BEM with frequency independent kernel functions [79, 80] resulting in linear EVPs for which well-developed software packages exist [81]. In the context of this thesis however, only exterior acoustic domains are of interest, since radiation damping is associated with far field sound radiation. When using the coupled FEM-BEM formulation as described in Sec. 2.1, the underlying EVP may be formulated based on Eq. (2.14) or (2.15). Setting the right-hand sides of the respective equations to zero yields

$$\left[\mathbf{K} - \mathrm{i}\tilde{\omega}\mathbf{D} - \tilde{\omega}^2\mathbf{M} + \mathrm{i}\tilde{\omega}\mathbf{C}_{\mathrm{sf}}\mathbf{H}^{-1}(\tilde{\omega})\mathbf{G}(\tilde{\omega})\mathbf{C}_{\mathrm{fs}} \right] \boldsymbol{\Psi} = \mathbf{0} \quad \text{and} \tag{2.36}$$

$$\left[\mathrm{i}\tilde{\omega}\mathbf{G}(\tilde{\omega})\mathbf{C}_{\mathrm{fs}} \left(\mathbf{K} - \mathrm{i}\tilde{\omega}\mathbf{D} - \tilde{\omega}^2\mathbf{M} \right)^{-1} \mathbf{C}_{\mathrm{sf}} + \mathbf{H}(\tilde{\omega}) \right] \boldsymbol{\Phi} = \mathbf{0}, \tag{2.37}$$

respectively. The displacement and pressure modes are denoted by the vectors $\boldsymbol{\Psi}$ and $\boldsymbol{\Phi}$, respectively. The EVPs in Eqs. (2.36) and (2.37) are nonlinear, since the BE matrices $\mathbf{H}(\tilde{\omega})$ and $\mathbf{G}(\tilde{\omega})$ implicitly depend on the (complex) eigenfrequency parameter $\tilde{\omega}$. They are replaced by

$$\mathbf{T}(\tilde{\omega})\mathbf{x} = \mathbf{0} \tag{2.38}$$

in the following for the sake of readability.

Newton methods

The solution of nonlinear EVPs emerging from frequency dependent BE formulations has been pioneered nearly half a century ago [82], but it is still a computationally challenging topic today with rather hesitant developments. Early algorithms for solving nonlinear acoustic EVPs were based on Newton's method [82], which often requires successive runs with a deflated matrix in order to find different eigenpairs. Moreover, Newton methods necessitate the derivative of the system matrix, which may be computed numerically (e.g. by finite difference approximation) or analytically. The finite difference method requires - besides being ill-conditioned [83] - computing steps in both the real and the imaginary directions. On the other hand, analytical differentiation requires intrusive modification of the BEM code in order to compute complex frequency derivatives of the Helmholtz integral equation.

Frequency approximation and linearization

A second family of structural acoustic eigensolvers may be summarized as methods based on frequency approximation and subsequent linearization. While the initial intention behind frequency approximations of BE matrices [48] was to avoid the numerical integration and assembly of BE matrices at each frequency point (c.f. Sec. 2.3.1), in fact, the resulting polynomial frequency dependency of the BE matrices also paved the way to modal analyses with BEM. The original nonlinear EVP can be converted to a polynomial EVP, whereas both truncated Taylor expansion [37, 84] and Chebyshev interpolation [50, 85] are possible. The polynomial EVP then admits solution by linearization, which however increases the system dimension by the polynomial degree. Peters et al. [73] have mitigated prohibitively large linearized EVPs by the unilateral Krylov subspace-based MOR given in Eq. (2.35). More general MOR techniques are yet to be applied to linearized structural acoustic EVPs. Another drawback concerns numerical instabilities associated with linearization of higher polynomial degrees, which in fact limits modal analysis to small (sub-) frequency ranges.

Instead of polynomial approximations, rational approximations of nonlinear EVPs have recently proven to be a promising alternative [85–87]. Rational approximations of the form in Eqs. (2.25) to (2.28) are incorporated into the vibroacoustic eigensolver developed in the framework of this thesis (Sec. 3.3).

Contour integral methods

Contour integral methods (CIM) [88–91] may be categorized as another family of eigensolvers. They stand out from other methods due to their low memory requirements and the suitability for

parallel computation. They essentially convert the large, nonlinear EVP into a small linear one. While many variants of CIM exist, the block Sakurai Sugiura method (block SS) [88] is reviewed in the following as a representative version of CIM. Block SS has been extensively applied to vibroacoustic EVPs based on BEM [20, 40, 92–94] as well as quadratic EVPs emerging from an acoustic infinite element discretization [95]. It is also the algorithmic basis of the work on modal radiation damping in this thesis (Sec. 3.1). Moreover, block SS is chosen to benchmark the newly developed vibroacoustic eigensolver (Sec. 3.3).

Block SS essentially transforms the nonlinear EVP in Eq. (2.38) to the generalized EVP

$$\mathcal{A}\mathbf{w} = \lambda\mathcal{M}\mathbf{w}, \tag{2.39}$$

in which $\mathcal{A}$ and $\mathcal{M}$ are the block Hankel matrices

$$\mathcal{A} = \begin{bmatrix} \mathbf{M}_0 & \mathbf{M}_1 & \dots & \mathbf{M}_{K-1} \\ \mathbf{M}_1 & & & \vdots \\ \vdots & & & \mathbf{M}_{2K-3} \\ \mathbf{M}_{K-1} & \dots & \mathbf{M}_{2K-3} & \mathbf{M}_{2K-2} \end{bmatrix}, \mathcal{M} = \begin{bmatrix} \mathbf{M}_1 & \mathbf{M}_2 & \dots & \mathbf{M}_K \\ \mathbf{M}_2 & & & \vdots \\ \vdots & & & \mathbf{M}_{2K-2} \\ \mathbf{M}_K & \dots & \mathbf{M}_{2K-2} & \mathbf{M}_{2K-1} \end{bmatrix}. \tag{2.40}$$

They comprise the moments $\mathbf{M}_l$ of the resolvent of the system matrix. The moment matrices are obtained by complex contour integration via

$$\mathbf{M}_l = \frac{1}{2\pi\mathrm{i}} \oint_{\mathcal{C}} z^l \mathbf{U}^{\mathrm{H}} \mathbf{T}^{-1}(z) \mathbf{V} \, \mathrm{d}z, \quad l = 0,...,2K-1, \tag{2.41}$$

in which the matrices $\mathbf{U}$ and $\mathbf{V}$ contain L randomly chosen source vectors as columns [96]. The eigenvector of the original system is retrieved from $\mathbf{x} = \mathbf{S}\mathbf{w}$, where $\mathbf{S} = [\mathbf{S}_0,...,\mathbf{S}_{K-1}]$ and

$$\mathbf{S}_l = \frac{1}{2\pi\mathrm{i}} \oint_{\mathcal{C}} z^l \mathbf{T}^{-1}(z) \mathbf{V} \, \mathrm{d}z, \quad l = 0,...,K-1. \tag{2.42}$$

The integrals in Eqs. (2.41) and (2.42) are evaluated along an elliptic contour $\mathcal{C}$ in the complex plane, which should be chosen such that it encloses the eigenvalues of interest. The elliptic contour is discretized via Eqs. (2.27) and (2.28), which admits evaluation of Eqs. (2.41) and (2.42) by the trapezoidal rule. The computations for each of the contour points z_j are independent of each other and hence admit an efficient parallel execution. Along with its easy and non-intrusive

implementation, this feature makes block SS an appealing method for solving nonlinear EVPs.

However, it is also well-known [97] that the higher order moments associated with a large K lead to ill-conditioning of the Hankel matrices in Eq. (2.40), which results in inaccurate solutions as well as non-physical eigenvalues, see e.g. the results in Sec. 4.2 of [29]. To overcome ill-conditioned Hankel matrices, Yokota and Sakurai [97] proposed a CIM in which a subspace based on resolvent moments is used in a Rayleigh Ritz procedure to extract the eigenvalues. Similar strategies have been employed for solving vibroacoustic EVPs [41, 52], however with the difference that the authors avoid higher order moments by sampling the resolvent matrix. Both, block SS and Rayleigh Ritz-based CIM are used to benchmark the vibroacoustic eigensolver (Sec. 3.3) developed in this thesis.

3 Summary of Achievements

This chapter summarizes the main scientific achievements that accumulate to the present thesis. The achievements are reported in more detail in the respective research papers attached in Appendix A. The papers summarized in Secs. 3.1 to 3.4 have undergone full peer-review and are published in international journals.

3.1 Investigation of radiation damping using finite and boundary element methods

The corresponding paper [20] with the title "Investigation of radiation damping in sandwich structures using finite and boundary element methods and a nonlinear eigensolver" is enclosed in Appendix A.1.

Summary

Using the coupled structural acoustic formulation described in Sec. 2.1, this work [20] systematically studies the acoustic radiation damping in sandwich structures. Harmonic and modal loss factors are computed by Eqs. (2.16) and (2.21) to determine the extent of radiation damping. The underlying nonlinear EVP is solved via the block SS contour integral method described in Sec. 2.4, which yields the complex eigenfrequencies and air-loaded modes of the sandwich structure.

Application of the numerical framework to various sandwich panel configurations clearly demonstrates the relevance of air loading. Eigenfrequency shifts of more than $2\,\%$ compared to the in-vacuo eigenfrequencies and radiation loss factors of up to $8\,\%$ are reported. It is also observed that radiation damping is strongly dependent on the type of the excitation and the boundary conditions in the low frequency range, while at higher frequencies, this effect becomes insignificant. As explained in Sec. 2.2, modal radiation loss factors coincide with the harmonic radiation loss factors, given that the respective mode is excited in the harmonic response analysis.

Furthermore, the numerically obtained radiation loss factors are compared to theoretical expressions as well as to experimental results reported in the literature. Satisfactory agreement is observed above the coincidence frequency range, while the commonly used theoretical expressions are found to be inadequate in the low frequency range with low modal density. Similarly, the experimental and numerical results differ from each other in the low frequency range due to the influences of boundary conditions, excitation and the modal behavior of reverberation chambers. The paper concludes with a discussion on possible errors occurring during an experimental assessment of radiation damping.

Contribution

I have extended the coupled FEM/BEM framework of the institute by implementing the nonlinear eigensolver, the mesh coupling algorithm for solid finite elements and the algorithm for diffuse field excitation. I have created the numerical models and designed all the studies. I have analyzed and interpreted the results and have written the manuscript for publication. S. Marburg gave the impetus

for my research on acoustic radiation damping by writing a successful funding proposal. He also developed the BE code and contributed to the work by critically reviewing the results.

3.2 A greedy algorithm for structural acoustic systems

The corresponding paper [28] with the title "A greedy reduced basis scheme for multifrequency solution of structural acoustic systems" is enclosed in Appendix A.2.

Summary

Harmonic response analyses of coupled structural acoustic systems require a significant computational effort when evaluating at a large number of frequency points. This is the main reason, why acoustic loading and associated phenomena such as radiation damping are widely neglected in vibroacoustic simulations. This work [28] contributes to the research on MOR of vibroacoustic systems that was outlined in Sec. 2.3.2. A novel strategy for a multi-frequency solution is introduced. It represents the first vibroacoustic MOR scheme that chooses the frequency samples based on an optimality criterion.

More specifically, the proposed method constructs a reduced basis that is spanned by the solutions at a few suitably chosen frequency samples within the frequency range of interest. Following a greedy strategy, a new frequency sample is selected in each iteration of the algorithm based on the solution that was worst approximated in the previous iteration. A least squares solver efficiently computes the approximations at intermediate frequencies as well as the a posteriori estimates of associated errors.

The efficiency of the proposed method is verified based on several vibroacoustic problems involving both interior and exterior acoustic domains. The most important observation is that the greedy algorithm automatically selects frequency samples around resonances, although modal quantities are not computed. This leads to a generally fast convergence of the method. Furthermore, refining the frequency resolution in an interval between resonances barely affects the total number of iterations, but it only increases the number of least squares solutions. The advantage of the proposed greedy algorithm over conventional frequency-wise strategies increases with the chosen frequency resolution.

Contribution

I have developed the code for the greedy reduced basis scheme, which represents an essential part of this work. I have created the numerical models and designed all the studies. I have analyzed and interpreted the results and have written major parts of the manuscript for publication. M. Voigt had the initial idea for this method and contributed with his mathematical background. C. Jelich gave valuable comments and helped to phrase the main results of the paper in a clear way. S. Marburg

developed the BE code and reviewed the manuscript critically.

3.3 A subspace iteration eigensolver for vibroacoustic problems

The corresponding paper [29] with the title "A subspace iteration eigensolver based on Cauchy integrals for vibroacoustic problems in unbounded domains" is enclosed in Appendix A.3.

Summary

Modal analyses are widely employed to compute eigenfrequencies and associated modes of dynamically loaded structures. When the effect of acoustic loading is included in the modal analysis, modal damping values associated with radiation damping of individual modes can also be computed. However when using BEM for the representation of the acoustic field, a modal analysis requires solution of an underlying nonlinear EVP. This work [29] presents a novel strategy for solving nonlinear structural acoustic EVPs. The strategy is based on FEAST [98, 99] and works by iteratively updating a spectral projection.

When applied to vibroacoustic problems involving BEM, the data required for the spectral projection can be reused in order to construct a rational approximation of the reduced but still nonlinearly frequency dependent EVP via Eq. (2.25). This facilitates iterative computation of eigenpairs at negligible recurring costs. Two tailored approaches are proposed to compute the spectral projection. In the case of strong acoustic loading, the Schur complement is formed as given by Eq. (2.33), and the resulting linear systems with multiple right-hand sides are addressed by a factorization of the finite element matrices and an iterative block Krylov solver. In the case of light acoustic loading, MOR is applied solely to the structural subsystem as stated in Eq. (2.35), which significantly alleviates the memory requirements as well as the computational cost for updating the spectral projection.

In comparison to the contour integral method presented in Sec. 2.4, the proposed eigensolver necessitates fewer BE matrices to be assembled and exhibits monotonic convergence. Moreover, the application to a musical bell indicates that accurate modal radiation damping values can be obtained despite the extremely weak air loading.

Contribution

B. Goderbauer developed an early version of the code while working on his Bachelor thesis, which was supervised by me. He has also created the numerical model of the bell. After he had submitted his thesis, I have revised major parts of the code including the rational approximation method and the update routine for the spectral projector. I have also implemented the contour integral method, which was used for benchmarking purposes. C. Jelich has developed the block Krylov solver, which was essential for the performance of the method. Once the software framework was set up, I have

carried out all the numerical studies and have written the manuscript for publication. M. Voigt had the initial idea for applying the FEAST algorithm to nonlinear acoustic EVPs and contributed with his mathematical background. S. Marburg once again reviewed the manuscript critically.

3.4 Hybrid numerical-experimental assessment of radiation damping

The corresponding paper [22] with the title "Hybrid assessment of acoustic radiation damping combining in-situ mobility measurements and the boundary element method" is enclosed in Appendix A.4.

Summary

This work [22] combines experiments with numerical techniques to achieve an accurate assessment of acoustic radiation damping. The dynamical behavior of the structure is determined by means of hammer excitation and scanning LDV. The resulting mobility matrix contains transfer functions relating the vibrational velocity to the excitation force. After characterization of the structural behavior, the sound radiation is evaluated by numerical simulation. For this purpose, the experimental mesh corresponding to the mobility matrix is coupled to an acoustic BE model by the Mortar method described in Sec. 2.1. Harmonic radiation loss factors are computed based on Eqs. (2.16) and (2.20).

The proposed hybrid approach does not require intricate constitutive modeling that goes along with FE discretization of structures involving complex materials. Furthermore, the measured mobility matrix reflects the actual (in-situ) mounting condition rather than idealized boundary conditions typically used in FE models. On the other hand, using BEM for the representation of the acoustic field avoids special measurement facilities and associated limitations. Perfectly diffuse acoustic fields can modeled even at low frequencies and the influence of acoustic short-circuiting at free edges and slits can be taken into account. Radiation loss factors for different types of excitation and acoustic conditions can be determined without requiring repeated mobility measurements.

The proposed hybrid procedure is applied to evaluate radiation loss factors of flat and curved honeycomb sandwich panels attached to a hollow concrete foundation. The results are compared to those obtained by the coupled FEM-BEM approach described Secs. 2.1 and 2.2.

Contribution

The initial idea of this work originated from my discussions with B. Roozen during his research stay at TUM in 2019. I designed the studies, built the specimens, carried out the measurements and interpreted the results under remote assistance of B. Roozen. The code for coupling the mobility matrices with BEM was developed by me, and I wrote the manuscript for publication. S. Marburg

developed the BE code. Both, B. Roozen and S. Marburg reviewed the manuscript critically.

4 Conclusion

Summary and applicability of the thesis

It was the ambition of this thesis to advance the research on acoustic radiation damping - a phenomenon that has yet received only little attention. Where engineers usually employ vast approximations or neglect radiation damping altogether, this thesis has delivered new techniques to assess its extent. The boundary element method is used for representing the exterior acoustic field and is combined either with a structural simulation model or with an experimental characterization of structural mobility. Both developed frameworks - the numerical and the hybrid numerical-experimental one - yield accurate radiation loss factors that are frequency and excitation dependent. Both frameworks have been derived in this thesis in a unified manner. Moreover, numerical modal analysis was applied to compute loss factors associated with acoustically loaded structural modes. These modal loss factors are an alternative measure for radiation damping and independent of frequency and excitation.

Furthermore, state-of-the-art tools in the field of numerical linear algebra have been implemented into vibroacoustic simulations in order to alleviate challenges associated with frequency dependent linear systems. The latter issue limits the efficiency of harmonic response analyses as well as modal analyses and hence hampers the assessment of acoustic radiation damping with BEM. In particular, a novel greedy reduced basis method has been developed for accelerating frequency sweeps. Its main feature is the optimal choice of frequency samples so that a small number of snapshots is sufficient to calculate vibroacoustic responses in large frequency ranges. Moreover, a novel strategy for solving nonlinear vibroacoustic EVPs involving BEM and FEM has been developed in this thesis. It facilitates accurate computation of modal radiation loss factors even in the case of weak structural acoustic interaction.

Although the content of this thesis is mainly methodological, it opens up the possibility for various applications. Computing radiation loss factors prior to an experimental campaign allows deducing the extent of other damping phenomena. For example, material inherent damping can be evaluated by subtracting numerically computed radiation loss factors from (combined material and radiation) loss factors obtained by experimental decay curves [94]. Such an approach avoids vacuum cham-

ber measurements for ruling out the influence of air [13, 14]. Moreover, including the effect of air loading and associated phenomena such as radiation damping generally leads to more accurate structural dynamics simulations, and is particularly important when designing weakly damped lightweight structures.

The methods developed in this thesis may also used to study other phenomena than radiation damping. For example, the hybrid numerical-experimental framework can be straight forwardly extended for a low frequency assessment of sound transmission involving nonstandard geometries. The newly developed vibroacoustic eigensolver is also suitable for determining dispersion curves of infinitely periodic, air-loaded metamaterials.

Current limitations and future work

Already at the beginning of the work on this thesis, it was foreseeable that a widespread consideration of radiation damping in the engineering community will be held back by the computational effort of structural acoustic simulations. Although including the effect of acoustic loading certainly yields a better reflection of the real multiphysics world, the additional numerical costs may actually outweigh this benefit. Therefore, in order to lower the barriers for considering radiation damping, the initial approach in this thesis project was to model the effect of acoustic loading in a purely structural simulation. In fact, in the funding proposal for this thesis project, S. Marburg already described spatially distributed devices such as local boundary conditions and damping elements that are tuned to mimic the effect of acoustic loading.

As it happens, the thesis took another path and rather focused on modeling acoustic loading directly by solving the underlying Helmholtz equation. A purely structural system of equations can then be derived from the coupled system by forming the Schur complement (c.f. Eq. (2.14)). However, at this point, it remains an open question whether alternative, more convenient approaches are possible. Given that above the coincidence frequency, radiation damping is mainly determined by bending stiffness and area density, it might be worth to investigate the applicability of global structural damping models in this higher frequency range. For example, band-averaged radiation loss factors could be precomputed by energy-based expressions [8, 12] and then used to define a hysteretic damping model via Eq. (2.2). Indeed, the research in this thesis has shown that energy-based expressions yield accurate estimates for radiation damping in the higher frequency range [20]. Moreover, radiation damping exhibits a smooth behavior with respect to frequency above coincidence, which facilitates the use of band-averaged loss factors.

In the lower frequency range however, such approximations are more difficult to realize due to the pronounced frequency and excitation dependence of radiation damping [20]. Acoustic condi-

tions such *baffled* or *unbaffled* and the associated effect of acoustic short circuiting also play a role [22]. Therefore, one might conclude that actually modeling the wave propagation by the Helmholtz equation is a more expedient measure to consider radiation damping in the low frequency range. Consequently, the acceleration of such vibroacoustic simulations by MOR techniques shall be in the focus of future research. First steps were taken in this thesis towards more efficient vibroacoustic simulations with BEM, covering both frequency sweeps and modal analyses [28, 29, 51]. In the near future, one can expect that combinations of frequency independent BE approximations and Krylov-based MOR [76, 77] will further alleviate the computational effort of vibroacoustic simulations involving BEM.

Apart from long CPU runtime, memory requirements are the main drawback of the coupled FEM-BEM formulation used in this thesis. Although above-mentioned MOR techniques reduce the dimension of the coefficient matrices, several matrices of original size still need to be assembled beforehand in order to set up frequency approximations. For single frequency calculations with BEM, data sparse formats are available to avoid explicit matrix assembly, requiring special algorithms to perform algebraic operations [55, 56]. First steps were already taken to extend data sparse BEM formats to a range of frequencies [57]. Further progress in this field will be beneficial for vibroacoustic frequency sweeps in the future, also in combination with MOR.

Furthermore, one apparent question remains unanswered in this thesis: Is it possible to utilize the phenomenon of radiation damping in order to deliberately mitigate vibrations in lightweight structures? A possible approach for this endeavor are periodically arranged structural resonators. When properly tuned, such an arrangement of resonators (also known as metamaterial) can increase sound radiation in certain frequency ranges [100, 101], and even additional mode shapes with high radiation efficiency can be created [102]. It might be worth to investigate whether they can be used to maximize radiation damping in certain frequency ranges, ideally without violating other acoustic requirements such as sound insulation. If successful, completely new and far-reaching possibilities will be opened up for enhancing damping in lightweight structures.

Bibliography

[1] T. Ehrig, K. Holeczek, N. Modler, and P. Kostka. Dynamic behaviour adaptation of lightweight structures by compressible constrained layer damping with embedded polymeric foams and nonwovens. *Applied Sciences*, 9(17):3490, 2019.

[2] C. Gnanasambandham, F. Fleissner, and P. Eberhard. Enhancing the dissipative properties of particle dampers using rigid obstacle-grids. *Journal of Sound and Vibration*, 484:115522, 2020.

[3] A. S. Tan, J. Belkner, A. Stroschke, and T. Sattel. Damping adjustment utilizing digital electrorheological valves with parallely segmented electrodes. *Smart Materials and Structures*, 28(7):075013, 2019.

[4] D. J. Mead. *Passive Vibration Control*. John Wiley & Sons Ltd, Chichester, United Kingdom, 1999.

[5] R. A. Mangiarotty. Acoustic radiation damping of vibrating structures. *Journal of the Acoustical Society of America*, 35(3):369–377, 1963.

[6] G. Maidanik. Response of ribbed panels to reverberant acoustic fields. *Journal of the Acoustical Society of America*, 34(6):809–826, 1962.

[7] C. E. Wallace. The acoustic radiation damping of the modes of a rectangular panel. *Journal of the Acoustical Society of America*, 81(6):1787–1794, 1987.

[8] M. J. Crocker and A. J. Price. Sound transmission using statistical energy analysis. *Journal of Sound and Vibration*, 9(3):469–486, 1969.

[9] A. Berry, J. L. Guyader, and J. Nicolas. A general formulation for the sound radiation from rectangular, baffled plates with arbitrary boundary conditions. *Journal of the Acoustical Society of America*, 88(6):2792–2802, 1990.

[10] C. H. Oppenheimer and S. Dubowsky. A radiation efficiency for unbaffled plates with experimental validation. *Journal of Sound and Vibration*, 199(3):473–489, 1997.

[11] B. Laulagnet and J. L. Guyader. Modal analysis of a shell's acoustic radiation in light and heavy fluids. *Journal of Sound and Vibration*, 131(3):397–415, 1989.

[12] K. Renji and P. S. Nair. On acoustic radiation resistance of plates. *Journal of Sound and Vibration*, 212(4):583–598, 1998.

[13] B. L. Clarkson and K. T. Brown. Acoustic radiation damping. *Journal of Vibration, Acoustics, Stress, and Reliability in Design*, 107:357–360, 1985.

[14] O. P. Hentschel, M. Bonhage, L. Panning-von Scheidt, J. Wallaschek, M. Denk, and P. A. Masserey. Analysis of an experimental setup for structural damping identification. *Journal of Theoretical and Applied Mechanics*, 54(1):27–39, 2016.

[15] R. Zhou and M. J. Crocker. Sound transmission loss of foam-filled honeycomb sandwich panels using statistical energy analysis and theoretical and measured dynamic properties. *Journal of Sound and Vibration*, 329(6):673–686, 2010.

[16] E. Reynders. Parametric uncertainty quantification of sound insulation values. *Journal of the Acoustical Society of America*, 135(4):1907–1918, 2014.

[17] A. Billon, C. Foy, J. Picaut, V. Valeau, and A. Sakout. Modeling the sound transmission between rooms coupled through partition walls by using a diffusion model. *Journal of the Acoustical Society of America*, 123(6):4261–4271, 2008.

[18] C. Scrosati, F. Scamoni, M. Bassanino, M. Mussin, and G. Zambon. Uncertainty analysis by a Round Robin Test of field measurements of sound insulation in buildings: Single numbers and low frequency bands evaluation - Airborne sound insulation. *Noise Control Engineering Journal*, 61(3):291–306, 2013.

[19] S. Kirkup. The boundary element method in acoustics: A survey. *Applied Sciences*, 9(8):1642, 2019.

[20] S. K. Baydoun and S. Marburg. Investigation of radiation damping in sandwich structures using finite and boundary element methods and a nonlinear eigensolver. *Journal of the Acoustical Society of America*, 147(3):2020–2034, 2020.

[21] N. B. Roozen, Q. Leclère, D. Urbán, T. Méndez Echenagucia, P. Block, M. Rychtáriková, and C. Glorieux. Assessment of the airborne sound insulation from mobility vibration measurements; a hybrid experimental numerical approach. *Journal of Sound and Vibration*, 432:680–698, 2018.

[22] S. K. Baydoun, N. B. Roozen, and S. Marburg. Hybrid assessment of acoustic radiation damping combining in-situ mobility measurements and the boundary element method. *Acta Acustica*, 6:44, 2022.

[23] M. Kaltenbacher, editor. *Computational Acoustics*. Springer, Cham, Switzerland, 2018.

[24] L. Thompson. A review of finite-element methods for time-harmonic acoustics. *Journal of the Acoustical Society of America*, 119(3):1315–1330, 2006.

[25] R. J. Astley, G. J. Macaulay, J.-P. Coyette, and L. Cremers. Three-dimensional wave-envelope elements of variable order for acoustic radiation and scattering. Part I. Formulation in the frequency domain. *Journal of the Acoustical Society of America*, 103(1):49–63, 1998.

[26] I. Harari and T. J. R. Hughes. A cost comparison of boundary element and finite element methods for problems of time-harmonic acoustics. *Computer Methods in Applied Mechanics and Engineering*, 97(1):77–102, 1992.

[27] D. J. Ewins. *Modal Testing: Theory, Practice and Application (Second Edition)*. Research Studies Press, Baldock, Hertfordshire, England, 2000.

[28] S. K. Baydoun, M. Voigt, C. Jelich, and S. Marburg. A greedy reduced basis scheme for multifrequency solution of structural acoustic systems. *International Journal for Numerical Methods in Engineering*, 121(2):187–200, 2020.

[29] S. K. Baydoun, M. Voigt, B. Goderbauer, C. Jelich, and S. Marburg. A subspace iteration eigensolver based on Cauchy integrals for vibroacoustic problems in unbounded domains. *International Journal for Numerical Methods in Engineering*, 122(16):4250–4269, 2021.

[30] K. J. Bathe. *Finite Element Procedures*. Prentice Hall, Englewood Cliffs, New Jersey, USA, 1996.

[31] C. W. de Silva. *Vibration: Fundamentals and Practice (Second Edition)*. CRC Press, Boca Raton, Florida, USA, 2006.

[32] S. Marburg and B. Nolte. A Unified Approach to Finite and Boundary Element Discretization in Linear Time-Harmonic Acoustics. In S. Marburg and B. Nolte, editors, *Computational Acoustics of Noise Propagation in Fluids. Finite and Boundary Element Methods*, pages 1–34. Springer, Berlin, Germany, 2008.

[33] M. Ochmann and H. Brick. Acoustical Radiation and Scattering above an Impedance Plane. In S. Marburg and B. Nolte, editors, *Computational Acoustics of Noise Propagation in Fluids. Finite and Boundary Element Methods*, pages 459–494. Springer, Berlin, Germany, 2008.

[34] H. Peters, S. Marburg, and N. Kessissoglou. Structural-acoustic coupling on non-conforming meshes with quadratic shape functions. *International Journal for Numerical Methods in Engineering*, 91(1):27–38, 2012.

[35] B. Flemisch, M. Kaltenbacher, and B. I. Wohlmuth. Elasto-acoustic and acoustic-acoustic coupling on non-matching grids. *International Journal for Numerical Methods in Engineering*, 67(13):1791–1810, 2006.

[36] M. J. Gander and C. Japhet. An Algorithm for Non-Matching Grid Projections with Linear Complexity. In M. Bercovier, M. J. Gander, R. Kornhuber, and O. Widlund, editors, *Domain Decomposition Methods in Science and Engineering XVIII*, pages 185–192. Springer, Berlin, Germany, 2009.

[37] H. Peters, N. Kessissoglou, and S. Marburg. Modal decomposition of exterior acoustic-structure interaction. *Journal of the Acoustical Society of America*, 133(5):2668–2677, 2013.

[38] S. Marburg and R. Anderssohn. Fluid structure interaction and admittance boundary conditions: Setup of an analytical example. *Journal of Computational Acoustics*, 19(1):63–74, 2011.

[39] D. Fritze, S. Marburg, and H.-J. Hardtke. FEM-BEM-coupling and structural-acoustic sensitivity analysis for shell geometries. *Computers and Structures*, 83(2–3):143–154, 2005.

[40] C.-J. Zheng, C.-X. Bi, C. Zhang, H.-F. Gao, and H.-B. Chen. Free vibration analysis of elastic structures submerged in an infinite or semi-infinite fluid domain by means of a coupled FE-BE solver. *Journal of Computational Physics*, 359:183–198, 2018.

[41] T. Liang, J. Wang, J. Xiao, and L. Wen. Coupled BE-FE based vibroacoustic modal analysis and frequency sweep using a generalized resolvent sampling method. *Computer Methods in Applied Mechanics and Engineering*, 345:518–538, 2019.

[42] F. Fahy and P. Gardonio. *Sound and Structural Vibration*. Academic Press, Oxford, United Kingdom, 2007.

[43] X. Li and S. Li. Modal parameter estimation for fluid-loaded structures from reduced order models. *Journal of the Acoustical Society of America*, 120(4):1996–2003, 2006.

[44] S. K. Baydoun and S. Marburg. Quantification of numerical damping in the acoustic boundary element method for two-dimensional duct problems. *Journal of Theoretical and Computational Acoustics*, 26(3):1850022, 2018.

[45] S. Marburg. A pollution effect in the boundary element method for acoustic problems. *Journal of Theoretical and Computational Acoustics*, 26(2):1850018, 2018.

[46] S. N. Chandler-Wilde, E. A. Spence, A. Gibbs, and V. P. Smyshlyaev. High-frequency bounds for the Helmholtz equation under parabolic trapping and applications in numerical analysis. *arXiv:1708.08415v5*, 2019.

[47] G. W. Benthien. Application of frequency interpolation to acoustic-structure interaction problems. Technical report, Naval Ocean Systems Center, 1989.

[48] S. M. Kirkup and D. J. Henwood. Methods for speeding up the boundary element solutions of acoustic radiation problems. *Journal of Vibration and Acoustics*, 144(3):347–380, 1992.

[49] C. Runge. Über empirische Funktionen und die Interpolation zwischen äquidistanten Ordinaten. *Zeitschrift für Mathematik und Physik*, 46:224–243, 1901.

[50] C. Effenberger and D. Kressner. Chebyshev interpolation for nonlinear eigenvalue problems. *BIT Numerical Mathematics*, 52(4):933–951, 2012.

[51] S. K. Baydoun, M. Voigt, and S. Marburg. Low-rank iteration schemes for the multi-frequency solution of acoustic boundary element equations. *Journal of Theoretical and Computational Acoustics*, 29(3):2150004, 2021.

[52] J. Xiao, J. Wang, T. Liang, and L. Wen. The RSRR method for solving large-scale nonlinear eigenvalue problems in boundary element method. *Engineering Analysis with Boundary Elements*, 93(1):150–160, 2018.

[53] L. N. Trefethen and J. A. C. Weideman. The exponentially convergent trapezoidal rule. *SIAM Review*, 56(3):385–458, 2014.

[54] A. P. Austin, P. Kravanja, and L. N. Trefethen. Numerical algorithms based on analytic function values at roots of unity. *SIAM Journal on Numerical Analysis*, 52(4):1795–1821, 2014.

[55] W. Hackbusch and B. Khoromskij. A sparse H-matrix arithmetic. Part 2: Application to multi-dimensional problems. *Computing*, 64:21–47, 2000.

[56] Y. Liu. *Fast Multipole Boundary Element Method: Theory and Applications in Engineering.* Cambridge University Press, United Kingdom, 2009.

[57] S. Dirckx, D. Huybrechs, and K. Meerbergen. Frequency extraction for BEM-matrices arising from the 3D scalar Helmholtz equation. *arXiv:2012.14287*, 2020.

[58] T. W. Wu, W. L. Li, and A. F. Seybert. An efficient boundary element algorithm for multi-frequency acoustical analysis. *Journal of Acoustical Society of America*, 94(1):447–452, 1993.

[59] S. Li. An efficient technique for multi-frequency acoustic analysis by boundary element method. *Journal of Sound and Vibration*, 283(3–5):971–980, 2005.

[60] X. Wang, H. Chen, and J. Zhang. An efficient boundary integral equation method for multi-frequency acoustics analysis. *Engineering Analysis with Boundary Elements*, 61:282–286, 2015.

[61] J.-P. Coyette, C. Lecomte, J.-L. Migeot, J. Blanche, M. Rochette, and G. Mirkovic. Calculation of vibro-acoustic frequency response functions using a single frequency boundary element solution and a Padé expansion. *Acta Acustica United with Acustica*, 85(3):371–377, 1999.

[62] S. Lefteriu, M. Souza Lenzi, H. Bériot, M. Tournour, and W. Desmet. Fast frequency sweep method for indirect boundary element models arising in acoustics. *Engineering Analysis with Boundary Elements*, 69:32–45, 2016.

[63] J. Baumgart, S. Marburg, and S. Schneider. Efficient sound power computation of open structures with infinite/finite elements and by means of the Padé-via-Lanczos algorithm. *Journal of Computational Acoustics*, 15(4):557–577, 2007.

[64] J. P. Tuck-Lee, P. M. Pinsky, and H. L. Liew. Multifrequency Analysis using Matrix Padé-via-Lanczos. In S. Marburg and B. Nolte, editors, *Computational Acoustics of Noise Propagation in Fluids. Finite and Boundary Element Methods*, pages 89–114. Springer, Berlin, Germany, 2008.

[65] Y. Saad and M. H. Schultz. GMRES: A generalized minimal residual algorithm for solving nonsymmetric linear systems. *SIAM Journal on Scientific and Statistical Computing*, 7:856–869, 1986.

[66] S. Marburg and S. Schneider. Performance of iterative solvers for acoustic problems. Part I. Solvers and effect of diagonal preconditioning. *Engineering Analysis with Boundary Elements*, 27(7):727–750, 2003.

[67] M. L. Parks, E. de Sturler, G. Mackey, D. D. Johnson, and S. Maiti. Recycling Krylov subspaces for sequences of linear systems. *SIAM Journal on Scientific Computing*, 28(5):1651–1674, 2006.

[68] S. Keuchel, J. Bierman, and O. von Estorff. A combination of the fast multipole boundary element method and Krylov subspace recycling solvers. *Engineering Analysis with Boundary Elements*, 65:136–146, 2016.

[69] U. Hetmaniuk, R. Tezaur, and C. Farhat. Review and assessment of interpolatory model order reduction methods for frequency response structural dynamics and acoustics problems. *International Journal for Numerical Methods in Engineering*, 90(13):1636–1662, 2012.

[70] A. S. Wixom and J. G. McDaniel. Fast frequency sweeps with many forcing vectors through adaptive interpolatory model order reduction. *International Journal for Numerical Methods in Engineering*, 100(6):442–457, 2014.

[71] C. Jelich, S. K. Baydoun, M. Voigt, and S. Marburg. A greedy reduced basis algorithm for structural acoustic systems with parameter and implicit frequency dependence. *International Journal for Numerical Methods in Engineering*, 2021.

[72] R. S. Puri, D. Morrey, A. J. Bell, J. F. Durodola, E. B. Rudnyi, and J. G. Korvink. Reduced order fully coupled structural–acoustic analysis via implicit moment matching. *Applied Mathematical Modelling*, 33(11):4097–4119, 2009.

[73] H. Peters, N. Kessissoglou, and S. Marburg. Modal decomposition of exterior acoustic-structure interaction problems with model order reduction. *Journal of the Acoustical Society of America*, 135(6):2706–2717, 2014.

[74] B. Vital. *Etude de quelques méthodes de résolution de problemes linéaires de grande taille sur multiprocesseur*. PhD thesis, Université de Rennes, 1990.

[75] M. H. Gutknecht. Block Krylov space methods for linear systems with multiple right-hand sides: An introduction. In A. H. Siddiqi, I. Du, and O. Christensen, editors, *Modern Mathematical Models, Methods and Algorithms for Real World Systems*. Anshan Ltd, Tunbridge Wells, United Kingdom, 2007.

[76] D. Panagiotopoulos, E. Deckers, and W. Desmet. Krylov subspaces recycling based model order reduction for acoustic BEM systems and an error estimator. *Computer Methods in Applied Mechanics and Engineering*, 359:112755, 2020.

[77] X. Xie and Y. Liu. An adaptive model order reduction method for boundary element-based multi-frequency acoustic wave problems. *Computer Methods in Applied Mechanics and Engineering*, 373:113532, 2021.

[78] M. Petyt, J. Lea, and G. Koopmann. A finite element method for determining the acoustic modes of irregular shaped cavities. *Journal of Sound and Vibration*, 45(4):495–502, 1976.

[79] P. K. Banerjee, S. Ahmad, and H. C. Wang. A new BEM formulation for the acoustic eigenfrequency analysis. *International Journal for Numercial Methods in Engineering*, 26(6):1299–1309, 1988.

[80] Z. S. Chen, G. Hofstetter, and H. A. Mang. A 3D boundary element method for determination of acoustic eigenfrequencies considering admittance boundary conditions. *Journal of Computational Acoustics*, 1(4):455–468, 1993.

[81] J. E. Roman, C. Campos, E. Romero, and A. Tomàs. SLEPc Users Manual. Technical report, Universitat Politècnica de València, 2020.

[82] G. de Mey. Calculation of eigenvalues of the Helmholtz equation by an integral equation. *International Journal for Numerical Methods in Engineering*, 10(1):59–66, 1976.

[83] J. N. Lyness and C. B. Moler. Numercial differentiation of analytic functions. *SIAM Journal of Numerical Analysis*, 4(2):202–210, 1967.

[84] S. M. Kirkup and S. Amini. Solution of the Helmholtz eigenvalue problem via the boundary element method. *International Journal for Numerical Methods in Engineering*, 36(2):321–330, 1993.

[85] M. El-Guide, A. Międlar, and Y. Saad. A rational approximation method for solving acoustic nonlinear eigenvalue problems. *Engineering Analysis with Boundary Elements*, 111:44–54, 2020.

[86] Y. Su and Z. Bai. Solving rational eigenvalue problems via linearization. *SIAM Journal on Matrix Analysis and Applications*, 32(1):201–216, 2011.

[87] S. Güttel, G. M. Negri Porzio, and F. Tisseur. Robust rational approximation of nonlinear eigenvalue problems. *MIMS EPrint*, 2020.24, 2020.

[88] J. Asakura, T. Sakurai, H. Tadano, T. Ikegami, and K. Kimura. A numerical method for nonlinear eigenvalue problems using contour integrals. *JSIAM Letters*, 1:52–55, 2009.

[89] W.-J. Beyn. An integral method for solving nonlinear eigenvalue problems. *Linear Algebra and its Applications*, 436(10):3839–3863, 2012.

[90] A. Kimeswenger, O. Steinbach, and G. Unger. Coupled finite and boundary element methods for fluid-solid interaction eigenvalue problems. *SIAM Journal on Numerical Analysis*, 52(5):2400–2414, 2014.

[91] M. C. Brennan, M. Embree, and S. Gugercin. Contour integral methods for nonlinear eigenvalue problems: A systems theoretic approach. *arXiv:2012.14979*, 2020.

[92] C.-J. Zheng, H.-F. Gao, L. Du, H.-B. Chen, and C. Zhang. An accurate and efficient acoustic eigensolver based on a fast multipole BEM and a contour integral method. *Journal of Computational Physics*, 305:677–699, 2016.

[93] C. Jelich, M. Karimi, N. Kessissoglou, and S. Marburg. Efficient solution of block Toeplitz systems with multiple right-hand sides arising from a periodic boundary element formulation. *Engineering Analysis with Boundary Elements*, 130:135–144, 2021.

[94] C. A. Geweth, S. K. Baydoun, F. Saati, K. Sepahvand, and S. Marburg. Effect of boundary conditions in the experimental determination of structural damping. *Mechanical Systems and Signal Processing*, 146:107052, 2021.

[95] F. Kronowetter, S. K. Baydoun, M. Eser, L. Moheit, and S. Marburg. A benchmark study on eigenfrequencies of fluid-loaded structures. *Journal of Theoretical and Computational Acoustics*, 28(2):2050013, 2020.

[96] T. Sakurai, Y. Futamura, and H. Tadano. Efficient parameter estimation and implementation of a contour integral-based eigensolver. *Journal of Algorithms & Computational Technology*, 7(3):249–270, 2013.

[97] S. Yokota and T. Sakurai. A projection method for nonlinear eigenvalue problems using contour integrals. *JSIAM Letters*, 5:41–44, 2013.

[98] E. Polizzi. A density matrix-based algorithm for solving eigenvalue problems. *Physical Review B*, 79(11):115112, 2009.

[99] B. Gavin, A. Międlar, and E. Polizzi. FEAST eigensolver for nonlinear eigenvalue problems. *Journal of Computational Science*, 27(2):107–117, 2018.

[100] C. C. Claeys, P. Sas, and W. Desmet. On the acoustic radiation efficiency of local resonance based stop band materials. *Journal of Sound and Vibration*, 333(14):3203–3213, 2014.

[101] J. Jung, C.-H. Jeong, and J. S. Jensen. Efficient sound radiation using a bandgap structure. *Applied Physics Letters*, 115:041903, 2019.

[102] J. Henneberg, A. Gerlach, H. Cebulla, and S. Marburg. The potential of stop band material in multi-frequency ultrasonic transducers. *Journal of Sound and Vibration*, 452:132–146, 2019.

A Appended Publications

A.1 Publication I

Investigation of radiation damping in sandwich structures using finite and boundary element methods and a nonlinear eigensolver

This paper is licensed under a Creative Commons Attribution (CC BY) license.

Investigation of radiation damping in sandwich structures using finite and boundary element methods and a nonlinear eigensolver

Suhaib Koji Baydoun[a)] and Steffen Marburg

Chair of Vibroacoustics of Vehicles and Machines, Technical University of Munich, Boltzmannstraße 15, Garching, 85748, Germany

ABSTRACT:

The fully coupled vibroacoustic interaction of sandwich panels is studied using the finite and the boundary element methods. The extent of radiation damping is quantified for various configurations based on both harmonic response analyses and modal analyses. The underlying nonlinear eigenvalue problem is solved using a projection method based on contour integration yielding the shifted (wet) eigenfrequencies, modal radiation loss factors, and air-loaded structural modes. The numerical results clearly illustrate the relevance of air-loading when studying the vibration of sandwich structures. Further, the numerically obtained estimates for radiation damping are compared to both theoretical expressions and experimental results found in the literature. Although good agreement is observed in general, the comparison indicates the limited applicability of commonly used theoretical expressions when coincidence occurs in a frequency range where the modes are still well separated. Moreover, possible sources of error when experimentally determining radiation damping are discussed in detail. The results presented in this paper provide deep insights into the phenomenon of acoustic radiation damping and help to estimate its relevance in future research. © 2020 Author(s). All article content, except where otherwise noted, is licensed under a Creative Commons Attribution (CC BY) license (*http://creativecommons.org/licenses/by/4.0/*).
https://doi.org/10.1121/10.0000947

I. INTRODUCTION

The exposure of human beings to vibration and noise can have implications ranging from annoyance to health damage. Hence, researchers of various fields, such as material scientists and control engineers, are concerned with the development of passive and active damping devices as well as the exploitation of material-inherent damping. This is particularly important for lightweight structures, which—generally speaking—are either stiff and weakly damped or exhibit high damping but rather poor elastic properties.[1–3]

However, an often neglected contribution to the overall damping of structures is the dissipation of vibrational energy due to sound radiation. While acoustic radiation damping is a rather insignificant aspect in many bulky engineering applications, it is the primary energy dissipating mechanism for stiff lightweight structures with large radiating surfaces. It follows that attempts to reduce the vibrational response of these lightweight structures by additional mechanical damping can only be successful if the extent of mechanical damping is comparable or larger than the extent of radiation damping.[4] Therefore, engineers are in need of reliable and flexible methods for the quantification of radiation damping in an early stage of the design process.

However, due to the coupled nature of the problem, involving the behaviors of both structure and surrounding fluid, radiation damping is not generally amenable to analytical quantifications. Early theoretical methods predict the modal radiation damping of rectangular plates[5,6] and cylindrical shells.[7] Expressions for frequency averaged radiation damping are also derived, assuming that a sufficiently large number of modes contributes to the vibration of the plate.[8] These methods are all based on theoretical expressions of the radiation resistance[9–11] or theoretical expressions of the acoustic impedance of the plates.[12] They are only valid for homogeneous plates that are confined in an acoustically rigid baffle prohibiting flow between the two sides of the plate. Later, correction factors are proposed to account for unbaffled plates[13] with arbitrary boundary conditions.[14] However, their applicability to more complex geometric and material configurations can hardly be judged.

Sandwich structures, consisting of two thin and stiff face sheets enclosing a thick, lightweight and often anisotropic core, account for such complex configurations. While sandwich structures excel at the ratio of bending stiffness to mass, they exhibit relatively high flexural wave speeds compared to those of solid plates with equivalent mechanical properties. In consequence, coincidence between bending and acoustic waves occurs at relatively low frequencies. Moreover, due to the anisotropy, sandwich panels do not only exhibit a single critical frequency, but rather a range of frequencies in which coincidence occurs, thus giving rise to efficient sound radiation and hence high acoustic radiation damping in a wide frequency range.

a)Electronic mail: suhaib.baydoun@tum.de, ORCID: 0000-0002-1184-065X.

Analytical expressions for the flexural vibration of sandwich panels can be derived from Hamilton's principle.[15] Experimental[16,17] and numerical approaches[18–20] have been followed to investigate the vibroacoustic behavior of sandwich panels with respect to different core and face materials, lay-ups, and geometric configurations—see also the review by D'Alessandro *et al.*[21] Besides vibroacoustic studies, many researchers have also made efforts to quantify material-inherent damping of sandwich panels to enhance damping by means of viscoelastic treatments.[2] Most of the experimental studies are conducted in air and hence the thereby obtained loss factors include the effects of acoustic radiation damping.

Clarkson and Brown deduced the radiation loss factors of a honeycomb sandwich platform by means of reference measurements inside a vacuum chamber.[22] Zhou and Crocker determined radiation damping of sandwich plates clamped between two reverberation chambers based on principles of energy flow.[19] Apart from these two articles, however, little published data on actual values for radiation damping of sandwich structures exist, although radiation damping can account for the major share in the overall damping and therefore undermine the effectiveness of additional mechanical damping.

In this paper, we employ a numerical framework based on the finite element method (FEM) and the boundary element method (BEM) in order to better understand the phenomenon of acoustic radiation damping. The structural and acoustic responses are fully coupled to enable the modeling of a mutual structural acoustic interaction as it occurs in many sandwich structures. The cores are represented by three-dimensional solid finite elements in order to capture local bending deformations of the individual face sheets that cause sound radiation in addition to the global bending deformations. Using this framework, we contribute in the following aspects to gain a deeper insight into the phenomenon of acoustic radiation damping:

- First, we study the extent of radiation damping for three sandwich panels subject to different boundary conditions in both acoustic full- and halfspaces. The harmonic radiation loss factors are obtained by relating the radiated sound power to the vibrational energy of the structure. The panels are excited by point forces as well as diffuse acoustic fields. The results indicate a strong influence of boundary conditions and excitations in the low frequency range, where the responses are mainly determined by modal behavior.
- Second, using a nonlinear eigensolver based on contour integration, we perform modal analyses of the air-loaded sandwich panels to deduce their modal radiation loss factors and eigenfrequencies. The latter are lowered compared to the *in vacuo* eigenfrequencies due to the effect of added mass and damping. The modal radiation loss factors, which are inherent properties of the structural acoustic system, agree well with the harmonic loss factors at the respective eigenfrequencies. Furthermore, we propose

a more effective strategy for checking and filtering the eigenvalues when using contour integration and also provide guidance in choosing the solver-specific parameters.

- Last, we compare our numerically obtained estimates for radiation damping to theoretical expressions and experimental results found in the literature, generally yielding a good agreement. However, the comparison also indicates the limited applicability of commonly used theoretical expressions when coincidence occurs in a frequency range where the modes are still well separated. Finally, we discuss experimental quantification of radiation damping and associated sources of error such as the reinjection of acoustic energy and the reliability of reverberation room measurements in the low frequency range.

II. NUMERICAL QUANTIFICATION OF ACOUSTIC RADIATION DAMPING

A. Coupled formulation for structural acoustic interaction

We consider the fully coupled structural acoustic interaction in order to determine the vibratory response of sandwich structures. Under the assumption of a harmonic time dependency $e^{-i\omega t}$, the equations of linear elasticity and acoustics are discretized using FEM[23] and direct collocation BEM.[24] The resulting systems of equations read

$$(\mathbf{K} - \omega^2 \mathbf{M})\mathbf{u} = \mathbf{f}_s + \mathbf{f}_f, \tag{1}$$

and

$$\mathbf{H}\mathbf{p} = \mathbf{G}\left(\mathbf{v}_f - \mathbf{v}_f^{\mathrm{i}}\right) + \mathbf{H}\mathbf{p}^{\mathrm{i}}. \tag{2}$$

Therein, $\mathbf{u}$ and $\mathbf{p}$ are the vectors of unknown displacement and sound pressure values at the nodes, respectively. The stiffness and mass matrices of the structure are denoted with $\mathbf{K}$ and $\mathbf{M}$, respectively. The structure is excited by external forces $\mathbf{f}_s$ as well as fluid forces $\mathbf{f}_f$. The latter act by virtue of the acoustic field. Structure-inherent damping is not considered in this work and, hence, acoustic radiation damping is the only dissipative mechanism occurring. Further, $\mathbf{H}$ and $\mathbf{G}$ are the frequency dependent boundary element (BE) matrices, relating the structural particle velocity $\mathbf{v}_f$ to the sound pressure. Acoustic excitation is taken into account by the incident sound pressure field $\mathbf{p}^{\mathrm{i}}$ and the corresponding incident particle velocity $\mathbf{v}_f^{\mathrm{i}}$. The angular frequency is defined as $\omega = 2\pi f$, and i denotes the imaginary unit.

Since we are particularly interested in applications that exhibit considerable levels of radiation damping, the influence of the acoustic field on the structural response is not generally negligible. Consequently, it is not sufficient to determine the *in vacuo* response of the structure by solving Eq. (1), and subsequently evaluate the acoustic field using Eq. (2) in a post-processing step. Instead, Eqs. (1) and (2) are mutually coupled on the sound radiating surface, i.e.,

$$\mathbf{f}_f = \mathbf{C}_{\mathrm{sf}}\mathbf{p} \quad \text{and} \quad \mathbf{v}_f = -\mathrm{i}\omega\mathbf{C}_{\mathrm{fs}}\mathbf{u}. \tag{3}$$
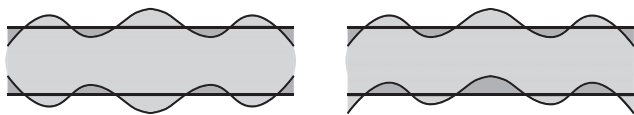
FIG. 1. Symmetric motion involving thickness deformation of the core (left) and antisymmetric motion corresponding to global bending deformation of the sandwich panel (right).

FIG. 2. Modeling of simply supported boundary conditions by constraining the displacement DOFs of the face sheet edges.

The mesh coupling is established by the coupling matrices $\mathbf{C}_{sf}$ and $\mathbf{C}_{fs}$, relating the displacement and pressure degrees of freedom (DOFs).[25] Since structural acoustic interaction is mainly relevant for thin-walled lightweight structures, most researchers rely on shell finite elements for modeling the structural subdomain.[18,20,25] While the sandwich panels considered in this work can certainly be modeled using layered shell formulations as well, nevertheless, we will follow a different approach involving three-dimensional solid finite elements for the representation of the thick core. Additionally, shell elements are employed for the thin face sheets. While this approach leads to more DOFs compared to the use of layered shell elements, it enables us to capture local bending deformations of the individual face sheets, which otherwise would not be possible. These local bending deformations of the face sheets—also known as symmetric motion—involve thickness deformations of the core. They cause sound radiation in addition to the global bending deformations (anti-symmetric motion). These two types of lamb waves,[26] which are shown in Fig. 1, coexist in sandwich panels.

Regarding the boundary conditions of the panel, both the freely suspended and the simply supported cases are considered in this work. The simply supported conditions are modeled by constraining the displacement DOFs of the face sheet edges, as is schematically shown in Fig. 2.

The approach for modeling the vibroacoustic behavior of a sandwich panel using finite and boundary elements is schematically depicted in Fig. 3. The shell finite elements that represent the face sheets are defined with an offset of half the shell thickness. In this way, their nodes coincide with the outer nodes of the solid elements representing the core. These nodes on the top and bottom surfaces are also the ones that are coupled to the nodes of the boundary element mesh. In the case of an unbaffled panel—i.e., a panel with free edges where acoustic short-circuiting occurs—a

single boundary element mesh with a closed surface is used. Otherwise, when the panel is confined in an acoustically rigid baffle, the two independent acoustic subdomains on each side of the panel are modeled using a halfspace formulation with a modified Green's function.[27] In this way, the dissipation of vibrational energy due to sound radiation is considered simultaneously on both sides of the baffled panel. The boundary element meshes corresponding to a baffled panel are shown in Fig. 4. Note that it is also possible to only model half of the baffled panel along with a single acoustic halfspace. However, this approach would require separate computations and subsequent superpositions of the symmetric and antisymmetric responses (cf. Fig. 1). While this would result in fewer DOFs, nevertheless, we use a full model involving two acoustic halfspaces for the sake of convenience.

In the case of a single acoustic subdomain, the global system of equations containing the coupling conditions emerges as

$$\begin{bmatrix} \mathbf{K} - \omega^2\mathbf{M} & -\mathbf{C}_{sf} \\ i\omega\mathbf{G}\mathbf{C}_{fs} & \mathbf{H} \end{bmatrix} \begin{bmatrix} \mathbf{u} \\ \mathbf{p} \end{bmatrix} = \begin{bmatrix} \mathbf{f}_s \\ -\mathbf{G}\mathbf{v}_f^i + \mathbf{H}\mathbf{p}^i \end{bmatrix}. \qquad (4)$$

If the panel is confined in a baffle, the global system comprises three subdomains. Assuming that just one side of the panel is excited by an incident sound field (which actually resembles the situation in a window test rig), the resulting monolithic equation is given as

$$\begin{bmatrix} \mathbf{K} - \omega^2\mathbf{M} & -\mathbf{C}_{sf}^{(I)} & -\mathbf{C}_{sf}^{(II)} \\ i\omega\mathbf{G}^{(I)}\mathbf{C}_{fs}^{(I)} & \mathbf{H}^{(I)} & 0 \\ i\omega\mathbf{G}^{(II)}\mathbf{C}_{fs}^{(II)} & 0 & \mathbf{H}^{(II)} \end{bmatrix} \begin{bmatrix} \mathbf{u} \\ \mathbf{p}^{(I)} \\ \mathbf{p}^{(II)} \end{bmatrix}$$
$$= \begin{bmatrix} \mathbf{f}_s \\ -\mathbf{G}^{(I)}\mathbf{v}_f^i + \mathbf{H}^{(I)}\mathbf{p}^i \\ 0 \end{bmatrix}, \qquad (5)$$
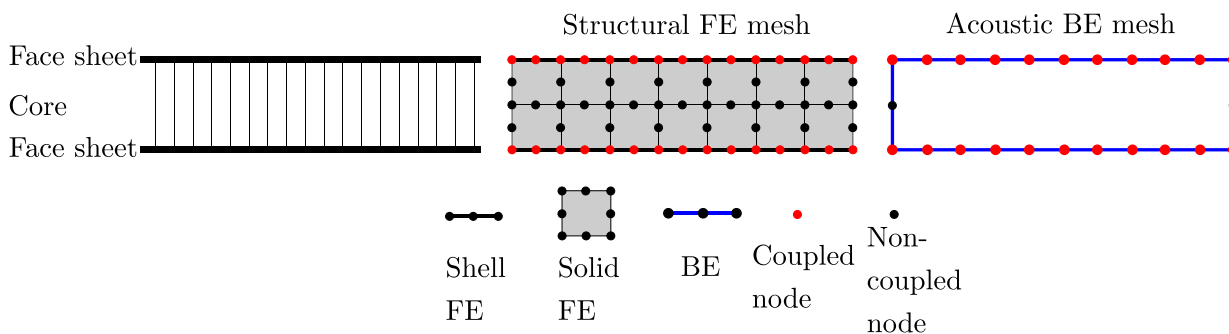

FIG. 3. (Color online) Cross-sectional schematic illustrating the numerical modeling of a (non-baffled) sandwich panel and the surrounding acoustic field. The structural FE mesh is coupled to the closed acoustic BE mesh via non-coincident nodes on the radiating surface.
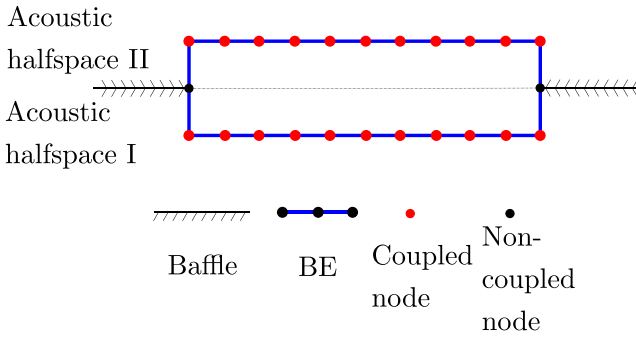
FIG. 4. (Color online) Cross-sectional schematic of two halfspace BE meshes representing the acoustic fields on either side of a baffled panel.

where $(\cdot)^{(I)}$ and $(\cdot)^{(II)}$ denote the acoustic halfspaces on the respective sides of the panel. In the case of geometrical symmetry with respect to the plane of the baffle, $\mathbf{H}^{(I)} = \mathbf{H}^{(II)}$ and $\mathbf{G}^{(I)} = \mathbf{G}^{(II)}$ hold, and consequently, the numerical integration for assembling the BE matrices needs to be performed only once.

The complex sound power P in linear time-harmonic acoustics can be obtained from

$$P = \frac{1}{2}\int_\Gamma p v_f^* \, d\Gamma, \tag{6}$$

where v_f denotes the fluid particle velocity, and $(\cdot)^*$ is the conjugate complex. In the discrete setting, the sound power is evaluated as a post-processing step. The nodal values for the sound pressure are related to the particle velocity via Eq. (2), and the integration of their interpolation functions results in the boundary mass matrix Θ. Finally, substitution by the acoustic impedance matrix $\mathbf{Z} = (\mathbf{H}^{-1}\mathbf{G})^T\Theta$ yields the complex sound power in the discrete setting

$$P = \frac{1}{2}\mathbf{v}_f^T \mathbf{Z} \mathbf{v}_f^*. \tag{7}$$

Only the real part $\mathrm{Re}(\cdot)$ of the above expression contributes to the radiation to the far-field and hence to the structural damping due to sound radiation. The latter is quantified by relating the radiated sound power to the power corresponding to the total energy of the vibrating structure.[28] The time-averaged total vibrational energy equals twice the time-averaged kinetic energy, or equivalently, twice the time-averaged potential energy. For harmonic problems, these energy quantities can be determined from the structural response via[29]

$$E_k = \frac{1}{2}\omega^2 \mathbf{u}^T(\mathbf{M} + \mathbf{M}_f)\mathbf{u}^*, \tag{8}$$

and

$$E_p = \frac{1}{2}\mathbf{u}^T \mathbf{K} \mathbf{u}^* - \frac{1}{2}\mathbf{f}_s^H \mathbf{u}, \tag{9}$$

where the first term in Eq. (9) corresponds to the energy due to the elastic strain, and the second term is the work done by

external forces. The evaluation of the kinetic energy E_k requires knowledge of the additional mass $\mathbf{M}_f$ due to acoustic loading. This frequency dependent mass contribution could be approximated by the second order term of a Taylor expansion of the acoustic impedance matrix $\mathbf{Z}$.[30] However, for our purposes it is more convenient to simply use the potential energy E_p to quantify the radiation loss factor. Hence, the radiation loss factor is expressed by[28]

$$\eta_r = \frac{\mathrm{Re}(P)}{|\omega E_p|}. \tag{10}$$

Note that the kinetic energy E_k could be equally used to evaluate the radiation loss factor. Recent results[31,32] show that spurious numerical damping could lead to an overestimation of damping phenomena when studying them with BEM. However, the occurrence of numerical damping does not seem to be an issue in exterior acoustics.

B. Modal analysis of structural acoustic interaction

Modal analyses provide useful information on the properties of the system, such as the eigenfrequencies of the fluid-loaded structure. In this work, in particular, it serves as an alternative way to quantify the extent of radiation damping. The modal radiation loss factors can be deduced from the complex eigenvalues of the structural acoustic system. At resonance, these modal loss factors are expected to agree with the continuous radiation loss factor defined in Eq. (10).

The purely structural equation subject to acoustic loading is obtained by forming the Schur complement of Eq. (4) and thereby omitting the pressure DOFs,[33] i.e.,

$$\underbrace{\left[\mathbf{K} - \omega^2\mathbf{M} + i\omega\mathbf{C}_{\mathrm{sf}}\mathbf{H}^{-1}\mathbf{G}\mathbf{C}_{\mathrm{fs}}\right]}_{\mathbf{B}(\omega)}\mathbf{u}$$
$$= \mathbf{f}_s + \mathbf{C}_{\mathrm{sf}}\left(\mathbf{p}^{\mathrm{i}} - \mathbf{H}^{-1}\mathbf{G}\mathbf{v}_f^{\mathrm{i}}\right), \tag{11}$$

in which $i\omega\mathbf{C}_{\mathrm{sf}}\mathbf{H}^{-1}\mathbf{G}\mathbf{C}_{\mathrm{fs}}$ can be interpreted as the effect of fluid loading. Note that the Schur complement of Eq. (5) can be obtained in a similar manner. By setting the right-hand side to zero, we arrive at the definition of the structural acoustic eigenvalue problem (EVP)

$$\mathbf{B}(\tilde{\omega})\mathbf{v} = \mathbf{0}, \tag{12}$$

with the fluid-loaded structural mode $\mathbf{v}$ and the complex eigenfrequency $\tilde{\omega}$. The EVP in Eq. (12) is nonlinear since the BE matrices $\mathbf{H}$ and $\mathbf{G}$ implicitly depend on the frequency.

Several methods have been proposed for the solution of Eq. (12) during the last years. Peters et al.[30] employed a truncated Taylor series to approximate the frequency dependent matrices, and the resultant polynomial EVP is solved using symmetric linearization. In a subsequent work, the computational effort associated with the linearized EVP is addressed by means of Krylov subspace model order reduction of the structural subproblem.[34] However, the success of this method strongly depends on the convergence radius of

the Taylor approximation and the decay of the coefficients of the polynomial approximation. As a remedy, the frequency range of interest needs to be subdivided, whereas proper choices of these sub-frequency ranges can hardly be made *a priori*.

Therefore, in recent years alternative approaches for the solutions of nonlinear EVPs have been proposed, which can be classified as *contour integral methods*.[35–38] Using contour integration, a nonlinear EVP is converted to a generalized EVP of reduced dimension that exhibits identical eigenvalues inside a predefined region in the complex plane. Contour integral methods are particularly appealing because of their general applicability and suitability for the execution on distributed parallel computers.

While we assume that the other contour integral methods would also fulfill our purpose of investigating air-loaded modes and radiation damping of sandwich panels, we choose to use the block Sakurai Sugiura method (block SS)[36,39] in this work. A comparison of different eigenvalue solvers is beyond the scope of this work. Moreover, we note that the focus of our contribution is not the further development of existing methods but rather its application in the context of air-loaded elastic structures. Most of following content on block SS can be also found in the papers by Asakura *et al.*[36] and Zheng *et al.*[36,39] Since we nevertheless propose a more effective strategy for checking and filtering the eigenvalues—which is crucial when using contour integral methods—the procedure is briefly outlined in what follows.

Block SS is a direct method, and it essentially works by replacing the nonlinear EVP in Eq. (12) by the generalized EVP

$$\mathbf{H}_1 \boldsymbol{\psi} = \lambda \mathbf{H}_2 \boldsymbol{\psi}, \qquad (13)$$

with the eigenpair $(\boldsymbol{\psi}, \lambda)$. The block Hankel matrices $\mathbf{H}_1, \mathbf{H}_2 \in \mathbb{C}^{KL \times KL}$ are defined as

$$\mathbf{H}_1 = \begin{bmatrix} \mathbf{M}_0 & \mathbf{M}_1 & \cdots & \mathbf{M}_{K-1} \\ \mathbf{M}_1 & & & \vdots \\ \vdots & & & \mathbf{M}_{2K-3} \\ \mathbf{M}_{K-1} & \cdots & \mathbf{M}_{2K-3} & \mathbf{M}_{2K-2} \end{bmatrix},$$

$$\mathbf{H}_2 = \begin{bmatrix} \mathbf{M}_1 & \mathbf{M}_2 & \cdots & \mathbf{M}_K \\ \mathbf{M}_2 & & & \vdots \\ \vdots & & & \mathbf{M}_{2K-2} \\ \mathbf{M}_K & \cdots & \mathbf{M}_{2K-2} & \mathbf{M}_{2K-1} \end{bmatrix}, \qquad (14)$$

where K and L are user-specified positive integers. The proper choice of K and L will be discussed in detail later on. The moments $\mathbf{M}_l \in \mathbb{C}^{L \times L}$ are computed from

$$\mathbf{M}_l = \frac{1}{2\pi i} \oint_C \sigma^l \mathbf{U}^{\mathrm{H}} \mathbf{B}^{-1}(\sigma) \mathbf{V} \, d\sigma, \quad l = 0, \dots, 2K-1, \qquad (15)$$

where $\mathbf{U}$ and $\mathbf{V}$ contain randomly chosen source vectors as columns, and $(\cdot)^{\mathrm{H}}$ denotes the Hermitian transpose. The original system matrix $\mathbf{B}$ is evaluated at the complex frequency parameter σ. The latter is defined along C—a closed non-self-intersecting continuous loop in the complex plane. Once the reduced EVP in Eq. (13) is solved, the fluid-loaded structural mode can be recovered from

$$\mathbf{v} = \mathbf{S}\boldsymbol{\psi}. \qquad (16)$$

The corresponding eigenvalue λ equals the complex eigenfrequency $\tilde{\omega}$ of the original system in Eq. (12). The block matrix $\mathbf{S} = [\mathbf{S}_0, \dots, \mathbf{S}_{K-1}]$ is also obtained by contour integration via

$$\mathbf{S}_l = \frac{1}{2\pi i} \oint_C \sigma^l \mathbf{B}^{-1}(\sigma) \mathbf{V} \, d\sigma, \quad l = 0, \dots, K-1. \qquad (17)$$

C. Algorithm and choice of parameters for modal analysis of moderately coupled structural acoustic interaction

The range of obtained eigenvalues is enclosed by the contour C along which the integrals in Eqs. (15) and (17) are evaluated. This contour needs to be predefined by the user. In the context of fluid-loaded structures, a suitable choice of the contour is an ellipse that has its major axis aligned with the real axis. The two vertices on the real axis correspond to the upper and lower limits $(f_{\max}, f_{\min})$ of the frequency range of interest. A suitable ellipse is shown in Fig. 5 and can be expressed by

$$\sigma(\theta) = \gamma + \rho(\cos\theta + i\zeta\sin\theta), \quad \theta \in [0, 2\pi), \qquad (18)$$

where $\gamma = (f_{\max} + f_{\min})/2$ and $\rho = (f_{\max} - f_{\min})/2$. The factor ζ defines the shape of the ellipse and should be chosen according to the expected ratio of imaginary and real parts of the eigenvalues. Generally, the ellipse should be wide and short ($\zeta < 1$)—especially in the case of weak to moderately strong structural acoustic coupling. With the definition of the contour at hand, the integrals in Eqs. (15) and (17) are approximated using the N-point trapezoidal rule, i.e.,

$$\hat{\mathbf{S}}_l = \frac{1}{iN} \sum_{j=1}^{N} \left(\frac{\sigma(\theta_j) - \gamma}{\rho} \right)^l \sigma'(\theta_j) \mathbf{B}^{-1}(\sigma(\theta_j)) \mathbf{V}, \qquad (19)$$

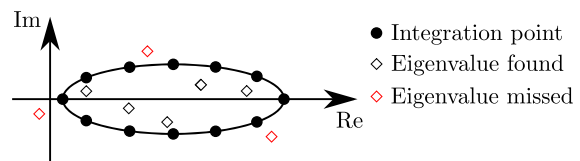$$\hat{\mathbf{M}}_l = \mathbf{U}^{\mathrm{H}} \hat{\mathbf{S}}_l, \qquad (20)$$

FIG. 5. (Color online) Elliptic contour in the complex plane enclosing the eigenvalues of interest.

where N denotes the number of integration points on the contour, and $\theta_j = 2\pi(j-1)/N$, $j = 1, ..., N$. Using the approximated moments $\hat{\mathbf{M}}_l$, the (approximated) Hankel matrices $\hat{\mathbf{H}}_1$ and $\hat{\mathbf{H}}_2$ can be assembled according to Eq. (14). Finally, the corresponding generalized EVP $\hat{\mathbf{H}}_1 \hat{\psi}_j = \hat{\lambda}_j \hat{\mathbf{H}}_2 \hat{\psi}_j$ is solved and the complex eigenfrequencies $\tilde{\omega}_j$, as well as the fluid-loaded modes $\mathbf{v}_j$, $j = 1, ..., KL$, are recovered from

$$\tilde{\omega}_j = \gamma + \rho \hat{\lambda}_j, \quad \mathbf{v}_j = \hat{\mathbf{S}} \hat{\psi}_j. \tag{21}$$

The main challenge with the use of block SS lies in the choice of the following parameters: the degree of moments K, the number of source vectors L, and the number of integration points N. These parameters are related to the computational effort of the method, as well as to the completeness of the determined eigenvalues, i.e., whether all eigenvalues lying inside the contour are found.

Given a fixed number of integration points N, Sakurai et al.[40] suggest to set the degree of moments to $K = N/4$ as a good compromise between accuracy and numerical efficiency of the algorithm. With $L = 1$, we have the original SS method,[35] while the choice $L > 1$ results in the block SS method,[36] which achieves higher accuracy at a similar numerical cost.[41] In this work, we found that the eigensolutions improved with an increasing number of L up to roughly $L = 10$. Higher values than that did not change the results anymore as long as the product KL was large enough. This product defines the dimension of the subspace and hence corresponds to the number of eigenvalues that are obtained from the reduced system. Therefore, KL should be at least as large as the expected number of eigenvalues inside the contour. This number can be estimated a priori by an empirical formula.[40] However, in our case of sandwich structures interacting with air, we will rather rely on the knowledge of the number of in vacuo eigenfrequencies inside the given frequency range $[f_{min}, f_{max}]$. More specifically, we solve the purely structural EVP

$$\left(\mathbf{K} - \omega_{dry}^2 \mathbf{M}\right) \mathbf{v}_{dry} = 0, \tag{22}$$

with the in vacuo modes $\mathbf{v}_{dry}$ and eigenfrequencies ω_{dry} prior to the solution of the structural acoustic EVP in Eq. (12). Then, assuming that in a given frequency range, the number of structural acoustic eigenvalues roughly equals the number n_{dry} of eigenfrequencies, we set the dimension of the reduced EVP such that $KL > n_{dry}$.

The number of integration points N determines the number of linear systems of equations $\mathbf{B}(\sigma)\mathbf{X} = \mathbf{V}$ that have to be solved for evaluating Eq. (19), accounting for the main computational effort. In cases where the algorithm is executed in a parallel computing environment, N is chosen according to the available computing nodes. Sakurai et al.[40] note that a large N is not necessary for an accurate quadrature and suggest, e.g., $N = 16$ or 32. Whereas the results of Zheng et al.[39] confirm this suggestion, they also show that iteratively increasing N is a suitable way for checking

whether all eigenvalues inside the contour are found and also for distinguishing them from spurious eigenvalues. The latter mainly occur due to the projection.

However, in the context of weak to moderately strong structural acoustic interaction, a more effective strategy for checking and filtering the eigenvalues is available based on the modal assurance criterion (MAC).[42] Assuming that the modes of a structure subject to light fluid-loading are similar to the in vacuo modes, the validity of a complex eigenvalue $\tilde{\omega}_j$ can be simply tested by checking the occurrence of its associated mode $\mathbf{v}_j$ in the range of in vacuo modes, i.e.,

$$\mathrm{MAC}(\mathbf{v}_j, \mathbf{v}_{dry,i}) = \frac{|\mathbf{v}_j^H \mathbf{v}_{dry,i}|^2}{\mathbf{v}_j^H \mathbf{v}_{dry,i} \mathbf{v}_j^H \mathbf{v}_{dry,i}}, \quad i = 1, ..., n_{dry}. \tag{23}$$

The values of MAC range from 0, indicating no correspondence between the two modes, to 1, representing a consistent correspondence. In the case of air-loaded sandwich panels, we can expect to find an in vacuo mode $\mathbf{v}_{dry}$ for each actual fluid-loaded mode $\mathbf{v}_j$ that satisfies MAC $= 0.95 ... 1.00$. Otherwise, $\mathbf{v}_j$ and the corresponding eigenvalue $\tilde{\omega}_j$ are identified as spurious. On the other hand, if we are interested in the complex eigenfrequencies corresponding to particular modes, a criterion based on Eq. (23) is useful to check if that eigenfrequency has been found by block SS. If not, the accuracy of the projection needs to be improved by increasing the number of integration points N—of course given that the underlying elliptic contour actually encloses that eigenvalue. Once all desired modes are found, the accuracy of eigenpairs $(\tilde{\omega}, \mathbf{v})$ can be assessed by inserting them into Eq. (12) and computing the backward error

$$\epsilon_{EVP} = \frac{||\mathbf{B}(\tilde{\omega})\mathbf{v}||}{||\mathbf{v}||}. \tag{24}$$

Furthermore, the accuracy of eigenpairs can be subsequently improved by repeating the contour integration (19) with additional integration points placed in between the previous ones. In this way, the additional numerical effort is limited to the computations required for the new integration points, while the intermediate solutions corresponding to the previous integration points can be reused. Thus, a strategy with a gradually increasing number of N is only marginally more expensive than a single execution of the procedure with the final (i.e., largest) number of N.

III. RADIATION DAMPING OF RECTANGULAR HONEYCOMB SANDWICH PANELS

In the following, we will study the vibroacoustic behavior of three honeycomb sandwich panels in air with particular focus on acoustic radiation damping. The results obtained using the presented numerical framework are then compared to theoretical expressions as well as to experimental results available in the literature.

Panel A consists of two plywood face sheets enclosing a paper honeycomb core. The vibroacoustic behavior of a

J. Acoust. Soc. Am. **147** (3), March 2020

Suhaib Koji Baydoun and Steffen Marburg   2025

similar panel is experimentally investigated in the pioneering work by Moore,[16] which has also served as a benchmark for other researchers in the past.[21,43] Panels B and C are made of plane weave fabric-reinforced graphite composite face sheets and a polyurethane foam-filled honeycomb core.[19] The dimensions and the material properties of the panels A, B, and C are presented in Table I. The freely suspended boundary condition is denoted with "-free" and the simply supported case with "-SS." For example, panel A subject to simply supported boundary conditions will be referred to as panel A-SS in what follows. Unless otherwise stated, the freely suspended panels are excited by a point force of $F_z = 1\,\text{N}$ at the corner node ($x = y = 0$, $z = h/2$), and the simply supported panels likewise at the center node ($x = l_x/2$, $y = l_y/2$, $z = h/2$). Moreover, excitation by diffuse acoustic fields will also be considered in Sec. III D. The definition of the coordinate system is depicted in Fig. 6.

A. Mesh and discretization error

Eight-noded quadrilateral shell finite elements based on the Reissner-Mindlin theory are employed for the modeling of the face sheets. The cores of the panels are modeled using 20-noded hexahedral solid finite elements. The respective stiffness and mass matrices are extracted from ANSYS.[44] For all three panels, a uniform finite element mesh with 48 and 96 elements along the in-plane directions and 2 elements in the thickness direction is used (recall that all 3 panels have an aspect ratio of roughly 2:1). The finite element (FE) meshes result in 240 000 displacement DOFs. This corresponds to three quadratic elements per bending wave length of panel A in the frequency range up to 2000 Hz. For panels B and C, this mesh results in at least 6 and 13 elements per bending wave length, respectively, in the considered frequency ranges.

TABLE I. Geometry and properties of the honeycomb sandwich panels taken from the literature (Refs. 16 and 19). Values that are not explicitly given in these references are assumed and marked with a star "*."

Face sheets		Panel A (Ref. 16)	Panel B (Ref. 19)	Panel C (Ref. 19)
Thickness	t	6.35 mm	0.5 mm	0.5 mm
Density	ρ_f	657 kg/m³	1600 kg/m³	1600 kg/m³
Young's modulus	E	7 GPa	49 GPa	39 GPa
Poisson's ratio	ν_a	0.3	0.15	0.15
Core				
Thickness	h	76.2 mm	6.35 mm	12.7 mm
Density	ρ_c	28 kg/m³	160 kg/m³	120 kg/m³
Young's modulus	E_x, E_y	4 MPa	10 MPa*	10 MPa*
Young's modulus	E_z	370 MPa	100 MPa*	100 MPa*
Shear modulus	G_{xy}	0.2 MPa	0.5 MPa*	0.5 MPa*
Shear modulus	G_{yz}	50 MPa	140 MPa	60 MPa
Shear modulus	G_{xz}	23 MPa	90 MPa	100 MPa
Poisson's ratio	ν_c	0.1	0.15	0.15
Dimensions[a]	$l_x \times l_y$	$1.22 \times 2.44\,\text{m}^2$	$1.12 \times 0.62\,\text{m}^2$	$1.12 \times 0.62\,\text{m}^2$

[a]The dimensions of panels B-SS and C-SS in the simulations are reduced to 0.88×0.42 m² in order to account for the dimension reduction due to the clamping in the window test rig (Ref. 19) and thus ensure comparability between the experimental and numerical results.
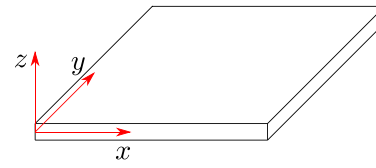
FIG. 6. (Color online) Coordinate system of the sandwich panels.

Quadrilateral boundary elements with bilinear interpolation functions are used for the discretization of the surrounding acoustic field. These elements have their DOF-carrying nodes inside the element, rather than on the element edges, resulting in a sound pressure interpolation that is discontinuous across element boundaries.[45] The corresponding BE matrices $\mathbf{H}$ and $\mathbf{G}$ are extracted from the non-commercial software AKUSTA.[45] A treatment for the nonuniqueness problem that occurs in exterior BE formulations is not required since the respective first irregular frequencies of the panels are beyond the frequency range of interest, e.g., the first spurious mode of panel A occurs at approximately 27 kHz.

Regarding the size of the boundary element mesh, there are no guidelines available in the literature for coupled structural acoustic radiation problems. Therefore, in this work, the adequate mesh size for the acoustic field is chosen based on a convergence study. Figure 7 shows the relative difference in radiated sound power of panel A-SS for different BE mesh sizes. These meshes do not conform with the above defined structural finite element mesh. Consequently, the relative difference shown in Fig. 7 is related to the discretization error of the acoustic field, as well as to the error introduced by the mesh coupling. It is calculated from $\epsilon_{\text{rel},P} = |P - P_{\text{ref}}|/P_{\text{ref}}$, where P_{ref} denotes the reference sound power for a mesh with 48 and 96 elements along the in-plane directions corresponding to 19 584 pressure DOFs for each acoustic halfspace. This reference BE mesh conforms with the above defined FE mesh. As we expected, the relative difference displayed in Fig. 7 decreases monotonically as we refine the mesh. Moreover, the relative difference is of the same order of magnitude at four different frequency points, although some of those frequencies lie well above the coincidence frequency range of the panel (see Sec. III E for discussion on coincidence).
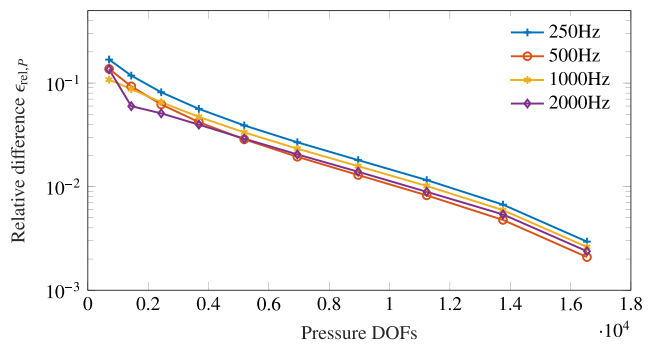
FIG. 7. (Color online) Relative difference in radiated sound power of panel A-SS for different BE mesh sizes. The reference sound power is obtained using a conforming BE mesh with 19 584 pressure DOFs for each acoustic halfspace.

Based on this convergence study, we choose the BE mesh with 24 and 48 elements along the in-plane directions for all upcoming simulations. This mesh has 5148 pressure DOFs for each halfspace and, similarly, 10 296 DOFs for the acoustic fullspace corresponding to the unbaffled panels. Compared to the reference mesh that has four times more DOFs, it results in a relative difference of less than 3.3% (0.14 dB) at all considered frequency points. Finally, in order to assess the influence of the discretization error on the eigenfrequencies, the modal analysis that is presented in Sec. III B was repeated with the reference mesh, resulting in maximum relative differences of 0.17% in the imaginary and 0.07% in the real part of the eigenvalues.

B. Modal analysis and eigenfrequencies

The modal analysis scheme presented in Sec. II is now applied to panel A to obtain its air-loaded modes and associated eigenfrequecies. From a preceding *in vacuo* analysis, we expect panel A-Free to have 15 eigenfrequencies in the frequency range $[f_{\min} = 10\,\text{Hz}, f_{\max} = 500\,\text{Hz}]$. Trivially, panel A-Free also exhibits six rigid body modes which are not affected by the acoustic loading. The *in vacuo* analysis of panel A-SS yields 11 eigenfrequencies in the frequency range $[f_{\min} = 100\,\text{Hz}, f_{\max} = 600\,\text{Hz}]$. These bounds are also chosen for the definition of the respective ellipses in Eq. (18). The number of integration points N was gradually increased until the accuracy of the eigenpairs stagnated, resulting in $N = 32$. Moreover, $K = 8$ moments, $L = 15$ source vectors, and an aspect ratio of $\zeta = 0.1$ were chosen for both panels. In the considered examples, we found that the eigensolutions are relatively insensitive to the choice of K and L as long as the resulting subspace was large enough and $L \geq 10$. After solving the generalized EVP, the modes corresponding to the eigenvalues lying inside the contour are checked using MAC as given in Eq. (23).

The eigenfrequencies of the air-loaded panel correspond to the real part of the eigenvalue, i.e., $f_j = \text{Re}(\tilde{\omega}_j)/(2\pi)$. They are given in Tables II and III, along with the *in vacuo* eigenfrequencies $f_{\text{dry},j}$ and their relative difference $\Delta_j = |f_{\text{dry},j} - f_j|/f_{\text{dry},j}$. As we expect, the eigenfrequencies of the air-loaded panels are generally lowered due

TABLE II. Comparison between *in vacuo* and air-loaded eigenfrequencies of panel A-SS.

j	$f_{\text{dry},j}$	f_j	Δ_j	$\epsilon_{\text{EVP},j}$
1	160 Hz	157 Hz	−2.39%	2.4×10^{-6}
2	222 Hz	218 Hz	−1.83%	3.6×10^{-6}
3	316 Hz	314 Hz	−0.67%	2.5×10^{-6}
4	322 Hz	317 Hz	−1.38%	1.7×10^{-6}
5	370 Hz	366 Hz	−0.96%	3.4×10^{-6}
6	431 Hz	430 Hz	−0.13%	5.3×10^{-6}
7	444 Hz	442 Hz	−0.44%	1.4×10^{-6}
8	507 Hz	503 Hz	−0.65%	5.8×10^{-6}
9	538 Hz	538 Hz	−0.14%	1.6×10^{-6}
10	544 Hz	541 Hz	−0.43%	1.2×10^{-6}
11	558 Hz	557 Hz	−0.10%	2.9×10^{-6}

TABLE III. Comparison between *in vacuo* and air-loaded eigenfrequencies of panel A-Free.

j	$f_{\text{dry},j}$	f_j	Δ_j	$\epsilon_{\text{EVP},j}$
1	69.5 Hz	67.7 Hz	−2.53%	4.4×10^{-6}
2	77.3 Hz	75.9 Hz	−1.85%	4.7×10^{-6}
3	157 Hz	154 Hz	−1.94%	6.0×10^{-6}
4	176 Hz	171 Hz	−2.74%	1.8×10^{-5}
5	229 Hz	225 Hz	−1.80%	1.3×10^{-5}
6	251 Hz	246 Hz	−2.26%	1.5×10^{-5}
7	255 Hz	251 Hz	−1.73%	4.1×10^{-5}
8	308 Hz	301 Hz	−2.26%	5.3×10^{-5}
9	324 Hz	318 Hz	−1.83%	1.9×10^{-5}
10	366 Hz	359 Hz	−2.18%	4.1×10^{-5}
11	390 Hz	389 Hz	−0.03 %	7.2×10^{-5}
12	403 Hz	394 Hz	−2.04 %	1.0×10^{-5}
13	439 Hz	432 Hz	−1.61 %	4.1×10^{-6}
14	453 Hz	446 Hz	−1.64 %	5.3×10^{-6}
15	459 Hz	458 Hz	−0.32 %	1.0×10^{-5}

to the effect of added mass and radiation damping. The actual extent of the frequency shift depends on the shape of the associated mode. For example, the eigenfrequency f_1 of panel A-SS associated with the fundamental bending mode is significantly lowered ($\Delta_1 = -2.39\,\%$), while the eigenfrequency f_{11} of panel A-Free that belongs to an in-plane mode is almost unaffected by the air-loading ($\Delta_{11} = -0.03\,\%$).

Regarding the numerical accuracy of the frequency shifts Δ_j, we distinguish between the discretization error and the accuracy of the eigensolver. As mentioned in Sec. III A, the discretization error of the wet eigenfrequencies of panel A-SS is at most 0.07%. Although this might seem sufficiently accurate at first sight, it nevertheless needs to be set in relation to the frequency shifts. In the presented examples, the discretization error is mostly 1 order of magnitude smaller than the computed frequency shifts Δ_j in both panels. The accuracy of the eigensolver is assessed by computing the relative residuals of the air-loaded eigenpairs by using Eq. (24). They are given in Tables II and III and show that errors of order $\mathcal{O}(10^{-5})$ are achieved. This verifies the accuracy of the presented modal analysis scheme.

C. Radiated sound power

Expressing the sound radiation by means of modal contributions is a popular procedure to accelerate active control applications. For instance, a few (orthogonal) surface velocity patterns are usually sufficient to approximate the total radiated sound power at a certain frequency. These patterns, also known as acoustic radiation modes,[46] are the eigenvectors of the acoustic impedance matrix and computed using BEM or analytical methods.[47]

Alternatively, we can express the radiated sound power in terms of the fluid-loaded modes of the structure. This requires orthonormalization[48] of the modal basis obtained from block SS such that

$$\mathbf{V}^{\text{T}} \mathbf{B}(\omega) \mathbf{V} = \mathbf{I} \tag{25}$$

holds with the orthonormal modal matrix $\mathbf{V}$ containing the fluid-loaded modes $\hat{\mathbf{v}}_j$ as columns. Due to orthonormalization with respect to the frequency dependent matrix $\mathbf{B}(\omega)$, these modes are now also frequency dependent. Given a structural force excitation $\mathbf{f}_s$, the structural displacement in Eq. (11) can be expressed by exploiting the condition (25), i.e.,

$$\mathbf{u} = \mathbf{V}\mathbf{V}^T\mathbf{f}_s. \qquad (26)$$

For an individual mode $\hat{\mathbf{v}}_j$, the modal particle displacement $\mathbf{d}_j$ at the acoustic nodes can be written as[30]

$$\mathbf{d}_j = \mathbf{C}_{\mathrm{fs}}\hat{\mathbf{v}}_j\hat{\mathbf{v}}_j^T\mathbf{f}_s. \qquad (27)$$

Inserting Eq. (27) into Eq. (7) yields the complex modal sound power contributions

$$P_{jk} = \frac{1}{2}\omega^2\mathbf{d}_j^T\mathbf{Z}\mathbf{d}_k^H. \qquad (28)$$

Figure 8 displays the real parts of the sound power resulting from point force excitations of panels A-SS and A-Free. Here, panel A-SS is not excited at the center but at the node $(x = 0.61\,\mathrm{m}, y = 1.754\,\mathrm{m}, z = 0.038\,\mathrm{m})$ to ensure that a larger number of modes participate in the response.

As expected, several resonances occur in the considered frequency ranges. In the case of panel A-SS, the peaks are noticeably rounded. Given that structure-inherent damping is not modeled here, this clearly indicates the effect of energy dissipation by sound radiation. While the first couple of resonances of A-Free exhibit sharp maxima, the effect of acoustic radiation damping also comes into play in the higher frequency range.

Besides the sound power that is obtained from a harmonic analysis, Fig. 8 also displays the diagonal modal contributions $\mathrm{Re}(P_{jj})$, as well as the superposition of all (diagonal and off-diagonal) contributions, i.e., $\sum_j\sum_k\mathrm{Re}(P_{jk})$. The total modal superposition agrees well with the harmonic sound power

except in the higher frequency range, where the modal basis is obviously not sufficient. The relative differences between the harmonic sound power and the total modal superposition are given in Fig. 9.

At the resonances, the diagonal values almost exclusively contribute to the radiated sound power. The rigid body modes of panel A-Free are also included in the modal basis, and determine the sound radiation up to around 50 Hz. At around 100 Hz, they even exceed the total radiated sound power, which is an indication that off-diagonal sound power contributions with negative signs occur, i.e., $\mathrm{Re}(P_{jk}) < 0$, $j \neq k$.

The modal displacements $\mathbf{d}_j$ are generally not orthogonal with respect to the acoustic impedance matrix $\mathbf{Z}$, and cross-coupling between two modes can occur. Therefore, the off-diagonal sound power contributions are not necessarily zero. In fact, the occurrence of these off-diagonal contributions can be interpreted in that the spatial distribution of inertial forces of the structure is different from the spatial distribution of the inertial forces due to the acoustic loading. We notice that despite the relatively weak structural acoustic interaction between the sandwich panels and the air, these off-diagonal values significantly contribute to the overall sound power radiation.

D. Acoustic radiation damping

By relating the power loss due to far-field sound radiation to the vibrational energy of the structure, the radiation loss factor quantifies the extent of acoustic radiation damping. The harmonic radiation loss factor as given in Eq. (10) is the result of a frequency-wise response analysis and generally depends on the excitation.

Figure 10 displays the radiation loss factor for the panels A-SS and A-Free subject to point-force excitation. While both panels show qualitatively similar behaviors with an increase of radiation damping toward the coincidence region and a subsequent plateauing, significant differences in the
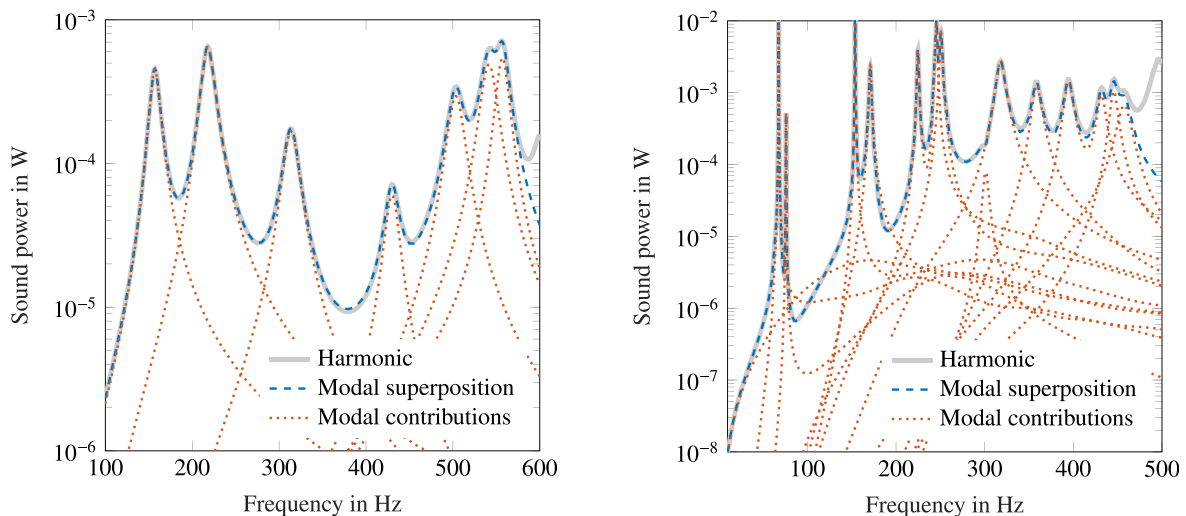

FIG. 8. (Color online) Radiated sound power of panels A-SS and A-Free subject to point-excitation. Results were obtained from a harmonic analysis, the total modal superposition, and the diagonal modal contributions.
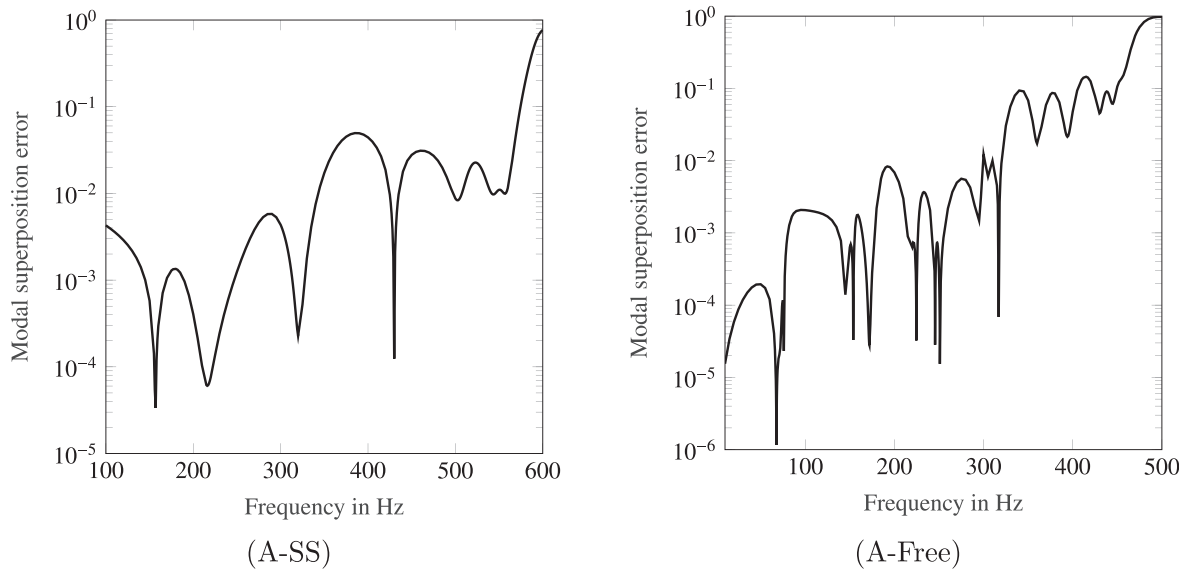
Suhaib Koji Baydoun and Steffen Marburg

FIG. 9. Relative difference between the radiated sound power of panels A-SS and A-Free, obtained from a harmonic analysis and the total modal superposition.

magnitudes are observed in the low frequency range. Panel A-SS already exhibits considerable radiation damping in the low frequency range by virtue of the fundamental bending mode that exhibits a monopole radiation characteristic. In contrast, the effect of acoustic short-circuiting in conjunction with freely moving edges of panel A-Free lead to much lower radiation loss factors in the low frequency range. At the higher frequency range, when the panels contain a few bending waves, the effect of boundary conditions becomes insignificant, and both panels exhibit similar radiation loss factors. Values of $\eta_r > 0.01$ across a wide frequency range indicate the relevance of acoustic radiation damping in honeycomb sandwich structures—particularly when considering that material-inherent loss factors are typically of the same order of magnitude.

Besides the boundary conditions, the excitation can have a significant influence on radiation damping at low frequencies as well. This is reflected in Fig. 11, which is a close-up of Fig. 10 in the low frequency range. Additionally, it shows averaged loss factors of the panels subject to 100 randomly
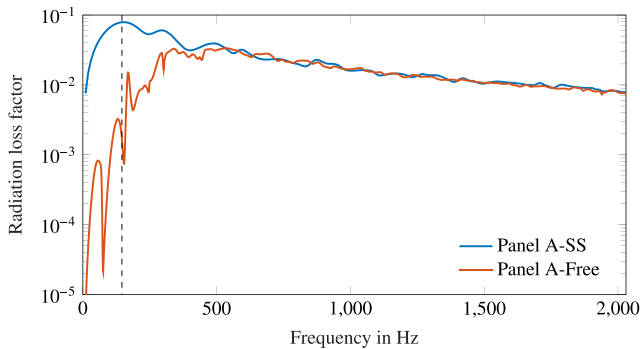

FIG. 10. (Color online) Harmonic radiation loss factors of panels A-SS and A-Free subject to point excitation. The dashed line indicates the estimated critical frequency [cf. Eq. (31)].

located point forces as well as loss factors for diffuse field excitation. The responses to a diffuse incident field were computed as the mean values of 50 simulations, where the excitation in each simulation was given by the summation of 1145 random incident plane waves arriving from uniformly distributed directions in space. For a detailed description of this procedure, we refer to the appendix of a paper by Rafaely.[49] Regarding the extent of radiation damping, we notice that the diffuse field excitation leads to higher loss factors in the low frequency range in both panels. This can be explained by the spatially uniform distribution of the incident pressure fields in the low frequency range that almost act like a plane wave excitation. For panel A-Free around 125 Hz in particular, this leads to monopole radiation characteristic which is not achieved by point excitation.

In addition to the harmonic radiation loss factor, modal loss factors can be obtained characterizing the radiation damping of each individual fluid-loaded structural mode. These modal radiation loss factors are properties of the structural acoustic system and hence independent of the excitation. At the complex eigenfrequency $\tilde{\omega}_j$, the modal radiation loss factor is defined as[4,50]

$$\eta_j = -2\frac{\mathrm{Im}(\tilde{\omega}_j)}{\mathrm{Re}(\tilde{\omega}_j)}, \tag{29}$$

in which $\mathrm{Im}(\tilde{\omega}_j)$ is negative due to the choice of the time dependency $e^{-\mathrm{i}\omega t}$. The modal loss factors are given in Fig. 11 for panels A-SS and A-Free at their respective eigenfrequencies. In the case of point excitation, the harmonic loss factors deviate from some of the modal loss factors, indicating that the respective modes are not (or not exclusively) excited in the harmonic analysis. This is particularly obvious for the in-plane mode of panel A-Free that occurs at $f_{11} = 389\,\mathrm{Hz}$ and exhibits only marginal radiation damping
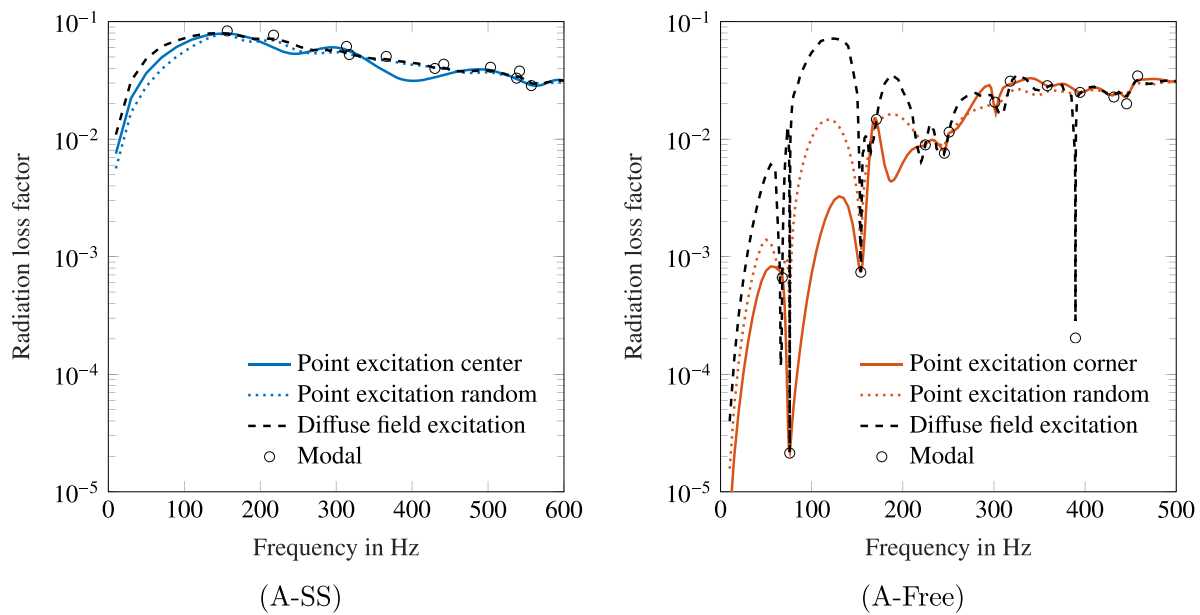
FIG. 11. (Color online) Harmonic radiation loss factors of panels A-SS and A-Free subject to point and diffuse field excitations. Additionally, modal loss factors are given at their respective eigenfrequencies.

($\eta_{11} = 2 \times 10^{-4}$). On the other hand, the harmonic loss factor corresponding to the diffuse field excitation coincides with all modal loss factors for both panels without exception. Summing up, both the modal and the harmonic radiation loss factors provide useful measures to characterize the extent of radiation damping.

E. Comparison to theoretical and experimentally obtained radiation loss factors

So far, we have placed our attention only on numerical methods and how they can be employed to study the radiation damping of sandwich structures. In the following, we will compare our numerical results to commonly used theoretical expressions and experimental results available in the literature.

Theoretical expressions for radiation damping rely on approximations of the radiation resistance R_r,[8,11] i.e.,

$$\eta_r = \frac{R_r}{\omega m_{\text{panel}}}, \tag{30}$$

where m_{panel} denotes the mass of the panel. Several authors have derived the radiation resistance of simply supported, baffled plates based on the concept of power flow,[8,9] and correction factors have been proposed for taking the effect of acoustic short-circuiting into account.[13] All of these expressions assume a multi-modal radiation of the panel and thus are not applicable in the low frequency range. A summary and discussion of these expressions for radiation resistance can be found in a publication by Renji and Nair[11] in which the authors also point out that some of the expressions in the above-mentioned literature have inconsistent factors. Here, we use the expression as given in Eq. (11) of the paper by Renji and Nair.[11]

The accuracy of theoretical radiation resistance estimates, in turn, depends on the prediction of the critical frequency. For composite panels with symmetric cross-ply laminates, the critical frequency f_c under consideration of transverse shear effects can be estimated from[51]

$$f_c^2 = \frac{c^4 \rho_s}{4\pi^2 D \left[(3+\alpha)/4 - c^2 \rho_s/N\right]}, \tag{31}$$

where ρ_s denotes the surface density of the panel, c is the speed of sound, and $\alpha = (D_{12} + 2D_{66})/D$ with $D = \sqrt{D_{11}D_{22}}$. The flexural rigidity values $D_{11}, D_{22}, D_{12}, D_{66}$, and the shear rigidity N can be obtained from the properties of the face sheets and the core based on laminate theory.[52] Using Eq. (31) yields critical frequency estimates of 146 Hz for panel A, 122 Hz for panel B, and 780 Hz for panel C.

The third-octave band-averaged theoretical estimates for the radiation loss factor resulting from Eq. (30) are given in Figs. 12 and 13, along with the numerically obtained results for panels A-SS, B-SS, and C-SS. The critical frequencies cannot be identified directly from the numerical results because this would require determining the bending wave content by means of a spatial Fourier transform. However, from Figs. 12 and 13 we can observe that the radiation loss factor exhibits a plateau in the higher frequency range. This plateauing that generally occurs above the critical frequency is in accordance with the theoretical results, while the actual radiation loss factors at the critical frequencies are significantly overestimated by the theoretical expressions. In the higher frequency range, where the radiation loss factors level out, the theoretical and numerical results of all three panels are in good agreement. This indicates that enough modes contribute to the radiation of the panel in this frequency range so that the theoretical expressions are valid. At lower

2030   J. Acoust. Soc. Am. **147** (3), March 2020
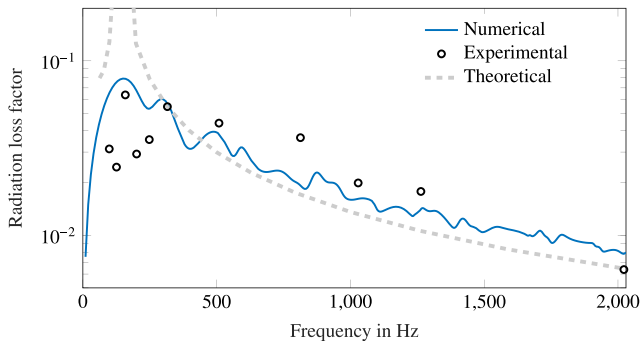
Suhaib Koji Baydoun and Steffen Marburg

FIG. 12. (Color online) Radiation loss factors of panel A-SS. Comparison of numerical results with experimentally determined values taken from the literature (Ref. 16) and theoretical expressions.

frequencies, however, the radiation damping of panels B-SS and C-SS strongly depends on which modes are excited. Moreover, the modes are still widely separated while significant radiation damping already occurs. However, as already mentioned above, the theoretical expressions assume a multi-modal radiation of the panel. This leads to the conclusion that they are not sufficient to comprehensively assess the radiation damping of such sandwich structures, at least when coincidence and, thus, efficient sound radiation already occur at low frequencies.

Furthermore, experimentally determined loss factors of similar panels are taken from the literature, and they are also compared to our numerical results in what follows. Panel A-SS was tested my Moore[16] in a window between two reverberation rooms. It was excited by a loudspeaker in the sending room, and the sound pressure, as well as the space averaged mean square accelerations of the panel, were measured in the receiving room. By relating the radiated sound power to the vibrational level, Moore[16] obtained third-octave band-averaged radiation efficiencies of panel A-SS (see Fig. 5.8 in Ref. 16). The associated radiation loss factor can be obtained from the radiation efficiency $\hat{\sigma}_r$ via

$$\eta_r = \frac{\rho c \hat{\sigma}_r}{\rho_s \omega}, \tag{32}$$

where ρ denotes the density of air. Zhou and Crocker[19] have conducted similar measurements to obtain the third-octave band-averaged radiation loss factors of the panels B-SS and C-SS. The panels were clamped in a window between two reverberation rooms and excited by a shaker. Since the loss factors resulting from the above-mentioned experiments are associated with the sound radiation of only one side of the panel, they are multiplied by a factor of 2 in order to compare them to our numerical results.

The experimentally determined radiation loss factors of panels A-SS, B-SS, and C-SS are displayed in Figs. 12 and 13, along with the numerical results. In general, the experimental and numerical results agree well for all three panels. Above the critical frequency, the experimental loss factors exhibit a similar leveling-off as the numerical results, although in this frequency range the theoretical estimates provide better agreements with the numerical results. Conversely, around the critical frequency, where the theoretical expressions significantly overestimate radiation damping, the experimental values provide better agreements with the numerical results than the theoretical estimates do. In the subcritical range, however, the experimentally obtained loss factors fall significantly below the numerical ones. Two explanations are possible for this discrepancy.

The first explanation is related to the boundary conditions of the panels. When testing panels in a window test rig, they are typically clamped between the two walls of adjacent rooms. This clamping, however, is far from ideally rigid and will, to a certain extent, always exhibit compliance. It is clear that the boundary conditions of a particular window test rig can hardly be reproduced in simulations, and as a compromise, simply supported boundary conditions were imposed on all face sheet edges, as shown in Fig. 2. The difference to the actual boundary conditions in the test
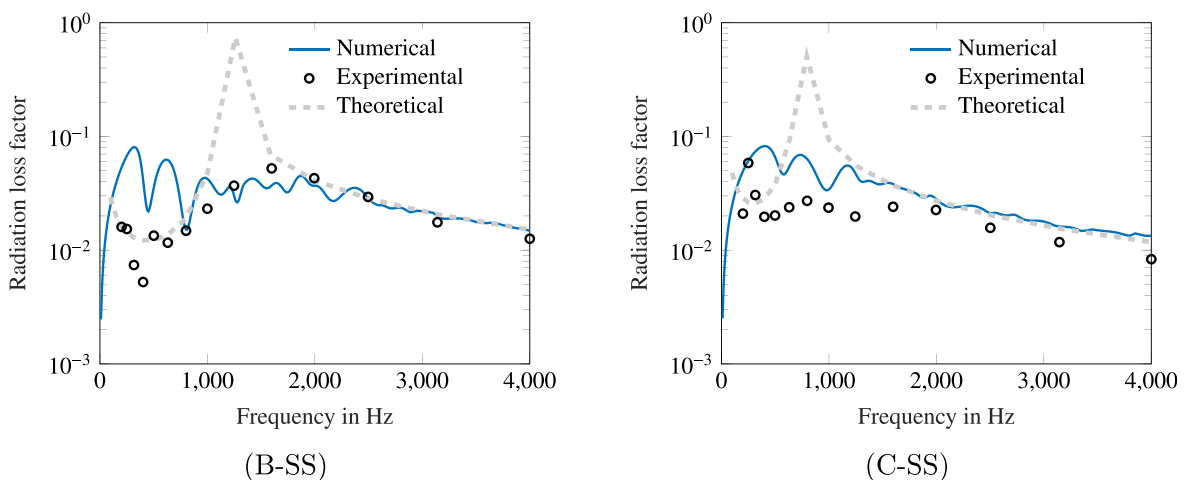

(B-SS)

(C-SS)

FIG. 13. (Color online) Radiation loss factors of panels B-SS and C-SS. Comparison of numerical results with experimentally determined values taken from the literature (Ref. 19) and theoretical expressions.

J. Acoust. Soc. Am. **147** (3), March 2020

Suhaib Koji Baydoun and Steffen Marburg   2031

rig will certainly have an influence on the low frequency results.

The second possible explanation for the discrepancy between the experimentally and numerically obtained loss factors is related to the reliability of reverberation room measurements in the low frequency range, in general. The low modal density of the room results in a nonuniform sound pressure field, and therefore microphone-based measurements are subject to high uncertainties. This issue could be addressed by a recently proposed experimental procedure in which mobility measurements are combined with a numerically obtained acoustic impedance matrix to compute the acoustic response.[53] In this way, experimental estimates of the radiation loss factor that only depend on the properties of the panel could be obtained.

In addition to the simply supported panels, the freely suspended, non-baffled panels B-Free and C-Free are also studied, and their respective numerical and experimental radiation loss factors are displayed in Fig. 14. Zhou and Crocker[19] obtained the experimental values by exciting the freely hanging panels with a shaker and measuring both the sound pressure in the reverberation room and the mean vibrational velocity of the panel. While the numerical and experimental loss factors qualitatively show similar behaviors with an increase toward the coincidence region and a subsequent plateau, the actual magnitudes differ significantly in the higher frequency range. There, the numerically determined loss factors are higher throughout than the experimental ones.

This deviation could be related to the reinjection of energy due to reflections in the reverberation rooms. While the numerical models assume that all the radiated sound energy disappears in the far-field, in fact, part of the acoustic energy in a reverberant room is transferred back to the panel and, hence, serves as an excitation in addition to the mechanical excitation by the shaker. This line of reasoning becomes clear when considering how Zhou and Crocker[19] obtained the radiation loss factor estimates from their

experimental data. For this purpose, recall the power balance inside a reverberation room, i.e.,

$$\omega(\eta_{room} + \eta_c)E_{room} = \omega\eta_r E_{panel}, \quad (33)$$

where E_{room} and E_{panel} denote the total mean energies of the acoustic field and the panel, respectively. The dissipation loss factor of the reverberation room η_{room} includes the sound power absorption of the walls due to air. The coupling loss factor η_c reflects the transfer of acoustic energy from the room to the panel—similar to the radiation loss factor η_r that quantifies the energy transfer from the panel to the acoustic field in the room. The energy quantities are given as

$$E_{room} = \frac{\bar{p}^2 V_{room}}{\rho c^2}, \quad E_{panel} = m_{panel}\bar{v}^2, \quad (34)$$

where $\bar{p}$ and $\bar{v}$ are the experimentally obtained averaged values for the sound pressure and the vibrational velocity. Further, V_{room} denotes the volume of the reverberation room. The coupling loss factor η_c in Eq. (33) is defined based on considerations of statistical energy analysis (SEA) from the reciprocal relationship[11]

$$\eta_c = \eta_r \frac{n_{panel}}{n_{room}}, \quad (35)$$

with the modal density of the panel n_{panel} and the modal density of the room n_{room}. Combining Eqs. (30), (33), (34), and (35), we arrive at an expression for the radiation resistance that reads

$$R_r = \frac{\omega\bar{p}^2 V_{room}\eta_{room}m_{panel}}{\rho c^2 m_{panel}\bar{v}^2 - \bar{p}^2 V_{room}\frac{n_{panel}}{n_{room}}}. \quad (36)$$

Indeed, Zhou and Crocker used another, simplified expression in order to deduce the radiation resistance from their experimental data. Their expression [cf. Eq. (21) in Ref. 19] reads
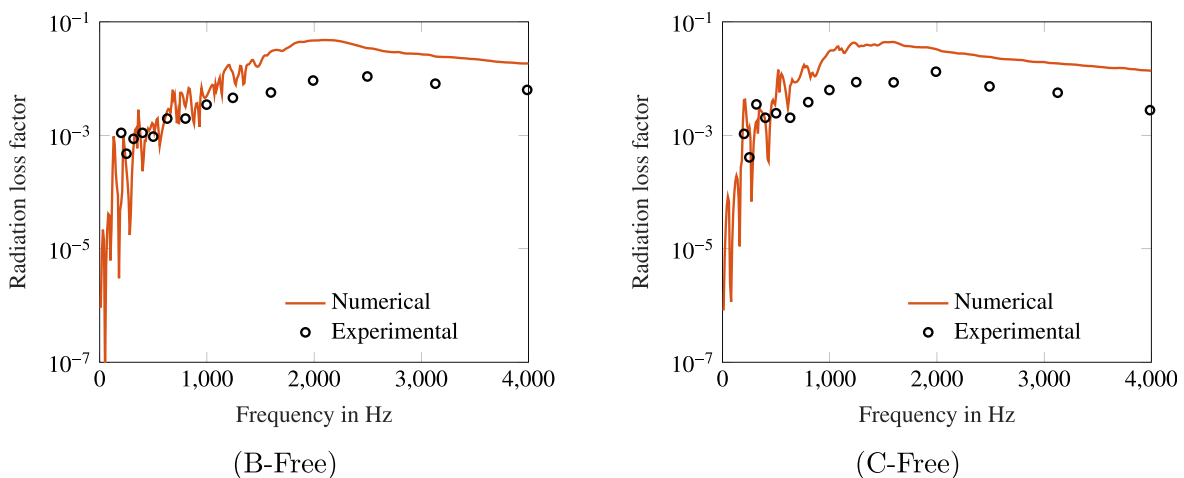

FIG. 14. (Color online) Radiation loss factors of panels B-Free and C-Free. Comparison of numerical results with experimentally determined values taken from the literature (Ref. 19). The deviation in the high frequency range could be related to reinjection of acoustic energy in the reverberation room.

Suhaib Koji Baydoun and Steffen Marburg

$$R_r = \frac{\omega \bar{p}^2 V_{\text{room}} \eta_{\text{room}}}{\rho c^2 \bar{v}^2}.$$ (37)

A comparison to Eq. (36) reveals that Eq. (37) misses the second term in the denominator and as a consequence, neglects the reinjection of acoustic energy into the panel. This could lead to an underestimation of the radiation resistance, which would explain the deviation between the numerical and experimental estimates for radiation damping that we observe in Fig. 14 in the higher frequency range. In future experiments, the second term in the denominator of Eq. (36) could be evaluated to assess its impact on the actual radiation damping values.

Finally, we note that the above-mentioned paper[19] is not the only publication of experimental results where the reinjection of acoustic energy is left unconsidered. In fact, in the pioneering work[22] on radiation damping of sandwich panels, Clarkson and Brown deduce radiation damping by means of reference measurements in a vacuum chamber. However, the measurements in air are conducted inside the (disabled) vacuum chamber as well, which clearly leads to reflection at the inner walls of the chamber, and therefore to unwanted reinjection of acoustic energy.

IV. SUMMARY AND CONCLUSION

Using a fully coupled FEM/BEM formulation, we have systematically studied the acoustic radiation damping of sandwich structures. The extent of radiation damping is quantified by the harmonic radiation loss factor relating the radiated sound power to the structure-inherent power. Besides harmonic response analyses, modal analyses of sandwich panels interacting with the surrounding air have also been performed. The underlying nonlinear EVP has been solved using a projection method based on contour integration, resulting in the complex eigenfrequencies and modes of the air-loaded structure. Spurious eigenvalues that arise due to the contour integration are identified by checking the occurrence of the associated air-loaded modes in the range of *in vacuo* modes. This criterion is also used to check the completeness of the eigenvalue solution. The final eigenvalues provide the shifted (wet) eigenfrequencies, as well as the modal radiation loss factors, of the sandwich structure.

The numerical framework has been applied to three honeycomb sandwich panels subject to various boundary conditions and excitations. The reduction in eigenfrequencies of more than 2% compared to the *in vacuo* eigenfrequencies clearly indicates the relevance of air-loading when studying the vibration of sandwich structures. Moreover, radiation loss factors of 8% in the coincidence region and larger than 1% across wide frequency ranges demonstrate that the phenomenon of acoustic radiation damping significantly contributes to the overall damping. Furthermore, it is observed that the simply supported, baffled panels exhibit significantly larger radiation damping than the freely suspended, unbaffled panels in the lower frequency range. At higher frequencies, the effects of boundary conditions and excitations are

insignificant. The modal radiation loss factors quantifying the radiation damping of each individual structural mode show excellent agreement with the harmonic radiation loss factors corresponding to the diffuse field excitation.

The comparison of the numerical results to the theoretical expressions for radiation damping yields good agreement above the critical frequency. However, commonly used theoretical expressions overestimate the radiation damping at the critical frequency, and they are also inaccurate in the lower frequency range, where the modes of the panel are widely separated and the response of the panel depends on the excitation. Given that sandwich structures exhibit high radiation damping already in the low frequency range, this deficiency of the theoretical expressions underlies the importance of numerical quantification of radiation damping.

Furthermore, we have compared our numerical results to experimentally obtained radiation loss factors found in the literature. While they qualitatively show similar behaviors with an increase toward the coincidence region and subsequent plateaus, we have also observed some significant deviations. In the case of the baffled panels, the deviation in the low frequency range could be explained by the effect of boundary conditions and also by the low modal density of reverberation rooms. A recently proposed procedure based on mobility measurements could resolve the latter issue.[53] The deviation in the loss factors of the unbaffled panels in the high frequency range could have its origin in the reinjection of acoustic energy into the panel when testing them in reverberation rooms. While the numerical models assume that all the radiated acoustic energy disappears in the farfield, in fact, part of the acoustic energy in a reverberant room serves as an excitation in addition to the mechanical excitation. The latter should be taken into consideration when experimentally determining radiation damping.

Future research will address the choice of nonlinear eigensolvers for computing air-loaded eigenfrequencies and modes. While the block SS method used in this paper is computationally efficient and achieved errors of order $\mathcal{O}(10^{-5})$ in the considered examples, it also has some disadvantages: Ill-conditioning of the Hankel matrices could result in inaccurate eigenpairs,[54] and the choice of input parameters could represent a daunting task for the engineer. Other contour integral methods[37,54] or iterative eigensolvers,[55] in conjunction with *in vacuo* modes as initial guesses, could prove to be more suitable. Proper benchmarking with regard to nonlinear FEM-BEM EVPs is certainly an issue for future research.

ACKNOWLEDGMENTS

[1]J. M. Lifshitz and M. Leibowitz, "Optimal sandwich beam design for maximum viscoelastic damping," Int. J. Solids Struct. **23**(7), 1027–1034 (1978).

[2]A. Treviso, B. Van Genechten, D. Mundo, and M. Tournour, "Damping in composite materials: Properties and models," Composites, Part B **78**, 144–152 (2015).

[3]M. Klaerner, M. Wuehrl, L. Kroll, and S. Marburg, "Amplitude-dependent damping: Experimental determination and functional interpretation for metal-plastic composites," Int. J. Struct. Stab. Dyn. **19**(5), 1941001 (2019).

[4]D. J. Mead, *Passive Vibration Control* (Wiley, Chichester, England, 1999).

[5]R. A. Mangiarotty, "Acoustic radiation damping of vibrating structures," J. Acoust. Soc. Am. **35**(3), 369–377 (1963).

[6]C. E. Wallace, "The acoustic radiation damping of the modes of a rectangular panel," J. Acoust. Soc. Am. **81**(6), 1787–1794 (1987).

[7]B. Laulagnet and J. L. Guyader, "Modal analysis of a shell's acoustic radiation in light and heavy fluids," J. Sound Vib. **131**(3), 397–415 (1989).

[8]M. J. Crocker and A. J. Price, "Sound transmission using statistical energy analysis," J. Sound Vib. **9**(3), 469–486 (1969).

[9]G. Maidanik, "Response of ribbed panels to reverberant acoustic fields," J. Acoust. Soc. Am. **34**(6), 809–826 (1962).

[10]C. E. Wallace, "Radiation resistance of a rectangular panel," J. Acoust. Soc. Am. **51**(3), 946–952 (1972).

[11]K. Renji and P. S. Nair, "On acoustic radiation resistance of plates," J. Sound Vib. **212**(4), 583–598 (1998).

[12]G. A. Kriegsmann, "Assessment of a new radiation damping model for structural acoustic interaction," J. Acoust. Soc. Am. **86**(2), 788–794 (1989).

[13]C. H. Oppenheimer and S. Dubowsky, "A radiation efficiency for unbaffled plates with experimental validation," J. Sound Vib. **199**(3), 473–489 (1997).

[14]A. Berry, J. L. Guyader, and J. Nicolas, "A general formulation for the sound radiation from rectangular, baffled plates with arbitrary boundary conditions," J. Acoust. Soc. Am. **88**(6), 2792–2802 (1990).

[15]A. C. Nilsson and B. Liu, "Prediction of some vibro-acoustic properties of sandwich plates with honeycomb and foam cores," J. Acoust. Soc. Am. **114**(3), 1600–1614 (2018).

[16]J. A. Moore, "Sound transmission loss characteristics of three layer composite wall constructions," Ph.D. thesis, Massachusetts Institute of Technology, Cambridge, MA, 1975.

[17]D. L. Palumbo and J. Klos, "Development of quiet honeycomb panels," NASA/TM-2009-215954, National Aeronautics and Space Administration (2009).

[18]Y.-J. Kim and J.-H. Han, "Identification of acoustic characteristics of honeycomb sandwich composite panels using hybrid analytical/finite element method," J. Vib. Acoust. **135**(1), 11006 (2013).

[19]R. Zhou and M. J. Crocker, "Sound transmission loss of foam-filled honeycomb sandwich panels using statistical energy analysis and theoretical and measured dynamic properties," J. Sound Vib. **329**(6), 673–686 (2010).

[20]R. Zhou and M. J. Crocker, "Boundary element analyses for sound transmission loss of panels," J. Acoust. Soc. Am. **127**(2), 829–840 (2010).

[21]V. D'Alessandro, G. Petrone, F. Franco, and S. De Rosa, "A review of the vibroacoustics of sandwich panels: Models and experiments," J. Sandwich Struct. Mater. **15**(5), 541–582 (2013).

[22]B. L. Clarkson and K. T. Brown, "Acoustic radiation damping," J. Vib. Acoust., Stress Reliab. Des. **107**, 357–360 (1985).

[23]M. Kaltenbacher, ed., *Computational Acoustics (CISM International Centre for Mechanical Sciences)* (Springer, Cham, Switzerland, 2018).

[24]S. Kirkup, "The boundary element method in acoustics: A survey," Appl. Sci. **9**(8), 1642 (2019).

[25]H. Peters, S. Marburg, and N. Kessissoglou, "Structural-acoustic coupling on non-conforming meshes with quadratic shape functions," Int. J. Numer. Methods Eng. **91**(1), 27–38 (2012).

[26]H. Lamb, "On waves in an elastic plate," Proc. R. Soc. London Ser. A **93**(648), 114–128 (1917).

[27]M. Ochmann and H. Brick, "Acoustical radiation and scattering above an impedance plane," in *Computational Acoustics of Noise Propagation in Fluids. Finite and Boundary Element Methods*, edited by S. Marburg and B. Nolte (Springer, Berlin, 2008), pp. 459–494.

[28]F. Fahy and P. Gardonio, *Sound and Structural Vibration* (Academic, Oxford, UK, 2007).

[29]K. J. Bathe, *Finite Element Procedures* (Prentice Hall, Englewood Cliffs, NJ, 1996).

[30]H. Peters, N. Kessissoglou, and S. Marburg, "Modal decomposition of exterior acoustic-structure interaction," J. Acoust. Soc. Am. **133**(5), 2668–2677 (2013).

[31]S. K. Baydoun and S. Marburg, "Quantification of numerical damping in the acoustic boundary element method for two-dimensional duct problems," J. Theor. Comput. Acoust. **26**(3), 1850022 (2018).

[32]S. N. Chandler-Wilde, E. A. Spence, A. Gibbs, and V. P. Smyshlyaev, "High-frequency bounds for the Helmholtz equation under parabolic trapping and applications in numerical analysis," arXiv:1708.08415v3 (2018).

[33]S. K. Baydoun, M. Voigt, C. Jelich, and S. Marburg, "A greedy reduced basis scheme for multifrequency solution of structural acoustic systems," Int. J. Numer. Methods Eng. **121**(2), 187–200 (2020).

[34]H. Peters, N. Kessissoglou, and S. Marburg, "Modal decomposition of exterior acoustic-structure interaction problems with model order reduction," J. Acoust. Soc. Am. **135**(6), 2706–2717 (2014).

[35]T. Sakurai and H. Sugiura, "A projection method for generalized eigenvalue problems using numerical integration," J. Comput. Appl. Math. **159**(1), 119–128 (2003).

[36]J. Asakura, T. Sakurai, H. Tadano, T. Ikegami, and K. Kimura, "A numerical method for nonlinear eigenvalue problems using contour integrals," JSIAM Lett. **1**, 52–55 (2009).

[37]W.-J. Beyn, "An integral method for solving nonlinear eigenvalue problems," Linear Algebra Appl. **436**, 3839–3863 (2012).

[38]T. Liang, J. Wang, J. Xiao, and L. Wen, "Coupled BE-FE based vibroacoustic modal analysis and frequency sweep using a generalized resolvent sampling method," Comput. Methods Appl. Mech. Eng. **345**, 518–538 (2019).

[39]C.-J. Zheng, C.-X. Bi, C. Zhang, H.-F. Gao, and H.-B. Chen, "Free vibration analysis of elastic structures submerged in an infinite or semi-infinite fluid domain by means of a coupled FE-BE solver," J. Comput. Phys. **359**, 183–198 (2018).

[40]T. Sakurai, Y. Futamura, and H. Tadano, "Efficient parameter estimation and implementation of a contour integral-based eigensolver," J. Algorithms Comput. Technol. **7**(3), 249–270 (2013).

[41]T. Ikegami, T. Sakurai, and U. Nagashima, "A filter diagonalization for generalized eigenvalue problems based on the Sakurai Sugiura projection method," J. Comput. Appl. Math. **233**, 1927–1936 (2010).

[42]R. J. Allemang, "The modal assurance criterion—Twenty years of use and abuse," Sound Vib. **37**(8), 14–21 (2003).

[43]W. Shengchun, D. Zhaoxiang, and S. Weidong, "Sound transmission loss characteristics of unbounded orthotropic sandwich panels in bending vibration considering transverse shear deformation," Compos. Struct. **92**(12), 2885–2889 (2010).

[44]ANSYS, *Theory Reference for the Mechanical APDL and Mechanical Applications Release 13* (ANSYS Inc., Canonsburg, PA, 2010).

[45]S. Marburg and S. Schneider, "Influence of element types on numeric error for acoustic boundary elements," J. Comput. Acoust. **11**(3), 363–386 (2003).

[46]G. V. Borgiotti, "The power radiated by a vibrating body in an acoustic fluid and its determination from boundary measurements," J. Acoust. Soc. Am. **88**, 1884–1893 (1990).

[47]J. Liu, Y. Liu, and J. S. Bolton, "Calculation of acoustic radiation modes by using spherical waves and generalized singular value decomposition," J. Acoust. Soc. Am. **146**(4), EL347–EL351 (2019).

[48]M. Baruch and I. Bar-Itzhack, "Optimal weighted orthogonalization of measured modes," AIAA J. **16**(4), 346–351 (1978).

[49]B. Rafaely, "Spatial-temporal correlation of a diffuse sound field," J. Acoust. Soc. Am. **107**(6), 3254–3258 (2000).

[50]X. Li and S. Li, "Modal parameter estimation for fluid-loaded structures from reduced order models," J. Acoust. Soc. Am. **120**(4), 1996–2003 (2006).

[51]K. Renji, P. S. Nair, and S. Narayanan, "Critical and coincidence frequencies of flat panels," J. Sound Vib. **205**(1), 19–32 (1997).

[52]R. M. Jones, *Mechanics of Composite Materials* (Taylor and Francis, Philadelphia, PA, 1998).

[53]N. B. Roozen, Q. Leclère, D. Urbán, T. Méndez Echenagucia, P. Block, M. Rychtáriková, and C. Glorieux, "Assessment of the airborne sound insulation from mobility vibration measurements; a hybrid experimental numerical approach," J. Sound Vib. **432**, 680–698 (2018).

[54]S. Yokota and T. Sakurai, "A projection method for nonlinear eigenvalue problems using contour integrals," JSIAM Lett. **5**, 41–44 (2013).

[55]B. Gavin, A. Międlar, and E. Polizzi, "Feast eigensolver for nonlinear eigenvalue problems," J. Comput. Sci. **27**, 107–117 (2018).

A.2 Publication II

A greedy reduced basis scheme for multifrequency solution of structural acoustic systems

WILEY

A greedy reduced basis scheme for multifrequency solution of structural acoustic systems

Suhaib Koji Baydoun[1] | **Matthias Voigt**[2] | **Christopher Jelich**[1] | **Steffen Marburg**[1]

[1]Chair of Vibroacoustics of Vehicles and Machines, Department of Mechanical Engineering, Technical University of Munich, Garching, Germany

[2]Institut für Mathematik, Technische Universität Berlin, Berlin, Germany

Correspondence
Suhaib Koji Baydoun, Chair of Vibroacoustics of Vehicles and Machines, Department of Mechanical Engineering, Technical University of Munich, Boltzmannstraße 15, 85748 Garching, Germany.
Email: suhaib.baydoun@tum.de

Summary

The solution of frequency dependent linear systems arising from the discretization of vibro-acoustic problems requires a significant computational effort in the case of rapidly varying responses. In this paper, we review the use of a greedy reduced basis scheme for the efficient solution in a frequency range. The reduced basis is spanned by responses of the system at certain frequencies that are chosen iteratively based on the response that is currently worst approximated in each step. The approximations at intermediate frequencies as well as the a posteriori estimations of associated errors are computed using a least squares solver. The proposed scheme is applied to the solution of an interior acoustic problem with boundary element method (BEM) and to the solution of coupled structural acoustic problems with finite element method and BEM. The computational times are compared to those of a conventional frequencywise strategy. The results illustrate the efficiency of the method.

KEYWORDS

boundary element method, greedy algorithm, multifrequency, reduced basis, structural acoustic interaction

1 | INTRODUCTION

Solving a sequence of linear systems of equations accounts for a significant computational effort that is required for the simulation of time-harmonic vibro-acoustic problems, particularly in the case of rapidly varying responses. Modal superposition is a popular numerical tool to address this issue and often used to avoid solutions for each individual frequency of interest. The respective eigenvalue problem needs to be solved only once and the responses at certain frequencies as well as the responses for different excitations are simply obtained by matrix vector multiplications. Especially in the case of both interior acoustic problems[1] and coupled structural acoustic problems in bounded domains,[2] modal superposition techniques based on the finite element method (FEM)[3] are well established. The respective coefficient matrices are independent of the frequency, and consequently, standard eigenvalue solvers[4] can be applied in a straightforward manner. However, in the case of exterior acoustic problems, the situation is different due to the representation of the unbounded acoustic domain. Three families of methods are available for addressing this issue: FEM with special boundary conditions,[5] the infinite element method (IFEM),[6] and the boundary element method (BEM).[7,8] The use of

conjugated Astley-Leis IFEM results in frequency independent coefficient matrices giving rise to the formulation of a generalized eigenvalue problem for determining acoustic radiation modes and normal modes.[9,10] However, making informed choice of the contributing modes for a superposition is still an active field of research.[11]

While BEM is particularly advantageous due to the implicit satisfaction of the far field radiation condition, its major drawback stems from the frequency dependence of the coefficient matrices. Special considerations such as the multiple reciprocity method[12] and the contour integral method[13,14] are usually employed to obtain acoustic modes with BEM. In the case of weakly coupled structural acoustic interaction, the superposition of isolated structural modes is sufficient to obtain a reduced model of the underlying vibro-acoustic problem. However, for lightweight structures submerged in heavy fluids, the in-vacuo modes do no longer form the modal basis. Hence, the modal analysis has to be performed including the effect of acoustic loading. When using BEM for the discretization of the fluid, this involves the solution of a nonlinear eigenvalue problem. Peters et al have proposed a frequency approximation of the boundary element impedance matrix[15,16] to overcome this issue, and more recently, the nonlinear structural acoustic eigenvalue problem has been solved using contour integration.[17,18]

Despite the abovementioned advances in numerical modal analysis, a frequencywise response analysis is still the most popular procedure for the calculation of vibro-acoustic responses in a frequency range. Moreover, implementations of eigenvalue solvers such as the contour integral method nevertheless require system evaluations at a considerable number of discrete frequency points. Therefore, in the following, we contribute to the acceleration of vibro-acoustic frequency response analysis as an alternative approach to the abovementioned modal superposition techniques.

During the last decades, many researchers have made effort to accelerate the frequency sweep of acoustic as well as structural acoustic problems. Moreover, efficient procedures for the assembly of boundary element matrices in a frequency range have been developed.[19-22] Approximating the acoustic response itself can also be efficient in cases where only a small partition of the solution is of interest.[23,24] Furthermore, the high numerical complexity associated to fully populated boundary element matrices led to the development of several fast algorithms[25,26] that have also been combined with multifrequency strategies.[27]

In addition, a number of publications[28-30] are concerned with efficient schemes for the actual solution of linear systems in a frequency range. In particular, projection-based model order reduction (MOR) techniques have been proposed to reduce the computational effort. They have been extensively reviewed for vibro-acoustic analyses using FEM.[28] In the context of coupled FEM-BEM analyses, MOR has been pioneered by the work of Peters et al,[31] in which the structural finite element matrices are reduced by means of Krylov subspace MOR, whereas the frequency-dependent boundary element matrices are left unchanged. More recently, resolvent sampling-based MOR has been proposed for the fully coupled FEM-BEM system.[30] In this method, the projection matrices are spanned by the response at some sampling points inside a frequency interval. Typically, such frequency sampling is done based on the Chebyshev nodes in an interval[15,30,32] without a priori knowledge of the solution and the occurrence of resonances. To the best of our knowledge, there is no strategy available allowing for an optimal choice of frequency samples that goes in hand with an estimation of the error introduced by the projective MOR in the context of vibro-acoustic analyses.

In this paper, we contribute to this subject by proposing a greedy reduced basis scheme for the solution of purely acoustic and coupled structural acoustic problems. In the context of a multifrequency analysis, a reduced basis method[33] expresses the (approximate) solution at each frequency point as a linear combination of a few basis vectors. In our case, these basis vectors are simply the solutions at suitably chosen frequency points within the frequency range of interest. When these basis vectors are chosen iteratively, based on the solution that is worst approximated by the current reduced basis in each step, this procedure is known as a greedy algorithm.[34,35]

Section 2 proceeds with a brief review of the coupled FEM-BEM formulation followed by a detailed description of the greedy reduced basis scheme and its implementation in Section 3. The method is then applied to the solution of an interior acoustic problem and to the solution of two coupled structural acoustic problems in Section 4. In all three examples, the greedy algorithm automatically constructs the basis vectors at or near resonances, thus leading to small errors in a few iterations. Section 5 concludes with a discussion on the applicability as well as the current limitations of the method. Generally speaking, the greedy reduced basis scheme proves to be particularly efficient, when the responses at a large number of frequency points are contained in a small subspace. Consequently, the common practice among engineers of oversampling the frequency range has less impact on the overall computational effort than when using a conventional frequencywise strategy. On the other hand, when the responses at different frequencies are not or hardly related to each other (eg, in the case of frequency dependent forcing vectors), conventional frequencywise strategies or modal superposition techniques could be more efficient.

2 | COUPLED FEM-BEM FORMULATION FOR STRUCTURAL ACOUSTIC INTERACTION

We consider fully coupled structural acoustic interaction problems using FEM[36] and BEM[8] for discretizing the equations of linear time-harmonic elastodynamics and acoustics, respectively. The resulting linear systems of equations for the structural and for the acoustic subdomain read

$$(\mathbf{K} - \omega^2 \mathbf{M})\mathbf{u} = \mathbf{f}_{\mathrm{s}} + \mathbf{f}_{\mathrm{f}}, \tag{1}$$

$$\mathbf{H}(\omega)\mathbf{p} = \mathbf{G}(\omega)\mathbf{v}_{\mathrm{s}}. \tag{2}$$

The column vectors $\mathbf{u} \in \mathbb{C}^{n_{\mathrm{s}} \times 1}$ and $\mathbf{p} \in \mathbb{C}^{n_{\mathrm{f}} \times 1}$ contain the unknown displacement and sound pressure degrees of freedom at the nodes. The stiffness and mass matrices of the structure are denoted as $\mathbf{K} \in \mathbb{R}^{n_{\mathrm{s}} \times n_{\mathrm{s}}}$ and $\mathbf{M} \in \mathbb{R}^{n_{\mathrm{s}} \times n_{\mathrm{s}}}$. Structural damping is not considered in this work. The boundary element matrices $\mathbf{H}(\omega) \in \mathbb{C}^{n_{\mathrm{f}} \times n_{\mathrm{f}}}$ and $\mathbf{G}(\omega) \in \mathbb{C}^{n_{\mathrm{f}} \times n_{\mathrm{f}}}$ are obtained by a collocation discretization of the Kirchhoff-Helmholtz integral equation, relating the structural particle velocity $\mathbf{v}_{\mathrm{s}} \in \mathbb{C}^{n_{\mathrm{s}} \times 1}$ to the sound pressure. These matrices are implicitly dependent on the angular frequency $\omega = 2\pi f$, where f is the frequency in Hz. The structure is excited by nodal forces $\mathbf{f}_{\mathrm{s}} \in \mathbb{C}^{n_{\mathrm{s}} \times 1}$. Equations (1) and (2) are coupled on the sound radiating boundary. There, the structure is subject to normal tractions due to the acoustic sound pressure, and the particle velocity in (2) is equal to the time derivative of the normal displacement on the boundary. The coupling conditions can be expressed as

$$\mathbf{f}_{\mathrm{f}} = \mathbf{C}_{\mathrm{sf}}\mathbf{p} \quad \text{and} \quad \mathbf{v}_{\mathrm{s}} = -\mathrm{i}\omega \mathbf{C}_{\mathrm{fs}}\mathbf{u}, \tag{3}$$

where $\mathbf{C}_{\mathrm{sf}} \in \mathbb{R}^{n_{\mathrm{s}} \times n_{\mathrm{f}}}$ and $\mathbf{C}_{\mathrm{fs}} \in \mathbb{R}^{n_{\mathrm{f}} \times n_{\mathrm{s}}}$ are the mesh coupling matrices obtained by a Galerkin projection.[37] The force vector $\mathbf{f}_{\mathrm{f}}$ can be interpreted as the acoustic loading on the structural nodes and i denotes the imaginary unit. Finally, the global system of equations containing the coupling conditions emerges as

$$\begin{bmatrix} \mathbf{K} - \omega^2 \mathbf{M} & -\mathbf{C}_{\mathrm{sf}} \\ -\mathrm{i}\omega \mathbf{G}(\omega)\mathbf{C}_{\mathrm{fs}} & \mathbf{H}(\omega) \end{bmatrix} \begin{bmatrix} \mathbf{u} \\ \mathbf{p} \end{bmatrix} = \begin{bmatrix} \mathbf{f}_{\mathrm{s}} \\ 0 \end{bmatrix}. \tag{4}$$

When only the structural response is of interest, (4) can be reformulated by forming the Schur complement and thereby omitting the pressure degrees of freedom,[16] ie,

$$\left[\mathbf{K} - \omega^2 \mathbf{M} + \mathrm{i}\omega \mathbf{C}_{\mathrm{sf}} \mathbf{H}(\omega)^{-1} \mathbf{G}(\omega)\mathbf{C}_{\mathrm{fs}} \right] \mathbf{u} = \mathbf{f}_{\mathrm{s}}. \tag{5}$$

Note that, often, the dimension of the acoustic subproblem is at least an order of magnitude smaller than the structural subproblem. Thus, when facing moderately large problems, the computation of $\mathbf{H}(\omega)^{-1}\mathbf{G}(\omega)$ is relatively inexpensive compared to the solution of (5). However, the reformulation of (4) into (5) deteriorates the sparsity pattern of the structural subsystem and hence precludes the solution of large-scale problems. In these cases, the solution of (4) using a preconditioned iterative scheme is more practical. Alternatively, (5) could be solved using a direct method in conjunction with MOR of the structural subsystem.[31] In the numerical examples in Section 4, we will consider both types of structural acoustic equation (4) and (5).

Many vibro-acoustic applications require a solution of (4) or (5) at a range of frequencies $\omega_1, \ldots, \omega_m$. Usually, each of the m linear systems are solved successively in an independent manner. In the proceeding sections, we propose an alternative approach based on a greedy algorithm.

3 | A GREEDY ALGORITHM FOR MULTIFREQUENCY ANALYSIS

First introduced in the context of combinatorial optimization problems, the general idea behind greedy algorithms is to repeatedly make the choice that is currently optimal. A prominent example for which locally optimal choices (the greedy choices) yield the globally optimal solution is the so-called minimum spanning tree problem. It is the task of connecting a number of vertices such that there exist routes among all vertices while minimizing the total length of the connecting edges. It can simply be proven that this problem can be solved by the following greedy strategy[38]: "In each step, add the shortest edge between two vertices that does not form a closed cycle with the current set of edges."

Beside the field of combinatorial optimization, greedy algorithms have nowadays become a popular tool for the construction of reduced bases in the context of parameterized partial differential equations.[39] As such, they represent an alternative to proper orthogonal decomposition (POD) methods, in which possibly large numbers of high-fidelity systems need to be evaluated in order to deduce adequate POD bases. Using greedy algorithms, the number of evaluations of the high-fidelity system is minimized by iteratively adding new basis vectors to the reduced basis.[40,41] However, they rely on an a posteriori error estimation for the whole parameter space in each iteration in order to optimally choose the next parameter sample. Consequently, their success is heavily dependent on the computational cost that is required for the solution of this optimization problem and the associated error estimation. In the following, we propose to extend the application of greedy algorithms to the solution of vibro-acoustic problems in a frequency range. A detailed description of the algorithm is provided including a cheap a posteriori error estimation giving rise to fast frequency range solutions.

For the sake of readability, the frequency dependent linear systems (4) and (5) are replaced by $\mathbf{A}(\omega)\mathbf{x}(\omega) = \mathbf{b}(\omega)$ with the frequency points of interest $\omega \in \mathcal{P} = \{\omega_1, \ldots, \omega_m\}$. Note that here, we consider the general case with a frequency dependent right-hand side $\mathbf{b}(\omega)$. In each iteration j of the greedy algorithm, a set of frequency samples $\mathcal{P}_j \subseteq \mathcal{P}$ is given as

$$\mathcal{P}_j = \{\omega^{(1)}, \ldots, \omega^{(j)}\}. \tag{6}$$

The corresponding reduced basis $\mathbf{X}_j$ is simply the concatenation of the solutions at these frequency samples, ie,

$$\mathbf{X}_j = \left[\mathbf{x}(\omega^{(1)}), \ldots, \mathbf{x}(\omega^{(j)})\right] \in \mathbb{C}^{n \times j}. \tag{7}$$

The current approximation at an arbitrary frequency point $\omega \in \mathcal{P}$ is then expressed by

$$\mathbf{x}(\omega) = \mathbf{x}(\omega^{(1)})y_1(\omega) + \cdots + \mathbf{x}(\omega^{(j)})y_j(\omega) = \mathbf{X}_j\mathbf{y}(\omega), \tag{8}$$

with $\mathbf{y}(\omega) \in \mathbb{C}^{j \times 1}$, where $\mathbf{y}(\omega)$ is the solution of the least squares problem

$$\min_{\mathbf{y}(\omega) \in \mathbb{C}^{j \times 1}} \|\mathbf{A}(\omega)\mathbf{X}_j\mathbf{y}(\omega) - \mathbf{b}(\omega)\|_2^2. \tag{9}$$

The main idea behind the greedy algorithm is to choose the next sample $\omega^{(j+1)}$ there, where the approximation (8) yields the largest relative residual. Therefore,

$$\omega^{(j+1)} = \underset{\omega \in \mathcal{P}}{\mathrm{argmax}} \|\mathbf{A}(\omega)\mathbf{X}_j\mathbf{y}(\omega) - \mathbf{b}(\omega)\|_2 / \|\mathbf{b}(\omega)\|_2 \tag{10}$$

holds and the next basis vector is calculated by solving the system

$$\mathbf{A}(\omega^{(j+1)})\mathbf{x}(\omega^{(j+1)}) = \mathbf{b}(\omega^{(j+1)}). \tag{11}$$

The procedure is repeated until a convergence criterion based on the relative residual is fulfilled for all $\omega \in \mathcal{P}$.

Regarding the computational efficiency of the method, it is crucial that a sufficiently accurate approximation of the solution in the whole frequency range is achievable by a linear combination of only a few $q \ll m$ solutions at sample frequencies, ie, with a small number of iterations q. From an algebraic point of view, this means that the frequency range solution $\mathbf{X} = [\mathbf{x}(\omega_1), \ldots, \mathbf{x}(\omega_m)] \in \mathbb{C}^{n \times m}$ admits a low rank approximation. More precisely, the singular values of $\mathbf{X}$ should exhibit exponential decay, which has been proven for an analytical frequency dependency of $\mathbf{A}(\omega)$ and $\mathbf{b}(\omega)$[42] and thus holds for the herein presented case. From a vibro-acoustic point of view, the admissibility of a low rank approximation can be understood in that the spatial distribution of the response exhibits a certain degree of regularity with respect to the frequency. Essentially, the well-known modal reduction technique is based on similar principles of superposition, but instead of superposing modes of the system, here, we use a linear combination of certain responses. In the context of modal superposition techniques, the contribution of the individual modes is expressed by the modal amplification factors. Similarly, using the herein proposed greedy algorithm, the iteratively chosen responses of the system are weighted by the scaling factors $\mathbf{y}$. Although modal quantities are not determined in the present method, we will later see that the frequencies close to resonances are intrinsically chosen as samples over the course of the iterations.

Beside the solution of q linear systems (recall that q corresponds to the total number of iterations), the main computational effort of the greedy algorithm stems from the minimization of (9) using a least squares solver along with an a posteriori error estimation. For both, the built-in MATLAB function lsqlin provides a straightforward implementation. While an error estimation is performed in each iteration for all the yet unconverged solutions and hence necessitate $\mathcal{O}(qm)$ calls of the least squares solver, the evaluation of a single least squares problem is rather inexpensive since $\mathbf{A}(\omega)\mathbf{X}_j$ has only a small number of columns. The numerical examples will show that the algorithm results in a significantly smaller computational effort than solving m linear systems independently.

The repeated evaluation of the least squares problems, however, requires preassembly and storage of all m possibly fully populated matrices in the main memory. The latter is the major drawback of the proposed method and currently limits its application to small-sized problems. There are two remedies in this regard. For medium-sized problems, the use of data sparse formats such as hierarchical matrices[26] resolves the memory issues. For large-scale problems, the proposed algorithm could be parallelized by solving the least squares problem (9) in a distributed memory environment and solving (11) on a shared memory environment. Although we expect that only a moderate amount of communication is required, systematic benchmarking is still needed to verify the applicability of the proposed scheme to large-scale multifrequency problems. However, this is not within the scope of the present work but planned for future research.

The greedy reduced basis scheme is summarized in Algorithm 1. In order to avoid least squares minimizations at frequency points with already converged solutions, a set of frequencies $\mathcal{P}_{\mathrm{sol}}$ is defined containing the frequencies at which the solution has been explicitly determined (line 23) as well the frequencies at which the least squares approximation already yields sufficient accuracy (line 15). Furthermore, the matrix products $\mathbf{A}(\omega_i)\mathbf{X}_j$ for setting up the least squares minimizations in line 13 are explicitly stored in the main memory to avoid recomputation in each iteration. Only the new column $\mathbf{A}(\omega_i)\mathbf{x}(\omega^{(j)})$ is added in each iteration. Since this matrix vector product needs to be evaluated $\mathcal{O}(qm)$ times, it accounts for the main computational effort beside the explicit solutions of q linear systems and the actual solutions of the $\mathcal{O}(qm)$ least squares problems.

Algorithm 1 Greedy algorithm for the multifrequency solution of structural acoustic problems

1: **input**
2:     system matrices $\mathbf{A}(\omega_i)$ and right-hand sides $\mathbf{b}(\omega_i)$ with $\omega_i \in \mathcal{P} = \{\omega_1, ..., \omega_m\}$
3:     relative error tolerance for the residual ϵ_{tol}
4:     frequency for first iteration $\omega^{(1)} \in \mathcal{P}$
5: **initialization**
6:     $j := 1$
7:     $\mathbf{r}(\omega_i) := \mathbf{b}(\omega_i) \,\forall \omega_i \in \mathcal{P}$
8:     solve $\mathbf{A}(\omega^{(j)})\mathbf{x}(\omega^{(j)}) = \mathbf{b}(\omega^{(j)})$
9:     $\mathbf{X}_j := \left[\mathbf{x}(\omega^{(j)})\right]$
10:     $\mathcal{P}_{\mathrm{sol}} := \left\{\omega^{(j)}\right\}$
11: **while** $\exists \omega_i \in \mathcal{P} : \|\mathbf{r}(\omega_i)\|_2 / \|\mathbf{b}(\omega_i)\|_2 > \epsilon_{\mathrm{tol}}$ **do**
12:     **for all** $\omega_i \in \mathcal{P}\backslash\mathcal{P}_{\mathrm{sol}}$ **do**
13:         solve $\displaystyle\min_{\mathbf{y}(\omega_i)\in\mathbb{C}^{j\times 1}} \|\mathbf{A}(\omega_i)\mathbf{X}_j\mathbf{y}(\omega_i) - \mathbf{b}(\omega_i)\|_2^2$, $\mathbf{r}(\omega_i) := \mathbf{A}(\omega_i)\mathbf{X}_j\mathbf{y}(\omega_i) - \mathbf{b}(\omega_i)$
14:         **if** $\|\mathbf{r}(\omega_i)\|_2 / \|\mathbf{b}(\omega_i)\|_2 < \epsilon_{\mathrm{tol}}$ **then**
15:             $\mathbf{x}(\omega_i) := \mathbf{X}_j\mathbf{y}(\omega_i)$, $\mathcal{P}_{\mathrm{sol}} := \mathcal{P}_{\mathrm{sol}} \cup \{\omega_i\}$
16:         **end if**
17:     **end for**
18:     **if** $\|\mathbf{r}(\omega_i)\|_2 / \|\mathbf{b}(\omega_i)\|_2 < \epsilon_{\mathrm{tol}} \,\forall \omega_i \in \mathcal{P}$ **then**
19:         **break**
20:     **end if**
21:     $\omega^{(j+1)} := \displaystyle\operatorname*{argmax}_{\omega_i\in\mathcal{P}} \|\mathbf{r}(\omega_i)\|_2 / \|\mathbf{b}(\omega_i)\|_2$
22:     solve $\mathbf{A}(\omega^{(j+1)})\mathbf{x}(\omega^{(j+1)}) = \mathbf{b}(\omega^{(j+1)})$
23:     $\mathbf{X}_{j+1} := \left[\mathbf{X}_j, \mathbf{x}(\omega^{(j+1)})\right] \in \mathbb{C}^{n\times j+1}$ $\mathcal{P}_{\mathrm{sol}} := \mathcal{P}_{\mathrm{sol}} \cup \left\{\omega^{(j+1)}\right\}$
24:     $j := j + 1$
25: **output**
26:     $\mathbf{x}(\omega_i)$ with $\|\mathbf{A}(\omega_i)\mathbf{x}(\omega_i) - \mathbf{b}(\omega_i)\|_2 / \|\mathbf{b}(\omega_i)\|_2 \le \epsilon_{\mathrm{tol}} \,\forall \omega_i \in \mathcal{P}$

4 | NUMERICAL EXAMPLES

The proceeding sections verify the efficiency of Algorithm 1 in the context of multifrequency analysis.

4.1 | Plane sound wave in a closed rigid duct

As a first numerical example, we consider a purely interior acoustic problem. This problem is well suited to demonstrate the convergence behavior of the greedy algorithm in the context of multifrequency analysis. A plane sound wave is excited by a harmonic particle velocity at the left end of a three-dimensional closed and air-filled duct of length $l = 3.4$ m and square cross section $w = 0.2$ m. The wave is fully reflected at the acoustically rigid right end. The speed of sound is $c = 340$ m/s. The system is free of dissipation, and hence, resonances occur at the integer multiples of 50 Hz. This problem is often used in the computational acoustics community for benchmarking purposes[43] and extensive studies on associated discretization errors with respect to mesh sizes and element types are available in the literature.[44,45]

The acoustic field is discretized using a uniform mesh of 1120 quadrilateral boundary elements with bilinear discontinuous sound pressure interpolation yielding 4480 degrees of freedom. We are interested in solving the resultant linear system (2) in the frequency range from 40 to 210 Hz with frequency steps of $\Delta f = 1$ Hz, ie, $m = 171$. Resonances are expected at 50, 100, 150, and 200 Hz. This problem is relatively well conditioned, ie, cond $\mathbf{A}(\omega_i) \approx 10^2$.

First, a standard generalized minimal residual (GMRes) algorithm[46] without restarts is used for the purpose of a comparison in terms of the computational time. The tolerance for the relative residual is set to $\epsilon_{\text{gmres}} = 10^{-5}$. All $m = 171$ linear systems have been successively solved requiring a total of 4463 iterations and a wall clock time of 96.44 s. This corresponds to an average of 0.564 s for the solution at each frequency point.

Using the greedy algorithm described in the previous section, a total of 10 iterations was required in order to meet the tolerance for the relative residual of $\epsilon_{\text{tol}} = 10^{-5}$ for all frequency points. Accordingly, a GMRes scheme has been applied for the solution at 10 out of 171 frequency points. These solutions correspond to the basis vectors used for the least squares approximations in the inner loop of Algorithm 1. In order to ensure sufficient accuracy of the basis vectors, a tolerance of $\epsilon_{\text{gmres}} = 10^{-8}$ was chosen for the GMRes scheme resulting in an elapsed time of 7.11 s. Moreover, 1562 matrix vector products were evaluated for the setup of the least squares problems resulting in 27.28 s. The solution of the least squares problems required a computational time of 2.84 s. In addition with the other parts of the algorithm that only marginally contribute to the computational effort, the total wall clock time added up to 37.32 s. This corresponds to an average of 0.218 s for the solution at each frequency point, and hence, a reduction by more than 60% compared to the conventional solution.

The convergence history of the greedy algorithm is given in Figure 1. The intermediate relative residuals after the first, sixth, and ninth iteration as well as the residual after convergence are shown. An initial frequency of 125 Hz has been chosen for the first iteration, which is the mid value of the considered frequency range. As expected, the solution at 125 Hz alone is not sufficient to approximate the solutions at other frequency points and hence only yields a decrease of the residual in its immediate vicinity. The residual after the sixth iteration exhibits six sharp minima (40, 50, 60, 125, 188, and 206 Hz), each corresponding to a GMRes solution in the outer loop and hence falling below the defined tolerance of
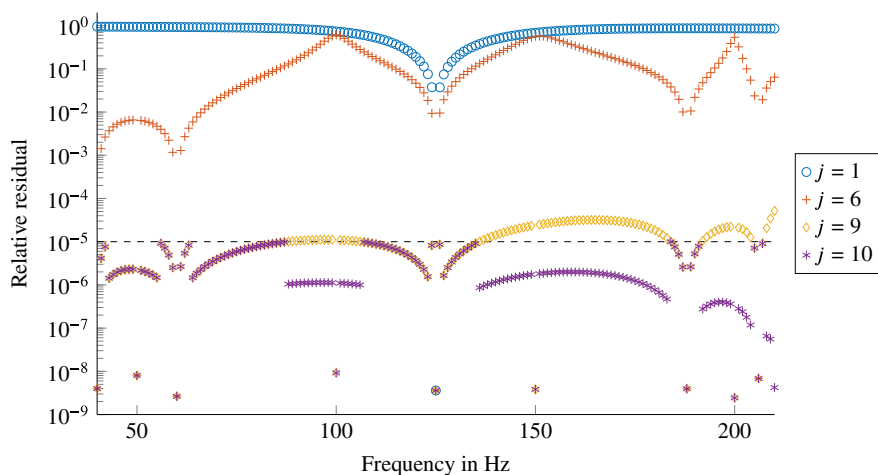

FIGURE 1 Relative residual over frequency after iterations 1, 6, 9, and 10 for the solution of the duct problem using a greedy algorithm [Colour figure can be viewed at wileyonlinelibrary.com]
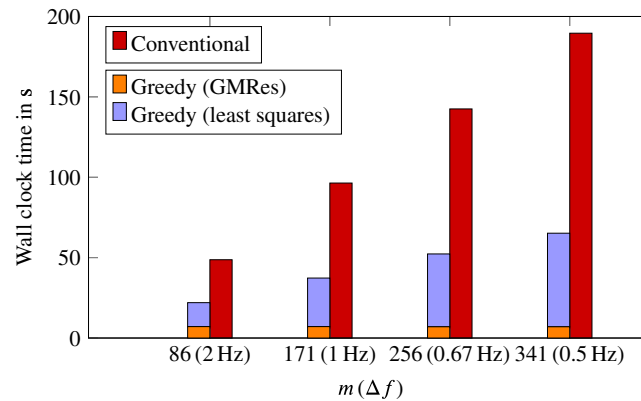
FIGURE 2 Comparison between conventional strategy and the greedy algorithm. Wall clock times for the solution of the duct problem in the frequency range from 40 to 210 Hz using different resolutions (ie, frequency steps Δf). The time required by the greedy algorithm is divided into the time for actual solving with generalized minimal residual (GMRes) and the time for the rest of the algorithm that mainly includes setup and solution of the least squares problems

$\epsilon_{\mathrm{gmres}} = 10^{-8}$. However, they are not yet sufficient for accurate least squares approximations at intermediate frequencies. This is particularly true for the solutions at the resonance frequencies of 100, 150, and 200 Hz that exhibit maxima in the residual. Consequently, the new basis vectors are calculated at those three frequencies in iterations seven to nine, resulting in a significant decrease of the residual across the whole frequency range. At this point, the solutions at the frequencies 40 to 87 Hz as well as 107 to 135 Hz and 184 to 191 Hz are already converged and thus not recomputed in the 10th (and last) iteration.

This example indicates the effectiveness of a greedy scheme in the context of a multifrequency analysis. Choosing the frequency at which the approximation is worst as the next sample sooner or later leads to evaluation of the frequency dependent system at (or near) its resonance frequencies. In the present example, convergence was achieved rather quickly once the responses close to the resonances were added to the reduced basis. This may lead to the intuitive assumption that including responses exactly at the eigenfrequencies of the system is essential for fast convergence of the algorithm. However, excluding the frequencies 50, 100, 150, and 200 Hz leads to the choice of neighboring frequency points (eg, 49 Hz instead of 50 Hz), and the algorithm requires the exact same number of iterations for this problem. Moreover, choosing the frequency interval in a mid-frequency range, and thereby omitting the responses around the first couple of eigenfrequencies of the system, does not deteriorate the convergence of the method. For example, the solution of this problem in the frequency range from 240 to 410 Hz with frequency steps of $\Delta f = 1$ Hz required 12 iterations in order to meet the tolerance of $\epsilon_{\mathrm{tol}} = 10^{-5}$. The larger number of iterations compared to the low-frequency analysis (12 instead of 10) could be associated with the reduced accuracy of the solutions due to larger discretization errors. Further mathematical study is required in this regard.

Our preliminary numerical studies also indicate that the convergence behavior is rather insensitive to the choice of the initial frequency $\omega^{(1)}$. Furthermore, refining the resolution of the frequency range of interest in this example does not lead to an increase of the total number of iterations. In general, additional frequency points in a rather smooth region only affect the number of least squares solutions and not the number of actual solutions of the system. This is also reflected in Figure 2, where the solution time of the duct problem is shown for different frequency resolutions. The time required for the actual solutions of the system is unchanged while the time required for the setup and solution of the least squares problems increases linearly with the number of frequency points m; however, the rate of increase is smaller than in the conventional solution strategy. Therefore, using the greedy algorithm, the common practice among engineers of oversampling the frequency range has less impact on the overall computational effort.

4.2 | Point-excited spherical shell in water

As a second example, we consider a structural acoustic interaction problem. A spherical shell made of steel is locally excited by a point force of $F = 1$ N and sound is radiated into the surrounding water. The geometrical parameters of the sphere and the material properties of steel and water are given in Table 1. Eight-noded quadrilateral shell finite elements based on the Reissner-Mindlin theory are employed to model the structural subdomain. Discontinuous quadrilateral boundary elements are used for the discretization of the acoustic subdomain. These boundary elements are

TABLE 1   Geometry of the sphere and properties of steel and water

Radius of sphere	r	5 m
Shell thickness	t	0.05 m
Density of steel	ρ_s	7860 kg/m^3
Young's modulus	E	210 GPa
Poisson's ratio	v	0.3
Density of water	ρ_f	1000 kg/m^3
Speed of sound	c	1482 m/s
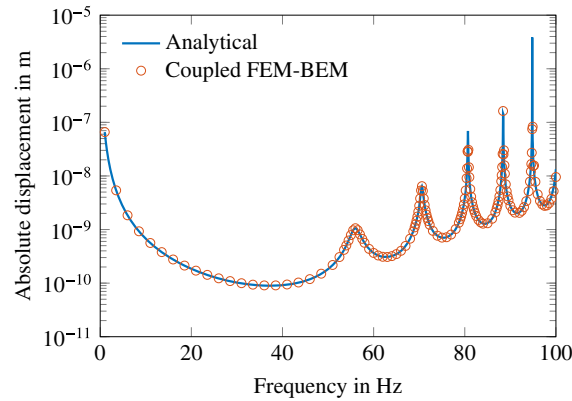
FIGURE 3   Absolute displacement at an angle of π with respect to the point of excitation for the steel spherical shell submerged in water. Comparison of analytical and numerical results. BEM, boundary element method; FEM, finite element method [Colour figure can be viewed at wileyonlinelibrary.com]

superparametric, ie, they are characterized by a four-noded bilinear sound pressure interpolation and a nine-noded biquadratic geometry approximation. Conforming meshes with 384 finite and boundary elements are employed corresponding to eight elements on a $\pi/2$ arc. After forming the Schur complement (5), the system has 6924 degrees of freedom. The problem is studied at $m = 138$ nonuniformly spaced frequency points up to 100 Hz. A treatment for irregular frequencies is not required in the considered frequency range since the first eigenfrequency of the corresponding interior acoustic Dirichlet problem is approximately 148 Hz.[47] The absolute displacement solution at a point located at an angle of π with respect to the point of excitation is shown in Figure 3 along with the analytical series solution.[48] Five resonances occur in the considered frequency range.

Due to the ill-conditioning of the Schur matrix (5), ie, $\text{cond}\,\mathbf{A}(\omega_i) = 10^5 \cdots 10^8$, the use of an iterative solver would require preconditioning. However, due to the lack of a suitable preconditioner, and given the relatively small number of degrees of freedom, a direct solver has been employed for successively solving $m = 138$ linear systems requiring a wall clock time of 693.14 s. This corresponds to an average of 5.02 s for the solution at each frequency point.

The greedy algorithm required a total of 20 iterations in order to meet the tolerance for the relative residual of $\epsilon_{tol} = 10^{-5}$ for all frequency points. Consequently, a direct solver was employed at 20 out of 138 frequencies resulting in an elapsed time of 98.19 s. Moreover, 2241 matrix vector products were evaluated for the setup of the least squares problems resulting in 93.63 s. The solution of the least squares problems required a computational time of 9.36 s. In total, the wall clock time added up to 201.33 s corresponding to an average of 1.46 s for the solution at each frequency point. However, this number is not comparable to the average time that was required by the conventional strategy due to the difference in achieved accuracies.

The convergence history of the greedy algorithm is shown in Figure 4. Again, similar to the duct problem, distinct maxima in the residual emerge at the five resonance frequencies after iteration $j = 12$. The predefined tolerance of $\epsilon_{tol} = 10^{-5}$ is met after iteration $j = 20$.

Furthermore, in order to assess the quality of the least squares approximations, the relative difference with respect to the conventional solution is studied in what follows. It can be expressed by

$$\delta(\omega_i) = \frac{\|\tilde{\mathbf{x}}(\omega_i) - \mathbf{x}(\omega_i)\|_2}{\|\tilde{\mathbf{x}}(\omega_i)\|_2}, \quad \omega_i = \omega_1, \ldots, \omega_m, \tag{12}$$
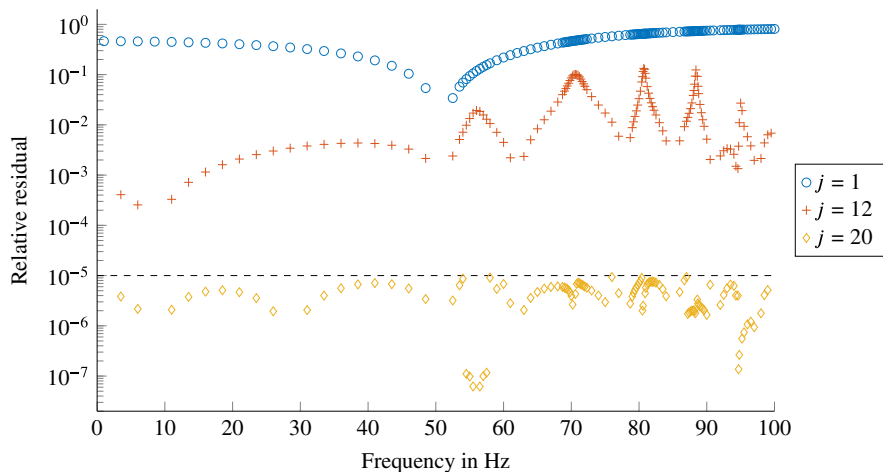
FIGURE 4 Relative residual over frequency after iterations 1, 12, and 20 for the solution of the submerged spherical shell using a greedy algorithm [Colour figure can be viewed at wileyonlinelibrary.com]
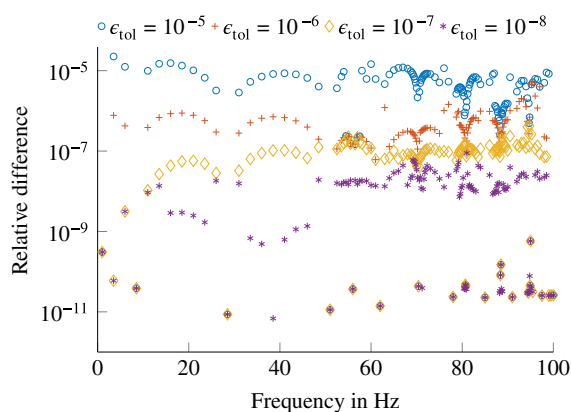

FIGURE 5 Relative difference in the 2-norm of the solution obtained with the greedy algorithm with respect to the conventional solution obtained using a direct solver. The relative difference is shown for different tolerances for the residual ϵ_{tol} in the greedy algorithm [Colour figure can be viewed at wileyonlinelibrary.com]

TABLE 2 Total number of iterations and wall clock times for different tolerances for the residual ϵ_{tol} in the greedy algorithm

ϵ_{tol}	Iterations	Wall clock time
10^{-5}	20	201.33 s
10^{-6}	21	221.31 s
10^{-7}	23	262.73 s
10^{-8}	38	386.65 s

where $\tilde{\mathbf{x}}(\omega_i)$ denotes the solution obtained using a direct solver and $\mathbf{x}(\omega_i)$ is the solution obtained by the greedy algorithm. Trivially, $\delta = 0$ at the frequencies that are chosen by the greedy algorithm for the calculation of the basis vectors. The relative differences δ are shown in Figure 5 for different tolerances ϵ_{tol} of the relative residual. The respective numbers of iterations and wall clock times of the greedy algorithm are provided in Table 2. For instance, a predefined tolerance of $\epsilon_{tol} = 10^{-5}$ yields a relative difference $\delta(\omega_i) \leq 10^{-4}$ in the whole frequency range $\omega_1, \ldots, \omega_m$. However, for tolerances smaller than $\epsilon_{tol} = 10^{-8}$ in this problem, the proposed scheme is less efficient than a conventional strategy using a direct solver for each frequency point.

These results lead to the conclusion that an a priori estimation of the condition numbers in the frequency range could provide indication of suitable tolerances ϵ_{tol} and consequently facilitate the decision whether to use the greedy algorithm or a conventional strategy. Relatively inexpensive algorithms for estimating 1-norm condition numbers exist[49,50] and the thereby gained knowledge could also be incorporated into the choice of the next sample (10). This is certainly an issue requiring future research.

4.3 | Honeycomb sandwich panel in air

Beside the case of structures submerged in water, structural acoustic interaction can also have a significant influence on the vibration response of lightweight structures in air, particularly for sandwich panels with large radiating surfaces. Clarkson and Brown were among the first to experimentally quantify the energy dissipation by virtue of sound radiation for a sandwich panel with honeycomb core.[51] They have shown that this phenomenon—commonly denoted as acoustic radiation damping—can exceed the extent of material-inherent damping by an order of magnitude. In the following, we apply the greedy algorithm for a vibro-acoustic analysis of a similar sandwich panel as the one tested by Clarkson and Brown.[51] However, we point out that the focus of the present analysis is set on the numerical analysis rather than on the acoustic radiation damping of sandwich structures.

The geometry of the six-sided panel with a central cut-out is shown in Figure 6. It is composed of an aluminum honeycomb core of 29 mm thickness and two 0.28 mm thick aluminum face sheets. The isotropic material properties of aluminum as well as the (assumed) equivalent orthotropic properties of the core are given in Table 3. In this example, additional structural damping is neglected, and hence, sound radiation is the only source of energy dissipation. The panel
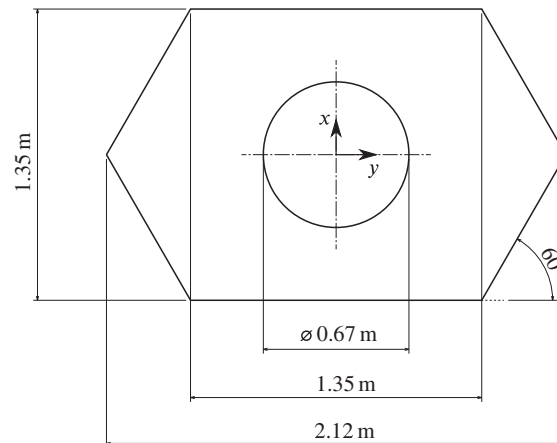

FIGURE 6 Geometry of the six-sided honeycomb sandwich panel with central cut-out. The panel is freely suspended in air without an acoustic baffle and excited by a harmonic point force at the tip ($x = 0$, $y = 1.06$ m)

TABLE 3 Properties of the face sheets and the honeycomb core

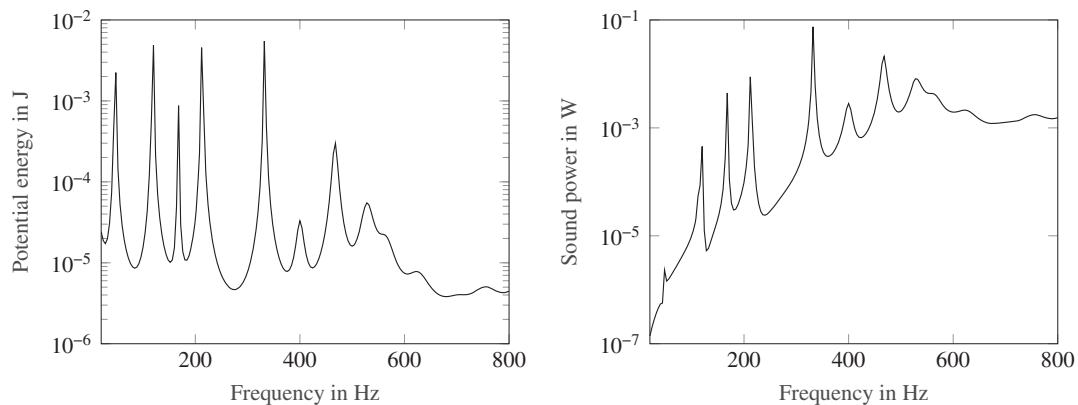| Aluminum face sheet		
Thickness	t	0.28 mm
Density	ρ_a	2780 kg/m^3
Young's modulus	E	73 GPa
Poisson's ratio	ν_a	0.34
Aluminum honeycomb core		
Thickness	h	29 mm
Density	ρ_c	44.8 kg/m^3
Young's modulus	E_x, E_y	18.9 MPa
Young's modulus	E_z	1.89 GPa
Shear modulus	G_{xy}	3 MPa
Shear modulus	G_{yz}	137.3 MPa
Shear modulus	G_{xz}	222.7 MPa
Poisson's ratio	ν_c	0.1

FIGURE 7   Total potential energy and radiated sound power of the point-excited sandwich panel

is freely suspended in air without an acoustic baffle and excited by a harmonic point force at the tip ($x = 0$, $y = 1.06$ m). We are interested in the vibro-acoustic response of the panel in the frequency range from 20 Hz to 800 Hz in frequency steps of $\Delta f = 4$ Hz, ie, $m = 196$.

Eight-noded quadrilateral shell finite elements and 20-noded hexahedral solid finite elements are employed for the discretization of the core and face sheets, respectively, resulting in a total of 22 131 displacement degrees of freedom. To model the acoustic subdomain, quadrilateral boundary elements with linear discontinuous sound pressure interpolation and a total of 1504 pressure degrees of freedom are employed. The nonconforming structural and acoustic meshes are coupled on the face sheets of the panel. In order to verify the accuracy of the discretization, the radiated sound power has been compared to a model with 10 times more degrees of freedom, resulting in a relative difference of less than 2.6% (0.11 dB) in the considered frequency range. A treatment for irregular frequencies is not required since the first eigenfrequency of the corresponding interior acoustic Dirichlet problem is approximately 6000 Hz.

The coupled system of Equations (4) is solved using a GMRes scheme with an incomplete LU factorization (ILU) for preconditioning the structural system $\mathbf{K} - \omega^2 \mathbf{M}$. Following the conventional frequencywise strategy, a total of 8623 iterations were required for solving all the $m = 196$ systems individually subject to a relative tolerance of $\epsilon_{\text{tol}} = 10^{-5}$. The total solution time including setup of the preconditioners added up to 105 minutes. The radiated sound power and the total potential energy of the vibrating panel are shown in Figure 7. While the first couple of resonances exhibit sharp peaks, the effect of acoustic radiation damping is clearly noticeable in the higher frequency range.

The greedy algorithm required a total of 43 outer iterations for the solution in the whole frequency range. The responses at the sampling frequencies were computed using the same preconditioned GMRes scheme as above with $\epsilon_{\text{gmres}} = 10^{-8}$ accounting for a wall clock time of 26 minutes. The setup and the solution of the least squares problems resulted in an elapsed time of 7 minutes. In total, the greedy algorithm required 33 minutes for the solution at all frequency points with a relative residual of less then $\epsilon_{\text{tol}} = 10^{-5}$. This corresponds to a speedup of more than three times compared to the conventional solution.

5 | CONCLUSION AND FUTURE WORK

A greedy reduced basis scheme has been proposed for the frequency range solution of vibro-acoustic problems. It is based on iteratively expanding the reduced basis by adding the frequency response that is currently worst approximated. The method has been applied to an interior acoustic problem as well as to coupled structural exterior acoustic problems. In all cases, convergence was reached relatively fast, and consequently, the actual solution of the system was only required at a few frequency points. The solutions at the other intermediate frequencies could be accurately approximated by linear combination using a least squares solver. Comparisons to conventional frequencywise strategies indicate the efficiency of the proposed scheme.

Although in all examples, frequencies near resonances were chosen for calculating the basis vectors during the iterations, preliminary studies have shown that explicit exclusion of eigenfrequencies from the frequency range of interest does not deteriorate convergence. Moreover, the algorithm seems to be insensitive to the choice of the initial frequency. Furthermore, refining the frequency resolution in a smooth region leads only to a marginal (if at all) increase in the total number of iterations. In general, refining the frequency resolution over a certain threshold only increases the effort

required for the setup and solutions of the least squares problems. Consequently, the common practice among engineers of oversampling the frequency range has less impact on the overall computational effort than when using a conventional frequencywise strategy.

The numerical examples were carried out using the same excitation for all frequency points. While the method allows for a straightforward application of frequency-dependent right-hand sides, the success of the greedy algorithm will in these cases depend on the regularity of the response with respect to the frequency. When the responses at different frequencies are not or hardly related to each other, conventional frequencywise strategies could be more efficient. Furthermore, when considering multiple forcing vectors, adding the responses for all excitations to the reduced basis at each frequency sample could diminish the efficiency of the method. As a remedy, a truncated singular value decomposition could be applied in order to reduce the number of algebraically independent right-hand sides. Detailed studies on the use of MOR in the context of fast frequency sweeps with FEM and many forcing vectors are available in the literature.[52,53] Similar studies are also planned for the herein presented greedy reduced basis scheme.

Moreover, in a future work, a priori estimation of the condition numbers could provide indication of suitable tolerances along with an a priori error estimation and also improve the choice of basis vectors. Furthermore, the applicability of the scheme will be extended to large-scale problems by incorporating data sparse formats[26] as well as by parallelizing the algorithm. The latter could be done by solving the least squares problems in a distributed memory environment and solving the actual linear systems on a shared memory environment. Systematic benchmarking will be conducted to verify the applicability of the proposed scheme to large-scale multifrequency problems.

ORCID

Suhaib Koji Baydoun https://orcid.org/0000-0002-1184-065X

REFERENCES

1. Petyt M, Lea J, Koopmann G. A finite element method for determining the acoustic modes of irregular shaped cavities. *J Sound Vib*. 1976;45(4):495-502.
2. Nefske D, Wolf JA Jr, Howell L. Structural-acoustic finite element analysis of the automobile passenger compartment: a review of current practice. *J Sound Vib*. 1982;80(2):247-266.
3. Kaltenbacher M. *Computational Acoustics*. Cham, Switzerland: Springer; 2018.
4. Bai Z, Demmel J, Dongarra J, Ruhe A, van der Vorst H. *Templates for the Solution of Algebraic Eigenvalue Problems: A Practical Guide*. Philadelphia, PA: SIAM; 2000.
5. Thompson L. A review of finite-element methods for time-harmonic acoustics. *J Acoust Soc Am*. 2006;119:1315-1330.
6. Astley RJ, Macaulay GJ, Coyette JP, Cremers L. Three-dimensional wave-envelope elements of variable order for acoustic radiation and scattering. Part I. Formulation in the frequency domain. *J Acoust Soc Am*. 1998;103(1):49-63.
7. von Estorff O. *Boundary Elements in Acoustics: Advances and Applications*. Southampton, UK: WIT Press; 2000.
8. Marburg S, Nolte B. A unified approach to finite and boundary element discretization in linear time-harmonic acoustics. In: Marburg S, Nolte B, eds. *Computational Acoustics of Noise Propagation in Fluids. Finite and Boundary Element Methods*. Berlin, Germany: Springer; 2008.
9. Marburg S. Normal modes in external acoustics. Part III: sound power evaluation based on superposition of frequency-independent modes. *Acta Acustica United Acustica*. 2006;92:296-311.
10. Moheit L, Marburg S. Infinite elements and their influence on normal and radiation modes in exterior acoustics. *J Comput Acoust*. 2017;25(4):1650020.
11. Moheit L, Marburg S. Normal modes and modal reduction in exterior acoustics. *J Theor Comput Acoust*. 2018;26(3):1850029.
12. de Mesquita Neto E, Carvalho ER, de França Arruda J, Pavanello R. Acoustic eigenvalue analysis by boundary element methods. In: Wu TW, ed. *Boundary Element Acoustics*. Southampton, UK: WIT Press; 2000.
13. Leblanc A, Lavie A. Solving acoustic nonlinear eigenvalue problems with a contour integral method. *Eng Anal Bound Elem*. 2013;37(1):162-166.
14. Zheng C-J, Gao H-F, Du L, Chen H-B, Zhang C. An accurate and efficient acoustic eigensolver based on a fast multipole BEM and a contour integral method. *J Comput Phys*. 2016;305:677-699.

15. Kirkup SM, Amini S. Solution of the Helmholtz eigenvalue problem via the boundary element method. *Int J Numer Methods Eng*. 1993;36(2):321-330.

16. Peters H, Kessissoglou N, Marburg S. Modal decomposition of exterior acoustic-structure interaction. *J Acoust Soc Am*. 2013;133(5):2668-2677.

17. Kimeswenger A, Steinbach O, Unger G. Coupled finite and boundary element methods for fluid-solid interaction eigenvalue problems. *SIAM J Numer Anal*. 2014;52(5):2400-2414.

18. Zheng C-J, Bi C-X, Zhang C, Gao H-F, Chen H-B. Free vibration analysis of elastic structures submerged in an infinite or semi-infinite fluid domain by means of a coupled fe-be solver. *J Comput Phys*. 2018;359:183-198.

19. Benthien GW, Schenk HA. Structural-acoustic coupling. In: Ciskowski RD, Brebbia CA, eds. *Boundary Element Methods in Acoustics*. London, UK: Computational Mechanics Publications, Elsevier Applied Science; 1991.

20. Kirkup SM, Henwood DJ. Methods for speeding up the boundary element solutions of acoustic radiation problems. *J Vib Acoust*. 1992;144(3):347-380.

21. Wu TW, Li WL, Seybert AF. An efficient boundary element algorithm for multi-frequency acoustical analysis. *J Acoust Soc Am*. 1993;94(1):447-452.

22. Zhang Q, Mao Y, Qi D, Gu Y. An improved series expansion method to accelerate the multi-frequency acoustic radiation prediction. *J Comput Acoust*. 2015;23(1):1450015.

23. Coyette J-P, Lecomte C, Migeot J-L, Blanche J, Rochette M, Mirkovic G. Calculation of vibro-acoustic frequency response functions using a single frequency boundary element solution and a padé expansion. *Acta Acustica United Acustica*. 1999;85(3):371-377.

24. Baumgart J, Marburg S, Schneider S. Efficient sound power computation of open structures with infinite/finite elements and by means of the Padé-via-Lanczos algorithm. *J Comput Acoust*. 2007;15(4):557-577.

25. Liu Y. *Fast Multipole Boundary Element Method: Theory and Applications in Engineering*. New York, NY: Cambridge University Press; 2009.

26. Hackbusch W, Khoromskij B. A sparse *H*-matrix arithmetic. part 2: Application to multi-dimensional problems. *Computing*. 2000;64:21-47.

27. von Estorff O, Rjasanow S, Stolper M, Zaleski O. Two efficient methods for a multifrequency solution of the Helmholtz equation. *Comput Vis Sci*. 2005;8:159-167.

28. Hetmaniuk U, Tezaur R, Farhat C. Review and assessment of interpolatory model order reduction methods for frequency response structural dynamics and acoustics problems. *Int J Numer Methods Eng*. 2012;90:1636-1662.

29. Keuchel S, Biermann J, von Estorff O. A combination of the fast multipole boundary element method and Krylov subspace recycling solvers. *Eng Anal Bound Elem*. 2016;65:136-146.

30. Liang T, Wang J, Xiao J, Wen L. Coupled BE-FE based vibroacoustic modal analysis and frequency sweep using a generalized resolvent sampling method. *Comput Methods Appl Mech Eng*. 2019;345:518-538.

31. Peters H, Kessissoglou N, Marburg S. Modal decomposition of exterior acoustic-structure interaction problems with model order reduction. *J Acoust Soc Am*. 2014;135(5):2706-2717.

32. Xiao J, Meng S, Zhang C, Zheng C. Resolvent sampling based Rayleigh-Ritz method for large-scale nonlinear eigenvalue problems. *Comput Methods Appl Mech Eng*. 2016;310:33-57.

33. Quarteroni A, Manzoni A, Negri F. *Reduced Basis Methods for Partial Differential Equations*. Cham, Switzerland: Springer International Publishing; 2016.

34. Edmonds J. Matroids and the greedy algorithm. *Mathematical Programming*. 1971;1(1):127-136.

35. Cormen TH, Leiserson CE, Rivest RL, Stein C. *Introduction to Algorithms*. 3rd ed. Cambridge, MA: The MIT Press; 2009.

36. Zienkiewicz OC, Taylor RL, Fox D. *The Finite Element Method for Solid and Structural Mechanics*. Oxford, UK: Butterworth-Heinemann; 2014.

37. Peters H, Marburg S, Kessissoglou N. Structural-acoustic coupling on non-conforming meshes with quadratic shape functions. *Int J Numer Methods Eng*. 2012;91(1):27-38.

38. Kruskal J. On the shortest spanning subtree and the traveling salesman problem. *Proc Am Math Soc*. 1956;7:48-50.

39. Rozza G, Huynh DBP, Patera AT. Reduced basis approximation and a posteriori error estimation for affinely parametrized elliptic coercive partial differential equations. *Arch Comput Methods Eng*. 2008;15:229-275.

40. Buffa A, Maday Y, Patera AT, Prud'homme C, Turinici G. A priori convergence of the greedy algorithm for the parametrized reduced basis method. *ESAIM Math Model Numer Anal*. 2012;46:595-603.

41. Binev P, Cohen A, Dahmen W, DeVore R, Petrova G, Wojtaszczyk P. Convergence rates for greedy algorithms in reduced basis methods. *SIAM J Math Anal*. 2011;43(3):1457-1472.

42. Kressner D, Tobler C. Low-rank tensor Krylov subspace methods for parametrized linear systems. *SIAM J Matrix Anal Appl*. 2011;32(4):1288-1316.

43. Hornikx M, Kaltenbacher M, Marburg S. A platform for benchmark cases in computational acoustics. *Acta Acustica United Acustica*. 2015;101(4):811-820.

44. Marburg S. A pollution effect in the boundary element method for acoustic problems. *J Theor Comput Acoust*. 2018;26(2):1850018.

45. Baydoun S, Marburg S. Quantification of numerical damping in the acoustic boundary element method for two-dimensional duct problems. *J Theor Comput Acoust*. 2018;26(3):1850022.

46. Saad Y, Schultz MH. Gmres: a generalized minimal residual algorithm for solving nonsymmetric linear systems. *SIAM J Sci Stat Comput*. 1986;7(3):856-869.

47. Marburg S, Wu T-W. Treating the phenomenon of irregular frequencies. In: Marburg S, Nolte B, eds. *Computational Acoustics of Noise Propagation in Fluids - Finite and Boundary Element Methods*. Berlin, Germany: Springer; 2008.

48. Junger MC, Feit D. *Sound, Structures, and Their Interaction*. Cambridge, MA: MIT Press; 1986.

49. Hager WM. Condition estimates. *SIAM J Sci Stat Comput*. 1984;5(2):311-316.

50. Higham NJ, Tisseur F. A block algorithm for matrix 1-norm estimation, with an application to 1-norm pseudospectra. *SIAM J Matrix Anal Appl*. 2000;21(4):1185-1201.

51. Clarkson BL, Brown KT. Acoustic radiation damping. *J Vib Acoust Stress Reliab Des*. 1985;107:357-360.

52. Meerbergen K, Bai Z. The Lanczos method for parameterized symmetric linear systems with multiple right-hand sides. *SIAM J Matrix Anal Appl*. 2010;31(4):1642-1662.

53. Wixom AS, McDaniel JG. Fast frequency sweeps with many forcing vectors through adaptive interpolatory model order reduction. *Int J Numer Methods Eng*. 2014;100:442-457.

A.3 Publication III

A subspace iteration eigensolver based on Cauchy integrals for vibroacoustic problems in unbounded domains

RESEARCH ARTICLE

WILEY

A subspace iteration eigensolver based on Cauchy integrals for vibroacoustic problems in unbounded domains

Suhaib Koji Baydoun[1] | **Matthias Voigt[2,3]** | **Benedikt Goderbauer[1]** | **Christopher Jelich[1]** | **Steffen Marburg[1]**

[1]Chair of Vibroacoustics of Vehicles and Machines, Technical University of Munich, Garching, Germany

[2]Fachbereich Mathematik, Bereich Optimierung und Approximation, Universität Hamburg, Hamburg, Germany

[3]Institut für Mathematik, Technische Universität Berlin, Berlin, Germany

Correspondence

Suhaib Koji Baydoun, Chair of Vibroacoustics of Vehicles and Machines, Technical University of Munich, Boltzmannstraße 15, 85748 Garching, Germany.
Email: suhaib.baydoun@tum.de

Abstract

Despite the potential and the increasing popularity of the boundary element method (BEM), modal analyses based on BEM are not yet put into engineering practice, mainly due to the lack of efficient solvers for the underlying nonlinear eigenvalue problem (EVP). In this article, we review a subspace iteration method based on FEAST for the solution of vibroacoustic EVPs involving the finite element method (FEM) and BEM. The subspace is obtained by applying a spectral projector and is computed by contour integration, whereas the contour is also used to subsequently solve the projected EVP by rational approximation. The computation of the projection matrices is addressed by two approaches. In the case of heavy fluid loading, we solve the underlying coupled linear systems by an iterative block Krylov method. In the case of light fluid loading, we exploit the fact that the coupled system admits accurate model order reduction solely based on the structural subsystem. Applications to a spherical shell and to a musical bell indicate that only a few contour points are required for an accurate solution without inducing spurious eigenvalues. The results are compared with those of a contour integral method and illustrate the efficiency of the proposed eigensolver.

KEYWORDS

boundary element method, FEAST, modal analysis, rational approximation, vibroacoustics

1 | INTRODUCTION

Vibroacoustics is a branch of physics dealing with oscillations of solid structures (vibrations) and mechanical waves in gases or liquids (acoustics). The study of vibroacoustics spans over various engineering disciplines often aiming at improving insulation and radiation characteristics of structures. For example, the mutual interaction between acoustics and elasticity is an essential aspect in the design process of phononic crystals[1] that are used to attenuate wave propagation in certain frequency bands. Our recent work has shown that acoustic loading can also have a significant effect on the dynamic properties of lightweight sandwich structures.[2] Moreover, it is crucial to consider these two physical phenomena simultaneously in numerical analysis, in order to enable meaningful comparisons to experiments,[3] which of course are conducted in a real multiphysics world.

Fully coupled numerical formulations describing the mutual interaction between structural vibrations and acoustic wave propagation are well established in the scientific literature[4,5] and appearing in commercial practice as well. The elastodynamic equations underlying the vibrating structure are typically discretized by the finite element method (FEM),[6] whereas several methods are available for addressing the surrounding, often unbounded acoustic domain. Here, we will consider the direct boundary element method (BEM) with a collocation discretization.[7] Compared with other strategies for modeling the acoustic field, BEM is particularly convenient in the case of unbounded domains. The discretization is restricted to the sound radiating surface and BEM does not require special boundary conditions for truncating the far-field sound radiation. Those advantages however come at the cost of an implicitly frequency-dependent kernel, which poses significant challenges when performing frequency sweep analyses or modal analyses.

In the case of frequency sweep analyses with BEM, the computational effort mainly stems from the assembly of coefficient matrices at each frequency point of interest along with the solution of the resulting sequence of linear systems. Early works on this topic focused on interpolating either the coefficient matrix,[8] the underlying kernel function,[9] or even the resulting response itself.[10] More recent work is concerned with efficient strategies for solving the sequence of linear systems by means of model order reduction[11-13] and greedy sampling.[14]

Along with frequency sweeps, modal analysis accounts for another fundamental tool to study the dynamical behavior and provides system-inherent properties such as eigenfrequencies and modal damping values. In the case of bounded acoustic domains, modal analyses based on FEM[15] or BEM with frequency-independent coefficient matrices[16,17] are well established. However, in the context of coupled structural exterior acoustic systems involving BEM, modal analyses require the solution of the underlying eigenvalue problem (EVP) that depends nonlinearly on the eigenvalue parameter. The solution of such nonlinear EVPs arising from frequency-dependent boundary element (BE) matrices dates back to the 1970s[18] and has since then drawn the attention of researchers from both mathematical and engineering communities. Despite the presence of this topic for nearly half a century and the growing number of boundary element software as well as eigensolver packages,[19] modal analyses based on BEM are not yet put into engineering practice. This hesitation may be largely attributed to the complicated choice of the adequate solver for the specific application at hand. For example in our case, an important distinction concerns the extent of fluid loading. Here, most papers focus on applications with heavy fluid loading[11,20,21] and address them by forming the Schur complement of the finite element (FE) submatrix with respect to the coupled system.[11,21] But in the case of light fluid loading, it may be more efficient and intuitive to form the Schur complement of the BE submatrix and treat the acoustic field as additional mass and damping contributions. Furthermore, most researchers rely on direct eigensolvers in order to avoid repeated assembly of frequency-dependent BE matrices. In the case of light fluid loading, iterative eigensolvers may actually be beneficial, since the in vacuo modes of such structures serve as a good initial guess and facilitate finding the wet (shifted) eigenfrequencies and modal damping values. The in vacuo modes may even be used a posteriori to check the occurrence of spurious eigenfrequencies.

The different approaches for solving nonlinear EVPs can be categorized into algorithms based on Newton's method, those based on polynomial and rational approximation[22] and methods based on contour integration.[23] The use of Newton's method is typically accompanied by deflation and hence requires subsequent computation of individual eigenpairs. Polynomial approximations are typically based on frequency sampling at Chebychev nodes[24] or truncated Taylor series.[20,25] When dealing with complex eigenvalues, the quality of these polynomial approximations quickly deteriorate when the eigenvalue lies apart from the real axis. Moreover, linerization of higher order polynomials induces numerical instabilities and thus precludes accurate computation of eigenpairs in large frequency ranges. Contour integral methods[21,26,27] account for another family of eigensolvers and are particularly appealing because of the low memory requirements and since the main computations can be executed in parallel. They essentially work by projecting the nonlinear EVP into a generalized EVP. However, the projection often leads to ill-conditioning[28] and results in spurious eigenvalues. Moreover, accurate projection via contour integration often requires a large number of integration points at which the BE matrices have to be explicitly assembled. Finally more recently, resolvent sampling based model order reduction has been employed for a Rayleigh–Ritz procedure.[11,29]

In this article, we extend two recent approaches—the nonlinear FEAST algorithm[30] and the linearization of rational approximations[31,32]—in order to solve structural acoustic EVPs with high accuracy and efficiency. The nonlinear FEAST (NLFEAST) is a generalization of the popular FEAST algorithm,[33] for which an open source library package[34] exists, and works by iteratively refining a projection matrix that is used for a Rayleigh–Ritz projection. However, the library package as well as the applications in the aforementioned paper[30] are limited to polynomial EVPs, leaving problems out of consideration that depend nonlinearly on the eigenvalue parameter. Structural acoustic EVPs fall into the latter category and—after projection by NLFEAST—still require solution of a nonlinear EVP. We address this issue by employing a rational approximation based on the Cauchy integral equation and subsequent linearization.[32] This enables us to simply reuse

the information for computing the projection matrix. Hence, the actual solution of the EVP comes at a negligible computational cost. Moreover, the same rational approximation is also used to avoid explicit assembly of the original system matrix at intermediate eigenvalues over the course of NLFEAST iterations. Finally, in order to enable fast computation of the projection matrix, we present two tailored approaches for solving the underlying coupled linear systems: In the case of heavy fluid loading, we form the Schur complement of the structural subsystem and employ an iterative block Krylov solver. In the case of light fluid loading, we form the Schur complement of the acoustic subsystem and employ an unilateral, frequency-independent model order reduction, which is computed solely based on the structural subsystem. The presented numerical framework enables efficient and accurate modal analysis of structural acoustic interaction without inducing spurious eigenfrequencies. Applications to an academic example of a spherical shell in water as well as a musical bell in air illustrate the performance of the method.

2 | COUPLED FINITE AND BOUNDARY ELEMENT METHODS FOR VIBRATION ANALYSIS IN UNBOUNDED ACOUSTIC DOMAINS

We consider time-harmonic problems involving a mutual interaction between structural vibrations and the surrounding acoustic field. The underlying equation of linear elasticity is addressed by FEM, resulting in the linear system

$$\left(\mathbf{K} - \omega^2 \mathbf{M}\right) \mathbf{u} = \mathbf{f}_\text{s} + \mathbf{f}_\text{f}. \tag{1}$$

Therein, $\mathbf{u} \in \mathbb{C}^{n_\text{s}}$ is a vector containing the n_s unknown displacement degrees of freedom (DOF). The angular frequency is defined as $\omega = 2\pi f$, where f is the frequency. The stiffness and mass matrices of the structure are denoted with $\mathbf{K}$, $\mathbf{M} \in \mathbb{R}^{n_\text{s} \times n_\text{s}}$. Structure-inherent damping is not considered in this work, but a damping matrix can be added to Equation (1) without affecting the further derivations. The structure is excited by external and fluid forces $\mathbf{f}_\text{s}, \mathbf{f}_\text{f} \in \mathbb{C}^{n_\text{s}}$ on the nodes. The latter act by virtue of the acoustic field which can be described by the Helmholtz equation. After a collocation discretization with BEM, the linear system of equations for the acoustic subdomain reads

$$\mathbf{H}(\omega)\mathbf{p} = \mathbf{G}(\omega)\mathbf{v}_\text{s} + \mathbf{p}_\text{i}, \tag{2}$$

where $\mathbf{p} \in \mathbb{C}^{n_\text{f}}$ is the vector containing the n_f unknown sound pressure DOFs. The BE matrices $\mathbf{H}(\omega), \mathbf{G}(\omega) \in \mathbb{C}^{n_\text{f} \times n_\text{f}}$ relate the structural particle velocity $\mathbf{v}_\text{s} \in \mathbb{C}^{n_\text{f}}$ to the sound pressure. Further, the acoustic field may be excited by a sound source with an incident pressure field $\mathbf{p}_\text{i} \in \mathbb{C}^{n_\text{f}}$. Quadrilateral boundary elements with discontinuous bilinear sound pressure interpolation are used in this work. Hence, neighboring boundary elements do not share their interpolation nodes.

Equations (1) and (2) are mutually coupled on the submerged surface of the structure. There, the structure is subject to normal tractions due to the acoustic sound pressure, and the particle velocity $\mathbf{v}_\text{s}$ equals the time derivative of the normal displacement on the boundary. Due to the use of discontinuous boundary elements, the interpolation nodes of the acoustic and structural subdomains do not coincide. Hence, the coupling conditions are reformulated in the weak sense. After discretization by the Bubnov–Galerkin approach, the coupling conditions can be expressed as[35]

$$\mathbf{f}_\text{f} = \mathbf{C}_\text{sf}\mathbf{p} \quad \text{and} \quad \mathbf{v}_\text{s} = -\mathrm{i}\omega\mathbf{C}_\text{fs}\mathbf{u}, \tag{3}$$

where $\mathbf{C}_\text{sf} \in \mathbb{R}^{n_\text{s} \times n_\text{f}}$ and $\mathbf{C}_\text{fs} \in \mathbb{R}^{n_\text{f} \times n_\text{s}}$ are the mesh coupling matrices that relate the displacement and pressure DOFs, and i denotes the imaginary unit. Combining Equations (1) to (3) yields the fully coupled linear system

$$\underbrace{\begin{bmatrix} \mathbf{K} - \omega^2 \mathbf{M} & -\mathbf{C}_\text{sf} \\ \mathrm{i}\omega\mathbf{G}(\omega)\mathbf{C}_\text{fs} & \mathbf{H}(\omega) \end{bmatrix}}_{\mathbf{L}(\omega)} \begin{bmatrix} \mathbf{u} \\ \mathbf{p} \end{bmatrix} = \begin{bmatrix} \mathbf{f}_\text{s} \\ \mathbf{p}_\text{i} \end{bmatrix}. \tag{4}$$

By forming the Schur complement of $\mathbf{H}(\omega)$ with respect to $\mathbf{L}(\omega)$ and thereby eliminating the pressure DOFs from Equation (4), we obtain a structural equation that includes the effect of acoustic loading,[20] that is,

$$\left[\mathbf{K} - \omega^2 \mathbf{M} + \mathrm{i}\omega\mathbf{C}_\text{sf}\mathbf{H}^{-1}(\omega)\mathbf{G}(\omega)\mathbf{C}_\text{fs}\right] \mathbf{u} = \mathbf{f}_\text{s} + \mathbf{C}_\text{sf}\mathbf{H}^{-1}(\omega)\mathbf{p}_\text{i}, \tag{5}$$

in which $i\omega\mathbf{C}_{sf}\mathbf{H}^{-1}(\omega)\mathbf{G}(\omega)\mathbf{C}_{fs}$ can be interpreted as the additional mass and damping contributions due to the acoustic field. The excitation on the right-hand side of Equation (5) comprises structural loading $\mathbf{f}_s$ as well as acoustic loading by virtue of the incident pressure field $\mathbf{p}_i$. Alternatively, the displacement DOFs can be eliminated from Equation (4) by forming the Schur complement of $\mathbf{K} - \omega^2\mathbf{M}$ with respect to $\mathbf{L}(\omega)$, which yields

$$\left[i\omega\mathbf{G}(\omega)\mathbf{C}_{fs}\left(\mathbf{K} - \omega^2\mathbf{M}\right)^{-1}\mathbf{C}_{sf} + \mathbf{H}(\omega)\right]\mathbf{p} = -i\omega\mathbf{G}(\omega)\mathbf{C}_{fs}\left(\mathbf{K} - \omega^2\mathbf{M}\right)^{-1}\mathbf{f}_s + \mathbf{p}_i. \tag{6}$$

Equation (6) can be interpreted as an acoustic equation incorporating the elasticity of the structure as admittance boundary condition.[36] By setting the right-hand sides of Equations (5) and (6) to zero, we obtain the structural acoustic EVPs

$$\left[\mathbf{K} - \tilde{\omega}^2\mathbf{M} + i\tilde{\omega}\mathbf{C}_{sf}\mathbf{H}^{-1}(\tilde{\omega})\mathbf{G}(\tilde{\omega})\mathbf{C}_{fs}\right]\boldsymbol{\psi} = \mathbf{0} \quad \text{and} \tag{7}$$

$$\left[i\tilde{\omega}\mathbf{G}(\tilde{\omega})\mathbf{C}_{fs}\left(\mathbf{K} - \tilde{\omega}^2\mathbf{M}\right)^{-1}\mathbf{C}_{sf} + \mathbf{H}(\tilde{\omega})\right]\boldsymbol{\phi} = \mathbf{0}, \tag{8}$$

respectively. The nonzero vectors $\boldsymbol{\psi}$ and $\boldsymbol{\phi}$ are the displacement and pressure modes, respectively. The EVPs in Equations (7) and (8) are nonlinear, since the BE matrices $\mathbf{H}(\tilde{\omega})$ and $\mathbf{G}(\tilde{\omega})$ implicitly depend on the complex eigenvalue parameter $\tilde{\omega}$. The real part of $\tilde{\omega}$ corresponds to the eigenfrequency and the imaginary part is associated with modal radiation damping. It is well known that if the matrix $\mathbf{H}(\tilde{\omega})$ is invertible, then $\tilde{\omega}$ is an eigenvalue of $\mathbf{L}(\tilde{\omega})$ if and only if $\tilde{\omega}$ is an eigenvalue of Equation (7). Similarly, if $\mathbf{K} - \tilde{\omega}^2\mathbf{M}$ is invertible, then $\tilde{\omega}$ is an eigenvalue of $\mathbf{L}(\tilde{\omega})$ if and only if $\tilde{\omega}$ is an eigenvalue of Equation (8). Furthermore, the nonzero vectors θ with $\mathbf{L}(\tilde{\omega})\theta = \mathbf{0}$ can be related with the eigenvectors $\boldsymbol{\psi}$ and $\boldsymbol{\phi}$, respectively.[37]

Both EVP formulations (7) and (8) have been considered in the literature,[2,11,20,21] but the proper choice between them has not yet been discussed in a comprehensive manner. Most researchers focus on applications with heavy fluid loading and address them by Equation (8). The linear systems that arise over the course of solving Equation (8) can be addressed by an iterative method once a factorization of the sparse and symmetric matrix $\mathbf{K} - \tilde{\omega}^2\mathbf{M}$ is computed. On the other hand, in the case of light fluid loading, it is more intuitive to form the Schur complement of the BE submatrix and treat the acoustic field as additional mass and damping contributions. Moreover, we will later see that the use of Equation (7) admits efficient unilateral model order reduction in the case of light fluid loading. We will consider both formulations (7) and (8) in the following and provide tailored solution schemes for both of them.

3 | FEAST FOR NONLINEAR STRUCTURAL ACOUSTIC EIGENVALUE PROBLEMS

Introduced in the context of linear EVPs, the original FEAST algorithm[33,38] essentially is a subspace iteration method which uses a Rayleigh–Ritz procedure in each iteration, that is,

$$\mathbf{A}_r = \mathbf{Q}^H\mathbf{A}\mathbf{Q}, \tag{9}$$

where $\mathbf{A}$ is the matrix of interest, $\mathbf{Q}$ is the complex-valued projection matrix, and $(\cdot)^H$ denotes the Hermitian transpose. The reduced matrix $\mathbf{A}_r$ contains some approximate eigenvalues of $\mathbf{A}$. Those eigenvalues are obtained by solving the EVP $\mathbf{A}_r\mathbf{X}_r = \Lambda\mathbf{X}_r$, and the approximate eigenvectors are retrieved from $\mathbf{X} = \mathbf{Q}\mathbf{X}_r$. Different from, for example, the Arnoldi algorithm which uses Krylov subspaces for $\mathbf{Q}$, FEAST constructs a subspace of fixed dimension by applying a spectral projector $\rho(\mathbf{A})$ to the desired eigenvectors. The spectral projection is accomplished by a Cauchy integral representation of the resolvent of $\mathbf{A}$, yielding the complex contour integration

$$\mathbf{Q} = \rho(\mathbf{A})\mathbf{X} = \frac{1}{2\pi i}\oint_C (z\mathbf{I} - \mathbf{A})^{-1}dz\,\mathbf{X}, \tag{10}$$

where $\mathbf{I}$ is the identity matrix. The shift z is defined along the contour C—a user-defined Jordan curve in the complex plane. Hence, FEAST yields the eigenvalues and corresponding eigenvectors lying in the domain $\mathcal{D}$ that is enclosed by C, see Figure 1. The numerical effort of FEAST is determined by the accuracy of the integration in Equation (10), that is,

the number of discrete integration points. The computation of the integrand at the individual integration points can be executed in parallel.

Gavin et al.[30] have recently provided another interpretation of the original FEAST algorithm by mentioning that it is essentially a generalized shift-and-invert iteration. Standard shift-and-invert iteration uses a single shift z, whereas the contour integration in Equation (10) corresponds to using multiple shifts simultaneously. Inspired by this, Gavin et al.[30] have proposed a nonlinear version of FEAST (NLFEAST) which in turn is a generalization of the residual inverse iteration.[39] Again, contour integration is used in NLFEAST to handle multiple shifts efficiently. However, the authors limit their applications to quadratic EVPs leaving open the application to analytic matrix functions that depend nonlinearly on the eigenvalue parameter. The next section briefly reviews the NLFEAST algorithm, whereafter Sections 3.2 to 3.4 present our contribution toward an accurate and efficient application to structural acoustic problems that depend nonlinearly on the eigenfrequency.

3.1 | General outline of the nonlinear FEAST algorithm

The nonlinear EVPs (7) and (8) are replaced by $\mathbf{T}(\tilde{\omega})\mathbf{x} = \mathbf{0}$, $\mathbf{T}(\tilde{\omega}) \in \mathbb{C}^{n \times n}$, $\mathbf{x} \in \mathbb{C}^n$ for the sake of readability. We are interested in a given number of eigenpairs $(\tilde{\omega}, \mathbf{x})$ whose eigenvalues $\tilde{\omega}$ lie in a predefined region $\mathcal{D}$ that is enclosed by a contour $\mathcal{C}$ in the complex plane. Since the imaginary parts of the complex eigenvalues—which correspond to radiation damping—are typically small, we use elliptic contours that have their major axis aligned with the real axis. The intersections of the ellipse with the real axis are the lower and upper bounds $[f_{\min}, f_{\max}]$ of the frequency range of interest. An exemplary ellipse is shown in Figure 1 and is expressed by

$$z(\theta) = \gamma + \delta(\cos\theta + \mathrm{i}\zeta\sin\theta), \quad \theta \in [0, 2\pi), \tag{11}$$

where $\gamma = (f_{\max} + f_{\min})/2$, $\delta = (f_{\max} - f_{\min})/2$ and $0 \le \zeta \le 1$.

Similar to its linear counterpart in Equation (9), NLFEAST uses a Rayleigh–Ritz projection to reduce the system dimension in each iteration. The resulting projected EVP

$$\mathbf{Q}^{\mathrm{H}}\mathbf{T}(\tilde{\omega})\mathbf{Q}\mathbf{y} = \mathbf{0}, \quad \mathbf{Q} \in \mathbb{C}^{n \times m}, \quad \mathbf{y} \in \mathbb{C}^m \tag{12}$$

is still nonlinear but of significantly reduced dimension $m \ll n$. The subspace dimension m is fixed throughout the iterations and should be at least as large as the number of expected eigenvalues inside $\mathcal{D}$ to ensure that all desired eigenvalues are captured. In our case, the number of eigenvalues can be either estimated a priori by an empirical formula,[40] or by a preceding in vacuo analysis—that is, by solving the linear EVP $\left(\mathbf{K} - \tilde{\omega}_{\mathrm{dry}}^2\mathbf{M}\right)\boldsymbol{\psi}_{\mathrm{dry}} = \mathbf{0}$.

Once Equation (12) is solved, the m eigenvalues lying closest to the center of $\mathcal{D}$ are determined by evaluating the scaled distance

$$d = (\mathrm{Re}(\tilde{\omega}) - \gamma)^2 + (\mathrm{Im}(\tilde{\omega})/\zeta)^2. \tag{13}$$

Those eigenvalues $\tilde{\omega}_1, \ldots, \tilde{\omega}_m$ and associated eigenvectors $\mathbf{y}_1, \ldots, \mathbf{y}_m$ are stored in $\boldsymbol{\Omega} = \mathrm{diag}(\tilde{\omega}_1, \ldots, \tilde{\omega}_m)$, $\boldsymbol{\Omega} \in \mathbb{C}^{m \times m}$ and $\mathbf{X} = [\mathbf{Q}\mathbf{y}_1, \ldots, \mathbf{Q}\mathbf{y}_m]$, $\mathbf{X} \in \mathbb{C}^{n \times m}$, respectively. They are used to update the search subspace $\mathbf{Q}$ via

$$\mathbf{Q} := \frac{1}{2\pi\mathrm{i}} \oint_{\mathcal{C}} \left(\mathbf{X} - \mathbf{T}^{-1}(z)\mathbf{B}\right)(z\mathbf{I}_m - \boldsymbol{\Omega})^{-1}\mathrm{d}z, \tag{14}$$
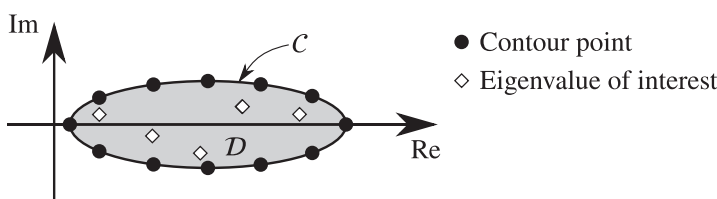

FIGURE 1 Elliptic contour $\mathcal{C}$ enclosing a complex domain $\mathcal{D}$, in which the desired eigenvalues lie

in which the residual matrix $\mathbf{B} \in \mathbb{C}^{n \times m}$ is obtained by

$$\mathbf{B} = \begin{bmatrix} \mathbf{T}(\tilde{\omega}_1)\mathbf{Q}\mathbf{y}_1, & \dots, & \mathbf{T}(\tilde{\omega}_m)\mathbf{Q}\mathbf{y}_m \end{bmatrix}. \tag{15}$$

The integrand in Equation (14) corresponds to the update rule for eigenvectors in the residual inverse iteration method with multiple shifts.[30,39] Its Cauchy integral representation (14) then yields an approximate spectral projection onto the eigenspace corresponding to the eigenvalues in $\mathcal{D}$.

With the definition of the contour (11) at hand, the integral can be evaluated using the trapezoidal rule, that is,

$$\mathbf{Q} := \sum_{j=1}^{N} w_j \left(\mathbf{X} - \mathbf{T}^{-1}(z_j)\mathbf{B} \right) \left(z_j \mathbf{I}_m - \mathbf{\Omega} \right)^{-1}, \tag{16}$$

where N denotes the number of integration points on the contour (cf. Figure 1). For an elliptic contour, the integration points and weights can, for example, be chosen as

$$z_j = \gamma + \delta \left(\cos\left(2\pi j/N\right) + \mathrm{i}\zeta \, \sin\left(2\pi j/N\right) \right), \quad j = 1, \dots, N \quad \text{and} \tag{17}$$

$$w_j = \frac{\delta}{N} \left(\zeta \, \cos\left(2\pi j/N\right) + \mathrm{i} \, \sin\left(2\pi j/N\right) \right), \quad j = 1, \dots, N. \tag{18}$$

The general procedure for solving structural acoustic EVPs with NLFEAST is summarized in Algorithm 1. Convergence of the algorithm is monitored by evaluating the maximum residual among the eigenpairs whose eigenvalues lie inside the contour, that is,

$$\varepsilon_{\max} = \max_{\tilde{\omega}_i \in \mathcal{D}} \frac{\|\mathbf{T}(\tilde{\omega}_i)\mathbf{Q}\mathbf{y}_i\|_2}{\|\mathbf{Q}\mathbf{y}_i\|_2}. \tag{19}$$

Alternatively, the accuracy of an eigenpair can be assessed by computing the relative residual by, for example,

$$\varepsilon_{\mathrm{rel},i} = \frac{\|\mathbf{T}(\tilde{\omega}_i)\mathbf{Q}\mathbf{y}_i\|_2}{\|\mathbf{T}(\tilde{\omega}_i)\|_1 \|\mathbf{Q}\mathbf{y}_i\|_2}, \tag{20}$$

which requires estimating the 1-norm of the system matrix.[41] Other matrix norms are also possible such as the $\infty-$ or Frobenius norm. Once the residual stagnates, the algorithm is terminated. If the accuracy is then deemed to be insufficient, the whole procedure can be repeated with the computed eigenvectors as new initial guess and by incorporating a more accurate solution strategy for the projected EVP in Equation (12). The latter is discussed in Section 3.3, where we will see that the accuracy can be increased while retaining information from the previous run.

The rate of convergence of the algorithm is mainly driven by the accuracy of the numerical integration in line 15, and thus by the number of contour points N. On the other hand, N also determines the number of linear systems $\mathbf{T}(z_j)\mathbf{Y} = \mathbf{B}$ that need to be solved in each iteration in line 15 accounting for the main computational effort. When the computations for each contour point are executed in parallel, N could be chosen according to the number of available computing nodes. The BE matrices associated with $\mathbf{T}(z_j)$ are stored in memory in order to avoid re-assembly in each iteration. In this respect, the use of data-sparse formats[42] or model order reduction of BE matrices[12] can alleviate the memory requirements. The initial guess of eigenvectors $\mathbf{X}^{(0)} \in \mathbb{C}^{n \times m}$ can either be random, or in the case of moderately strong structural acoustic interaction, $\mathbf{X}^{(0)}$ can be chosen as the in vacuo modes of the structure. If one is then interested in the complex eigenfrequencies corresponding to those particular modes, the eigenvalue selection in lines 10 and 18 could be made based on a modal assurance criterion.[43]

Regarding the computational efficiency, several issues need to addressed when applying Algorithm 1 to structural acoustic EVPs (7) and (8):

- Firstly, the repeated evaluation of the residuals in Equation (15) requires assembling the frequency-dependent BE matrices at m eigenvalues in each iteration.
- Secondly, the projected EVP in Equation (12) is still nonlinear and requires a tailored solution scheme.
- Lastly, an efficient solver for linear systems $\mathbf{T}(z_j)\mathbf{Y} = \mathbf{B}$ with multiple right-hand sides is required. This is particularly important since a factorization of the coupled system matrices in Equations (5) and (6) is generally not feasible.

Algorithm 1. NLFEAST for structural acoustic eigenvalue problems

1: **input**
2:     complex domain $\mathcal{D}$ enclosed by elliptic contour $\mathcal{C}$ as given by Eq. (11)
3:     number of contour points N
4:     system matrices $\mathbf{T}(z_j)$ at contour points $z_j, j = 1, \dots, N$
5:     initial (possibly random) guess for eigenvectors $\mathbf{X}^{(0)}$
6: **initialization**
7:     $\mathbf{Q} := \mathbf{X}^{(0)}$
8:     orthonormalize columns of $\mathbf{Q}$
9:     solve $\mathbf{Q}^H \mathbf{T}(\tilde{\omega}) \mathbf{Q} \mathbf{y} = \mathbf{0}$ for eigenpairs $(\tilde{\omega}_i, \mathbf{y}_i)$
10:     select m eigenvalues $\tilde{\omega}_1, \dots, \tilde{\omega}_m$ closest to the center of $\mathcal{D}$ by evaluating Eq. (13)
11:     $\mathbf{\Omega} := \mathrm{diag}\,(\tilde{\omega}_1, ..., \tilde{\omega}_m)$
12:     $\mathbf{X} := [\mathbf{Q}\mathbf{y}_1, \dots, \mathbf{Q}\mathbf{y}_m]$
13:     $\mathbf{B} := [\mathbf{T}(\tilde{\omega}_1)\mathbf{Q}\mathbf{y}_1, \dots, \mathbf{T}(\tilde{\omega}_m)\mathbf{Q}\mathbf{y}_m]$
14: **while** $\max\limits_{\tilde{\omega}_i \in \mathcal{D}} \|\mathbf{T}(\tilde{\omega}_i)\mathbf{Q}\mathbf{y}_i\|_2 / \|\mathbf{Q}\mathbf{y}_i\|_2$ has not stagnated **do**
15:     $\mathbf{Q} := \sum_{j=1}^{N} w_j \left(\mathbf{X} - \mathbf{T}^{-1}(z_j)\mathbf{B} \right) \left(z_j \mathbf{I}_m - \mathbf{\Omega} \right)^{-1}$
16:     orthonormalize columns of $\mathbf{Q}$
17:     solve $\mathbf{Q}^H \mathbf{T}(\tilde{\omega}) \mathbf{Q} \mathbf{y} = \mathbf{0}$ for eigenpairs $(\tilde{\omega}_i, \mathbf{y}_i)$
18:     select m eigenvalues $\tilde{\omega}_1, \dots, \tilde{\omega}_m$ closest to the center of $\mathcal{D}$ by evaluating Eq. (13)
19:     $\mathbf{\Omega} := \mathrm{diag}\,(\tilde{\omega}_1, ..., \tilde{\omega}_m)$
20:     $\mathbf{X} := [\mathbf{Q}\mathbf{y}_1, \dots, \mathbf{Q}\mathbf{y}_m]$
21:     $\mathbf{B} := [\mathbf{T}(\tilde{\omega}_1)\mathbf{Q}\mathbf{y}_1, \dots, \mathbf{T}(\tilde{\omega}_m)\mathbf{Q}\mathbf{y}_m]$
22: **output**
23:     eigenvalues $\tilde{\omega}_i \in \mathcal{D}$ and associated eigenvectors $\mathbf{Q}\mathbf{y}_i$

The next subsections present remedies for those three aspects, thereby enabling efficient application of Algorithm 1 to large-scale structural acoustic EVPs.

3.2 | Rational approximation of frequency-dependent boundary element matrices

The repeated evaluation of the residuals in Equation (15) deteriorates the numerical efficiency of NLFEAST when the frequency-dependent BE matrices $\mathbf{H}(\tilde{\omega})$ and $\mathbf{G}(\tilde{\omega})$ are assembled explicitly for all intermediate (not yet converged) eigenvalues in each iteration. Several approaches for accelerating the setup of BE matrices have been proposed in the literature.[8] Typically, polynomial approximations based on frequency sampling at Chebychev nodes[24] or truncated Taylor series[20] are employed in this regard. However when evaluating at complex eigenvalues $\tilde{\omega}$ that lie apart from the real axis, the quality of those polynomial approximations quickly deteriorates.

Therefore, we will use a Cauchy integral representation of the BE matrices which—after discretization with the trapezoidal rule—yields a rational approximation. For a detailed discussion on different approximations inside complex regions, we refer to the review by Austin et al.[44] The approximate BE matrices read

$$\mathbf{H}(\tilde{\omega}) \approx \sum_{j=1}^{N} \mathbf{H}(z_j) v_j(\tilde{\omega}) \quad \text{and} \quad \mathbf{G}(\tilde{\omega}) \approx \sum_{j=1}^{N} \mathbf{G}(z_j) v_j(\tilde{\omega}), \tag{21}$$

where the scalar-valued rational functions v_j are given by

$$v_j(\tilde{\omega}) = \frac{w_j}{z_j - \tilde{\omega}} \left(\sum_{k=1}^{N} \frac{w_k}{z_k - \tilde{\omega}} \right)^{-1}. \tag{22}$$

The error introduced by these rational approximations depends on the fluctuation of the entries of $\mathbf{H}(\tilde{\omega})$ and $\mathbf{G}(\tilde{\omega})$ with respect to the frequency. For example, the relative error in $\mathbf{H}(\tilde{\omega})$ can be assessed by

$$\varepsilon_{\mathbf{H}}(\tilde{\omega}) = \frac{\|\mathbf{H}(\tilde{\omega}) - \sum_{j=1}^{N} \mathbf{H}(z_j)v_j(\tilde{\omega})\|_{\mathrm{F}}}{\|\mathbf{H}(\tilde{\omega})\|_{\mathrm{F}}}, \tag{23}$$

where $\| \cdot \|_{\mathrm{F}}$ denotes the Frobenius norm. However, an evaluation of Equation (23) is generally not feasible and an alternative way is required for assessing the approximations given in Equations (21) and (22). For this purpose, we first notice that the frequency dependence of a BE matrix entry can be generally characterized by a product of a monomial and an exponential function,[45] that is,

$$h(\tilde{\omega}) = \tilde{\omega}^p e^{\mathrm{i}r\tilde{\omega}/c}, \tag{24}$$

with the speed of sound c and the nonnegative integer exponent p. Given the frequency dependence of the single and double layer potential in the collocation BE formulation, $p = 1$ is a suitable choice. Further, the spatial distance r should be chosen as the largest distance between two points on the discretized boundary. Then, an error estimate can be obtained from

$$\varepsilon_h(\tilde{\omega}) = \frac{|h(\tilde{\omega}) - \sum_{j=1}^{N} h(z_j)v_j(\tilde{\omega})|}{|h(\tilde{\omega})|}. \tag{25}$$

In practice, $\varepsilon_h(\tilde{\omega})$ could be probed at a few points inside the complex domain $\mathcal{D}$ and the number of contour points N could be increased until an acceptable accuracy is achieved. We will see in Section 4.1 that an error estimate based on Equation (25) is in reasonable accordance with the relative error given by Equation (23).

For the convenient choice of using the same elliptic contour for the rational approximation as for the computation of the search subspace in Equation (16), the setup of the rational approximation does not require any additional numerical effort. The BE matrices $\mathbf{H}(z_j)$ and $\mathbf{G}(z_j)$ are readily available and the contour points z_j and associated weights w_j are identical to those in Equations (17) and (18). In this case, Equation (16) is a trapezoidal rule approximation of the Cauchy integral representation of eigenfunctions, which in turn includes BE matrices with the same underlying trapezoidal rule approximation. Therefore, we expect that the approximation of BE matrices do not further impair the convergence rate of NLFEAST nor the accuracy of the final eigenpairs. Finally, we note that some intermediate eigenvalues may also lie outside of the contour, particularly in the first couple of iterations of NLFEAST. Although the rational approximations (21) yield exponential convergence only inside the contour,[46] they are still used in these cases to evaluate the residual (15).

3.3 | Solution of the projected nonlinear eigenvalue problem

A tailored procedure for solving the projected (but still nonlinear) EVP (12) is crucial, since it determines the final accuracy of the eigenpairs obtained by NLFEAST. The dimension of the EVP (12) is rather small, and hence it would admit the application of various nonlinear eigensolvers for dense systems that are available in the mathematical literature.[47,48] However, with regard to computational efficiency, we would favor an eigensolver that requires minimal additional effort in each NLFEAST iteration and in particular, avoids repeated assembly of the original system matrix. In this respect, an obvious choice would be to simply employ a rational approximation as has already been done for the acceleration of the residual computation in Equation (15). However, instead of only approximating the BE matrices as given in Equation (21), an approximation of the entire coupled system matrix $\mathbf{T}(\tilde{\omega})$ is necessary in order to obtain a rational EVP that can be subsequently linearized. The rational approximation of the projected EVP (12) is obtained by quadrature of the Cauchy integral representation of $\mathbf{Q}^{\mathrm{H}}\mathbf{T}(\tilde{\omega})\mathbf{Q}$ and reads

$$\sum_{j=1}^{N_{\mathrm{p}}} \left(\mathbf{Q}^{\mathrm{H}}\mathbf{T}(\hat{z}_j)\mathbf{Q} \frac{w_j}{\hat{z}_j - \tilde{\omega}} \right) \mathbf{y} = \mathbf{0}, \tag{26}$$

where N_{p} denotes the number of quadrature points. Again, for the convenient choice of the same underlying elliptic contour and trapezoidal rule as for the computation of the projection matrix in NLFEAST, $N_{\mathrm{p}} = N$ holds. In that case,

the quadrature points for the rational approximation of the EVP are identical to the contour points in Equation (17) (i.e., $\hat{z}_j = z_j$), and the BE matrices at the contour points can be reused.

For solving the rational EVP (26), we follow the approach of El-Guide et al.[32] and reformulate the problem as a generalized EVP

$$\mathcal{A}\mathbf{w} = \lambda \mathcal{M}\mathbf{w} \tag{27}$$

with identical eigenvalues $\tilde{\omega} = \lambda$. The block matrices in Equation (27) are defined as

$$\mathcal{A} = \begin{bmatrix} \hat{z}_1 \mathbf{I}_m & & & & \mathbf{I}_m \\ & \hat{z}_2 \mathbf{I}_m & & & \mathbf{I}_m \\ & & \ddots & & \vdots \\ & & & \hat{z}_{N_p} \mathbf{I}_m & \mathbf{I}_m \\ -\hat{\mathbf{T}}_1 & -\hat{\mathbf{T}}_2 & \ldots & -\hat{\mathbf{T}}_{N_p} & \mathbf{0} \end{bmatrix}, \quad \mathcal{M} = \begin{bmatrix} \mathbf{I}_m & & & & \\ & \mathbf{I}_m & & & \\ & & \ddots & & \\ & & & \mathbf{I}_m & \\ & & & & \mathbf{0} \end{bmatrix}, \tag{28}$$

where $\hat{\mathbf{T}}_j = \mathbf{Q}^H \mathbf{T}(\hat{z}_j)\mathbf{Q}w_j$. The eigenvector of interest $\mathbf{y}$ is retrieved from

$$\mathbf{w} = \begin{bmatrix} \mathbf{v}_1^T, & \ldots, & \mathbf{v}_{N_p}^T, & \mathbf{y}^T \end{bmatrix}^T, \quad \mathbf{v}_j = \frac{\mathbf{y}}{\hat{z}_j - \tilde{\omega}}. \tag{29}$$

The main issue with the linearization of EVPs is the significant increase of the system dimension. El-Guide et al.[32] address this issue by subspace iteration in which the columns of the projection matrix are individually computed by inverse power iteration. In our case, the inflation of the EVP associated with the linearization is mitigated by the projection (12), where the projection matrix (16) and the rational approximation of the EVP (26) can be based on the same contour points. The computational effort for solving the linearized EVP is reduced to an order of $\mathcal{O}\left((mN_p)^3\right)$. We will later see that a small number N_p is sufficient to achieve a high accuracy and hence, the solution of the reduced nonlinear EVP in Equation (12) only marginally contributes to the overall computational time for the NLFEAST algorithm. Lastly, we note that the final accuracy of the eigenpairs could be improved by adaptively increasing N_p in subsequent runs of NLFEAST by adding new quadrature points $\hat{z}_j$ in-between the previous ones.

3.4 | Efficient solution of coupled systems with multiple right-hand sides

The main computational effort of the NLFEAST algorithm stems from the solution of the N linear systems

$$\mathbf{T}(z_j)\mathbf{Y}_j = \mathbf{B}, \quad j = 1, \ldots, N, \tag{30}$$

in each iteration in order to update the projection matrix via Equation (16). For a discussion on efficient solution strategies for Equation (30), we need to distinguish between the two structural acoustic formulations given by Equations (7) and (8). When forming the Schur complement of $\mathbf{K} - z_j^2 \mathbf{M}$ with respect to coupled block matrix in (4), the system matrices read

$$\mathbf{T}(z_j) = \mathrm{i}z_j \mathbf{G}(z_j)\mathbf{C}_{\mathrm{fs}}\left(\mathbf{K} - z_j^2 \mathbf{M}\right)^{-1}\mathbf{C}_{\mathrm{sf}} + \mathbf{H}(z_j), \tag{31}$$

whereas using the Schur complement of $\mathbf{H}(z_j)$ yields

$$\mathbf{T}(z_j) = \mathbf{K} - z_j^2 \mathbf{M} + \mathrm{i}z_j \mathbf{C}_{\mathrm{sf}} \mathbf{H}^{-1}(z_j)\mathbf{G}(z_j)\mathbf{C}_{\mathrm{fs}}. \tag{32}$$

The system in Equation (31) admits efficient application of an iterative solver to Equation (30) once a factorization of the sparse and symmetric matrix $\mathbf{K} - z_j^2 \mathbf{M}$ is stored. Linear systems with multiple right-hand sides such as Equation (30) are usually solved by successively applying standard iterative schemes to obtain the solutions to each forcing vector individually. More efficient approaches such as subspace recycling[49] or block Krylov solvers[50] enable to carry over information

among the solutions to different forcing vectors. In this work, we will employ a block variant of the generalized minimal residual (GMRes) method.[51,52] While block Krylov solvers have been successfully applied to acoustic BE equations,[53] to the best of our knowledge, the present contribution is the first application to coupled structural acoustic systems with multiple right-hand sides.

Block Krylov solvers generally work by refining the solution $\mathbf{Y}_k$ in each iteration k such that

$$\mathbf{Y}_k - \mathbf{Y}_0 \in \mathcal{K}_k\left(\mathbf{T}(z_j), \mathbf{R}_0\right) \tag{33}$$

holds, where $\mathbf{Y}_0$ and $\mathbf{R}_0 = \mathbf{B} - \mathbf{T}(z_j)\mathbf{Y}_0$ denote the initial guess and the corresponding initial residual, respectively. The block Krylov subspace $\mathcal{K}_k$ is given by

$$\mathcal{K}_k\left(\mathbf{T}(z_j), \mathbf{R}_0\right) = Range\begin{bmatrix} \mathbf{R}_0 & \mathbf{T}(z_j)\mathbf{R}_0 & \dots & \mathbf{T}(z_j)^{k-1}\mathbf{R}_0 \end{bmatrix}. \tag{34}$$

In the case of block GMRes, the orthonormal basis vectors spanning the subspace $\mathcal{K}_k$ are computed via a block Arnoldi process. The resulting block subspace is of much larger dimension compared with the subspace in standard GMRes, and hence a faster convergence can be expected.

Having discussed the solution when using the formulation (31), we now turn our attention to the Schur complement of the acoustic subsystem in Equation (32). Here, an iterative solution would require evaluation of $\mathbf{H}^{-1}(z_j)\mathbf{G}(z_j)\mathbf{C}_{\mathrm{fs}}\mathbf{Y}_j^{(k)}$ in each iteration k. In order to avoid two nested iterations, we employ a model order reduction[54] to the frequency-independent structural subsystem and thereby enable a direct solution of Equation (30). The reduced system (32) reads

$$\mathbf{T}_{\mathrm{r}}(z_j) = \mathbf{V}^{\mathrm{T}}\left[\mathbf{K} - z_j^2\mathbf{M} + \mathrm{i}z_j\mathbf{C}_{\mathrm{sf}}\mathbf{H}^{-1}(z_j)\mathbf{G}(z_j)\mathbf{C}_{\mathrm{fs}}\right]\mathbf{V}, \tag{35}$$

in which $\mathbf{V} \in \mathbb{R}^{n_s \times q}$ could be a Krylov subspace or spanned by the in vacuo modes of the structure. In this work, we choose a Krylov basis, which is computed once for the whole frequency range of interest.[55] Once the Krylov basis is established, the reduced system $\mathbf{T}_{\mathrm{r}}(z_j)$ can be explicitly formed by evaluating $\mathbf{H}^{-1}(z_j)\mathbf{G}(z_j)\mathbf{C}_{\mathrm{fs}}\mathbf{V}$ using the above described block GMRes. The N reduced matrices $\mathbf{T}_{\mathrm{r}}(z_j)$ can be saved and reused in all subsequent NLFEAST iterations. Hence, the computational effort of solving the high-fidelity system in Equation (30) in each iteration boils down to the effort of computing $\mathbf{V}$ and reducing the coupled system matrices at each contour point only once via Equation (35). The actual solution in each iteration requires negligible computational effort. The memory requirements to store the system matrices are reduced as well.

4 | FIRST NUMERICAL EXAMPLE: MODAL ANALYSIS OF A SUBMERGED SPHERICAL SHELL

As a first example, we consider a spherical shell submerged in water. Its geometrical and material parameters are listed in Table 1. A finite element mesh with 864 eight-noded quadrilateral finite elements based on the Reissner Mindlin theory is used to discretize the sphere. This corresponds to twelve elements on a $\pi/2$ arc and 15,564 displacement DOFs. The acoustic field is represented by a conforming BE mesh with discontinuous bilinear interpolation functions and 3456 pressure DOFs. We first illustrate the application of NLFEAST to perform a modal analysis in Section 4.1, and then compare the performance to a contour integral method in Section 4.2.

4.1 | Eigenvalue solution using NLFEAST

In this section, we use NLFEAST to compute the eigenpairs of the submerged sphere in the frequency range from $f_{\min} = 34$ Hz to $f_{\max} = 82$ Hz. As illustrated in Figure 2, these frequency bounds are used to define the elliptic contour. A treatment for the nonuniqueness problem in BEM is not required in this frequency range, but would be needed above the first interior Dirichlet eigenfrequency of approximately 148 Hz. The Burton–Miller formulation[56] would resolve this issue, however care has to be taken since the spurious eigenfrequencies are not eliminated altogether but only moved away from the real axis.[57] They could be distinguished from the actual ones based on the sign of the imaginary parts, given a

proper choice of the coupling parameter in the Burton–Miller formulation.[58] Based on the analytical solution,[59] we expect three distinct eigenvalues in the considered frequency range with geometric multiplicities of five, seven, and nine, respectively. The aspect ratio of the elliptic contour is set to $\zeta = 0.05$. The dimension of the search space in NLFEAST is set to $m = 21$, which is sufficient to capture all eigenvalues. The initial eigenvectors $\mathbf{X}^{(0)}$ are chosen randomly. The convergence criterion for block GMRes is defined such that relative residuals smaller than $\varepsilon_{\text{gmres}} = 10^{-12}$ are achieved for all right-hand sides. In this example, we use the Schur complement of the structural subsystem resulting in the EVP formulation given by Equation (8).

Figure 3 displays the convergence behavior of NLFEAST for different numbers of contour points N, and a fixed number of $N_{\text{p}} = 16$ for the solution of the projected EVP (26) by rational approximation. The accuracy is assessed by the maximum residual defined in Equation (19), in which $\mathbf{T}(\tilde{\omega}_i)$ is evaluated explicitly without the approximations in Equations (21) and (22). In this example, all $m = 21$ eigenvalues were found regardless of the number of contour points in the first iteration after the initialization step. No spurious eigenvalues occurred in any of the test cases with NLFEAST. As expected, the number of contour points N (and thus the quality of the projection matrix $\mathbf{Q}$) determines the convergence rate of NLFEAST, whereas the final accuracy of the eigenpairs is unaffected by this choice. Even when using only $N = 6$ contour points, a maximum residual of $\varepsilon_{\text{max}} = 4 \cdot 10^{-10}$ is achieved after a couple of iterations. Note that in this example, the

Radius of sphere	5 m
Shell thickness	0.05 m
Density of steel	7860 kg/m^3
Young's modulus	210 GPa
Poisson's ratio	0.3
Density of water	1000 kg/m^3
Speed of sound	1500 m/s

TABLE 1 Geometry of the sphere and properties of steel and water

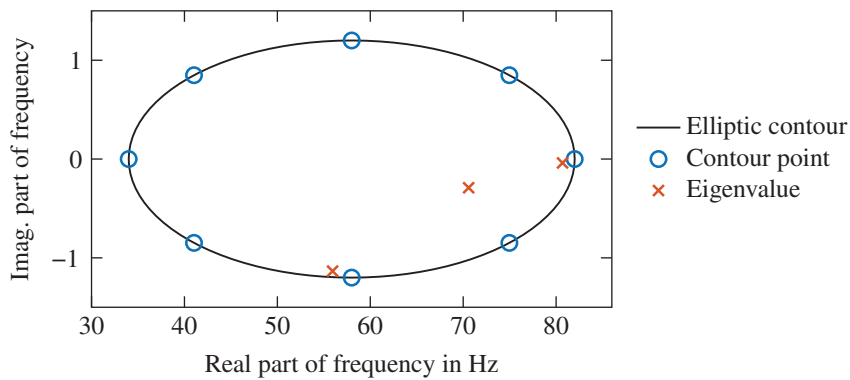**FIGURE 2** Exemplary contour points used for NLFEAST. Additionally, three distinct eigenvalues occurring in the considered frequency range are shown
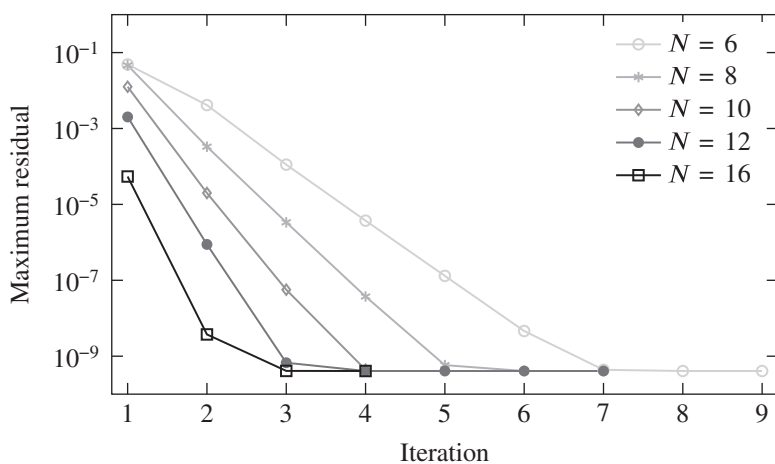

FIGURE 3 Maximum residual among the eigenpairs whose eigenvalues lie inside the contour for different numbers of contour points N. The number of quadrature points for solving the projected EVP is set to $N_{\text{p}} = 16$

1-norm of the system matrix is of order $\mathcal{O}(10^0)$ in the whole frequency range on interest and hence, the absolute and relative residuals are roughly in the same order of magnitude, cf. Equations (19) and (20). For example, the above mentioned maximum residual of $\varepsilon_{\max} = 4 \cdot 10^{-10}$ corresponds to a relative residual of $\varepsilon_{\mathrm{rel}} = 6 \cdot 10^{-11}$.

The final accuracy of the eigenpairs is mainly controlled by the accuracy with which the projected EVP is solved. The latter is in turn dependent on the number of quadrature points N_{p} for the rational approximation in Equation (26). This is illustrated in Figure 4, where now $\varepsilon_{\max}$ is displayed for different values of N_{p} and a fixed number of contour points $N = 12$. We observe that the final residuals stagnate at different values depending on the number of N_{p}. For example, when using $N_{\mathrm{p}} = 6$, the maximum residual stagnates at $\varepsilon_{\max} = 7 \cdot 10^{-4}$. Rational approximations with more than $N_{\mathrm{p}} = 16$ did not further improve the results beyond $\varepsilon_{\max} = 4 \cdot 10^{-10}$.

In Section 3.2, we have proposed rational approximations of the BE matrices (21) in order to avoid their explicit assembly in each iteration. Figure 5 displays thereby introduced relative error $\varepsilon_{\mathbf{H}}(\tilde{\omega})$ given by Equation (23) when using $N = 12$ contour points. The plot is generated by 1683 uniformly distributed points in the complex plane and linear interpolation in-between them. We notice that $N = 12$ contour points are sufficient to achieve errors $\varepsilon_{\mathbf{H}}(\tilde{\omega})$ of order $\mathcal{O}(10^{-10})$ inside the elliptic contour. The error estimator for an matrix entry given in Equation (25) yields a maximum value of $\varepsilon_h(\tilde{\omega}) = 6 \cdot 10^{-9}$, which is in reasonable accordance to the actual error shown in Figure 5. The influence of the rational approximations of the BE matrices on the convergence of NLFEAST is examined in Figure 6. The residuals with and without approximation are compared for $N = 8$ contour points and a varying number of points N_{p} for the rational approximation. We notice that the rational approximations only have a negligible impact on the convergence rate as well as on the final accuracy—at least up to $N_{\mathrm{p}} = 12$. When using $N_{\mathrm{p}} = 16$, the rational approximations prevent the eigenpair from reaching the same final accuracy as is reached when the BE matrices are explicitly formed. It stagnates at $\varepsilon_{\max} = 3 \cdot 10^{-9}$ while without the rational approximations, $\varepsilon_{\max} = 4 \cdot 10^{-10}$ is achieved. However, in view of the significant saving of computational effort, this minor deterioration of accuracy is deemed acceptable—also because other sources of inaccuracies such as discretization errors typically have a larger impact.

As discussed in Section 3.4, the computational effort is mainly associated with the solution of linear systems (30) with multiple right-hand sides for updating the projection matrix via Equation (16). The performances of conventional and block GMRes are compared with each other in Figure 7 by counting the equivalent matrix vector multiplications. When using conventional GMRes, the linear systems are solved individually for each right-hand side. The corresponding relative residuals are plotted one after the other in Figure 7 yielding the apparent sawtooth shape (i.e., each tooth corresponds to one right-hand side). The complete solution requires 822 matrix vector multiplications within GMRes corresponding to an average of 39 multiplications for the solution to each right-hand side.

In contrast, block GMRes solves the linear system (30) for all right-hand sides simultaneously by performing one matrix multiplication in each iteration. For the sake of comparability with conventional GMRes, each of those operations are counted as $m = 21$ equivalent matrix vector multiplications. The dashed red curve represents the relative residual associated with the first right-hand side. It exhibits a significantly steeper slope than conventional GMRes due to the larger dimension of the underlying (block) Krylov subspace. This also leads to a faster overall convergence which is illustrated by the solid red curve. The latter displays the maximum relative residual among all right-hand sides. In total, block GMRes requires 15 iterations and a total of 315 equivalent matrix vector multiplications. In terms of computational
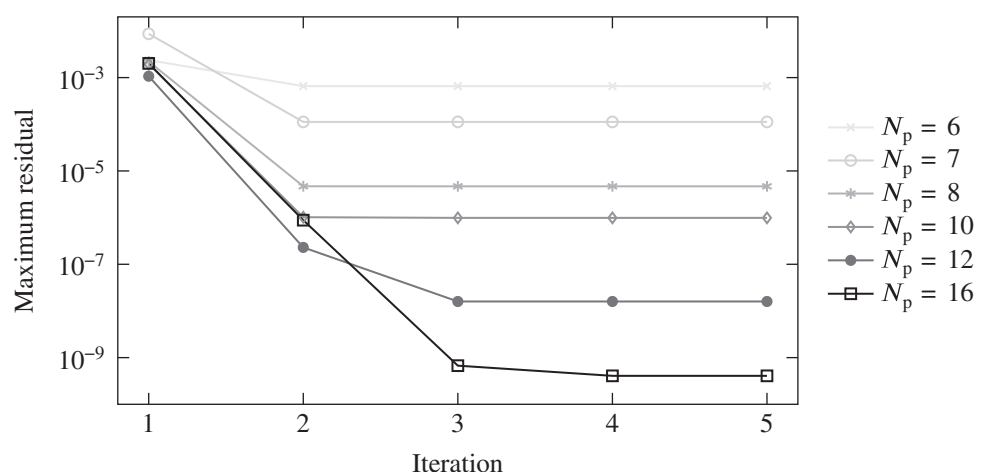

FIGURE 4 Maximum residual among the eigenpairs whose eigenvalues lie inside the contour for different numbers N_{p} for solving the projected EVP. The number of contour points is set to $N = 16$
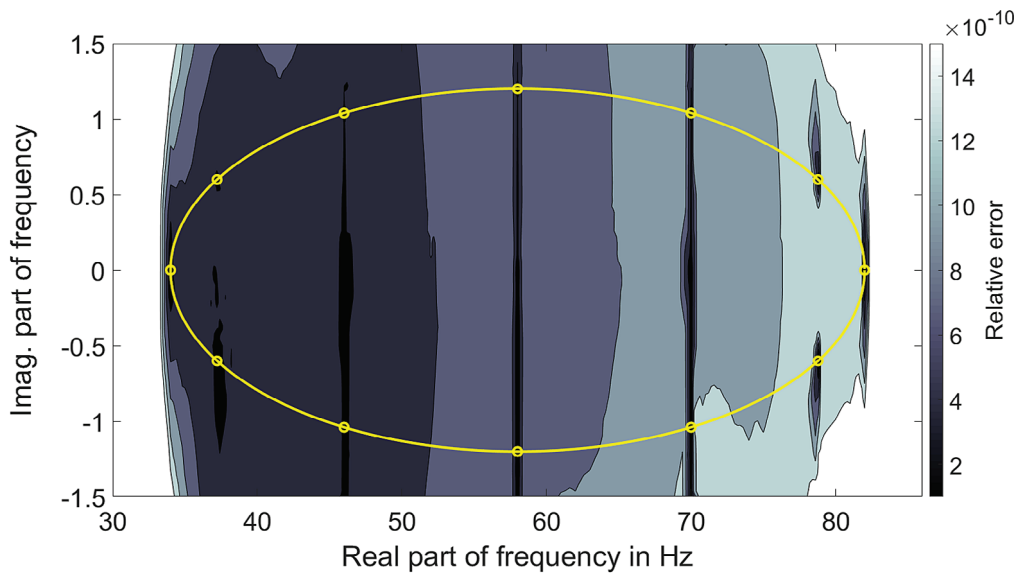
FIGURE 5 Relative error of the rational approximation given by Equations (21) and (22) when using $N = 12$ contour points on the ellipse. This plot is generated by 1683 uniformly distributed points in the complex plane and linear interpolations in-between them
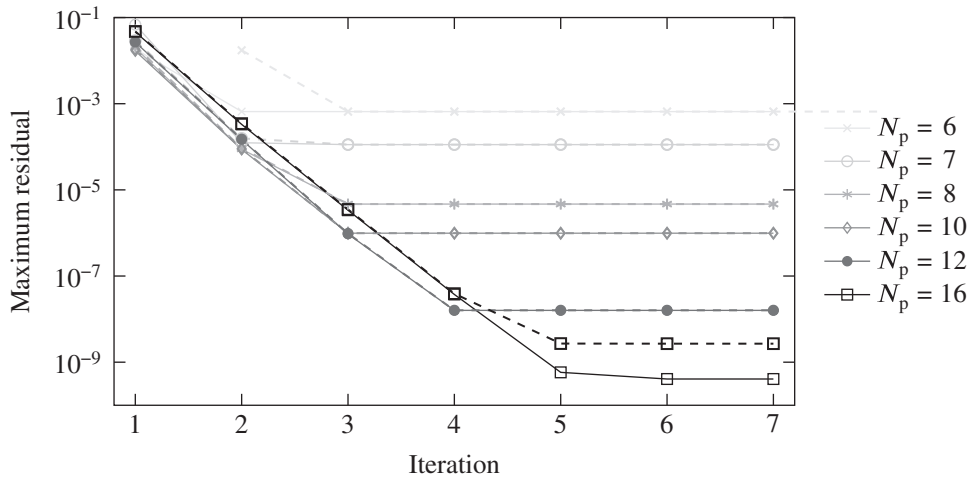

FIGURE 6 Maximum residual among the eigenpairs whose eigenvalues lie inside the contour for different numbers N_p for solving the projected EVP. The number of contour point is set to $N = 8$. Additionally, dashed lines display the residuals when using rational approximations of the BE matrices given in Equations (21) and (22)
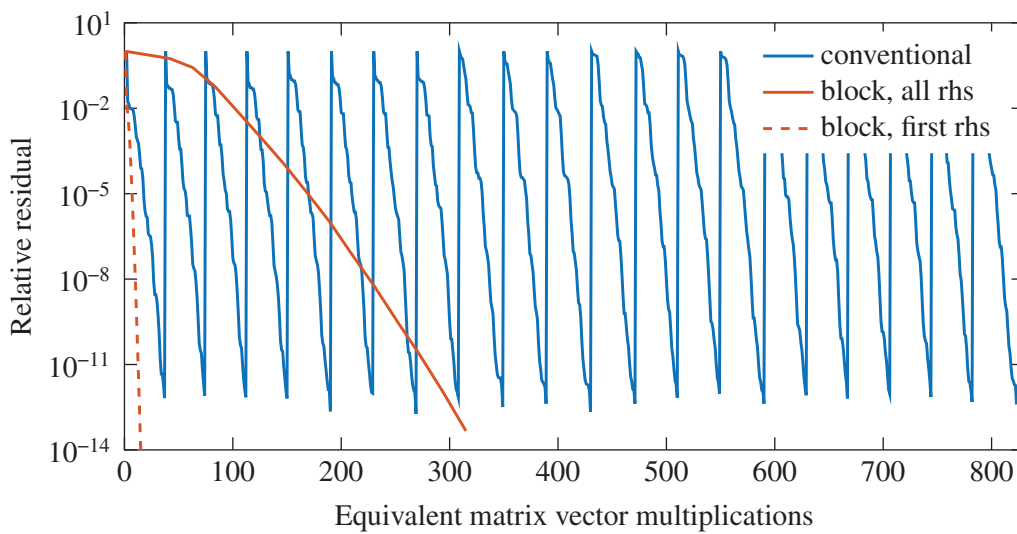
FIGURE 7 Performances of conventional and block GMRes for solving the linear system (30) with multiple right-hand sides (rhs)

time, block GMRes additionally benefits from efficient memory usage due to less frequent access to the stored matrices. In this example, block GMRes yields a speed up of more than eight times compared with conventional GMRes.

4.2 | Comparison to contour integral methods

In the following, we briefly compare the performance of NLFEAST to two other nonlinear eigensolvers.

4.2.1 | Comparison to the block Sakurai Sugiura method

The *block Sakurai Sugiura method* (block SS)[26] is a contour integral method based on resolvent moments and essentially transforms the nonlinear EVP to a generalized EVP involving block Hankel matrices. The block Hankel matrices contain moments of the resolvent of the system matrix up to an user-defined degree, whereas the moment matrices are computed with respect to a number L of random source vectors via complex contour integration. The algorithmic details of block SS can be found in the literature.[21,26,40]

The computational efforts of both NLFEAST and block SS mainly comprise the assembly of BE coefficient matrices and the solution of linear systems at the contour points. The latter aspect is studied in Figure 8, which shows the maximum residual over the number of solved linear systems. NLFEAST is executed with $N_p = 16$ and different numbers N of contour points. As we have already seen in the previous section, the residual in NLFEAST decreases monotonically until stagnation. In the case of block SS, we also observe that the residuals generally decrease with an increasing N (and thus increasing number of linear systems). However, there are also some apparent fluctuations in Figure 8, even though the random source vectors are kept the same among all runs of block SS for the sake of comparability. In other words, the accuracy of the eigenpairs computed by block SS may actually deteriorate in some cases even when more integration points are used for the projection. Moreover, we note that spurious eigenvalues occurred in all our test cases with block SS although we perform a singular value decomposition and truncation of the Hankel matrices as suggested by Asakura et al.[26] These spurious eigenvalues associated with large residuals are not included in Figure 8.

Figure 8 also indicates the number of linear systems that need to be solved in order to reach the final (i.e., highest possible) accuracy. For the sake of comparability, we define a threshold of $\varepsilon_{max} = 10^{-8}$. When using block SS with $L = 21$, a total of $N = 32$ contour points (i.e., the solution of 32 linear systems) are required in order reach that threshold. Compared with that, NLFEAST is an iterative scheme that solves N linear systems in each iteration. For example with $N = 8$, the threshold is reached after five iterations, which corresponds to a total number of 40 linear systems. Similarly, when using $N = N_p = 16$ contour points, only two iterations are required summing up to a total of 32 linear systems.

Table 2 lists the associated computational times for the solution of those systems as well as the times that are required for the assembly of the BE matrices. Regarding the solution of linear systems, NLFEAST benefits from the reuse of the LU factorizations of $\mathbf{K} - z_j^2 \mathbf{M}$ over the course of the iterations. Hence, given a certain number of linear systems and right-hand sides, the solution time of NLFEAST is slightly shorter. Note that we also use block GMRes for solving the
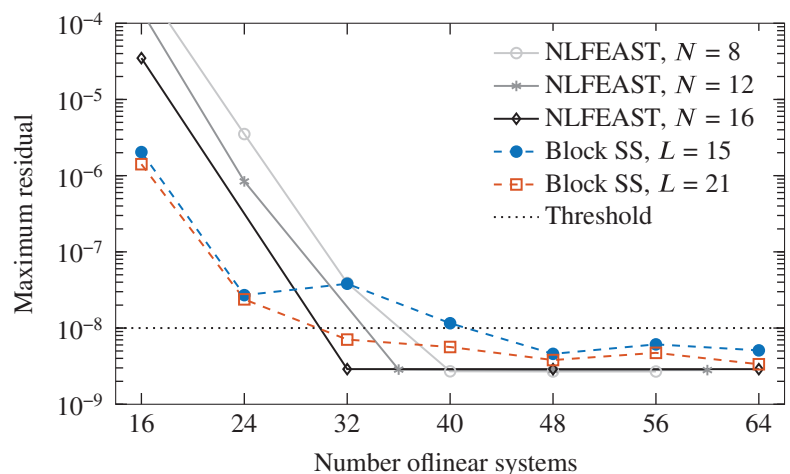

FIGURE 8 Number of linear systems that need to be solved to reach a threshold of $\varepsilon_{max} = 10^{-8}$. All computations with NLFEAST are conducted using $N_p = 16$. The Hankel matrices in block SS contain moments up to a degree of 3. The associated computational times are listed in Table 2

	NLFEAST			**Block SS**	
	$N = 8$	$N = 12$	$N = 16$	$L = 15$	$L = 21$
Num. matrix assembly	16	24	16	48	32
Num. linear solves	40	36	32	48	32
Time matrix assembly	912 s	1368 s	912 s	2736 s	1824 s
Time matrix approx.	43 s	40 s	40 s	–	–
Time linear solve	219 s	207 s	221 s	279 s	240 s
Total time[a]	1174 s	1615 s	1173 s	3015 s	2064 s

TABLE 2 Computational effort that is required to solve the benchmark EVP with $\varepsilon_{max} \leq 10^{-8}$

Note: Associated convergence behavior is plotted in Figure 8.

[a]The total time does not refer to the total wall clock time for the execution of the algorithms but only includes matrix assembly, rational approximation, and solution of linear systems. The other (marginal) contributions, which are mostly identical in all test cases, are neglected.

linear systems arising in block SS. But actually, the major saving does not stem from the decrease of solution time but from the fact that NLFEAST requires significantly less contour points in order to achieve the highest possible accuracy (with a minimum number of $N = N_p = 13$). As a result of this, fewer BE matrices need to be explicitly assembled. In this example, the assembly of $\mathbf{H}(z_j)$ and $\mathbf{G}(z_j)$ at a single contour point took 57 s while the time for computing the rational approximation via Equation (21) only marginally contributed to the total time. Summing up, depending on the respective solver parameters, NLFEAST required 22 % to 61 % less computational time then block SS to achieve the final accuracy. Of course these numbers may change depending on the dimension of the problem and in the case of parallel computing, also on the number of available computing nodes.

4.2.2 | Comparison to the Sakurai Sugiura method with Rayleigh Ritz projection

The ill-conditioning of the Hankel matrices in block SS has been addressed in a paper by Yokota and Sakurai,[28] in which the authors suggest a Rayleigh Ritz procedure to extract the eigenvalues from the resolvent moments based subspace. This procedure is known as the *Sakurai Sugiura method with Rayleigh Ritz projection* (SSRR). While SSRR is expected to give more accurate results than block SS, it needs to be accompanied by a nonlinear eigensolver for the projected (but still nonlinear) EVP. This nonlinear EVP of small size can be conveniently solved by block SS with a large number L of source vectors without impairing the computational efficiency. A similar strategy has been employed for the solution of acoustic EVPs based on BEM,[29] however with the difference that the Rayleigh Ritz projector is built by sampling the resolvent matrix.

Our experience with SSRR is in line with those reported in previous works[28,29] and indicates that the method is computationally more efficient and robust than block SS. For example, with $L = 21$ and a degree of moments of 3, SSRR only requires $N = 18$ contour points to reach the threshold of $\varepsilon_{max} = 10^{-8}$ (recall that block SS required $N = 32$ and NLFEAST $N = N_p = 13$). Compared with NLFEAST, fewer linear systems need to be solved in SSRR, but still, NLFEAST requires less computational time in this example since fewer BE matrices need to be explicitly assembled. Further, we note that although the occurrence of spurious eigenvalues is effectively mitigated in SSRR, we still encountered them when solving the projected EVP via block SS, even with a very small degree of moments and large number L of source vectors. In contrast, no spurious eigenvalues occur when combining SSRR with the rational approximation method presented in Section 3.3.

5 | SECOND NUMERICAL EXAMPLE: QUANTIFICATION OF MODAL RADIATION DAMPING IN A MUSICAL BELL

A bell excited by a clapper radiates sound by an ensemble of its fundamental modes, where each of them is characterized by an initial amplitude, eigenfrequency and a decay rate. While the eigenfrequencies can be anticipated by an in vacuo modal analysis of the bell, the decay characteristics, which make up for the desired sound of the bell, depend on the

acoustic radiation damping of each individual mode.[60] It is the yearlong experience of bell founders that enables them to manually tune the bell after casting.

In this second numerical example, we apply the NLFEAST algorithm in order to determine radiation damping values associated with modes of a bronze musical bell. The main geometrical and material parameters of the bell are listed in Table 3. The bell is discretized using 20-noded hexahedral solid finite elements resulting in a total of 26,769 displacement DOFs. The respective stiffness and mass matrices are extracted from ANSYS. Figure 9 shows the mesh of the bell. The outer surfaces of the solid elements are coupled to a conforming acoustic BE mesh consisting of 2560 bilinear discontinuous elements with a total of 10,240 pressure DOFs.

The modal analysis of the bell in interaction with surrounding air is performed using an elliptic contour with $f_{\min} = 80$ Hz, $f_{\max} = 390$ Hz, $\zeta = 0.05$, and $N = N_p = 48$. A treatment for the nonuniqueness problem in BEM is not required. From a preceding in vacuo analysis, we expect $m = 10$ eigenpairs in the considered frequency range. The in vacuo modes are also used as the initial guess of eigenvectors $\mathbf{X}^{(0)}$ in NLFEAST. Due to the light fluid loading, the coupled system (4) admits accurate model order reduction solely based on the structural subsystem. Hence, we form the Schur complement of the acoustic subsystem resulting in the EVP formulation given by Equation (7). The system matrices at the contour points are reduced by a Krylov subspace model order reduction as described in Section 3.4. The Krylov basis is computed using a random initial vector at a single expansion point of 250 Hz. A dimension of $q = 40$ for the Krylov basis is required in order to obtain all eigenpairs in this example. Hence, the computational effort of the modal analysis basically comprises the setup of the BE matrices and solution of a single linear system $\mathbf{H}(z)\mathbf{X} = \mathbf{G}(z)\mathbf{C}_{\mathrm{fs}}\mathbf{V}$ with $q = 40$ right-hand sides for each contour point. Compared with that, using the EVP formulation (8) based on the Schur complement of the structural subsystem would necessitate solution of a linear system with multiple right-hand sides for each contour point every time when the projection matrix needs to be updated. The memory requirements for storing the system matrices of reduced dimension q is negligible. In contrast, using the EVP formulation (8) would require storage of several BE matrices of original dimension. Moreover, using the latter approach, we were not able to find accurate eigenpairs, which may be attributed to ill-conditioning of the FE matrices $\mathbf{K} - \omega^2\mathbf{M}$. In this example, NLFEAST requires two iterations to reach the final accuracy.

The first five distinct modes of the bell and the associated eigenfrequencies are shown in Figure 10. Note that due to rotational symmetry, all modes occur with a geometric multiplicity of two. While the eigenfrequencies corresponding to the real parts of the eigenvalues remain almost unaffected by air loading, the imaginary parts of the eigenvalues characterize the extent of acoustic radiation damping. Radiation damping corresponding to an individual mode can be expressed

TABLE 3 Geometry of the bell and properties of bronze and air

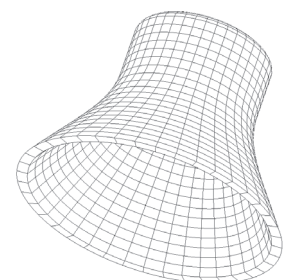|	
Height of the bell	1.2 m
Thickness of the bell	0.07 m
Radius at top end	0.45 m
Radius at bottom end	0.87 m
Density of bronze	8750 kg/m^3
Young's modulus	98.6 GPa
Poisson's ratio	0.34
Density of air	1.22 kg/m^3
Speed of sound	340 m/s

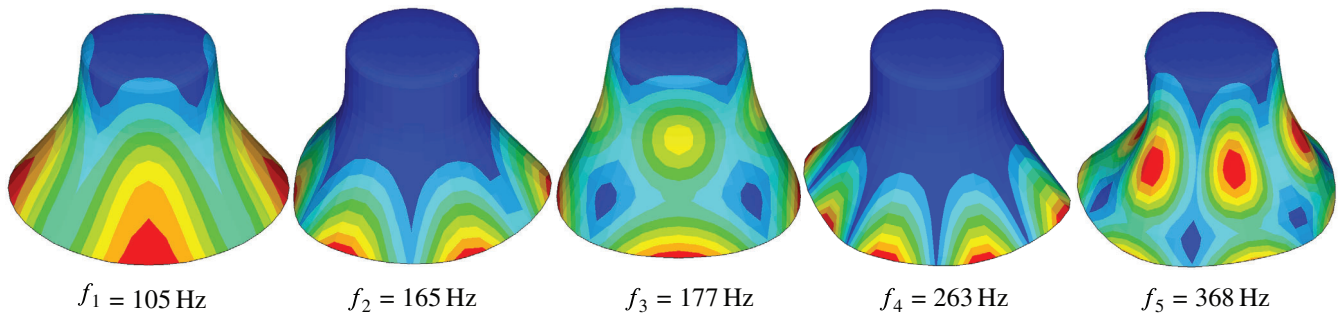
FIGURE 9 Finite element mesh of the bell

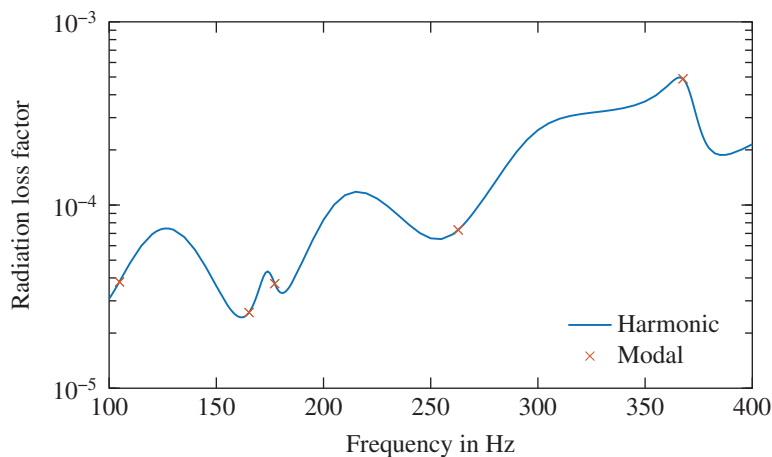**FIGURE 10** First five distinct modes and associated eigenfrequencies of the bell

FIGURE 11 Modal and harmonic radiation loss factors of the bell

by the modal loss factor

$$\eta_i = -2\frac{\text{Im}\,(\tilde{\omega}_i)}{\text{Re}\,(\tilde{\omega}_i)}, \tag{36}$$

where $\text{Im}\,(\tilde{\omega}_i)$ is negative due to the harmonic time dependency $e^{-i\omega t}$. Beside modal loss factors, harmonic loss factors are an alternative way to quantify radiation damping and can be computed by a frequencywise response analysis.[2] They can serve us to verify the modal loss factors and thus the accuracy of the computed eigenvalues. Figure 11 shows the modal loss factors obtained by NLFEAST as well as harmonic loss factors of the bell subject to point force excitation. The latter are obtained by computing the radiated sound power in a standard frequency sweep analysis, which can be performed either based on the Schur complement of the acoustic subsystem in conjunction with the above described Krylov subspace model order reduction or based on the Schur complement of the structural subsystem without model order reduction. The maximum relative difference in radiated sound power between these two approaches is $2.5 \cdot 10^{-5}$ which undermines that the coupled system admits accurate model order reduction solely based on the structural subsystem. Figure 11 also indicates that although the imaginary parts of the eigenvalues are very small, the resulting modal loss factors agree well with the harmonic ones at the respective eigenfrequencies.

6 | SUMMARY AND CONCLUSION

We have proposed a subspace iteration method for the solution of nonlinear structural acoustic EVPs. At its core, the method is based on the nonlinear FEAST algorithm and essentially works by iteratively refining a projection matrix that is obtained by applying a spectral projector. We have shown that in the context of structural acoustic problems involving complex eigenvalues, the information for computing the projection matrix can be recycled in two ways and thus giving rise to a tailored eigensolver. Firstly, the integration points are reused for a rational approximation of the projected but

still nonlinear EVP. This enables an accurate computation of eigenpairs at a negligible additional cost without inducing spurious eigenvalues. Secondly, the integration points are also reused to approximate the BE matrices at intermediate eigenvalues thereby avoiding their assembly in each FEAST iteration. Only a few points are sufficient to achieve small errors in the BE matrices, and hence to retain the convergence rate of FEAST while significantly reducing the numerical effort.

In consequence, the actual computation of the projection matrix remains the only computationally expensive task required for solving the EVP. In this respect, we provide two tailored approaches for updating the projection matrix. In the case of heavy fluid loading, we form the Schur complement of the structural subsystem and employ block GMRes for solving the underlying coupled linear systems with multiple right-hand sides. Compared with standard GMRes, we have achieved a speed-up of eight times in our test cases. In the case of light fluid loading, we exploit the fact that the coupled system admits accurate model order reduction solely based on the structural subsystem. By forming the Schur complement of the acoustic subsystem and computing the reduced coupled matrices again by block GMRes, we are able to significantly reduce both the memory requirements and the effort for updating the projection matrix.

Applications to a submerged spherical shell and to a musical bell have verified the proposed method. Comparison to resolvent moments based contour integral methods indicates two major advantages of the proposed eigensolver. While both methods yield similar final (i.e., highest possible) accuracies, the proposed method requires a significantly smaller number of contour points. Hence, less BE matrices need to be explicitly assembled. Moreover, in all our test cases, the proposed method yielded monotonous convergence without inducing spurious eigenvalues inside the contour. Finally, the application to a bell in interaction with air has shown that accurate modal radiation damping values are obtained despite the very weak acoustic loading.

DATA AVAILABILITY STATEMENT
The data that support the findings of this study are available from the corresponding author upon reasonable request.

ORCID
Suhaib Koji Baydoun https://orcid.org/0000-0002-1184-065X
Christopher Jelich https://orcid.org/0000-0002-2617-3116

REFERENCES
1. Li FL, Wang YS, Zhang C. Bandgap calculation of two-dimensional mixed solid-fluid phononic crystals by Dirichlet-to-Neumann maps. *Phys Scr*. 2011;84:055402.
2. Baydoun SK, Marburg S. Investigation of radiation damping in sandwich structures using finite and boundary element methods and a nonlinear eigensolver. *J Acoust Soc Am*. 2020;147(3):2020-2034.
3. Hentschel OP, Bonhage M, Panning-von Scheidt L, Wallaschek J, Denk M, Masserey PA. Analysis of an experimental setup for structural damping identification. *J Theor Appl Mech*. 2016;54(1):27-39.
4. Everstine GC, Henderson FM. Coupled finite element/boundary element approach for fluid-structure interaction. *J Acoust Soc Am*. 1990;87(5):1938-1947.
5. Ohayon R, Soize C. *Structural Acoustics and Vibration. Mechanical Models, Variational Formulations and Discretization*. London, UK: Academic Press; 1998.
6. Bathe KJ. *Finite Element Procedures*. Englewood Cliffs, NJ: Prentice Hall; 1996.
7. Kirkup S. The boundary element method in acoustics: a survey. *Appl Sci*. 2019;9(8):1642.
8. Kirkup SM, Henwood DJ. Methods for speeding up the boundary element solutions of acoustic radiation problems. *J Vib Acoust*. 1992;144(3):347-380.
9. Wu TW, Li WL, Seybert AF. An efficient boundary element algorithm for multi-frequency acoustical analysis. *J Acoust Soc Am*. 1993;94(1):447-452.
10. Coyette JP, Lecomte C, Migeot JL. Calculation of vibro-acoustic frequency response functions using a single frequency boundary element solution and a Padé expansion. *Acta Acust United Ac*. 1999;85(3):371-377.
11. Liang T, Wang J, Xiao J, Wen L. Coupled BE-FE based vibroacoustic modal analysis and frequency sweep using a generalized resolvent sampling method. *Comput Methods Appl Mech Eng*. 2019;345:518-538.

12. Panagiotopoulos D, Deckers E, Desmet W. Krylov subspaces recycling based model order reduction for acoustic BEM systems and an error estimator. *Comput Methods Appl Mech Eng*. 2020;359:112755.

13. Xie X, Liu Y. An adaptive model order reduction method for boundary element-based multi-frequency acoustic wave problems. *Comput Methods Appl Mech Eng*. 2021;373:113532.

14. Baydoun SK, Voigt M, Jelich C, Marburg S. A greedy reduced basis scheme for multifrequency solution of structural acoustic systems. *Int J Numer Methods Eng*. 2020;121(2):187-200.

15. Petyt M, Lea J, Koopmann G. A finite element method for determining the acoustic modes of irregular shaped cavities. *J Sound Vib*. 1976;45(4):495-502.

16. Banerjee PK, Ahmad S, Wang HC. A new BEM formulation for the acoustic eigenfrequency analysis. *Int J Numer Methods Eng*. 1988;26(6):1299-1309.

17. Chen ZS, Hofstetter G, Mang HA. A 3d boundary element method for determination of acoustic eigenfrequencies considering admittance boundary conditions. *J Comput Acoust*. 1993;1(4):455-468.

18. de Mey G. Calculation of eigenvalues of the Helmholtz equation by an integral equation. *Int J Numer Methods Eng*. 1976;10:59-66.

19. Roman JE, Campos C, Romero E, Tomàs A. *SLEPc Users Manual. Technical Report*. Valencia, Spain: Universitat Politècnica de València; 2020.

20. Peters H, Kessissoglou N, Marburg S. Modal decomposition of exterior acoustic-structure interaction. *J Acoust Soc Am*. 2013;133(5):2668-2677.

21. Zheng CJ, Bi CX, Zhang C, Gao HF, Chen HB. Free vibration analysis of elastic structures submerged in an infinite or semi-infinite fluid domain by means of a coupled FE-BE solver. *J Comput Phys*. 2018;359:183-198.

22. Güttel S, Negri Porzio GM, Tisseur F. Robust rational approximation of nonlinear eigenvalue problems. *MIMS EPrint*. 2020;2020(24).

23. Brennan MC, Embree M, Gugercin S. Contour integral methods for nonlinear eigenvalue problems: a systems theoretic approach; 2020. arXiv:2012.14979.

24. Effenberger C, Kressner D. Chebyshev interpolation for nonlinear eigenvalue problems. *BIT Numer Math*. 2012;52(4):933-951.

25. Kirkup SM, Amini S. Solution of the Helmholtz eigenvalue problem via the boundary element method. *Int J Numer Methods Eng*. 1993;36:321-330.

26. Asakura J, Sakurai T, Tadano H, Ikegami T, Kimura K. A numerical method for nonlinear eigenvalue problems using contour integrals. *JSIAM Lett*. 2009;1:52-55.

27. Kimeswenger A, Steinbach O, Unger G. Coupled finite and boundary element methods for fluid-solid interaction eigenvalue problems. *SIAM J Numer Anal*. 2014;52(5):2400-2414.

28. Yokota S, Sakurai T. A projection method for nonlinear eigenvalue problems using contour integrals. *JSIAM Lett*. 2013;5:41-44.

29. Xiao J, Meng S, Zhang C, Zheng C. Resolvent sampling based Rayleigh-Ritz method for large-scale nonlinear eigenvalue problems. *Comput Methods Appl Mech Eng*. 2016;310:33-57.

30. Gavin B, Miȩdlar A, Polizzi E. FEAST eigensolver for nonlinear eigenvalue problems. *J Comput Sci*. 2018;27:107-117.

31. Güttel S, van Beeumen R, Meerbergen K, Michiels W. NLEIGS: a class of fully rational Krylov methods for nonlinear eigenvalue problems. *SIAM J Sci Comput*. 2014;36(6):A2842-A2864.

32. El-Guide M, Miȩdlar A, Saad Y. A rational approximation method for solving acoustic nonlinear eigenvalue problems. *Eng Anal Bound Elem*. 2020;111:44-54.

33. Polizzi E. A density matrix-based algorithm for solving eigenvalue problems. *Phys Rev B*. 2009;79(11):115112.

34. Polizzi E. FEAST eigenvalue solver v4.0 user guide; 2020. arXiv:2002.04807.

35. Peters H, Marburg S, Kessissoglou N. Structural-acoustic coupling on non-conforming meshes with quadratic shape functions. *Int J Numer Methods Eng*. 2012;91(1):27-38.

36. Marburg S, Anderssohn R. Fluid structure interaction and admittance boundary conditions: setup of an analytical example. *J Comput Acoust*. 2011;19(1):63-74.

37. Su Y, Bai Z. Solving rational eigenvalue problems via linearization. *SIAM J Matrix Anal Appl*. 2011;32(1):201-216.

38. Tang PTP, Polizzi E. FEAST as a subspace iteration eigensolver accelerated by approximate spectral projection. *SIAM J Matrix Anal Appl*. 2014;35(2):354-390.

39. Neumaier A. Residual inverse iteration for the nonlinear eigenvalue problem. *SIAM J Numer Anal*. 1985;22(5):914-923.

40. Sakurai T, Futamura Y, Tadano H. Efficient parameter estimation and implementation of a contour integral-based eigensolver. *J Algorithms Comput Technol*. 2013;7(3):249-270.

41. Higham NJ, Tisseur F. A block algorithm for matrix 1-norm estimation, with an application to 1-norm pseudospectra. *SIAM J Matrix Anal Appl*. 2000;21(4):1185-1201.

42. Hackbusch W, Khoromskij B. A sparse H-matrix arithmetic. Part 2: application to multi-dimensional problems. *Comput Secur*. 2000;64:21-47.

43. Allemang RJ. The modal assurance criterion - twenty years of use and abuse. *Sound Vib*. 2003;37:14-20.

44. Austin AP, Kravanja P, Trefethen LN. Numerical algorithms based on analytic function values at roots of unity. *SIAM J Numer Anal*. 2014;52(4):1795-1821.

45. Xiao J, Wang J, Liang T, Wen L. The RSRR method for solving large-scale nonlinear eigenvalue problems in boundary element method. *Eng Anal Bound Elem*. 2018;93:150-160.

46. Trefethen LN, Weideman JAC. The exponentially convergent trapezoidal rule. *SIAM Rev*. 2014;56(3):385-458.

47. Voss H. Nonlinear eigenvalue problems. In: Hogben L, ed. *Handbook of Linear Algebra*. Boca Raton, FL: Chapman & Hall/CRC Press; 2014:115:1-115:24.

48. Güttel S, Tisseur F. The nonlinear eigenvalue problem. *Acta Numerica*. 2017;26:1-94.

49. Parks ML, de Sturler E, Mackey G, Johnson DD, Maiti S. Recycling Krylov subspaces for sequences of linear systems. *SIAM J Sci Comput*. 2006;28:1651-1674.

50. Gutknecht MH. Block krylov space methods for linear systems with multiple right-hand sides: an introduction. In: Siddiqi AH, Duff I, Christensen O, eds. *Modern Mathematical Models, Methods and Algorithms for Real World Systems*. Tunbridge Wells, UK: Anshan Limited; 2007.

51. Saad Y, Schultz MH. GMRES: a generalized minimal residual algorithm for solving nonsymmetric linear systems. *SIAM J Sci Stat Comput*. 1986;7:856-869.

52. Vital B. *Etude de quelques méthodes de résolution de problemes linéaires de grande taille sur multiprocesseur* [PhD thesis]. Université de Rennes; 1990.

53. Zheng CJ, Gao HF, Du L, Chen HB, Zhang C. An accurate and efficient acoustic eigensolver based on a fast multipole BEM and a contour integral method. *J Comput Phys*. 2016;305:677-699.

54. Peters H, Kessissoglou N, Marburg S. Modal decomposition of exterior acoustic-structure interaction problems with model order reduction. *J Acoust Soc Am*. 2014;135(6):2706-2717.

55. Puri RS, Morrey D, Bell AJ, Durodola JF, Rudnyi EB, Korvink JG. Reduced order fully coupled structural-acoustic analysis via implicit moment matching. *Appl Math Model*. 2009;33(11):4097-4119.

56. Burton AJ, Miller GF. The application of integral equation methods to the numerical solution of some exterior boundary-value problems. *Proc R Soc Lond*. 1971;323:201-220.

57. Zheng CJ, Chen HB, Gao HF, Du L. Is the Burton-Miller formulation really free of fictitious eigenfrequencies? *Eng Anal Bound Elem*. 2015;59:43-51.

58. Chen X, He Q, Zheng CJ, Wan C, Bi CX, Wang B. A parameter study of the Burton-Miller formulation in the BEM analysis of acoustic resonances in exterior configurations. *J Theor Comput Acoust*. 2020;2050023.

59. Junger MC, Feit D. *Sound, Structures, and Their Interaction*. Cambridge, MA: MIT Press; 1986.

60. Yu Y, Kwak BM. Design sensitivity analysis of acoustical damping and its application to design of musical bells. *Struct Multidiscip Optim*. 2011;44:421-430.

A.4 Publication IV

Hybrid assessment of acoustic radiation damping combining in-situ mobility measurements and the boundary element method

TECHNICAL & APPLIED ARTICLE   **OPEN ⊘ ACCESS**

Hybrid assessment of acoustic radiation damping combining in-situ mobility measurements and the boundary element method

Suhaib Koji Baydoun[1,*], N.B. Roozen[1,2], and Steffen Marburg[1]

[1] Technical University of Munich, TUM School of Engineering and Design, Chair of Vibroacoustics of Vehicles and Machines, Boltzmannstraße 15, 85748 Garching, Germany

[2] KU Leuven, Laboratory of Acoustics, Soft Matter and Biophysics, Department of Physics and Astronomy, Celestijnenlaan 200D, Leuven 3001, Belgium

Abstract – A hybrid experimental-numerical approach is proposed for assessing acoustic radiation damping – a major energy dissipating mechanism in lightweight structures. The vibrational behavior is characterized by distributed mobility measurements using laser Doppler vibrometry allowing to realistically capture the mechanical behavior of the structure under test. The experimentally obtained matrix of mobilities are coupled to a boundary element model to evaluate the radiated sound power numerically. Thereby, acoustic measurements and associated low frequency limitations are avoided, which results in two salient features of the proposed hybrid approach: modeling of diffuse incident acoustic fields and consideration of acoustic short-circuiting induced by slits and gaps. These features contribute to an accurate and excitation-dependent estimation of acoustic radiation damping in the low frequency range. The proposed hybrid approach is applied to flat and C-shaped aluminum sandwich panels mounted onto a tub-shaped foundation. The results are compared to those obtained by a previously reported numerical method.

1 Introduction

Composite structures such as honeycomb sandwich panels exhibit excellent elastic properties but only low material inherent damping. The latter issue is addressed extensively by material scientists and engineers with a view to mitigate unwanted vibrations by means of passive and active damping devices. Clearly, an effective design of such damping treatments requires accurate quantification of damping in the first place [1]. In fact, accurate quantification of different damping contributions is an essential aspect in the design process of lightweight structures. An important and yet often neglected damping contribution in light-weight structures is known as *acoustic radiation damping* [2]. It refers to the energy dissipation of vibrating structures due to far-field sound radiation.

The earliest and perhaps most straight forward approach for assessing radiation damping is based on in-vacuo reference measurements [3, 4]. Clarkson and Brown deduced damping values of a honeycomb sandwich panel by relating the input power of a shaker to the average vibrational velocity [3]. By conducting the same experiments in air and in-vacuo, they were able to distinguish between acoustic radiation damping and material inherent damping of the panel. Zhou and Crocker followed a different approach and determined radiation damping of sandwich panels clamped in a window between two reverberation rooms by measuring both the surface velocity and the sound pressure in the receiving room [5].

In contrast to numerical modeling, such experiments allow to properly capture the elastic behavior of structures involving complex material configurations. This is an important aspect since radiation damping is particularly relevant in lightweight structures that are designed to achieve a high ratio of bending stiffness to mass. However, in the majority of the cases, experimental set-ups imply significant limitations on the specimen's geometry and also on the boundary conditions, which make in-situ measurements difficult. For example, a vacuum chamber needs to be large enough to accommodate the specimen, and it can be cumbersome to access all surfaces by laser Doppler vibrometry (LDV) in order to measure the vibration levels. Moreover, excitation by incident acoustic fields is not possible, although radiation damping strongly depends on the type of excitation at low frequencies.

Similar restrictions hold for sound transmission facilities, which limit the geometry of the specimen to the shape of the window cut-out between the two rooms. Moreover,

---

*Corresponding author: suhaib.baydoun@tum.de

the clamping inside the window hardly resembles the actual mounting condition, which can falsify the dynamic response at low frequencies. Indeed, acoustic measurements are generally subject to large uncertainties in the low frequency range: Measurements inside reverberation rooms are based on the assumption of diffuse acoustic fields, which become invalid due to the modal behavior of the room [6], and the effectiveness of absorbent treatments in anechoic chambers is also limited below the cut-off frequency [7].

Besides experimental approaches, radiation damping can be estimated numerically based on a vibroacoustic simulation model. In our previous work, the finite (FEM) and the boundary element method (BEM) were combined with a nonlinear eigensolver in order to derive radiation damping values corresponding to certain structural modes [8]. The main advantage of that numerical approach compared to the above mentioned experimental methods is that the acoustic conditions and associated effects such as scattering and short-circuiting can be accurately modeled even at low frequencies. Further, the coupled FEM–BEM approach allows to capture the modal behavior of the structure and thus the excitation dependence of radiation damping. However, the corresponding eigenfrequencies depend on the actual boundary conditions, which can hardly be reproduced in a simulation. Usually, idealized boundary conditions are employed in finite element models such as *clamped* or *simply supported*. Often, it is difficult to tell which of these conditions resembles the actual configuration, and indeed the truth in many cases lies somewhere in between. Inaccurately modeled boundary conditions can subject acoustic quantities to large errors when sound radiation is mainly driven by edge and corner motions. Moreover, prestress occurring in assembled components can have implications on sound radiation as well, but is difficult to accurately model in simulations.

The uncertainty associated with boundary conditions, excitation and acoustic measurements in the low frequency range is illustrated in Figure 1, which shows radiation damping values of a foam-filled honeycomb sandwich panel. The experimental values are taken from the literature [5] and were obtained by the authors in a window test rig between two reverberation rooms using shaker excitation. Figure 1 compares those experimental values to theoretical estimates [9, 10] based on principles of power flow as well as to radiation damping values computed by the FEM–BEM approach assuming an infinitely extended acoustic baffle and five randomly positioned point forces as excitation. All three methods show good agreement to each other in the higher frequency range above coincidence, which occurs around 780 Hz. However, we also observe significant deviations in the lower frequency range where the modes of the panel are widely separated and radiation damping strongly depends on the excitation. The deviation between the experimental and the numerical results are likely attributed to the effect of boundary conditions, the excitation and also to the low modal density of the reverberation rooms. Our conclusion is that reliable methods for predicting radiation damping in the low frequency range are currently not available.
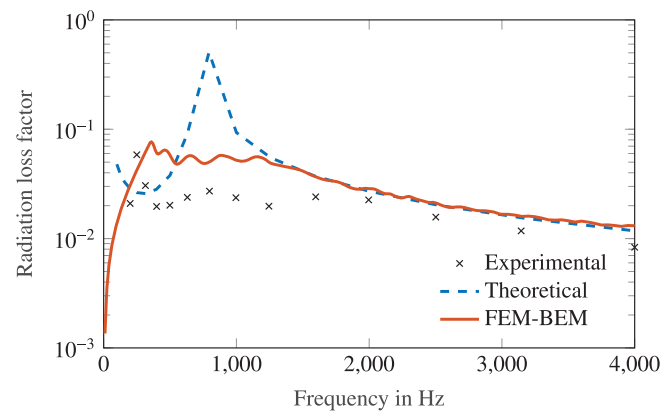

Figure 1. Radiation loss factors of a sandwich panel with foam-filled honeycomb core. Comparison of experimental values taken from the literature [5] to theoretical estimates as well as to numerical results obtained by a FEM–BEM approach.

The uncertainties related to boundary conditions, excitation and diffuse acoustic fields in the low frequency range are widely addressed in literature – not exactly with regard to acoustic radiation damping but in the context of sound transmission loss [11–14]. Different to radiation damping, which is a generally relevant aspect in lightly damped structures, sound transmission analysis only applies to partitions between sending and receiving rooms and does not require measuring the structural response.

Usually, researchers focus on either experimental or numerical methods and then use the respectively other one for the purpose of verification. However, as discussed above, both approaches exhibit shortcomings that are of different origins. An intuitive and yet often overlooked alternative is to combine the advantages of numerical and experimental methods in a hybrid approach. Examples in the literature include fitting the equations of motions with respect to measured transfer functions [15] and experimental-numerical evaluation of sound radiation of a boat hull [16]. Shephard et al. combined an experimental modal analysis with a lumped parameter model for the representation of underwater sound radiation [17]. In this way, the authors were able to numerically include the effect of added mass after performing the measurements in air. A similar approach has been studied in the context of active control by using simulated measurement data and the boundary element method [18]. More recently, Roozen et al. [19] characterized sound transmission by means of mobility measurements and the Rayleigh integral method – an approach that may be categorized as vibration-based sound power measurement [20, 21].

In this work, we propose a combined experimental-numerical procedure, which extends the currently available methods for assessing radiation damping to the low frequency range. On the one hand, we characterize the dynamical behavior of complex materials by an experimental method – ideally even in the actual mounting condition. On the other hand, we avoid acoustic measurements and associated limitations and instead, employ the boundary element method (BEM) [22] to characterize the acoustic

field. For our purpose of evaluating damping by far-field sound radiation, BEM is particularly appealing because it does not require special treatments for modeling unbounded acoustic domains. Moreover, in comparison to analytical evaluation of sound radiation [19], the use of BEM allows to consider complex geometries as well as acoustic short circuiting induced by slits and gaps. The latter plays a significant role in the sound insulation and radiation at low frequencies [23, 24], which will be demonstrated later in this paper. The proposed hybrid framework contributes to an accurate low-frequency assessment of acoustic radiation damping covering the following aspects:

- Firstly, the dynamic response is evaluated by taking the actual mounting condition into account, thus avoiding idealized mechanical boundary conditions.
- Secondly, the actual acoustic field and associated effects such as scattering and short-circuiting are considered without the need of acoustic measurement facilities.
- Lastly, radiation damping can be evaluated under any excitation including diffuse incident fields.

The paper is organized as follows. Section 2 describes the experimental-numerical framework and provides details regarding the coupling, the modeling of diffuse incident fields and the evaluation of radiation damping. The procedure is applied in Sections 3 and 4 to flat and curved honeycomb sandwich panels. The influences of excitation and acoustic conditions on radiation damping in the low frequency range are investigated and the results are compared to those obtained by a previously reported numerical method. The paper concludes in Section 5 with a summary of the main findings and a discussion of future applications and studies.

2 Combined experimental-numerical evaluation of vibroacoustic responses

Despite the above-discussed drawbacks at low frequencies, experimental assessment of radiation damping offers several advantages compared to a purely numerical assessment. The behavior of complex materials is properly taken into account, and when the measurements are conducted in the actual mounting condition, even the effect of the mechanical boundary conditions can be realistically addressed. In this work, we exploit these advantages and characterize the dynamical behavior of structures by an experimental procedure. The structural response is given by

$$\mathbf{v}_\mathrm{r} = \mathbf{Y}(\omega)[\mathbf{f}_\mathrm{s} + \mathbf{f}_\mathrm{i}], \qquad (1)$$

in which $\mathbf{Y}(\omega) \in \mathbb{C}^{n_\mathrm{r} \times n_\mathrm{e}}$ is the experimentally determined matrix of mobilities relating the force excitation to the surface velocity. The angular frequency is defined as $\omega = 2\pi f$. We consider the general case in which the vector $\mathbf{v}_\mathrm{r} \in \mathbb{C}^{n_\mathrm{r}}$ contains three velocity degrees of freedom (DOF) for each node on the response grid – that is one velocity DOF for each spatial dimension. The same applies to the excitation vector in square brackets on the right-hand

side of equation (1), which is defined on a (possibly different) excitation grid. It comprises structural excitation $\mathbf{f}_\mathrm{s} \in \mathbb{C}^{n_\mathrm{e}}$ as well as excitation $\mathbf{f}_\mathrm{i} \in \mathbb{C}^{n_\mathrm{e}}$ by an incident acoustic field.

The acoustic field, which comprises incident and scattered sound waves, is described by the Helmholtz equation and evaluated numerically, thus avoiding the use of acoustic measurement facilities and associated limitations. In the context of this work, mainly unbounded acoustic domains are of interest, since acoustic radiation damping is associated with far-field sound radiation. In this regard, BEM [22] is particularly well-suited for solving the Helmholtz equation, since it does not require special treatments for truncating the far-field sound radiation. Reformulation of the Helmholtz equation by the Kirchhoff integral theorem and subsequent discretization by direct collocation BEM yields the linear system of equations [25]

$$\mathbf{H}\mathbf{p} = \mathbf{G}\big(\mathbf{v}_\mathrm{f} - \mathbf{v}_\mathrm{f}^\mathrm{i}\big) + \mathbf{H}\mathbf{p}^\mathrm{i}. \qquad (2)$$

The vectors $\mathbf{p} \in \mathbb{C}^{n_\mathrm{f}}$ and $\mathbf{v}_\mathrm{f} \in \mathbb{C}^{n_\mathrm{f}}$ contain the complete sound pressure and fluid particle velocities, i.e., the sum of the respective incident and scattered fields. The coefficient matrices $\mathbf{H}$ and $\mathbf{G}$ are fully populated and frequency dependent. Acoustic sources are considered by the incident sound pressure $\mathbf{p}^\mathrm{i}$ and the corresponding incident particle velocity $\mathbf{v}_\mathrm{f}^\mathrm{i}$.

The fluid loading on the structure can be expressed by the coupling condition

$$\mathbf{f}_\mathrm{f} = \mathbf{C}_\mathrm{ef}\mathbf{p}, \qquad (3)$$

where the coupling matrix $\mathbf{C}_\mathrm{ef} \in \mathbb{R}^{n_\mathrm{e} \times n_\mathrm{f}}$ relates the acoustic quantities on the BE mesh to the excitation grid. Its computation is presented in Section 2.1. Substituting equation (2) into equation (3) yields

$$\mathbf{f}_\mathrm{f} = \mathbf{C}_\mathrm{ef}\mathbf{H}^{-1}\mathbf{G}\mathbf{v}_\mathrm{f} + \underbrace{\mathbf{C}_\mathrm{ef}\big(\mathbf{p}^\mathrm{i} - \mathbf{H}^{-1}\mathbf{G}\mathbf{v}_\mathrm{f}^\mathrm{i}\big)}_{\mathbf{f}_\mathrm{i}}. \qquad (4)$$

The first term on the right-hand side of equation (4) can be interpreted as a reaction force acting on the structure by virtue of the acoustic field. It includes the effects of radiation damping and added mass, which are included in the measured mobility matrix $\mathbf{Y}(\omega)$ in equation (1). The second term on the right-hand side is the excitation force due to the incident acoustic field. It equals the force vector $\mathbf{f}_\mathrm{i}$ on the right-hand side of equation (1). Once the structural velocity $\mathbf{v}_\mathrm{r}$ is evaluated for a given excitation, the fluid particle velocity is obtained by the continuity condition

$$\mathbf{v}_\mathrm{f} = \mathbf{C}_\mathrm{fr}\mathbf{v}_\mathrm{r}, \qquad (5)$$

where the matrix $\mathbf{C}_\mathrm{fr} \in \mathbb{R}^{n_\mathrm{f} \times n_\mathrm{r}}$ establishes the coupling between the experimental response grid and the BE nodes. Finally, the sound pressure field can be computed via equation (2).

The proposed hybrid procedure can be incorporated into the design process once subcomponents or prototypes

are available. For example, in-situ mobility measurements could be conducted on a prototype hull of a transport vehicle, and the results could in turn be used to asses the acoustic loading transmitted to the inside. Once the mobility matrix $\mathbf{Y}(\omega)$ is determined, the acoustic response to different excitations can be computed without repeating the experiments. As we will see in Section 2.2, even the response to diffuse incident fields can be computed in the low frequency range without need of special facilities.

But of course, these advantages come at the cost of experimentally determining the mobility matrix $\mathbf{Y}(\omega)$ of a possibly three-dimensional, large scale structure. While the associated effort may have been prohibitive a decade ago, nowadays it becomes manageable due to the arising developments and automation of LDV. The excitation in the measurements is carried out by means of an automated modal hammer in this work. While it is indeed cumbersome to re-position the hammer and to repeat the LDV scan, oftentimes one is only interested in a local excitation, e.g., in an excitation by a point or line force. In these cases, it is not necessary to excite the whole surface of the structure, since only certain columns of $\mathbf{Y}(\omega)$ are needed. Moreover, symmetry properties can also be exploited to reduce the measurement effort in many applications [19]. Finally, we note that the proposed hybrid procedure is predominantly a low frequency method, and hence, coarse response and excitation grids are generally sufficient. Details on the experimental procedure for determining the mobility matrix $\mathbf{Y}(\omega)$ are reported for the test cases in Sections 3.2 and 4.

2.1 Mesh coupling

The response and excitation grids need to be coupled to the BE mesh in order to exchange field quantities between the subdomains, see equations (3) and (5). The continuity, for example between the surface velocity $\vec{v}_r$ of the structure and the fluid particle velocity v_f, can be expressed by the scalar equation

$$\vec{n} \cdot \vec{v}_r = v_f, \tag{6}$$

where $\vec{n}$ is the normal vector on the surface pointing away from the acoustic domain. In the discrete setting, equation (6) can only be satisfied when the response points in the mobility measurement coincide with the interpolation nodes of the acoustic BE mesh. However, there are several reasons that support the use of nonconforming BE meshes: The appropriate resolution of the response grid in the experiment can be well anticipated based on the expected number of bending waves of the occurring structural modes. On the other hand, regarding BEM, there is no meshing guideline available in the context of coupled structural acoustic problems and hence, convergence studies are necessary in order to judge the appropriateness of a given BE discretization. Moreover, when coincidence occurs in the frequency range of interest, the acoustic mesh needs to be finer than the structural grid. A gradual refinement of a BE mesh in this context is computationally affordable in most cases. In contrast, repeating the mobility measurements on a finer grid is excessively

time-consuming if not prohibitive. The use of non-conforming meshes also allows the choice of different interpolation functions in the BE model.

When using non-conforming BE meshes, the continuity condition in equation (6) needs to be reformulated in a weak sense, i.e. [26]

$$\int_\Gamma \phi \, \vec{n} \cdot \vec{v}_r \mathrm{d}\Gamma = \int_\Gamma \phi \mathbf{v}_f \mathrm{d}\Gamma, \tag{7}$$

in which Γ denotes the submerged surface. Following a Bubnov–Galerkin approach, the test function ϕ is chosen as the interpolation function of the fluid domain. After discretization, equation (7) can be written in matrix from

$$\int_\Gamma \mathbf{N}_f^T \mathbf{n}^T \mathbf{N}_r \mathrm{d}\Gamma \, \mathbf{v}_r = \int_\Gamma \mathbf{N}_f^T \mathbf{N}_f \mathrm{d}\Gamma \, \mathbf{v}_f, \tag{8}$$

where $\mathbf{N}_f$ and $\mathbf{N}_r$ contain the interpolation functions associated with the BE mesh and the response grid in the experiment, respectively. Rearranging equation (8) yields the coupling matrix introduced in (5), i.e. [27]

$$\mathbf{C}_{fr} = \left[\int_\Gamma \mathbf{N}_f^T \mathbf{N}_f \mathrm{d}\Gamma \right]^{-1} \int_\Gamma \mathbf{N}_f^T \mathbf{n}^T \mathbf{N}_r \mathrm{d}\Gamma. \tag{9}$$

Note that the matrix in square brackets is also known as the boundary mass matrix $\mathbf{\Theta}$. Similar derivations are possible for the coupling matrix $\mathbf{C}_{ef}$, which was introduced in equation (3) to relate field quantities in the BE domain to the excitation grid.

The response and excitation grids used in the mobility measurements are defined respectively by subdividing the surface of the structure into quadrilateral elements. Both, response and excitation elements have shape functions which approximate the geometry of the surface. The nodes associated with those shape functions are denoted as geometrical nodes and they are located on the edges and boundaries of the element, i.e. neighboring elements share common geometrical nodes. Further, the above introduced interpolation functions contained in $\mathbf{N}_r$ (and similarly those in $\mathbf{N}_e$ for the excitation grid) establish a spatial approximation of field quantities. The associated nodes are called interpolation nodes. In the experiment, the structure under test needs to be excited at interpolation nodes of the excitation grid and the response needs to be measured at the interpolation nodes of the response grid. In order to avoid excitation and measurements on the edges and corners of the structure, interpolation nodes are placed inside the elements leading to discontinuous approximation of field quantities across element boundaries. In this work, quadrilateral elements with eight-noded, bi-quadratic geometry approximation and constant interpolation functions are used for the excitation and response grids. For the acoustic BE mesh, quadrilateral elements with nine-noded, bi-quadratic geometry approximation and discontinuous, bi-linear interpolation functions are employed. These elements are shown in Figure 2.

The integral in equation (9) cannot be evaluated element-wise, since the interpolation functions of the response
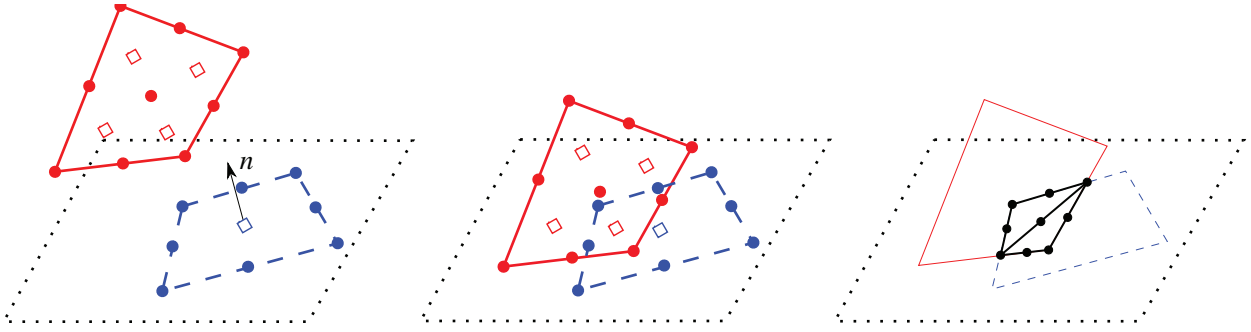
Figure 2. Schematic of the mortar projection of a master acoustic element (solid, red) onto the auxiliary plane (dotted) defined by an overlapping slave structural element (dashed, blue) and subsequent definition of triangular integration cells. Solid circles represent geometrical nodes and hollow squares represent interpolation nodes.

grid are not continuous across acoustic boundary elements and vice versa. This issue is overcome by a Mortar method [28], which works as follows: First, the acoustic boundary elements are defined as the master elements, and the elements on the response grid are defined as the slave elements, respectively, and pairs of overlapping elements are identified by a search algorithm. Then, an auxiliary projection plane and a corresponding normal vector are defined based on the slave element. The master element is then projected onto that plane, the resulting intersection area is subdivided into triangular elements, and integration is performed over them. The procedure is schematically depicted in Figure 2.

2.2 Diffuse field excitation

One of the main advantages of the proposed hybrid approach is the capability to experimentally determine the response to diffuse acoustic fields without unwanted effects associated with the measurement room. Usually, experimental characterization of structures subject to diffuse field excitation are conducted in reverberation rooms. These rooms need to be large enough in order to avoid modal behavior of the incident acoustic field, which is often an issue in the low frequency range. In contrast, application of incident acoustic fields in BEM only relies on accurate modeling of the scatterer's geometry.

There are three different approaches available to numerically predict the response to a diffuse acoustic field [29, 30]: (1) excitation by a set of random plane waves, (2) stochastic analysis based on power spectral densities (PSD), and (3) actual modeling of a large-enough reverberant room. Modeling a cavity that is large-enough to admit a diffuse sound field is computationally prohibitive when using a conventional BEM formulation. The approach based on PSD allows analytical modeling of the diffuse field but requires singular value decomposition and truncation of the PSD matrix in order to avoid inversion of fully populated BE matrices. But even with truncation of the PSD matrix, the plane wave approach, which was originally proposed by Rafaely [31], has been shown to be more efficient [29] and is thus followed here. The energy quantity of interest is computed as the average value among multiple simulations.

In each of those simulations, the structure is excited by a combination of N incident plane waves. The incident sound pressure $p^{\mathrm{i}}(\vec{x})$ and corresponding particle velocity $v_{\mathrm{f}}^{\mathrm{i}}(\vec{x})$ at the interpolation node with the coordinate vector $\vec{x}$ are obtained from

$$p^{\mathrm{i}}(\vec{x}) = \frac{1}{\sqrt{N}} \sum_{i=1}^{I} \sum_{j=1}^{J} p_{i,j} \mathrm{e}^{\mathrm{i}\left(\vec{k}_{i,j} \cdot \vec{x} + \theta_{i,j}\right)}, \quad \text{and} \qquad (10)$$

$$v_{\mathrm{f}}^{\mathrm{i}}(\vec{x}) = \frac{1}{\sqrt{N}} \sum_{i=1}^{I} \sum_{j=1}^{J} \frac{p_{i,j}}{\rho c} \vec{n} \cdot \vec{k}_{i,j} \mathrm{e}^{\mathrm{i}\left(\vec{k}_{i,j} \cdot \vec{x} + \theta_{i,j}\right)}. \qquad (11)$$

The plane waves arrive from spatially uniformly distributed directions and are arranged on a semi-sphere. The corresponding wave vectors are given as

$$\vec{k}_{i,j} = \frac{\omega}{c} \left[\cos \alpha_i \sin \beta_j, \, \sin \alpha_i \sin \beta_j, \, \cos \beta_j\right]^{\mathrm{T}}, \qquad (12)$$

with $\alpha_i = i\pi/I$ and $\beta_j = 2j\pi/J$. Further, I is the integer value of $\sqrt{N\pi/4}$ and J is the integer value of $2I\sin\alpha_i$. Each of the N plane waves have a normally distributed amplitude $p_{(i,j)}$ and a random phase $\theta_{(i,j)}$.

2.3 Hybrid evaluation of radiation damping

The extent of radiation damping can be quantified either by modal loss factors, which are properties of the structural acoustic system, or by excitation dependent loss factors, which are a result of a harmonic response analysis [8]. Once the vibroacoustic response is evaluated by equations (1)–(5), the excitation dependent radiation loss factor for a specific frequency point is obtained via [32]

$$\eta_{\mathrm{r}} = \frac{P}{|\omega E_{\mathrm{tot}}|}. \qquad (13)$$

The time-averaged radiated sound power P can be computed from the acoustic quantities via

$$P = \frac{1}{2} \mathrm{Re}\left(\mathbf{p}^{\mathrm{T}} \mathbf{\Theta} \mathbf{v}_{\mathrm{f}}^{*}\right), \qquad (14)$$

where $(\cdot)^*$ denotes the conjugate complex and $\text{Re}(\cdot)$ refers to the real part of a complex quantity. The definition of the boundary mass matrix $\boldsymbol{\Theta}$ was introduced in equation (9) and the paragraph thereafter. Note that the imaginary part of the complex sound power corresponds to near-field sound radiation, which has a mass-like effect on the structure and hence, does not dissipate energy.

For time-harmonic problems, the time-averaged total vibrational energy E_{tot} in equation (13) equals twice the time-averaged kinetic energy or alternatively, twice the time-averaged potential energy. The latter requires knowledge of the (static) stiffness matrix of the structure under test, which can not be estimated by mobility measurements. Instead, in the proposed hybrid procedure, we will compute the time-averaged total vibrational energy based on the kinetic energy of the structural acoustic system, i.e.

$$E_{\text{tot}} = \frac{1}{2}\mathbf{v}_{\text{r}}^{\text{T}}\left(\mathbf{M}_{\text{r}} - \frac{\text{i}}{\omega}\mathbf{C}_{\text{rf}}\mathbf{H}^{-1}\mathbf{G}\mathbf{C}_{\text{fr}}\right)\mathbf{v}_{\text{r}}^*, \qquad (15)$$

in which the mass matrix $\mathbf{M}_{\text{r}}$ of the structure under test is set up by estimating the structural mass contribution of each element on the response grid. For structures with uniform thickness and mass density, the mass contribution of each element is simply its area percentage times the total mass of the structure. Equation (15) also includes energy contributions of the fluid field, where the imaginary part of $\mathbf{H}^{-1}\mathbf{G}$ corresponds to the additional mass effect of the fluid, while the real part corresponds to the energy dissipated by sound radiation. A more elaborate discussion of equation (15) and the alternative way of evaluating the total energy are given in Appendix A.

3 Assessment of radiation damping of rectangular honeycomb sandwich panels

3.1 Set-up of the demonstrator

The set-up of the demonstrator is shown in Figure 3. A flat aluminum honeycomb sandwich panel is mounted onto a tub-shaped concrete foundation. The foundation has a square cross section of 0.8×0.8 m^2, a height of 0.4 m and a vertically tapered wall thickness of around 0.06–0.1 m. The short edges of the rectangular panel are glued into aluminum F-profiles, which are then screwed onto the upper edge of the foundation. The long edges of the panel are not fixed and hence permit air flow between the two sides of the panel. The free length of the panel is approximately 0.750 m whereas two panel widths are studied. The studied panels are denoted with letters A and B, and their dimensions are given in Table 1. The material properties of aluminum and the honeycomb core are provided in Table 2. The concrete foundation is assumed to be rigid in this work.

3.2 Mobility measurements

The mobility matrix is determined by using an automated modal hammer (NV Tech SAM1 [33]), which allows to measure the exerted force by means of a force cell in the
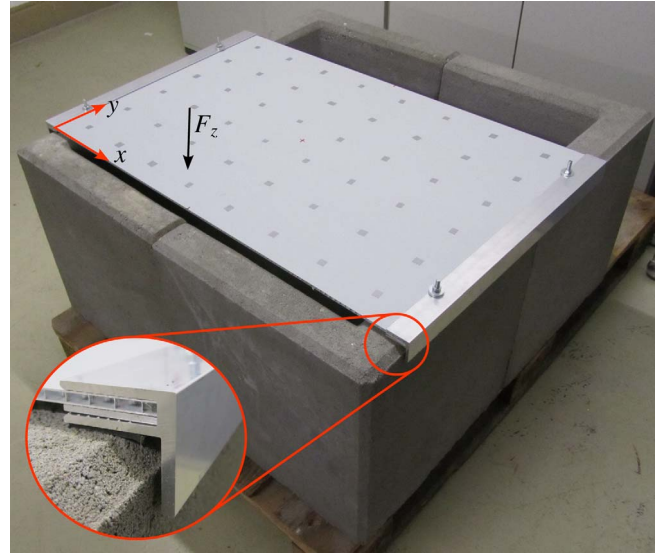

Figure 3. Set-up of the demonstrator including an aluminum honeycomb sandwich panel mounted onto a concrete foundation. The black arrow indicates the location of the point force introduced in Section 3.4.

hammer tip. The device is placed inside the concrete foundation using a flexible measurement stand allowing to position the hammer tip at the nodes of the excitation grids. A uniform excitation grid of 6×4 ($n_{\text{e}} = 24$) is used for panel A, and likewise 6×2 ($n_{\text{e}} = 12$) for panel B in order to derive the respective mobility matrices.

The velocity response is measured by means of scanning LDV using a single head Polytec PSV 500 system. The PSV 500 includes a camera for geometry alignment so that Euler compensation is applied to correct for the angle of laser beam incidence. Regarding the resolution of response grids, preceding (in-vacuo) modal analyses of the panels have been conducted with FEM in order to estimate the number of bending waves in the considered frequency range up to 625 Hz. Then, the response grids are defined such that a minimum of three elements capture one bending wave length. This corresponds to a response grid of 8×6 ($n_{\text{r}} = 48$) for panel A, and likewise 8×4 ($n_{\text{r}} = 32$) for panel B. The resulting mobility matrices $\mathbf{Y}(\omega)$ are of dimension 48×24 and 32×12, respectively. Reflective tape is applied to the surfaces of the panels in order to improve the signal-to-noise ratio, see Figure 3. The velocity response is only measured on the top side of the panel and hence, the mobility data needs to be copied to the bottom side in order to couple the mobility matrix to the three-dimensional BE mesh. This approach is valid as long as the response of the panel only involves anti-symmetric bending motion, i.e. thickness deformation of the core does not occur, which is a reasonable assumption in the low frequency range.

The mobility matrix $\mathbf{Y}(\omega)$ is obtained by relating the measured velocities at the response nodes to the measured force at the excitations nodes. The corresponding transfer functions are evaluated based on a H$_1$-estimator in the frequency range up to 625 Hz with a resolution of approximately 0.4 Hz. Rectangular window functions are applied

Table 1. Dimensions of aluminum honeycomb sandwich panels.

		Panel A	Panel B
Face sheet thickness, front	t_f	0.5 mm	0.5 mm
Face sheet thickness, back	t_b	0.5 mm	0.5 mm
Core thickness	h	3 mm	4.5 mm
Dimensions	$l_x \times l_y$	0.752×0.5 m^2	0.748×0.2 m^2

Table 2. Material properties of aluminum face sheets and aluminum honeycomb core.

Aluminum face sheets		
Density	ρ_f	2690 kg/m^3
Young's modulus	E	70 GPa
Poisson's ratio	v_a	0.3
Aluminum honeycomb core		
Density	ρ_c	135 kg/m^3
Young's modulus	E_x, E_y	10 MPa[*]
Young's modulus	E_z	360 MPa
Shear modulus	G_{xy}	1 MPa[*]
Shear modulus	G_{yz}	280 MPa
Shear modulus	G_{xz}	140 MPa
Poisson's ratio	v_c	0.01[*]

[*] Values that are not explicitly given by the manufacturer are

to the velocity as well as to the force signals in order to perform a fast Fourier transformation (FFT). The measurement time is large enough so that the signals die out within the window. All measurements are repeated ten times and complex frequency domain averaging is used to reduce the noise that is not phase correlated.

Although the mobility matrix $\mathbf{Y}(\omega)$ is subsequently coupled to different BE models representing the acoustic conditions (1)–(3), the actual measurement of $\mathbf{Y}(\omega)$ is conducted only once in a standard laboratory without absorbent treatments on the walls. This is a convenient choice and neglects the influence of the acoustic field on the structural response. This assumption will be justified later in Section 3.5, in which fully coupled FEM–BEM simulations are presented for the purpose of verification.

3.3 Boundary element models

As described in Section 2.1, the acoustic field around the panel is discretized by quadrilateral boundary elements with discontinuous bilinear interpolation functions. Uniform meshes with 36×24 elements along the in-plane directions of panel A, and 48×12 elements for panel B are employed. Moreover, the following three models for the acoustic domain are used in this work to study the effect of acoustic boundary conditions:

- Condition (1): The panel is assumed to be confined in an infinitely large acoustic baffle that prohibits flow between its two sides. Two independent acoustic sub-domains on each side are modeled using a halfspace formulation with a modified Green's function [34]. This condition resembles the situation in a window
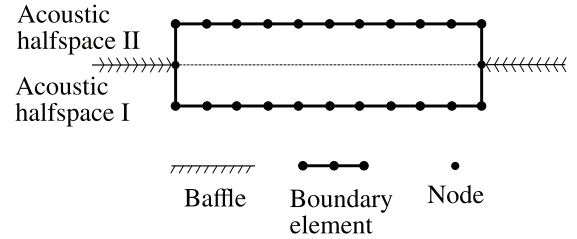
Figure 4. Cross-sectional schematic of a baffled panel modeled by two acoustic half-space BE meshes.

test rig. The corresponding BE model is schematically illustrated in Figure 4.
- Condition (2): The panel is assumed to be unbaffled and is situated in an acoustic full space. A single BE mesh with a closed surface is used. This condition resembles the situation in an anechoic chamber.
- Condition (3): The concrete foundation is additionally modeled. The sound waves radiated from the panel are scattered on the rigid surfaces of the foundation. A corresponding BE mesh of the foundation accommodating panel A is shown in Figure 8.

The numerals 1–3 after the alphabetical designation denote the considered configuration – e.g. panel A confined in a baffle will be referred to as panel A-1 in what follows.

3.4 Results obtained by hybrid procedure

This section studies radiation damping of the panels using the hybrid procedure described in Section 2. The focus is set on the influences of acoustic condition and excitation on radiation damping. The panels are excited by point forces, monopole sources and by diffuse incident fields. The point forces with magnitude of $F_z = 1$ N are located at ($x = 0.31$ m, $y = 0.06$ m, $z = h/2$) of panel A, and likewise at ($x = 0.31$ m, $y = 0.05$ m, $z = h/2$) of panel B. The coordinate system is defined such that the x-axis points in the direction of the long edges and the xy-plane coincides with the midplane of the panel, see Figure 3. The monopole sources are located at ($x = 1$ m, $y = 0$ m, $z = 0.3$ m). The responses to diffuse incident fields are computed as the mean value of 300 sample simulations as described in Section 2.2. The excitation in each simulation is given by the summation of $N = 1145$ incident plane waves with normally distributed amplitudes with a mean value of 1 Pa and random phases. The convergence of the response to diffuse field excitation with respect to the number of sample simulations will be analyzed later in this section.

Figure 5 shows the experimentally determined point mobility of panel A. The corresponding radiated sound power and total power are plotted in Figure 6 for conditions (1)–(3). Those power quantities are computed using equations (14) and (15), and are later required to evaluate the extent of radiation damping. When comparing panels A-1 and A-2, we notice a considerable difference in radiated sound power in the low frequency range. This can be explained by the acoustic short circuiting occurring in panel A-2 (i.e. the panel with unbaffled condition), which significantly reduces radiation efficiency. The difference in radiated sound power narrows with increasing frequency. The radiated sound power of panel A-3 (i.e. the panel with foundation) lies in between the curves of panels A-1 and A-2 for the most part of the considered frequency range, expect when cavity resonances occur inside the foundation. At the respective resonance frequencies, the radiated sound power of panel A-3 exhibits noticeable peaks that are marked with vertical dashed gray lines in Figure 6. The total power of the three panels shows only marginal differences, which arise due to the different BE matrices in the computation of the kinetic energy (cf. Eq. (15)). The structural velocity is the same for all three panels since the mobility measurement is only conducted once. A similar analysis based on a fully coupled FEM–BEM procedure will be presented in Section 3.5.

The resulting radiation loss factors are shown in Figure 7 for panels A and B in conditions (1)–(3). Sharp minima in the loss factors occur at the eigenfrequencies that are associated with bending modes in which sound pressure cancellation occurs between neighboring half-cells. This cancellation decreases in effect with increasing frequency. The baffled panels (A-2 and B-2) exhibit high radiation damping already in the low frequency range due to the first bending mode that radiates sound like a piston without cancellation. In contrast, the unbaffled panels (A-1 and B-1) show much lower damping values due to the sound pressure cancellation at the edges, as already discussed in the context of Figure 6. As radiation efficiency increases with frequency, the curves converge to each other. Distinct maxima in radiation damping occur around the cavity resonance frequencies of panel A-3. They are related to the sound power peaks encountered in Figure 6. Note that panel B is only 200 mm wide and hence do not work as a closure of the tub-shaped foundation, which explains why this panel does not exhibit cavity resonances.

While the analysis in Figure 7 is limited to point force excitation, the main advantage of the proposed hybrid procedure is the capability to model excitation by incident acoustic fields. The procedure is illustrated in Figure 8 for panel A-3 at 145 Hz. First, an incident field with sound pressure $\mathbf{p}_i$ is created and the resulting excitation force $\mathbf{f}_i$ is computed by BEM via equation (4). Then, the structural response is evaluated via equation (1) using the experimental mobility matrix. Subsequent projection onto the BE mesh by equation (5) yields the fluid particle velocity. The latter only takes values on the panel, since the foundation is assumed to be rigid, see middle subplot in Figure 8. Finally, the complete sound pressure field $\mathbf{p}$ is computed by
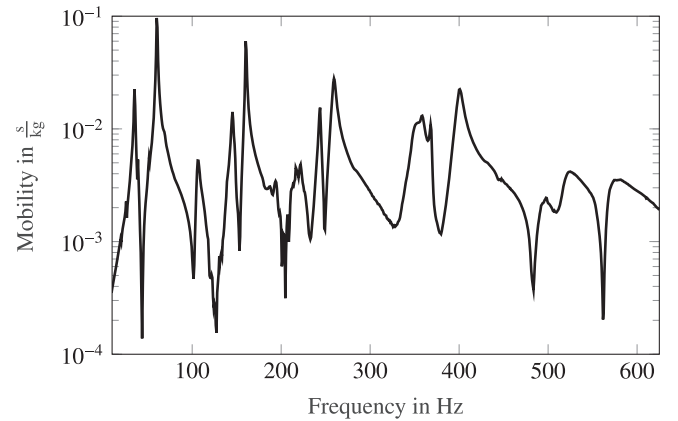

Figure 5. Measured point mobility of panel A at ($x = 0.31$ m, $y = 0.06$ m, $z = h/2$).

BEM and the radiation loss factor can be evaluated in a post processing step.

The radiation loss factors for diffuse field excitation are obtained by constructing multiple realizations of incident acoustic fields such as the one shown on the left subplot in Figure 8. The verification of this averaging approach is presented in Figure 9, which plots the mean value for the radiation loss factor of panel A-3 at 145 Hz with increasing number of incident field realizations. Each additional realization corresponds to a simulation with $N = 1145$ random incident plane waves. We notice that a number of 300 realizations is a reasonable compromise between computational effort and accuracy. This also holds for other frequency points and test cases in this work.

Figure 10 studies the excitation dependence of radiation damping. Loss factors for excitations by point forces, monopole sources and diffuse incident fields are shown. We notice significantly higher radiation damping when the panel is subject to incident acoustic fields. This can be explained by the spatially uniform distribution of the incident pressure field in the low frequency range that almost acts like a plane wave excitation. In frequency regions apart from the eigenfrequencies, this leads to a more uniform sound pressure distribution on the panel than is achieved by a point force excitation. At the eigenfrequencies however, radiation loss factors are expected to be independent of the excitation when the respective mode is (exclusively) excited. In that case, they are equal to the corresponding modal radiation loss factor [8]. This aspect is illustrated on the right subplot of Figure 10, in which all the structural resonance frequencies of panel B are marked with vertical dashed gray lines. We can observe that the loss factors for the three different types of excitation coincide at these frequencies. Note that a similar behavior is expected from panel A, but exceptions occur when the frequency resolution is too coarse, or when the respective mode is not exclusively excited.

The left subplot of Figure 10 shows extremely high radiation loss factors occurring around the cavity resonance frequencies of panel A-3. At 537 Hz, even $\eta_r = 1$ is approached, which indicates that almost all of the vibrational energy is
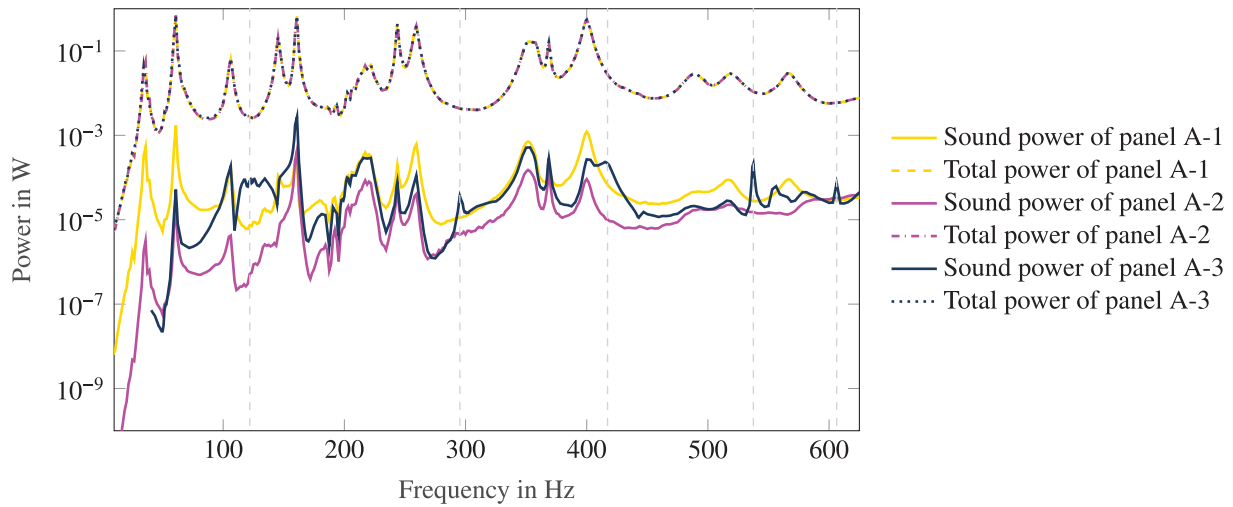
Figure 6. Radiated sound power and power corresponding to total vibrational energy of point-excited panel A evaluated by hybrid procedure. Vertical dashed gray lines indicate cavity resonances occurring in panel A-3.
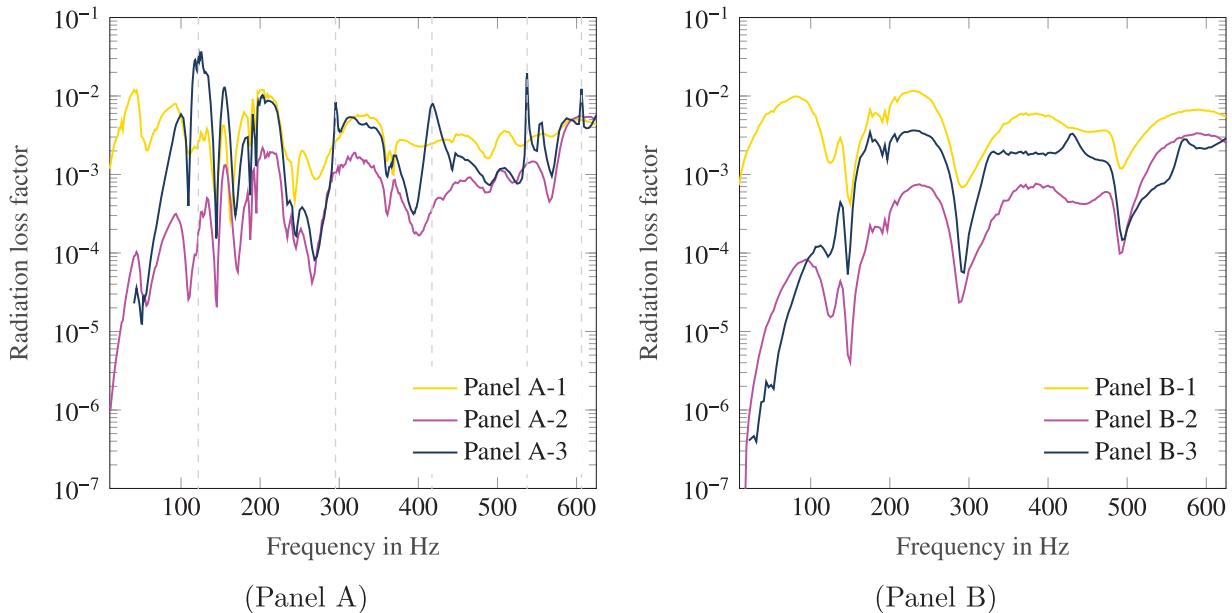

(Panel A)   (Panel B)

Figure 7. Radiation loss factors evaluated by hybrid procedure for point force excitation. Vertical dashed gray lines indicate cavity resonances occurring in panel A-3.

dissipated by sound radiation. This is a surprising result and requires further investigation in the future. It might be even possible to exploit the effect of (higher order) cavity resonances in order to deliberately dissipate vibrational energy by radiation damping.

3.5 Comparison to results obtained by coupled FEM–BEM procedure

The panels are now analyzed by a purely numerical FEM–BEM approach for the purpose of verification and comparison. The acoustic BE model is coupled to an FE model of the sandwich panel consisting of eight-noded quadrilateral shell elements based on the Reissner–Mindlin

theory for the representation of the face sheets and twenty-noded hexahedral solid elements for the core. The FE meshes of the panels comprise the same number of elements in the in-plane directions as the respective BE meshes. The mounting of the panels is modeled by constraining the translational DOFs along the center line of the short edges. Moreover, the relative displacement among the nodes on the short edges are also constrained in order to avoid unrealistic local deformation of the core. The FE modeling of the sandwich panels is schematically illustrated in Figure 11. A hysteretic loss factor of $\eta_s = 0.01$ is used in all upcoming simulations. While this is an assumed value, we note that structural damping has a negligible influence on radiation damping, as long as it is light and spatially homogeneous.
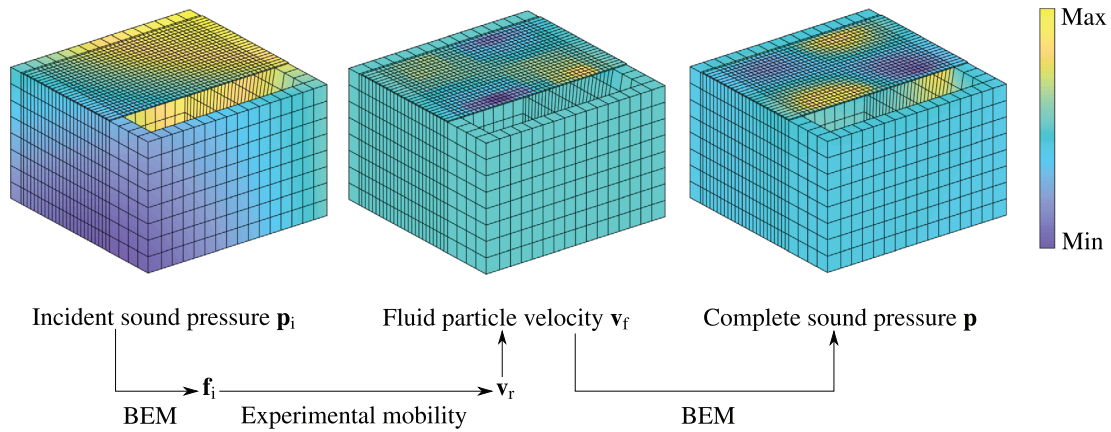
Incident sound pressure $\mathbf{p}_i$ Fluid particle velocity $\mathbf{v}_f$ Complete sound pressure $\mathbf{p}$

Figure 8. Hybrid procedure for evaluating the response to incident acoustic fields. The forcing vector corresponding to an incident acoustic field is computed by BEM. Then, the structural response is determined using the measured matrix of mobilities. Finally, the resulting acoustic field is computed by BEM. All subsplots show the real parts of the respective complex-valued quantities.

Figure 12 shows the power quantities of panel A in conditions (1)–(3) subject to point force excitation at $(x = 0.31\ \mathrm{m},\ y = 0.06\ \mathrm{m},\ z = h/2)$. The results are computed by a fully coupled FEM–BEM procedure and are largely similar to the ones in Figure 6, which were obtained by the hybrid procedure. The only difference is that the FEM–BEM approach allows to include the reaction force due to the acoustic response and thus, capture the effect of acoustic conditions on the total vibrational energy. (Recall that the structural velocity was the same for all three acoustic conditions in the hybrid procedure, since the mobility measurement was only conducted once.) However, despite the mutual structural acoustic coupling, we only notice marginal differences in the total vibrational energy occurring in the vicinity of the resonance peaks, which are slightly shifted and rounded at higher frequencies due to the structural and acoustic damping contributions. This finding justifies that the mobility measurements reported in Section 3.2 were only conducted once per panel in a standard laboratory without absorbent treatments on the walls.

Figure 13 shows a comparison of diffuse field radiation loss factors obtained by the hybrid and the FEM–BEM procedure. We notice a good agreement across the whole frequency range for both panels. For panel B, even the resonance frequencies match the numerically predicted ones well with deviations ranging between 5% and 25%. This indicates that the simply supported boundary conditions in the FE model resembles the actual mounting condition with acceptable accuracy (cf. Fig. 3). Note that neither material properties nor the boundary conditions were "tuned" in the FE model in order to match the experimental results.

4 Assessment of radiation damping of a C-shaped aluminum sandwich panel

The second test case involves a C-shaped sandwich panel with a total thickness of 4 mm consisting of aluminum face sheets and a Polyethylen core. Due to prestress
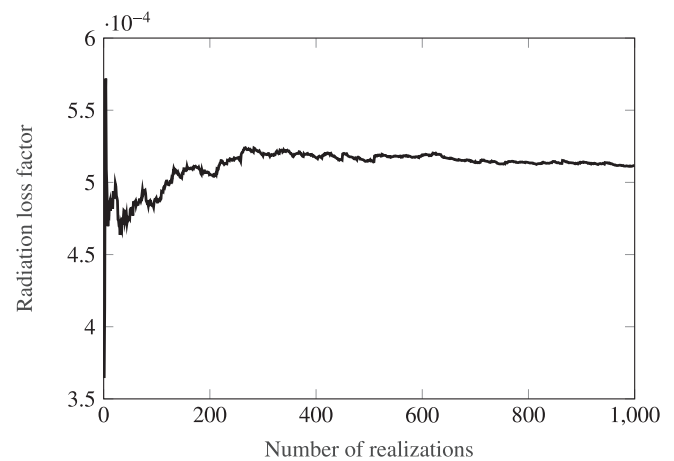

Figure 9. Mean value of the radiation loss factor of panel A-3 at 145 Hz with increasing number of random incident field realizations.

resulting from the bending of the panel during manufacturing, its elastic properties are subject to uncertainties, which makes the panel a suitable application for the proposed hybrid procedure. The set up is shown in Figure 14. The panel has a depth of 500 mm and a radius of 365 mm, which corresponds to an unfolded length of 1147 mm. Aluminum L-profiles are screwed onto the straight edges of the panel, which are then mounted onto the concrete foundation. The geometrical dimensions of the foundation were provided in Section 3.1. The material parameters of the unprocessed sandwich panel are listed in Table 3.

Only point force excitation is considered for this test case. The point force acts in radial direction and is located inside the C-shaped panel at an angular coordinate of approximately $0.13\ \pi$ and a distance of 100 mm from the edge in longitudinal direction. The excitation in the mobility measurement is again realized by a modal hammer that is positioned inside the concrete foundation (see Fig. 14). The velocity response in radial direction is measured by LDV, whereas the scanning process is divided into four runs
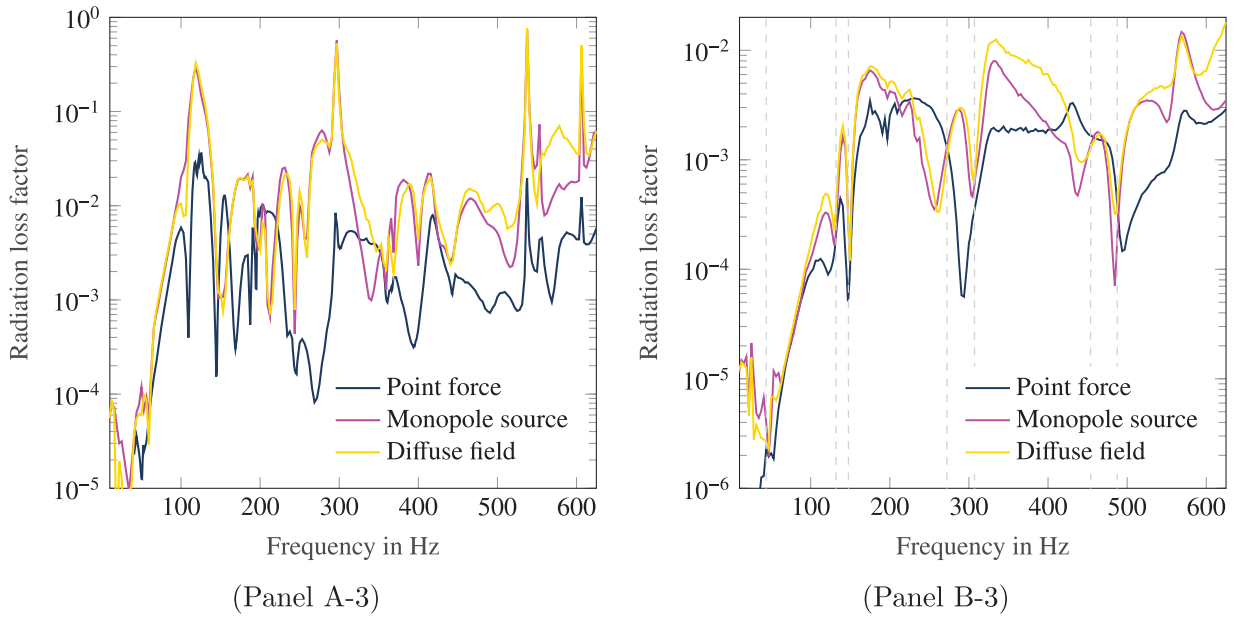
(Panel A-3)

(Panel B-3)

Figure 10. Radiation loss factors evaluated by hybrid procedure. Comparison among different types of excitation. Vertical dashed gray lines indicate structural resonances in panel B-3, at which the three loss factors are expected to coincide.
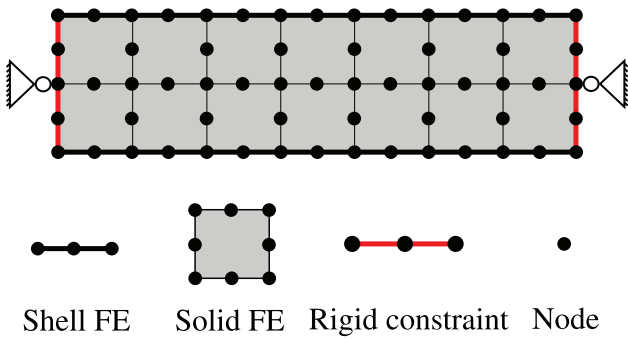

Figure 11. Cross-sectional schematic illustrating the FE modeling of a sandwich panel.

in order to ensure that all points on the response grid are well accessed by the laser. In each of the runs, the LDV is (re-)positioned and a $\pi/4$ arc of the surface is respectively measured. The force signal in the hammer is used as reference to retrieve phase information of all responses. Based on the anticipated structural modes, a uniform response grid of 5 points in longitudinal times 30 points in circumferential direction is employed, resulting in a total of $n_r = 150$ response points. The corresponding transfer functions are computed in the frequency range up to 375 Hz with a resolution of approximately 0.16 Hz. The frequency steps are smaller as compared to the test case in Section 3.2, since a longer measurement time was required to ensure that the signal has died out.

Acoustic radiation damping of the C-shaped panel is assessed by the proposed hybrid procedure. In this test case, only radiation into a free acoustic field is considered, and hence, the BE model only includes the panel but not the concrete foundation. No acoustic baffles are modeled either.

The BE mesh consists of 10 elements in longitudinal times 64 elements in circumferential direction. The resulting radiation loss factors are displayed in Figure 15. In addition, the loss factors obtained by the coupled FEM–BEM approach are also plotted. The underlying FE model of the sandwich panel is defined similar to ones described in Section 3.5 and comprises the same number of elements in the longitudinal and circumferential directions as the BE mesh.

In the considered frequency range, the C-shaped panel exhibits rather low radiation damping. The loss factors predicted by the hybrid and the purely numerical approach agree qualitatively with each other. Both of them indicate a gradual increase from $\eta_r = 10^{-5}$ to maximum values of around $\eta_r = 0.003$. However, we also notice significant differences, particularly around the dips at resonance frequencies. The latter are poorly predicted by the FE model, most likely due to the inadequate assumption of simply supported boundary conditions and due to prestress resulting from the bending of the panel during manufacturing. These findings encourage the use the proposed hybrid procedure for an accurate assessment of radiation damping in the low frequency range under consideration of the actual mounting condition and realistic material properties.

5 Summary and conclusion

A hybrid experimental-numerical approach has been proposed for assessing acoustic radiation damping. The transfer functions characterizing the structural mobility are experimentally determined by means of automated hammer excitation on a grid and scanning LDV. Given the fact that radiation damping is particularly relevant in complex material configurations with a high ratio of bending stiffness to mass, this approach offers the advantage of
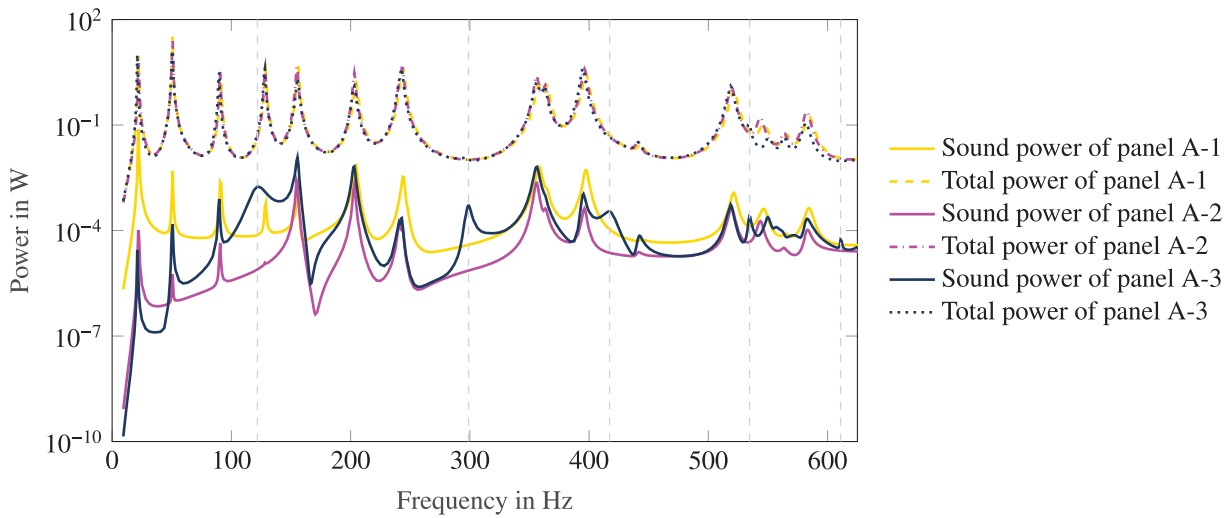
Figure 12. Radiated sound power and power corresponding to total vibrational energy of point-excited panel A evaluated by fully coupled FEM–BEM procedure. Vertical dashed gray lines indicate cavity resonances occurring in panel A-3.
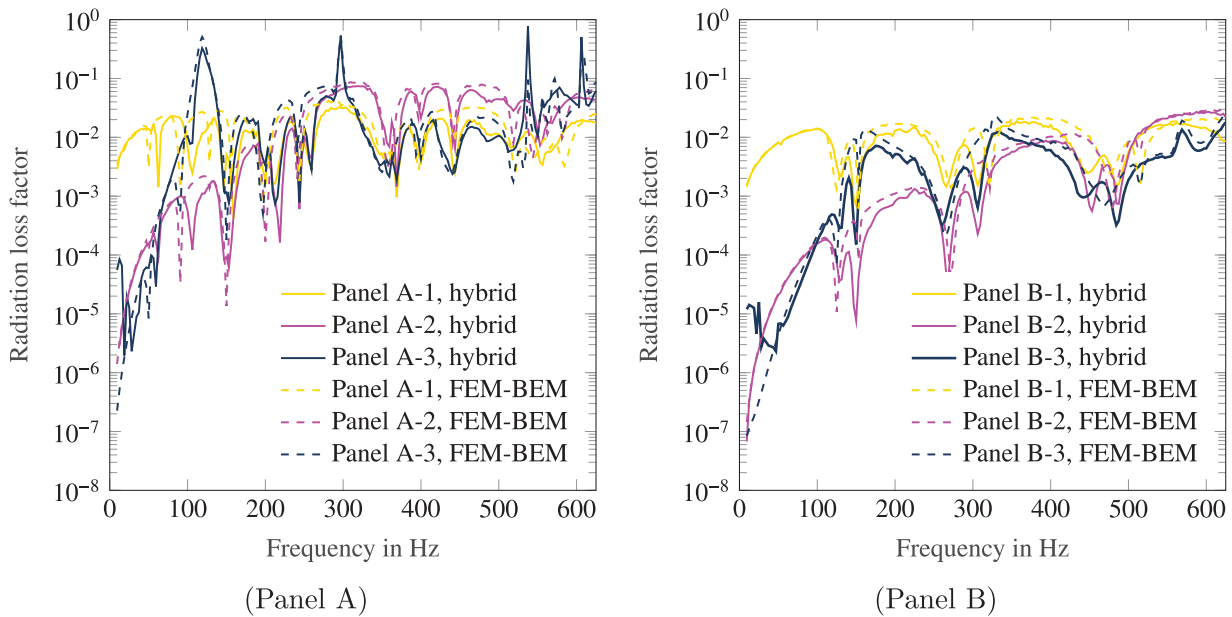

(Panel A)   (Panel B)

Figure 13. Radiation loss factors for diffuse field excitation. Comparison of hybrid approach to FEM–BEM procedure.

avoiding intricate constitutive modeling. Moreover, mobility measurements allow consideration of the actual mounting condition. The latter has a significant influence on the participating structural modes and thus radiation damping in the low frequency range.

While the structural behavior is characterized experimentally, the acoustic response that is needed for assessing radiation damping is computed by simulation. Thus, the limitations associated to acoustic measurements are avoided. The experimentally obtained matrix of mobilities is coupled to an acoustic BE model allowing to compute the response to diffuse acoustic fields even in the low frequency range. Moreover, the actual acoustic field can be modeled including the effect of acoustic short circuiting due to slits and gaps.

Rectangular aluminum honeycomb panels mounted onto a tub-shaped foundation served as demonstrator for verifying the proposed hybrid procedure. The structural mobilities of the panels were determined once and then coupled to various BE models resembling different acoustic conditions. The results illustrate that radiation damping is strongly dependent on the actual acoustic condition in the low frequency range. Moreover, using the same matrix of mobilities, radiation loss factors for excitation by point forces, monopole sources and diffuse incident fields were computed. Finally, radiation loss factors of a C-shaped panel were determined, in which the material properties are difficult to predict due to prestress. The findings underline the importance to properly consider mounting conditions, excitation and the actual acoustic field for an

Figure 14. Set up of the demonstrator including a C-shaped aluminum sandwich panel mounted onto a concrete foundation. A modal hammer inside the foundation provides the excitation for the mobility measurements. The red cross approximately indicates the point of excitation on the inside of the panel.

Table 3. Material properties of aluminum sandwich panel with Polyethylen core.

Aluminum face sheets		
Thickness	t	0.5 mm
Density	ρ_f	2690 kg/m^3
Young's modulus	E	70 GPa
Poisson's ratio	v_a	0.3
Polyethylen core		
Thickness	h	3 mm
Density	ρ_c	1603 kg/m^3
Young's modulus	E_c	1 GPa[*]
Poisson's ratio	v_c	0.1[*]

[*] Values that are not explicitly given by the manufacturer are assumed and marked with an asterisk.

accurate low-frequency assessment of radiation damping. Clearly, these demands can hardly be met by a purely experimental approach and thus, support the use of the proposed hybrid procedure.

Surprisingly high radiation loss factors were observed around the cavity resonance frequencies indicating that a large fraction of the vibrational energy is dissipated by sound radiation. This result requires further investigation in the future as it might open up new possibilities for exploiting radiation damping in order to deliberately dissipate vibrational energy.

Besides the assessment of radiation damping, this hybrid framework could also be used for evaluating sound transmission without the need of special facilities. This does not only include standard sound insulation measurements of partitions between two rooms. Further applications include the assessment of transmitted acoustic loading to the inside of transport vehicles. For example, space telescopes are subject to heavy acoustic loading during launch and typically carry vulnerable payloads such as cameras
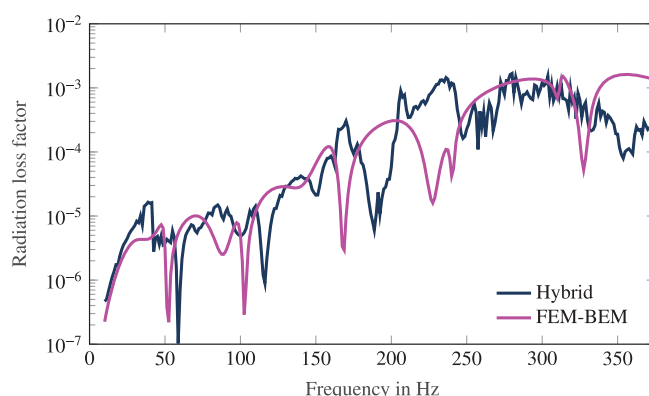

Figure 15. Radiation loss factor of the C-shaped aluminum sandwich panel subject to point force excitation. Comparison of hybrid approach to FEM–BEM procedure.

and scientific instruments. Often, the primary structures of spacecrafts also feature gaps and slits to address thermal expansion, which can hardly be addressed by purely acoustic measurements.

While we have briefly compared the results of the proposed hybrid approach to those obtained by a coupled FEM–BEM approach, proper benchmarking with respect to state-of-the-art experimental methods (e.g. ISO 3745) is an ongoing task.

Conflict of interest

The authors declare no conflict of interest.

Acknowledgments

References

1. D.J. Mead: Passive vibration control, John Wiley & Sons Ltd, Chichester, England, 1999.
2. R.A. Mangiarotty: Acoustic radiation damping of vibrating structures. Journal of the Acoustical Society of America 35, 3 (1963) 369–377.
3. B.L. Clarkson, K.T. Brown: Acoustic radiation damping. Journal of Vibration, Acoustics, Stress, and Reliability in Design 107 (1985) 357–360.
4. O.P. Hentschel, M. Bonhage, L. Panning-von Scheidt, J. Wallaschek, M. Denk, P.A. Masserey: Analysis of an experimental setup for structural damping identification. Journal of Theoretical and Applied Mechanics 54, 1 (2016) 27–39.
5. R. Zhou, M.J. Crocker: Sound transmission loss of foam-filled honeycomb sandwich panels using statistical energy analysis and theoretical and measured dynamic properties. Journal of Sound and Vibration 329, 6 (2010) 673–686.

6. C. Scrosati, F. Scamoni, M. Bassanino, M. Mussin, G. Zambon: Uncertainty analysis by a round robin test of field measurements of sound insulation in buildings: single numbers and low frequency bands evaluation – airborne sound insulation. Noise Control Engineering Journal 61, 3 (2013) 291–306.

7. P. Bonfiglio, F. Pompoli: Numerical methodologies for optimizing and predicting the low frequency behavior of anechoic chambers. Journal of the Acoustical Society of America 134, 1 (2013) 285–291.

8. S.K. Baydoun, S. Marburg: Investigation of radiation damping in sandwich structures using finite and boundary element methods and a nonlinear eigensolver. Journal of the Acoustical Society of America 147, 3 (2020) 2020–2034.

9. M.J. Crocker, A.J. Price: Sound transmission using statistical energy analysis, Journal of Sound and Vibration 9, 3 (1969) 469–486.

10. K. Renji, P.S. Nair: On acoustic radiation resistance of plates. Journal of Sound and Vibration 212, 4 (1998) 583–598.

11. A. Billon, C. Foy, J. Picaut, V. Valeau, A. Sakout: Modeling the sound transmission between rooms coupled through partition walls by using a diffusion model. Journal of the Acoustical Society of America 123, 6 (2008) 4261–4271.

12. E. Reynders: Parametric uncertainty quantification of sound insulation values. Journal of the Acoustical Society of America 135, 4 (2014) 1907–1918.

13. A. Arjunan, C.J. Wang, K. Yahiaoui, D.J. Mynors, T. Morgan, V.B. Nguyen, M. English: Development of a 3d finite element acoustic model to predict the sound reduction index of stud based double-leaf walls. Journal of Sound and Vibration 333 (2014) 6140–6155.

14. C.W. Isaac, M. Pawelczyk, S. Wrona: Comparative study of sound transmission losses of sandwich composite double panel walls. Applied Sciences 10, 4 (2020) 1543.

15. M. Okuma: Low frequency noise and vibration analysis of boat based on experiment-based substructure modeling and synthesis, in Vibro-Impact Dynamics of Ocean Systems and Related Problems, R.A. Ibrahim, V.I. Babitsky, M. Okuma, Eds., Springer, Berlin, Heidelberg. 2009, pp. 203–214.

16. T. Tomatsu, T. Otsuka, M. Okuma, T. Okada, T. Ikeno, K. Shiomi: Sound-radiation analysis for boat hull based on hammering test and bem, in Proceedings of ASME 2005 International Design Engineering Technical Conferences and Computers and Information in Engineering Conference, September 24–28, 2005, Long Beach, California USA, pp. 259–264.

17. M. Shepherd, J.B. Fahnline, T.P. Dare, S.A. Hambric, R.L. Campbell: A hybrid approach for simulating fluid loading effects on structures using experimental modal analysis and the boundary element method. Journal of Acoustical Society of America 138, 5 (2015) 3073–3080.

18. M. Xia, S. Li: A combined approach for active vibration control of fluid-loaded structures using the receptance method. Archive of Applied Mechanics 88 (2018) 1683–1694.

19. N.B. Roozen, Q. Leclère, D. Urbán, T. Méndez Echenagucia, P. Block, M. Rychtáriková, C. Glorieux: Assessment of the airborne sound insulation from mobility vibration measurements; a hybrid experimental numerical approach. Journal of Sound and Vibration 432 (2018) 680–698.

20. C.B. Goates, C.B. Jones, S.D. Sommerfeldt, J.D. Blotter: Sound power of vibrating cylinders using the radiation resistance matrix and a laser vibrometer. Journal of the Acoustical Society of America 148, 6 (2020) 3553–3561.

21. T.P. Bates, I.C. Bacon, J.D. Blotter, S.D. Sommerfeldt: Vibration-based sound power measurements of arbitrarily curved panels. Journal of the Acoustical Society of America 151, 2 (2022) 1171–1179.

22. S. Kirkup: The boundary element method in acoustics: a survey. Applied Sciences 9, 8 (2019) 1642.

23. N. Trompette, J.-L. Barbry, F. Sgard, H. Nelisse: Sound transmission loss of rectangular and slit-shaped apertures: experimental results and correlation with a modal model. Journal of the Acoustical Society of America 125, 1 (2009) 31–41.

24. T. Shimizu, Y. Kawai, D. Takahashi: Numerical analyses and experimental evaluation of reduction technique for sound transmission through gaps. Applied Acoustics 99 (2015) 97–109.

25. S. Marburg, B. Nolte: A unified approach to finite and boundary element discretization in linear time-harmonic acoustics, in Computational Acoustics of Noise Propagation in Fluids. Finite and Boundary Element Methods, S. Marburg, B. Nolte, Eds., Springer, Berlin, Germany. 2008, pp. 1–34.

26. A. de Boer, A.H. van Zuijlen, H. Bijl: Comparison of conservative and consistent approaches for the coupling of non-matching meshes. Computer Methods in Applied Mechanics and Engineering 197 (2008) 4284–4297.

27. H. Peters, S. Marburg, N. Kessissoglou: Structural-acoustic coupling on non-conforming meshes with quadratic shape functions. International Journal for Numerical Methods in Engineering 91, 1 (2012) 27–38.

28. B. Flemisch, M. Kaltenbacher, B.I. Wohlmuth: Elasto-acoustic and acoustic-acoustic coupling on non-matching grids. International Journal for Numerical Methods in Engineering 67, 13 (2006) 1791–1810.

29. P. Rong, M. Abele, O. von Estorff: Comparison of different methods for simulating acoustic diffuse field excitations. Acta Acustica United with Acustica 99 (2013) 931–939.

30. A. Panteghini, A. Feriani, E.A. Piana, N.B. Roozen: Evaluation of the sound reduction index of flat panels through FE models accounting for fluid-structure interaction: stochastic versus plane wave superposition methods. Journal of Sound and Vibration 509 (2021).

31. B. Rafaely: Spatial-temporal correlation of a diffuse sound field. Journal of the Acoustical Society of America 107, 6 (2000) 3254–3258.

32. F. Fahy, P. Gardonio: Sound and structural vibration, Academic Press, Oxford, United Kingdom, 2007.

33. P. Blaschke, T. Mallareddy, D. Alarcòn: Application of a scalable automatic modal hammer and a 3D scanning laser doppler vibrometer on turbine blades, in Proceedings of the 4th VDI conference in vibration analysis and identification, VDI Berichte, vol. 2259, 2016.

34. M. Ochmann, H. Brick: Acoustical radiation and scattering above an impedance plane, in Computational Acoustics of Noise Propagation in Fluids. Finite and Boundary Element Methods S. Marburg, B. Nolte, Eds., Springer, Berlin, Germany. 2008, pp. 459–494.

Appendix A

Assessment of the total vibrational energy in coupled structural acoustic systems

The discretized equation of motion of a structural acoustic system, in which BEM is applied to the acoustic subdomain, reads

$$\left[\mathbf{K} - \omega^2\mathbf{M} + \mathrm{i}\omega\mathbf{C}_{\mathrm{rf}}\mathbf{H}^{-1}\mathbf{G}\mathbf{C}_{\mathrm{fr}}\right]\mathbf{u} = \mathbf{f}, \qquad (16)$$

where $\mathbf{u}$ is the unknown displacement vector, $\mathbf{K}$ and $\mathbf{M}$ are the structural stiffness and mass matrices, and $\mathbf{f}$ is the excitation force. The matrix $\mathrm{i}\omega\mathbf{C}_{\mathrm{rf}}\mathbf{H}^{-1}\mathbf{G}\mathbf{C}_{\mathrm{fr}}$ introduces additional mass and damping forces due to the acoustic field. Structural damping is neglected in the following.

As discussed in Section 2.3, the time-averaged total vibrational energy E_{tot} can be expressed as twice the time-averaged potential energy, i.e.

$$E_{\mathrm{tot}} = \frac{1}{2}\mathbf{u}^{\mathrm{T}}\mathbf{K}\mathbf{u}^* - \frac{1}{2}\mathbf{f}^{\mathrm{H}}\mathbf{u}. \qquad (17)$$

where the first term in equation (17) corresponds to the energy due to the elastic strain and the second term is the work done by external forces. In view of equation (16), it is obvious that E_{tot} may also be written as

$$E_{\mathrm{tot}} = \frac{1}{2}\mathbf{u}^{\mathrm{T}}\left(\omega^2\mathbf{M} - \mathrm{i}\omega\mathbf{C}_{\mathrm{rf}}\mathbf{H}^{-1}(\omega)\mathbf{G}(\omega)\mathbf{C}_{\mathrm{fr}}\right)\mathbf{u}^*, \qquad (18)$$

which is equivalent to equation (15). When using e.g. FEM for modeling of the structural vibration [8], the evaluation of equation (17) is more favorable, since it does not involve fully populated BE matrices. All the necessary quantities including the stiffness matrix $\mathbf{K}$ are readily available.

However, as discussed in Section 2.3, the situation is different when characterizing the structural behavior by mobility measurements. In that case, it is not possible to estimate the (static) stiffness matrix $\mathbf{K}$, and the approach in equation (18) is more appropriate. Finally, we note that the expressions in equations (17) and (18) are not fully equivalent to each other when structural damping contributions are considered.